Anabaena Sensory Rhodopsin : effect of mutations on the ultrafast photo-isomerization dynamics

Damianos Agathangelou

UNIVERSITÉ DE STRASBOURG

ÉCOLE DOCTORALE PHYSIQUE ET CHEMIE-PHYSIQUE

Institut de Physique et Chimie des Matériaux de Strasbourg

THÈSE **présentée par :**

Damianos Agathangelou

soutenue le: **14 Janvier 2019**

pour obtenir le grade de : **Docteur de l'Université de Strasbourg**

Discipline/ Spécialité: **Chimie Physique**

Anabaena Sensory Rhodopsin : Effect of mutations on the ultrafast photo-isomerization dynamics

---

DIRECTEUR DE THÈSE:

Dr. Stefan Haacke	Professeur, Université de Strasbourg

RAPPORTEURS :

Dr. Rolf Diller	Professeur, University of Kaiserslautern
Dr. Steve Meech	Professeur, University of East Anglia

EXAMINATEURS :

Dr. Vincent Robert	Professeur, Université de Strasbourg
Dr. Tatiana Domratcheva	Professeur associé, Max-Planck Heidelberg

Contents

Acknowledgments

Initially, I would like to say thanks to my PhD supervisor Prof. Stefan Haacke for giving me the opportunity to work in the Biodyn group. During the last three and a half years I earned a lot of things by his side,he taught me how to do serious research, understanding deeply the topics we are working on and also how to be autonomous.

In addition I would like to express my thanks to our collaborators involved in the project. These are: Massimo Olivucci, Maria Del Carmen Marín, Yoelvis Orozco-Gonzalez, Nicolas Ferré, Elisa Pieri, K-H Jung, Hideki Kandori, Yoshitaka Kato, Rei Abe Yoshizumi, Tiago Buckup, Partha Pratim Roy and Giulio Cerullo. It was a joy to work with you and I believe we had a nice and fruitful collaboration.

At this point I will refer to each of the Biodyn members and thank them for everything they have taught me and shared with me along the time we spent together. I really appreciate and respect them as persons and researchers and I am willing to keep our close friendship relation even after leaving from Strasbourg.

I start with Mr. Olivier Crégut whom I consider as my Lab father. Since the day I arrived in IPCMS on March 5th 2015 he was there for me every single day spending hours and hours on explaining and teaching me everything about optics and lasers. Every time he was entering the door and I mentioned “Mr Olivier we have a problem” he always had a smile and was ready to help me without hesitating. Whenever I asked him if he thinks we have everything working fine, his response was “I would say it’s not bad”, which is the definition of the word “perfect” in my dictionary.

I continue with Johanna Brazard with whome I have spent the last two and a half years since her arrival in July 2016. Johanna was the person who removed all the stress from me and we worked together mainly on developing the 2DES setup and HPLC. I will never forget our visit in Milan in March 2017. Johanna am really sorry for stabing you with the needles and for skipping lunch the first day. Rumours say that until today there is some of our protein spilled on the optical table. Whenever I will face some problems I will always bring in mind the expression “Lets wish for the best”.

Anastasia “τρέλλα μου” we were together for three years in the same team working in different rooms but we could always find some time to make fun and laugh with the people around us during coffee brakes. I will always have in mind how calm and silent you were when somebody was trying to offend your work. Obviously am joking, and I promise to keep our greek temperament wherever I go; it’s our signature.

Youssef “my post-doc”. You were taking care of me the first one and a half year despite your own work. You taught me how to avoid being anxious and control my stress; believe me I don’t feel anything now. I really take seriously your advices and I hope we will work together in the future.

Dr. Li Liu you know how much I appreciate you. I remember our arguing time during my Erasmus visit. The next years we became very close friends and you taught me a lot of things including noodles. Even when I was sick you were passing by my house to leave me some drugs (it sounded a bit weird) and even cook for me. I will never forget our visits at the Chinese restaurant with the hot-pot and off-course the chocolate treasures you had hidden in the office.

Edo "pucci" thank you very much for getting me addicted to smoking again, it's great to have good Mediterranean friends who want their friends to gain health problems. Every day you were reminding me how important it is to bother working people while laughing and how to say "no" to everybody. Maybe sometimes we were a nightmare for people around (I don't mention names) but I think everybody needs an Edo for changing their daily routine. Thank you very much for answering all my questions in chemistry, spending several hours explaining me stuff (remember the Feynman diagrams).

Thomas you were the first person who showed me how an up-conversion setup works and I was calling you "boss". I will never forget our first meeting with Stefan, where you were supporting me and encouraging me to start the presentation. Thank you also for being very annoying in the office while listening your rock-death-metal music; I enjoyed it. As a scientist, you are always un-pleased with the results and you want everything to work perfectly. Thus, I take you as an example.

Moussa, it's been already two years since you left but I don't forget you. Thank you very much for sharing your pump probe setup with me and for teaching me how to work efficiently only until 18h00 (this never happened for me). I won't forget you presence in the lab singing Celine Dion while doing the laser alignment. Off course the best moments were when you were accidentally hitting your head on the metallic supports above the optical table.

Vincent Kemlin the hardcore post-doc. Thank you very much for the "grilling" during group meeting presentations. I found it very useful for me and I admit this was one of the factors helping to improve myself. The interaction with you helped me to get more inside the topics of 2DES and lasers. I will always remember our "random example".

Robin Pierron, your arrival in the group last March gave me another good friend. We didn't interact so much but you gave me good vibes when performing experiments and writing. From now on I will speak with you only in American.

Finally, I would like to thank Jérémie Leonard for all the useful discussions we had. As a group leader, you were asking the right questions and making the comments directly to the point solving in this way many of our problems. I keep in mind one incidence when I was forced to lie to you in order to bring you in the lab and make you a birthday surprise. Your response "I trusted you and you lied to me" will prevent me for doing the same in the future; maybe not.

In addition I want to thank all my friends in Strasbourg and Cyprus with which we had a great time outside of the institute. Those were Despoina, Eva, Vasiliki, Anna, Nataly and Paolo from Strasbourg and Giorgos, Constantinos, Andreas, Evanthia, Tasos from Cyprus.

I would like to put my friend Arthur in honorable mentions for the good time we had in Strasbourg inside and outside of the institute. Thanks a lot for all the advices mainly concerning food and gym.

I kept last my family which are the people I owe everything in my life. These are my mother Maria, my father Giannakis, my brothers Andreas and Eirineos and my cousins Tasos, Andri and Nikos. I know they have hard time due to my absence during the last 10 years I have been studying abroad. For this reason this thesis is dedicated to them. In addition to my family I include my best friend and "brother" Evros who was the one getting me in the research direction. We had a dream together to become experimental physicists one day, since we were studying in Greece and we are on a good way to achieve it now. Finally, I would also like to thank Rene for all the support during the first two years of my PhD.

Résumé de thèse de doctorat

Introduction

Notre domaine de recherche porte sur l'étude photophysique des protéines rétiniennes et en particulier des Rhodopsines Sensorielles. Ce sont des systèmes photosensibles qui, lors de l'absorption de la lumière, subissent un changement de conformation appelé isomérisation. Ce dernier processus est ultrarapide ($<10^{-12}$s) et se déroule sur le chromophore rétinien de la protéine. Grâce au mécanisme d'isomérisation, l'énergie du photon absorbé est convertie en énergie chimique et est utilisée par le système pour l'exécution d'une fonction biologique spécifique. Nos études se concentrent sur cette étape initiale de la réaction chimique où nous voulons déterminer la vitesse et l'efficacité de ce processus, et comment celles-ci sont influencées par l'environnement protéique. C'est un principe très général qui s'applique à de nombreux photocapteurs biologiques (PYP, GFP, etc.) et fait encore l'objet de débats.

Outre notre intérêt pour les protéines rétiniennes, une partie de nos travaux est consacrée au développement de nouveaux outils spectroscopiques. Dans ce contexte, une installation de spectroscopie électronique bidimensionnelle femtoseconde est développée, qui utilise une paire d'impulsions à phase bloquée de moins de 10fs à 400 nm pour l'excitation. Le but de développer ce spectromètre est d'étudier l'hétérogénéité structurelle présente dans des systèmes similaires aux protéines rétiniennes en prenant l'avantage de résoudre le processus d'excitation de manière spectrale.

Anabaena Sensory Rhodopsin - Effet des mutations sur la dynamique de photo-isomérisation ultra-rapide

Le meilleur exemple connu de protéine rétinienne dans la nature est la rhodopsine (Rh), responsable de la vision chez les organismes vertébrés. L'isomérisation dans Rh se produit à environ 200fs[1], avec une efficacité exceptionnelle de 67% [2]. Pour cet exemple, Nature adapte et optimise l'environnement protéique afin que la réaction se produise rapidement et efficacement. Dans le cadre de cette dernière déclaration, nous étudions une rhodopsine microbienne appelée rhodopsine sensorielle Anabaena (ASR) fig.1a, qui représente un système modèle alternatif nous donnant l'occasion de voir l'effet de l'environnement protéique sur deux protéines différentes tout-trans (AT). conformations / isomères rétiniens 13-cis (13C) dans le même environnement protéique (fig.1b)[3],[4].

Le rapport des isomères dans les protéines dépend des conditions d'éclairage externe (intensité et longueur d'onde) qui atteignent un état photostationnaire, dit adapté à la lumière (LA). Fait intéressant, lors de l'incubation dans l'obscurité à la température ambiante, la population d'AT dépasse 97%, ce qui définit l'état appelé DA (Adapté à l'obscurité). AT et 13C subissent deux photo-cycles distincts s'interconversant sur une échelle de temps de la milliseconde (fig.1c) [5],[6].

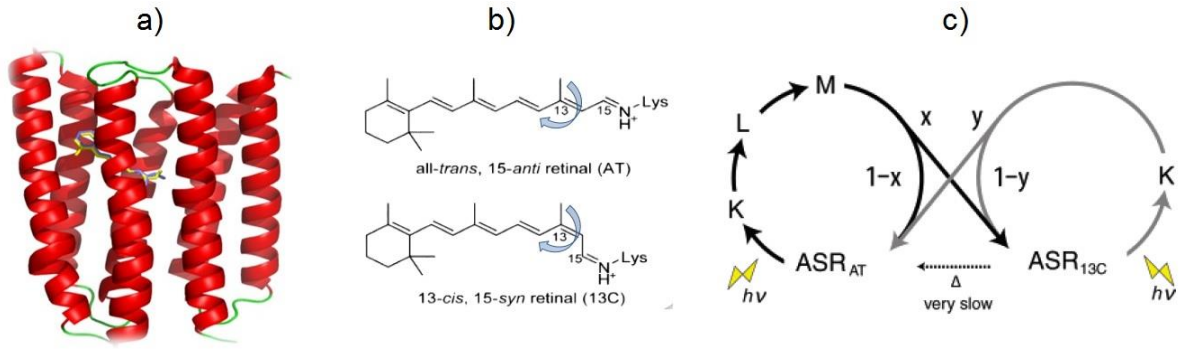

Fig.1: a) Structure cristallographique à rayons X ASR tracée à l'aide de la plateforme PyMol (données utilisées de la banque de protéines RCSB, bibliothèque: 1XIO); b) all-trans, 15-anti (AT) et 13-cis, 15-syn (13C) sont les conformations à l'état fondamental du PSBR; les flèches bleu clair indiquent la liaison C-C à laquelle se produit l'isomérisation. c) schéma de la référence 48 montrant les deux photo-cycles distincts se produisant pour les deux conformères d'état fondamental; Les lettres majuscules représentent les différents états intermédiaires formés dans chaque photocycle, tandis que x et y représentent les rapports de ramification des isomères AT et 13C.

L'absorption à l'état d'équilibre des isomères AT et 13C dans chaque protéine est illustrée à la figure 2a. Il a été montré que le décalage spectral de la transition S0→S1 est largement dominé par les interactions électrostatiques plutôt que par les effets stériques [7]. Dans le cas des mutants, nous avons observé un décalage vers le bleu du maximum d'absorption par rapport à l'ASR de type AT Wild, pouvant atteindre jusqu'à environ 33 nm dans le cas du mutant L83Q. Cette dernière est due à l'O-H dont l'extrémité négative est dirigée vers l'azote SB protoné, stabilisant ainsi S0.

La détermination expérimentale de l'ESL de chaque isomère dans la protéine a été obtenue en utilisant la technique de spectroscopie d'absorption transitoire (T.A.S) avec des impulsions laser inférieures à 50fs. La région de sondage pour l'enregistrement des différentes signatures spectroscopiques s'étendait de 330 nm (UV) à 1400 nm (NIR). Afin de mieux contrôler les conditions expérimentales en termes de contribution des isomères dans les échantillons, une chromatographie en phase liquide à haute performance (HPLC) a été utilisée.

La durée de vie de l'état excité de chaque isomère est déterminée par des mesures TAS dans la région NIR où se trouve la contribution de l'émission stimulée (SE). La contribution SE correspond à la transition de la décroissance de la population du premier état excité S1 à l'état fondamental S0. Une comparaison des traces cinétiques de cette contribution est montrée à la figure 2b, pour les isomères AT.

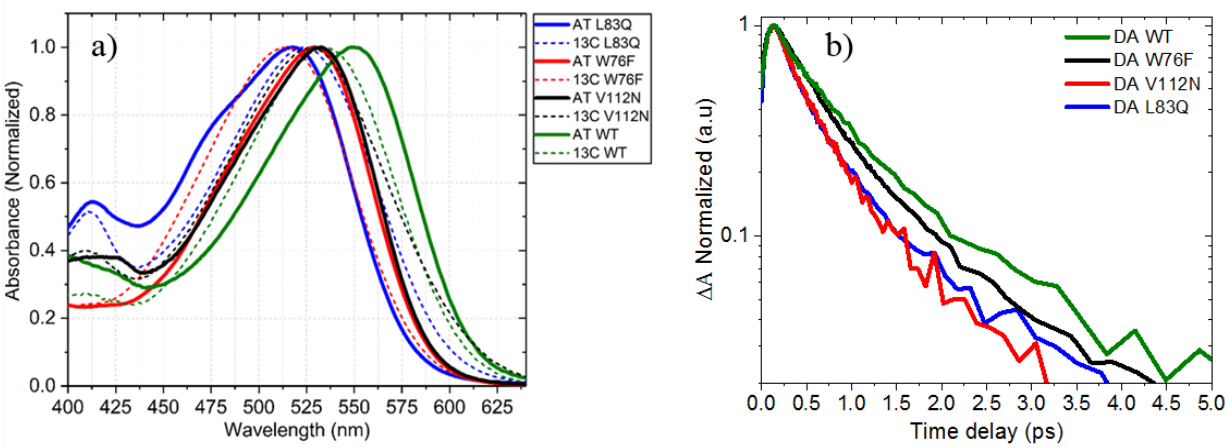

Fig. 2 a) Absorption à l'état d'équilibre des isomères AT et 13C pour le WT-ASR et les mutants; b) Tracés cinétiques de la longueur d'onde centrale de la contribution de la SE dans la région spectrale du proche infrarouge

La protéine native ASR appelée Wild Type (WT) présentait une différence de facteur 4,5 de la vitesse d'isomérisation des deux isomères. La forme AT s'isomérise à moins de 0,83ps, tandis que la forme 13C se forme à moins de 0,2ps. Dans tous les cas, les isomères AT des mutants absorbent à des longueurs d'onde plus courtes que WT-ASR et montrent une décroissance de l'état excité bi-exponentielle avec une amplitude dominante> 70% sur la constante de temps courte. À partir des ajustements, nous trouvons (0,50 ± 0,04) ps et (1,86 ± 0,2) ps pour AT W76F, (0,34 ± 0,04) ps et (1,27 ± 0,2) ps pour AT V112N et (0,28 ± 0,04) ps et (1,26 ± 0,2) ps pour AT L83Q. Les ESL sont identifiées au temps de décroissance moyen, c'est-à-dire (0,70 ± 0,05) ps pour W76F, (0,52 ± 0,05) ps pour V112N et (0,48 ± 0,05) ps pour L83Q. L'accélération de la réaction de photo-isomérisation chez les mutants décalés vers le bleu suggère une pente plus raide de la surface d'énergie potentielle à l'état excité (PES) que dans le WT-ASR. Ceci peut être expliqué de manière provisoire par une dégénérescence surélevée entre les états S1 et S2 lors de mutations, contrairement à AT WT-ASR où le mélange électronique entre S1 et S2 est plus important, induisant ainsi un PES plat au voisinage de la région de Franck-Condon.

Complémentaire dans le cas de l'isomère 13C (fig. 3), un traitement similaire des données a également entraîné une désintégration de l'état excité bi-exponentiel. Le temps de chute moyen pondéré a été déterminé comme étant (2,1 ± 0,3) ps pour 13C W76F, (0,52 ± 0,05) ps pour 13C L83Q, (0,41 ± 0,05) ps pour 13C V112N et (0,19 ± 0,05) ps pour 13C WT-ASR . Contrairement aux isomères AT, la réaction de photo-isomérisation chez les mutants décalés dans le bleu semble ralentir.

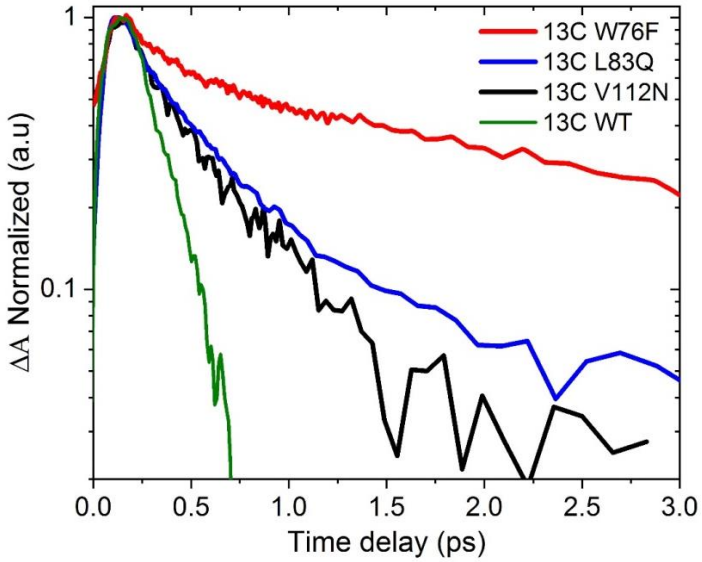

Fig. 3 : Tracés cinétiques normalisés à partir de la longueur d'onde individuelle de SE pour 13C-PSBR dans WT ASR et mutants

La polarité différente des acides aminés remplacés (mutations) accompagnée du caractère de transfert de charge de l'état excité peut expliquer les vitesses d'isomérisation observées expérimentalement. Les mutations modifient la surface d'énergie potentielle (PES) des états excités, la rendant plus raide ou plus plate que celle de la protéine native, entraînant ainsi des vitesses de réaction plus rapides ou plus lentes respectivement.

Les mesures TAS effectuées dans la plage spectrale UV-VIS ont révélé des signatures oscillatoires de modes vibratoires actifs à l'état excité et fondamental pour tous les mutants (figure 4), mais leur rôle fonctionnel dans la réaction à l'état excité n'est pas clair. La figure 4a montre une courbe cinétique à une longueur d'onde centrale ESA de AT W76F où les oscillations sont> 4 fois supérieures au bruit de fond. Celles-ci sont isolées en soustrayant une décroissance exponentielle double appropriée des données (figure 4a). En explorant une large plage de 27 nm (444-471 nm) (figure 4c), les résidus de longueur d'onde individuelle correspondent à la superposition (lignes brunes). Une FFT des résidus moyennés (ligne verte) donne le spectre de puissance présenté à la figure 2d avec des contributions dominantes à certaines fréquences. Le résultat général de cette analyse est la présence de modes de vibration situés à (70 ± 20) cm^{-1}, (160 ± 20) cm^{-1}, (210 ± 20) cm^{-1} et (300 ± 20) cm^{-1}. dans tous les mutants et WT ASR. Les modes> 160 cm-1 proviennent de l'état excité, tandis que la fréquence la plus basse comprise entre 60 et 70 cm^{-1} et détectée dans la région PA correspond aux oscillations du sol. Les décalages bleu / rouge de la fréquence de chaque mode se produisent dans une plage de ± 20 cm^{-1}, en fonction de la protéine et de la plage de détection.

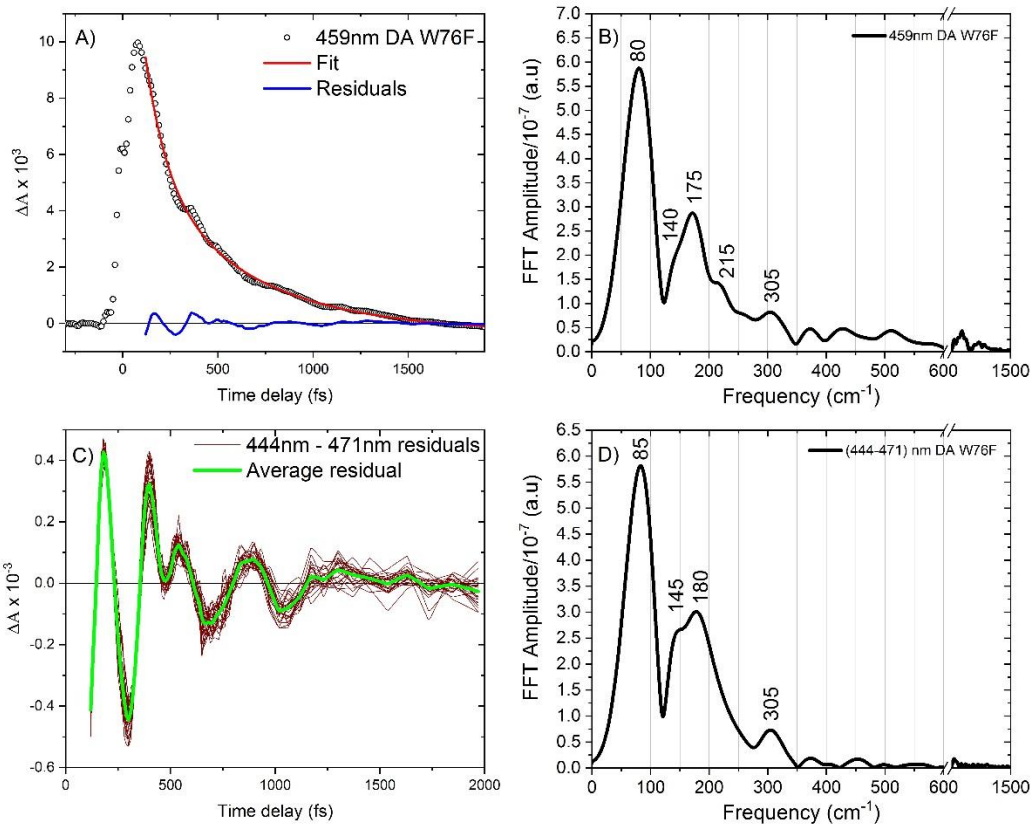

Fig. 4: Procédure d'extraction des oscillations à partir de données T.A. A) Trace cinétique à 459 nm de DA W76F; Les cercles noirs correspondent aux données expérimentales tandis que les lignes continues rouges et bleues s'adaptent et les résidus, respectivement. B) FFT des résidus déterminés à partir de A). C) Résidus de traces de cinétique dans la gamme de 441nm à 471nm (lignes avec la couleur du vin) et moyenne (vert clair). D) FFT de résidus moyenne de C). Une pause est utilisée pour montrer le bruit de fond défini, qui est ici l'amplitude des pics >1100cm^{-1}.

Un projet parallèle, étroitement lié au projet principal, concerne la production de mutants ASR à rendement quantique de fluorescence amélioré, par rapport au WT-ASR. Les calculs avancés QM / MM effectués par le groupe du professeur Massimo Olivucci ont prédit que des mutations simples ou doubles d'ASR pourraient potentiellement entraîner une augmentation de la fluorescence Q.Y de ces mutants. En réalisant ce type d'ingénierie de l'environnement protéique, il devrait être possible de créer des mutants avec des surfaces d'énergie potentielles spécifiques, en termes de forme et d'énergie relative.

Des mesures pour la détermination de l'ESL et du rendement quantique de fluorescence relatif ont été effectuées. Dans ce dernier but, une configuration de fluorescence sensible à l'état stable a été construite. Les résultats dans le cas du mutant W76S / Y179F ont montré une augmentation relative de Q.Y de fluorescence de 8 par rapport à AT WT ASR (fig. 5a). Ce dernier résultat est également corroboré par la durée de vie ESL déterminée à partir des données SE, alors que nous observons une augmentation relative environ 7 fois supérieure de l'ESL (fig. 5b). Dans le cas du mutant L83Q, un comportement opposé est observé lorsque nous avons une réduction de l'ESL d'un facteur deux, mais deux fois plus grande, Q.Y. relative. Ces dernières observations sont expliquées en termes de mélange électronique S1 et S2. Puisque S2 est un état non réactif, ce mélange conduit à un plateau défavorable de la

surface d'énergie potentielle de l'état excité. Ainsi, plus le mélange est prononcé, plus la durée de vie est longue.

Dans le cas du mutant W76S / Y179F, différents isomères, outre le canonique tout-trans et le 13-cis, sont présents dans l'état fondamental, comme nous l'avons déterminé à partir de notre appareil HPLC. Afin de déterminer que l'isomère AT est effectivement responsable de l'augmentation du QY de fluorescence et de l'ESL, nous avons effectué des expériences sur trois états photostationnaires DA, OA et GA (à l'aide d'une LED verte) où le pourcentage des isomères de différence variait. La clarification de notre hypothèse a également été appuyée expérimentalement et est en outre en accord avec les prévisions théoriques. Nous concluons donc que le mutant W76S / Y179F qui a montré une augmentation de Fl. QY et ESL peuvent être utilisés en optogénétique car les mutants Arch3 déjà utilisés pour différentes applications présentent des propriétés comparables[8].

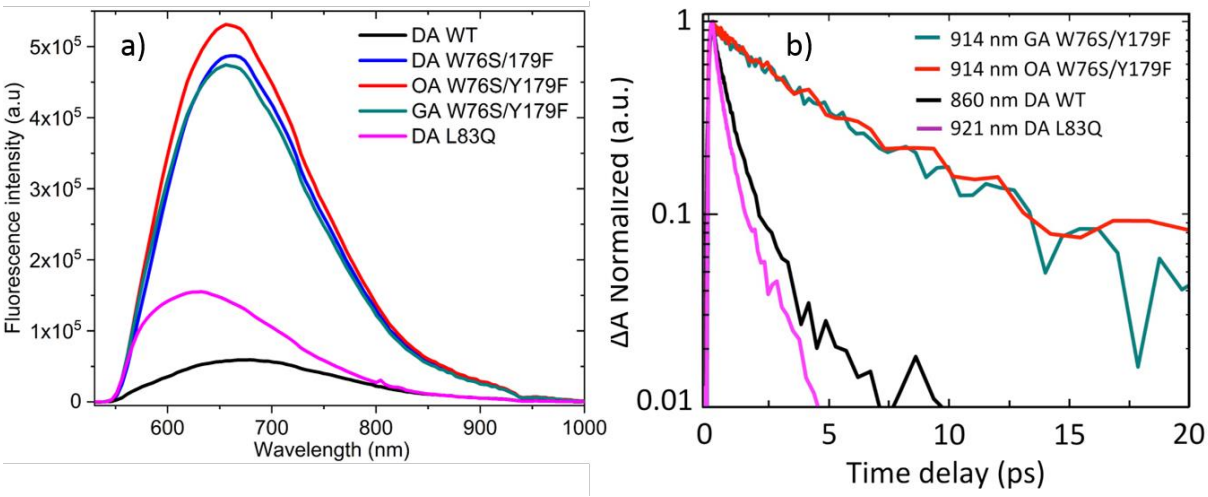

Fig. 5 (a) Fluorescence à l'état stable pour le mutant AT WT-ASR, DA L83Q et W76S / Y179F (b) Tracés cinétiques de la longueur d'onde centrale de la contribution de la SE pour des échantillons DA WT, DA L83Q, OA et GA W76S / Y179F.

Configurations expérimentales

Une partie de mon travail dans cette thèse consistait à mettre à niveau un spectromètre T.A utilisé auparavant pour la spectroscopie à cohérence vibratoire (VCS) en un spectromètre 2DES fonctionnant dans la plage spectrale UV-Vis. Le spectromètre 2DES utilise une paire d'impulsions de moins de 10fs verrouillées en phase dans la plage du proche UV-bleu 360-430nm et peut être utilisé pour réaliser 2DES sur des systèmes (bio) moléculaires absorbant dans cette gamme spectrale.

Le système TWINS (Translating Wedge-based Identical Pulses eNcoding System) permet de générer deux répliques colinéaires verrouillées en phase de l'impulsion Red-NIR et, conséquence du SFG, deux impulsions proches de l'UV verrouillées en phase. Selon le concept inventé par Brida et al [9], [10], le système TWINS est composé de trois blocs (A, B, C, comme indiqué à la fig.6) en matériau a-BBO. Ce matériau est choisi en raison de ses propriétés de biréfringence, car dans ce type de cristaux uniaxiaux négatifs, l'indice de réfraction ordinaire (o) a des valeurs supérieures à celles de l'extraordinaire.

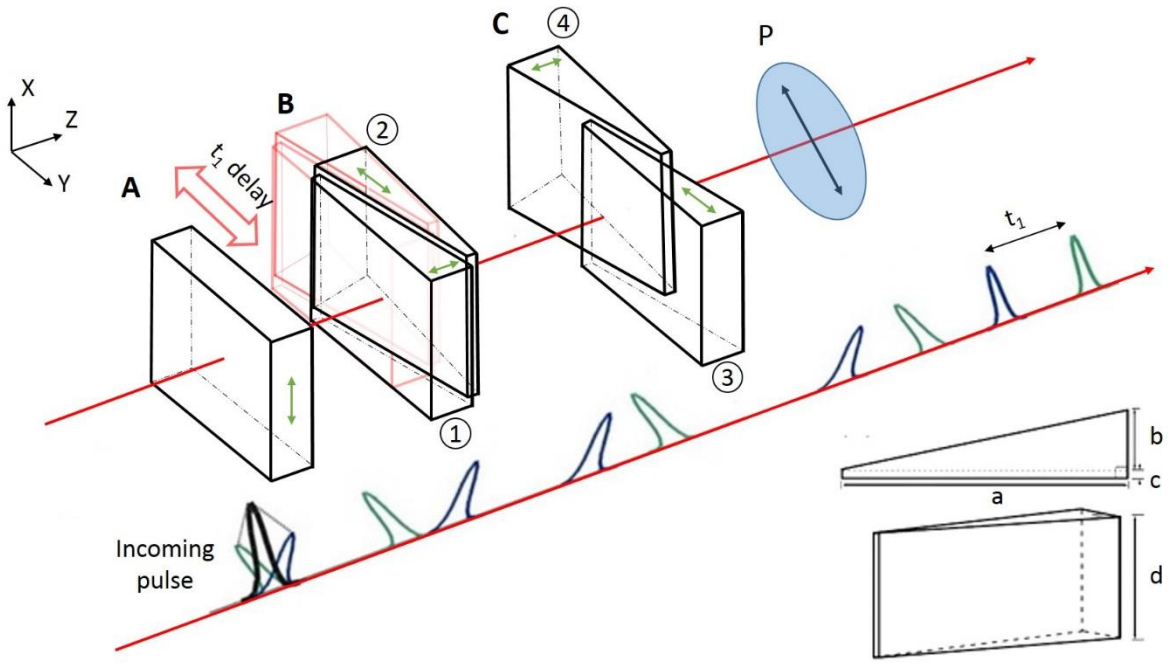

Fig. 6: Système TWINS composé d'une plaque a-BBO et de quatre cales a-BBO coupées le long d'axes optiques différents (figure adaptée de la référence 10); les axes optiques de chaque élément optique sont indiqués par des flèches vertes à double face. Le bloc A crée un retard négatif initial entre les impulsions polarisées Y et X (épaisseur 2,4 mm). Le bloc B est monté sur un étage motorisé dont la translation, dans la direction Y, modifie le chemin optique de l'impulsion polarisée en Y, introduisant un retard entre les impulsions. Le bloc C sert à corriger l'inclinaison du front de phase et la direction légèrement non colinéaire des impulsions après la sortie du bloc B. Le polariseur P à la fin de la séquence projette les deux impulsions sur un axe de polarisation linéaire incliné à 45 °. Les cales conçues pour les jumeaux ont des dimensions a = 25 mm, b = 3,1 mm et c = 0,5 mm avec un sommet de bord ~ 7 °.

Le bloc A est responsable de la division de l'impulsion entrante en deux impulsions à polarisations perpendiculaires et de même intensité, tout en créant simultanément un retard initial entre elles. Le bloc B, qui est composé d'une paire de coins, sépare dans l'espace et dans le temps (avec une précision attoseconde) les deux polarisés orthogonalement. Ainsi, la variation du retard entre les deux impulsions peut être obtenue. Le bloc C chevauche spatialement la paire de deux impulsions avec le polariseur P les projetant dans une polarisation unique.

Pour prouver le principe, nous avons enregistré une autocorrélation à résolution spectrale des impulsions proche de l'UV-Vis, enregistrée en faisant varier le délai entre les deux répliques IR-Rouge avec le dispositif TWINS (fig. 7). Comme le montre la figure, le spectre d'impulsions structuré est chiffré sur la carte de traces d'autocorrélation, avec des preuves des interférences constructives et destructives lors du déplacement du moteur TWINS. Ce dernier prouve clairement que nous sommes capables de produire deux répliques colinéaires du pouls UV-Bleu et de retarder l'une par rapport à l'autre. Ce type de mesure d'autocorrélation est utilisé dans la procédure d'étalonnage avant d'effectuer des mesures 2DES (en ayant les deux répliques dispersées dans le spectromètre) et permet ainsi de récupérer l'axe d'excitation..

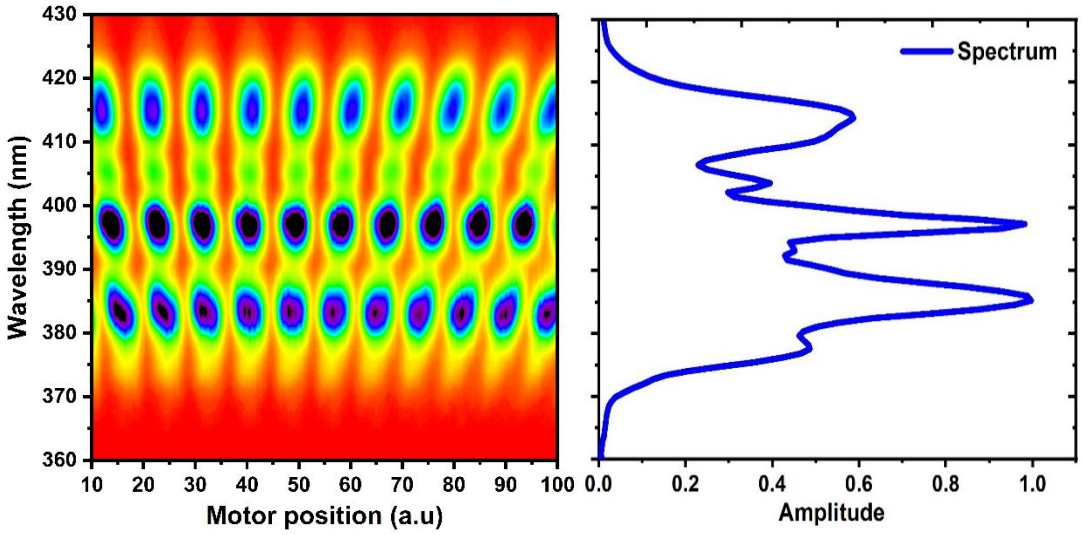

Fig. 7: Autocorrélation à résolution spectrale des impulsions proches de l'UV-Vis enregistrées en faisant varier le délai entre les deux répliques IR rouge avec le dispositif TWINS; à droite le spectre des impulsions à t1 = 0fs est montré pour comparaison

Une partie de mon doctorat en 3ème année a été consacrée à la construction d'un spectromètre à absorption transitoire fonctionnant dans la plage spectrale NIR. Des améliorations supplémentaires ont également été apportées à la plage de détection du spectromètre UV-Vis. La figure 8 récapitule un résumé de ce travail concernant la fenêtre de commande dans les deux configurations avec différents niveaux de bruit (fig.8a). La sensibilité des deux configurations est illustrée à la fig.8b où, pour les longueurs d'onde avec le niveau de bruit le plus faible, nous pouvons atteindre une sensibilité de $\Delta OD < 20x10^{-6}$, suffisamment élevée pour obtenir un très bon rapport signal sur bruit et déterminer le ESL des différents échantillons avec la plus grande précision possible.

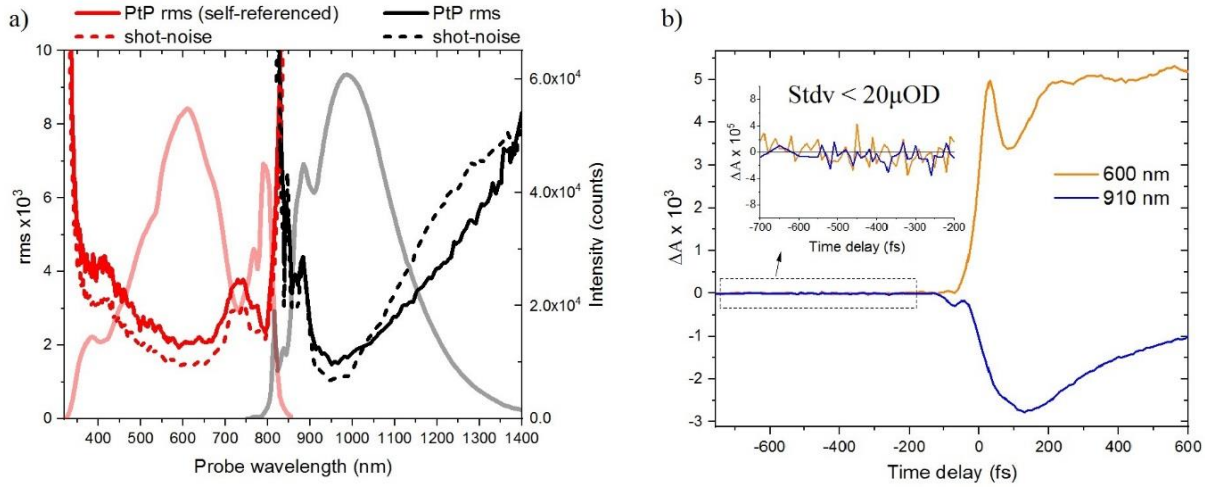

Fig. 8 : a) Détection équilibrée et non équilibrée pour les configurations UV-Vis et NIR, respectivement; Le bruit de tir est représenté par des lignes pointillées; Pt RMS plus de 1000 impulsions indiquées par des lignes continues; WL pour chaque région de sondage indiquée par des lignes épaisses transparentes b) Les traces cinétiques avec des retards de temps négatifs démontrent la sensibilité des configurations; Les traces cinétiques des configurations UV-Vis (ligne orange) et NIR (ligne bleue) montrent respectivement un Stdv <20x10^{-6} après une moyenne de 2500 spectres différentiels (temps d'acquisition de 5s)

Conclusions

À partir de notre analyse, l'ESL des deux isomères a été déterminée pour tous les échantillons. Initialement, nous avons confirmé les rapports antérieurs sur WT ASR avec une ESL pour les isomères AT et 13C de 0,83ps et 0,2ps respectivement. De plus, les mutations ponctuelles introduites aux positions 76, 83 et 112 semblaient accélérer la réaction d'isomérisation des isomères de l'AT, accompagnées d'un décalage vers le bleu de leurs maxima d'absorption (fig. 9). L'impact le plus important a été observé pour le mutant L83Q avec une réduction d'environ 2 fois de l'ESL (0,48ps). L'origine de cette différence a été attribuée au mélange électronique S1 / S2 (travail de calcul de M. Del Carmen Marín, Y.Orozco-Gonzalez et M.Olivucci).

Au contraire, l'effet sur le 13C-PSBR est exprimé par une augmentation de l'ESL. De manière surprenante, dans le cas du mutant W76F, une ESL différant d'un ordre de grandeur est observée. En cartographiant les résultats obtenus pour le 13C-PSBR, nous voyons que le décalage dans l'absorption s'accompagne d'une augmentation de l'ESL contrairement au cas d'AT.

En plus de l'ESL, nous avons fourni des informations concernant l'activité vibratoire des modes à basse fréquence (plage <400 cm^{-1}). Les expériences réalisées pour les protéines DA et LA ont abouti à quatre modes basse fréquence présentés pour tous les mutants et WT-ASR compris entre 60 cm^{-1} et 400 cm^{-1}. Ces derniers résultats ont déjà été rapportés dans la littérature pour d'autres protéines de la rétine, en attribuant ces modes aux torsions délocalisées du squelette du chromophore.

Nos travaux sur les mutants ASR ont abouti à la découverte d'un mutant W76S / Y179F qui présente une augmentation d'environ 8 fois du rendement quantique de fluorescence par rapport à WT-ASR. Le mutant en question a une durée de vie picoseconde (ESL de 5,7 ps) avec une fluorescence QY ($2,17x10^{-3}$) pas trop éloignée des mutants Arch3 améliorés appliqués en optogénétique. Dans le manuscrit soumis présenté dans cette thèse, une comparaison à l'égard de WT-ASR et du mutant L83Q est décrite. Les calculs de trajectoire de réaction et de trajectoire montrent que le changement observé dans l'ESL est dû à un changement opposé du caractère de transfert de charge de l'état S1 de la molécule. De tels changements peuvent être décrits comme une augmentation du caractère diradical 2Ag non réactif le long des séries L83Q, WT, W76S / Y179F. La variation de L83Q à WT est dominée par un effet électrostatique alors que la variation de WT à W76S / Y179F est contrôlée par des effets stériques: une modification des détails de la coordonnée d'isomérisation.

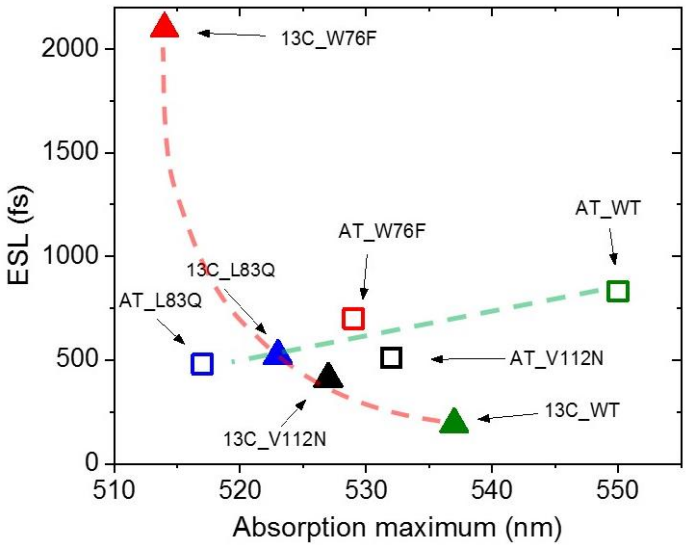

Fig. 9 : ESL en ce qui concerne les maxima d'absorption des isomères AT (carrés) et 13C (triangles) dans WT-ASR et les trois mutants. Les lignes pointillées vertes et rouges sont des repères pour l'œil, montrant la tendance des PSBR AT et 13C-PS respectivement.

Concernant notre contribution au développement de nouveaux outils spectroscopiques, nous avons pu mettre à niveau le spectromètre T.A précédemment utilisé pour la spectroscopie à cohérence vibratoire (VCS) en un spectromètre 2DES fonctionnant dans le domaine spectral UV-Vis. Le spectromètre 2DES utilise une paire d'impulsions de moins de 10fs à verrouillage de phase situées dans la plage du proche UV-bleu à 360-430nm et peut être utilisé pour réaliser des 2DES sur des systèmes (bio) moléculaires absorbant dans cette gamme spectrale.

En outre, un spectromètre T.A performant dans la plage spectrale NIR (800-1400) nm a été construit, utilisé pour l'étude d'échantillons ASR. Cette dernière configuration permet de mesurer des signaux $<10^{-3}$, avec un niveau de bruit pouvant aller jusqu'à ~ $20x10^{-6}$ sur 5s de temps d'acquisition à 910 nm.

Références

[1] D. Polli *et al.*, "Conical intersection dynamics of the primary photoisomerization event in vision," *Nature*, vol. 467, no. 7314, pp. 440–443, Sep. 2010.

[2] J. E. Kim, M. J. Tauber, and R. A. Mathies, "Wavelength Dependent Cis-Trans Isomerization in Vision †," *Biochemistry*, vol. 40, no. 46, pp. 13774–13778, Nov. 2001.

[3] K.-H. Jung, V. D. Trivedi, and J. L. Spudich, "Demonstration of a sensory rhodopsin in eubacteria: Sensory rhodopsin in eubacteria," *Molecular Microbiology*, vol. 47, no. 6, pp. 1513–1522, Mar. 2003.

[4] O. A. Sineshchekov, V. D. Trivedi, J. Sasaki, and J. L. Spudich, "Photochromicity of *Anabaena* Sensory Rhodopsin, an Atypical Microbial Receptor with a *cis* -Retinal Light-adapted Form," *Journal of Biological Chemistry*, vol. 280, no. 15, pp. 14663–14668, Apr. 2005.

[5] A. Kawanabe and H. Kandori, "Photoreactions and Structural Changes of Anabaena Sensory Rhodopsin," *Sensors*, vol. 9, no. 12, pp. 9741–9804, Dec. 2009.

[6] A. Kawanabe, Y. Furutani, K.-H. Jung, and H. Kandori, "Photochromism of *Anabaena* Sensory Rhodopsin," *Journal of the American Chemical Society*, vol. 129, no. 27, pp. 8644–8649, Jul. 2007.

[7] D. Agathangelou *et al.*, "Effect of point mutations on the ultrafast photo-isomerization of Anabaena sensory rhodopsin," *Faraday Discussions*, vol. 207, pp. 55–75, 2018.

[8] M. del C. Marín *et al.*, "Fluorescence Enhancement of a Microbial Rhodopsin via Electronic Reprogramming," *Journal of the American Chemical Society*, vol. 141, no. 1, pp. 262–271, Jan. 2019.

[9] D. Brida, C. Manzoni, and G. Cerullo, "Phase-locked pulses for two-dimensional spectroscopy by a birefringent delay line," *Optical Society of America*, vol. 37, pp. 3027–3029, Aug. 2012.

[10] J. Réhault, M. Maiuri, A. Oriana, and G. Cerullo, "Two-dimensional electronic spectroscopy with birefringent wedges," *Review of Scientific Instruments*, vol. 85, no. 12, p. 123107, Dec. 2014.

Part I

General Introduction

1 General introduction - Thesis content

Our research interest is located on the photo-physical study of retinal proteins and particularly Sensory Rhodopsins. These are light-sensitive systems which upon light absorption undergo a conformational change called isomerization. The latter process is ultrafast ($<10^{-12}$s) and takes place on the protein's retinal chromophore. Through the isomerization mechanism, the absorbed photon's energy is converted into chemical energy and is used by the system for the execution of a specific biological function. Our studies are focused on this initial step of the chemical reaction where we want to determine the speed and the efficiency of this process, and how these are influenced by the protein environment.

The best known example of such a system is Rhodopsin (Rh), which is responsible for vision in vertebrate organisms. Isomerization in Rh occurs within ~200fs, with an outstanding 67% efficiency[1]. For this example, nature tunes and optimises the protein environment in order for the reaction to occur fast and simultaneously efficient. In the frame of the latter statement, we study a microbial rhodopsin called Anabaena Sensory Rhodopsin (ASR), which represents an alternative model system giving us the opportunity to see the effect of the protein environment on two different all-trans (AT) and 13-cis (13C) retinal conformations/isomers in the same protein environment.

The studies on the native protein (WT-ASR) are described in chapter 3, where the excited state lifetimes and isomerization quantum yields are determined for both ground state reactants. In chapter 4, our work extends on the study of point mutated proteins, by replacement of specific residues in the proximity of the retinal chromophore. Thus, a comparison between different environments is presented, which interestingly have an opposite effect on AT and 13C isomers. Chapter 5 shows a work on fluorescent ASR mutants where, in collaboration with the quantum chemistry team of Prof. M. Olivucci (U Siena & Bowling Green) the origin of the fluorescence enhancement is identified.

Beside our interest on retinal proteins, part of our work is devoted to the development of new spectroscopic tools. In this context, a femtosecond two-dimensional electronic spectroscopy setup is developed, which uses a pair of phase-locked ~sub-10fs pulses at 400nm for excitation. The potential application of the 2DES spectrometer is on (bio)molecular systems which absorb in the near-UV-blue spectral range. In addition, a transient absorption spectrometer performing in the NIR spectral range was developed, and used for the study of the retinal proteins. A detailed description of the experimental setups and the data treatment procedures are presented in chapter 2.

This PhD work took place in the BIODYN group of the Department of Ultrafast Optics and Nanophotonics (DON) at Institut de Physique et Chimie des Matériaux de Strasbourg (IPCMS), in close partnership with theoreticians (M.Olivucci, N.Ferré) and experimentalists (T.Buckup, G.Cerullo). ASR samples were kindly provided by the groups of K-H.Jung and H.Kandori.

References

(1) Kim, J. E.; Tauber, M. J.; Mathies, R. A. Wavelength Dependent Cis-Trans Isomerization in Vision †. *Biochemistry* **2001**, *40* (46), 13774–13778. https://doi.org/10.1021/bi0116137.

Part II

Experimental techniques and Data treatment

2.1.1 Non-linear Optics

The interaction of light with matter is a mainstream in nonlinear optics. When a dielectric medium experiences very low intensity of light; such as ambient light, the optical properties of the material remain almost independent of the light intensity. In this case the relationship between the induced macroscopic polarization $\vec{P}$ and the applied electric field $\vec{E}$ remains linear according to eq.1, where ε_0 and χ_e are the vacuum permittivity and electric susceptibility of the medium respectively.

$$\vec{P}(\omega) = \varepsilon_0 \chi_e \vec{E}(\omega) \qquad eq.\ 1$$

On the contrary, when the magnitude of the $\vec{E}$ reaches high values ~10^{14} W/cm^{-2}; which is the case for pulsed femtosecond lasers, then anharmonic terms rise for χ and thus it can be expressed as a power series of $\vec{E}$ (eq.2).

$$\vec{P} = \sum_{i=0}^{n} \vec{P}_i = P_0 + \varepsilon_0(\chi^{(1)}\vec{E} + \chi^{(2)}\vec{E}^2 + \chi^{(3)}\vec{E}^3 + \cdots + \chi^{(i)}\vec{E}^i) \qquad eq.\ 2$$

Under these conditions, the induced dipoles oscillate at higher frequencies than the fundamental of the applied field (i.e 2ω, 3ω etc). Furthermore, these dipoles may oscillate coherently (with a definite phase relation between them), meaning that in certain circumstances they add together constructively (phase matching) producing a much larger intensity. Depending on the material used and the polarization of the electric field several nonlinear phenomena can be observed[1]. Some of these phenomena are sum frequency generation (SFG), second harmonic generation (SHG), optical parametric amplification (OPA) and white light generation (WLG).

2.1.2 Sum Frequency Generation (SFG)

Sum frequency generation is a $\chi^{(2)}$ process which is observed when two polarized waves are met in a non-centrosymmetric medium, fully complying to momentum and energy conservation laws. In principle the medium is birefringent (nonlinear crystal), with the incoming waves experiencing different propagation paths depending on their polarization (along the ordinary or extraordinary optical axes of the crystal).

The phase matching conditions in terms of wave vectors is

$$\overrightarrow{k_1} + \overrightarrow{k_2} = \overrightarrow{k_3} \quad eq.\ 3$$

while simultaneously the energy conservation law requires that

$$\omega_1 + \omega_2 = \omega_3 \quad eq.\ 4$$

Generally the produced signal (ω_3) is polarized perpendicularly to at least one of the two mixing waves and at higher energy (sum of ω_1 and ω_2)[2]. When the polarization of the two incident waves is the same, the phase matching is Type I (o + o = e), while the alternative case with perpendicular polarizations for waves 1 and 2 results in Type II (o+e→e or e+o→e). Depending on the cut angle of the crystals ellipsoid (θ and φ), the thickness and the mixing frequencies, the SFG process can result in broader bandwidth conversion and higher efficiency[3].

An example of SFG is shown in fig.21, where a broadband NIR pulse generated in a Hollow Core Fiber (HCF) filled with Neon gas is up-converted with a quasi-monochromatic 800nm pulse. The phase matching was type II on a 80μm thick BBO crystal resulting in a broad UV-Vis pulse centered at 400nm.

2.1.3 Second Harmonic Generation (SHG)

A degenerate case of **SFG** is the **SHG** process, where two photons of the incident beam, with the same wave vectors $\overrightarrow{k_1} = \overrightarrow{k_2} = \overrightarrow{k_\omega}$ and frequencies $\omega_1 = \omega_2 = \omega$, generate a third photon in the $\overrightarrow{k_3} = \overrightarrow{k_{2\omega}}$ direction and double frequency $\omega_3 = 2\omega$. Thus, equations 3 and 4 can be written as follows

$$\overrightarrow{k_\omega} + \overrightarrow{k_\omega} = \overrightarrow{k_{2\omega}} \quad , \quad \omega + \omega = 2\omega$$

This is the most efficient way to generate a laser pulse by frequency doubling the incident beam. An example of SHG in this thesis, is the generation of a 400nm pulse serving as the pump beam in a non-collinear optical amplifier (section 2.1.5) operating in the visible spectral range. There ~160μJ of the 800nm fundamental beam propagate in a β-barium borate (BBO) crystal resulting in ~40μJ pulse centered at 400nm.

2.1.4 White light generation (WLG)

White light generation is a $\chi^{(3)}$ nonlinear process occurring when an intense light pulse is focused in transparent mediums (i.e fused silica, sapphire etc)[4]. The general result is spectral broadening due to self-phase-modulation (SPM) of the pulse[5]. In this case, the beam impinging on a material of thickness L, the refractive index of the medium becomes a linear function of the intensity according to equation 5

$$n(t) = n_0 + n_2 I(t) \quad \text{eq. 5}$$

In this way, the nonlinear refraction coefficient n_2 is related to $\chi^{(3)}$ with the effect of time variations giving rise to phase changes in the optical carrier wave as shown in eq.6.

$$\varphi(t) = \omega_0 t - \frac{\omega_0}{c_0} n(t) L \quad \text{eq. 6} \qquad \omega(t) = \frac{d\varphi(t)}{dt} = \omega_0 \left(1 - \frac{n_2 L}{c_0} \frac{dI}{dt}\right) \quad \text{eq. 7}$$

The latter leads to a variation of the instantaneous frequency (eq.7), where the leading edge of the pulse (dI/dt>0) is shifted to lower frequencies and supplementary the trailing edge (dI/dt<0) to higher frequencies[6]. This brief description explains the spectral broadening observed.Other processes which contribute also to the WLG such as self-focusing, and self-steepening are not commented. In this thesis WLG produced in a 2mm CaF_2 crystal (300nm-840nm) or in a 4mm YAG (800nm-1400nm), serves as probe pulses in transient absorption experiments (fig.1).

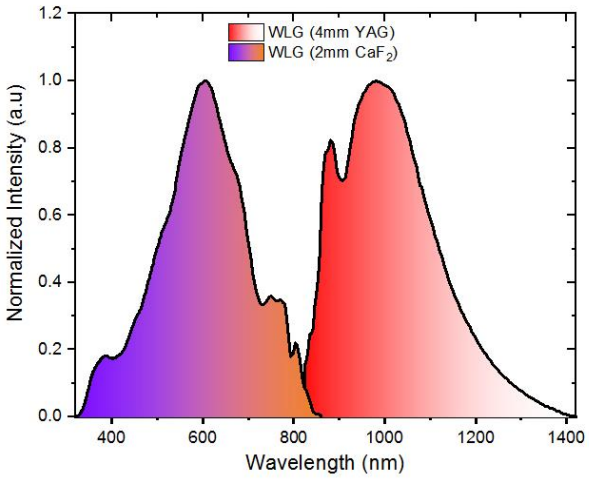

Fig. 1 : WLG in a 2mm thick CaF_2 crystal (320nm-850nm) and a 4mm YAG crystal (800nm-1400nm); WL probe in CaF_2 crystal recorded through KG-1 and KG-5 color filters; WL probe in YAG crystal recorded through RG-9 and RG-850 long pass filters;

2.1.5 Optical Parametric Amplification (OPA)

The purpose of using this nonlinear process arises from the need of pulses different in frequency and shorter in duration than the fundamental laser source in the μJ energy range. Parametric Amplification takes place in a second order nonlinear crystal analogous to the case of SFG. Here, instead of mixing two frequencies ω_1 and ω_2 to get the sum of the two (ω_3), the opposite process is observed (similar to difference frequency generation). A photon of frequency ω_p (called pump) is absorbed by a virtual level of the material and two photons at frequencies ω_i (idler) and ω_s (signal) are emitted. In an OPA, a high intensity beam (pump) transfers its energy to a lower in intensity and varying in frequency beam (called signal or seed), while a third beam (idler) is also generated with $\omega_i<\omega_s<\omega_p$.

Some of the crucial parameters for the process efficiency are the phase mismatch Δk, the pump wavelength λ_p and intensity I_p, the effective nonlinear coefficient d_{eff} and length L of the crystal as described in detail by Cerullo et al[6,7].

$$\Delta k = k_p - k_s - k_i \quad eq.\ 8 \qquad \Gamma = \sqrt{\frac{8\pi^2 d_{eff} I_p}{n_i n_s n_p \lambda_i \lambda_s \varepsilon_0 c_0}} \quad eq.\ 9$$

Including these individual parameters in a global parameter Γ (nonlinear coefficient) while assuming a perfect phase matching (Δk=0) in the large gain approximation $\Gamma L \gg 1$, the equations describing signals (I_s) and idlers (I_i) intensities can be derived.

$$I_s(L) \cong \frac{1}{4} I_{so} e^{(2\Gamma L)} \quad eq.\ 10 \quad , \quad I_i(L) \cong \frac{\omega_i}{4\omega_s} I_{so} e^{(2\Gamma L)} \quad eq.\ 11$$

Thus the gain of the process G can be defined as the ratio of the signals intensity after the process I_s (L) with respect to the one before I_{so}.

$$G = \frac{I_s(L)}{I_{so}} = \frac{1}{4} e^{(2\Gamma L)} \quad \text{eq. 12}$$

Equation 12 shows that the gain grows exponentially upon increasing crystals length L and the nonlinear coefficient Γ. In addition, the phase matching bandwidth which critically depends on the group velocity mismatch between signal and idler is given by eq.13.

$$\Delta v = 2\frac{(ln2)^{\frac{1}{4}}}{\pi}\left(\frac{\Gamma}{L}\right)^{\frac{1}{4}}\frac{1}{\left|\frac{\partial^2 k_S}{\partial {\omega_S}^2}+\frac{\partial^2 k_i}{\partial {\omega_i}^2}\right|} \quad \text{eq. 13}$$

The type of phase matching I or II corresponds to broader or narrower amplification bandwidth respectively.

In the same framework as described above, generation of ultrashort pulses <10fs may be achieved by using Non-collinear Optical Parametric Amplifiers (NOPA). The difference with respect to OPAs is the geometry of the beams when phase matching is obtained. While in OPAs pump and signal beam are collinear, in NOPAs they have a small angle $\alpha < 8°$ (fig.2a).

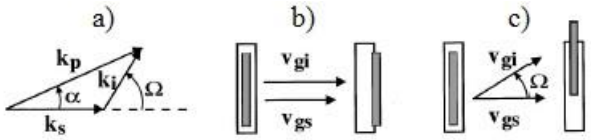

Fig. 2 : Scheme describing a) a non-collinear interaction geometry; b) signal and idler geometrical configuration in the case of collinear interaction; and c) non-collinear interaction (ref.7)

According to fig.2a the idler is emitted at an angle Ω with respect to the signal and the phase matching condition becomes a wave vector equation according to eq.14 and 15. Δk_{par} and Δk_{per} is the mismatching projected on directions parallel and perpendicular to the signal wave vector.

$$\Delta k_{par} = k_p \cos a - k_s - k_i \cos \Omega = 0 \quad \text{eq. 14}$$

$$\Delta k_{per} = k_p \sin a - k_i \sin \Omega = 0 \quad \text{eq. 15}$$

It is found that when the signal group velocity equals the projection of the idler group velocity along the signal's direction (eq.16), then broadband phase matching is achieved.

$$v_{gs} = v_{gi} \cos \Omega \quad \text{eq. 16}$$

NOPAs are also able to work in narrowband operation when a broadband chirped pulse serves as the seed beam. Usually the seed beam is a white light generated in sapphire plates or YAG crystals. When WL is used as a seed, idler's phase stability is ensured as was demonstrated by Baltuska et al[8].

Fig. 3 shows the scheme of the NOPA used as excitation source in the pump-probe experiments described in the thesis. Initially 0.16mJ of 40fs pulses at 800nm (1KHz) enter the amplifier and are splitted in a 90:10 ratio using a beam splitter. The 90% of the energy is used to generate the pump beam via SHG on a type I BBO and the 10% for generating the seed beam via WLG in a 2mm sapphire plate (Sa). The pump and seed are spatially overlapped on a type II BBO for obtaining amplification with the temporal overlap of the two established by a manual delay line (D.L). Collimation of the amplified signal is achieved by a concave mirror (S.M) and the dispersion compensation is achieved by setting several bounces on a pair of chirped dielectric mirrors (DCM12 from LaserQuantum).

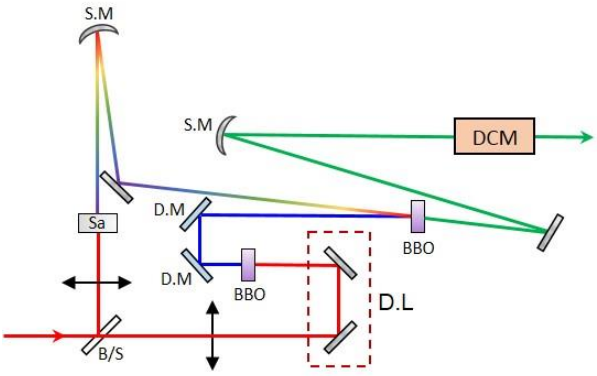

Fig. 3 : Scheme describing the NOPA operating in the visible range

An example of broadband and narrowband operation is shown in fig.4. In broadband operation sub-10fs pulses are supported by the spectrum, while in narrowband operation a 30-40fs duration is supported. The pulse-to-pulse intensity fluctuations of all the pulses were in the range of 0.3% to 0.6%, monitored by a photodiode over 1000 pulses.

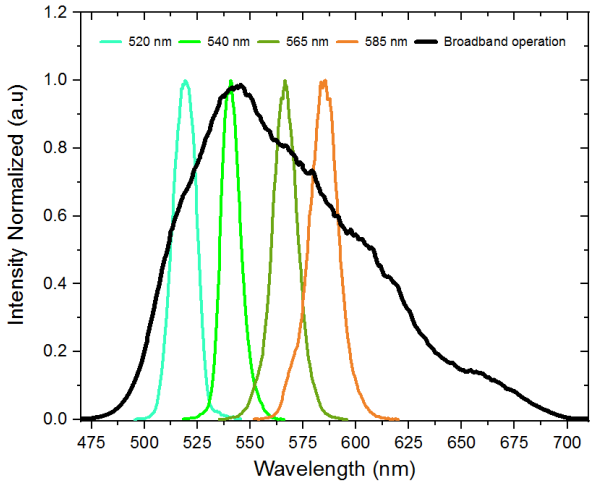

Fig. 4: NOPA spectra operating in the Visible range; Black solid line shows the output spectrum in broadband operation and coloured solid lines the different spectra obtained for narrowband operation

2.1.6 Pulse Shaper – 4f line

A *4f* line or zero dispersive line is a pulse shaper, which allows access to the amplitude and phase of a pulse in the spectral domain. Originally it is composed by two gratings and two lenses/curved mirrors (fig.5a). The role of the first grating is to angularly disperse the different spectral components. Afterwards a lens located at distance *f* away from the grating, focuses each of these individual frequencies on small diffraction spots, at the Fourier plane (mask at FP). In this configuration at the F.P all the spectral components are spatially separated and focused. Then another couple of lens and grating placed at mirror positions are recombining all the individual frequencies and delivering them in a single collimated beam at the output of the 4f-line[9].

An equivalent and space saving apparatus is the half 4f-line shown in fig.5b; the latter will be used for explaining briefly the concept of operation. In this thesis, our *4f* line is based on the half *4f* line configuration, where instead of lenses, a spherical mirror is used and a variable slit is placed at the Fourier plane serving as the mask (see fig.6). The slit is a spectral ($\boldsymbol{M_\omega}$)

and spatial mask (M_X) simultaneously. The different geometric properties such as, incident angle θ_i on the grating, diffraction angle θ_d, central wavelength λ_0, focal length f and grating period d, define the frequency resolution of the pulse shaper as explained below.

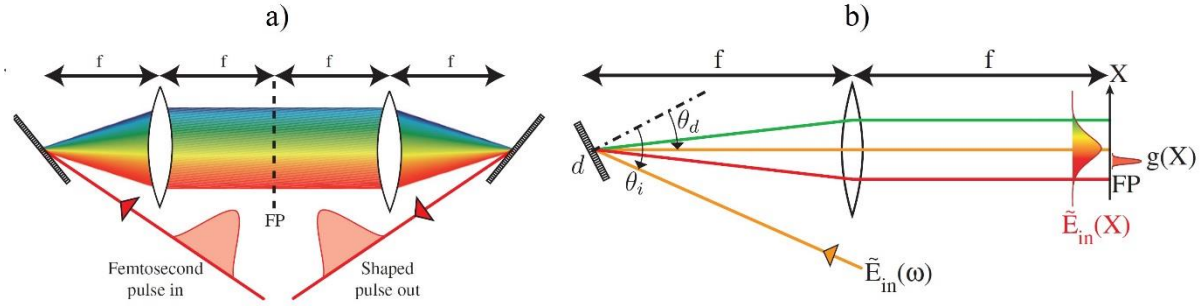

Fig. 5 : 4f line pulse shapers schemes (figure from ref.9) a) the zero dispersion line consists of two gratings and two lenses, each placed at a relative distance equal to the focal length of the lenses; in the absence of a mask the incoming pulse remains unchanged on the output b) scheme of half 4f line; the different notations on the scheme are used in the text below for the theoretical description

In our description, we consider a Gaussian beam propagation and linear dispersion, in which a certain frequency ω_k can be written as a function of the spatial coordinate in the Fourier plane X with the finite size due to diffraction at the F.P being Δx_0.

$$X_k = \alpha\omega_k \ , \quad \Delta x_0 = 2ln(2)\frac{\cos\theta_i}{\cos\theta_d}\frac{f\lambda_0}{\pi\Delta x_{in}} \quad , \ \alpha = \frac{{\lambda_0}^2 f}{2\pi cd\cos\theta_d} \qquad \text{eq. 17}$$

The frequency resolution $\delta\omega$ of the apparatus is determined by the ratio between Δx_0 and parameter α. The latter, is defined by the 4f line geometry. The Fourier transform of $\delta\omega$ corresponds to a time window T as shown in eq.18.

$$\delta\omega = \Delta x_0/\alpha \quad , \quad T = 4\ln(2)/\delta\omega \qquad \text{eq. 18}$$

As shown in the scheme (fig.5b), the incoming pulse $\tilde{E}_{in}(\omega)$ is diffracted by a grating with an angle θ_d (incident angle is θ_i) where at a distance *f,* a lens focuses each spectral component at the FP. Just after the F.P the electric field of the pulse can be written as in eq.19 with *g(X)* being the spatial extension of a given frequency component.

$$\tilde{E}_{after}(\omega, X) = \tilde{E}_{in}(\omega)g(X - \alpha\omega)M_X(X) \qquad \text{eq. 19}$$

$$g(X) = \exp[-2\ln(2)(X/\Delta x_0)^2] \qquad \text{eq. 20}$$

Assuming that the spatial profile is unaffected by the mask, then the relation between (M_ω) and (M_X) holds.

$$M_\omega(\omega) = M_X(\alpha\omega) \qquad \text{eq. 21}$$

Thus, after the backwards propagation (reflection on a flat mirror close to the FP) the electric field of the output pulse is given by eq.22 where *H(ω)* is the convolution between the spectro-spatial function *g(ω)* describing the pulse profile and the spectro-spatial mask (M_ω).

$$\tilde{E}_{out}(\omega) = H(\omega)\tilde{E}_{in}(\omega) \quad \text{eq. 22}$$

$$H(\omega) = \int M_{\omega'}\, g(\omega' - \omega)d\omega' = M_{\omega} \otimes g(\omega) \quad \text{eq. 23}$$

Thus, the spectro-spatial filtering of an incoming pulse described by $\tilde{E}_{in}(\omega)$, will result in a spectrally narrower pulse and simultaneously temporally broadened as the relationship between bandwidth and duration holds; the 4f line ensures that no dispersion is induced by the filtering process.
In this thesis, we use the 4f line for shaping a NIR pulse centered at 800nm with 40fs duration to generate a quasi-monochromatic NIR pulse at 800nm with ~1ps duration. This pulse is afterwards used for the generation of a pair of sub-10fs pulses at 400nm by SFG with a pair of 7fs NIR pulses (see section 2.3.3).

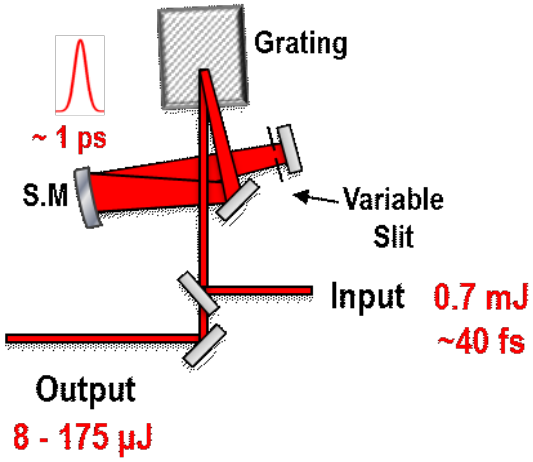

Fig. 6 : Half 4f line used for producing a tuneable quasi-monochromatic NIR pulse; Instead of lenses a 2-inch concave mirror is used, while a variable slit is playing the role of the spectro-spatial mask at the Fourier plane; From an input pulse with 40fs duration and 0.7mJ we can output up to ~1ps long pulses, conserving simultaneously the nearly Gaussian temporal shape of the pulse; S.M: spherical mirror (concave)

2.2.1 Transient absorption spectroscopy (TAS)

The most common spectroscopic technique which allows to follow in time photochemical reactions with femtosecond resolution is the transient absorption spectroscopy. It measures the changes in the absorption spectrum of a sample after perturbation by an ultrashort pulse[10]. Two laser pulses are involved, one called pump and the other one called probe (fig.7). The arrival of the pump pulse (resonant with an electronic transition of the sample) at t=0, perturbs the system allowing the appearance of new transitions with specific spectral characteristics (fig.8a). After a certain delay t=T, the probe pulse which is much lower in intensity, arrives on the sample and dissipates its energy along these transitions already activated by the pump. The signal measured $\Delta A(\lambda,t)$ is the difference between the probe's absorption when the pump is present $A(\lambda,t)_w$ and when not $A(\lambda,t)_{w/o}$.

According to Beer-Lambert's law:

$$\Delta A(\lambda,t) = A(\lambda,t)_w - A(\lambda,t)_{w/o} = -log_{10}\frac{I_w}{I_{w/o}} \quad \text{eq. 24}$$

The interaction scheme in TAS results in the build-up of a macroscopic third order nonlinear polarization $P_{NL}^{(3)}$ in the sample. Initially, the pump pulse prepares a coherent vibrational state on an excited electronic surface (creates population) and the probe interrogates this state by

an absorption to a third electronic state or by stimulated emission back to the ground state[11]. In this description for a given delay between pump and probe, the latter measures the first-order linear absorption of the nonstationary ground and excited state. Therefore, the TAS signal for a given time delay t can be written as:

$$\Delta A(\lambda, t) = \Delta c \sum_{i=1}^{N} n_i(t)\, \varepsilon_i(\lambda, t) \times l \quad \text{eq. 25}$$

where Δc is the pump induced concentration change of the absorbing species in their ground states, $n_i(t)$ the normalized electronics population kinetics of states "i" accounting for all species involved in the reaction $\varepsilon_i(\lambda,t)$ is the time dependent extinction coefficient of state i and "l" the path length of the sample's cell. The sum runs over all states involved in or populated by the photo-reaction.

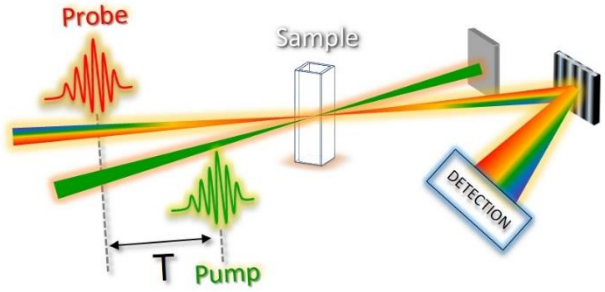

Fig. 7 : Scheme describing transient absorption technique

The different signal contributions appear as positive and negative signatures in TAS (fig.8b). Particularly, ground state bleach (GSB) corresponds to the depletion of the ground state's population upon excitation of the sample. The concentration in the ground state when the pump is on, is decreased in comparison with the pump off. Thus, the result is a negative signal (blue shade) in the wavelength range of ground state absorption. In another case, stimulated emission (SE) corresponds to the transition from the first electronic state to the ground state. With the pump on, population in S_1 increases and upon arrival of the probe photons, photons from the excited population are emitted; in a way analogous to Einstein's stimulated emission description for a two-level system. The increase of light in detection (negative extinction coefficient), will lead to the appearance of a negative signal (green shade) in TAS. The spectral shape of SE is analogous to the fluorescence emission and thus can be found at longer wavelengths in comparison with GSB due to shifts (i.e Stokes shift)[12]. Furthermore, excited state absorption (ESA) corresponds to allowed transitions from population of the first electronic state to higher electronic states. The concentration in the initial S_1 state increases when the pump is on, in comparison with the absence of the pump, resulting in a positive signal (red shade) at certain wavelength regions. Finally, upon excitation of a system (photochemical system or biological), is possible to form long lived molecular states or isomerized states (conformational change occurs), from where transitions to higher electronic states are allowed. The photo-induced absorption to these photo-product states, in a way analogous to ESA, is reflected as a positive TAS signal (orange shade) called photoproduct absorption (PA).

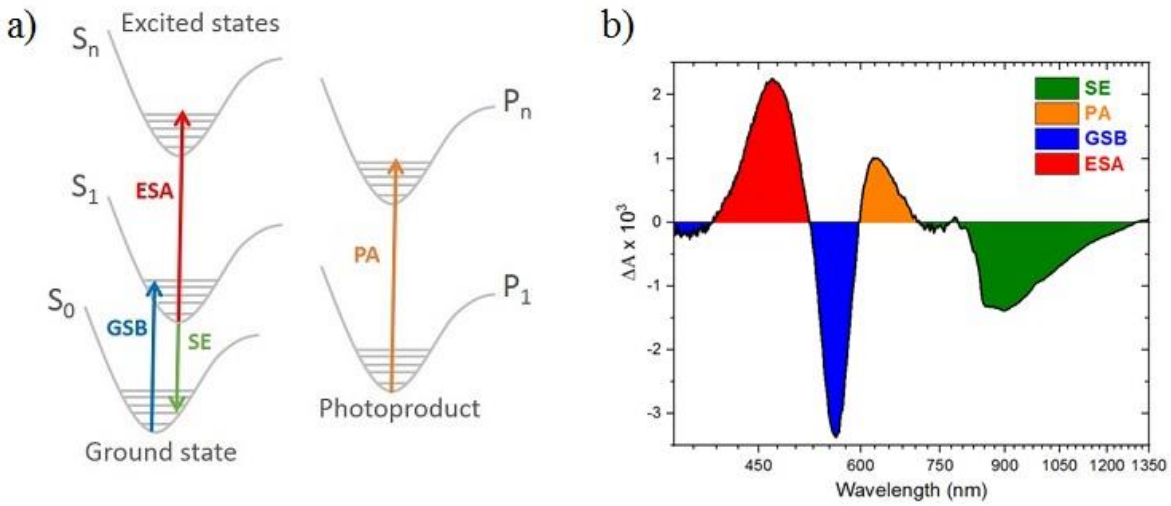

Fig. 8 : a) Electronic transitions observed by TAS shown with coloured arrows; The different signal contributions according to the electronic levels: GSB, ground state bleach; ESA, excited state absorption; SE, stimulated emission; PA, photoproduct absorption b) ΔA signal at t=270fs for Dark Adapted Wild Type ASR; The different signal contributions are shown with different color

2.2.2 Pump-probe setup

The overview of the TAS setup used in this thesis has been previously described by Gueye et al.[13], with an application in vibrational coherent spectroscopy (VCS) demonstrated. However, an upgraded version of the experimental setup is shown here (fig.9) with a novel NIR spectrometer developed (dashed blue frame) and a NOPA serving as the excitation source (section 2.1.5). The latter allowed us to perform TAS on retinal proteins with the probing range spanning from UV to NIR (320nm-1400nm).

Briefly, the fundamental source is a Ti:sapphire amplified laser system, operating at 1kHz repetition rate, delivering 40fs pulses at 800nm. A portion of the fundamental ~0.2mJ, is used for the generation of pump and probe pulses. A first beam splitter (B/S) reflects ~0.16mJ used for seeding a NOPA. The output pulse can be used alternatively in the UV-Vis or in the NIR setups using a flip-mirror. The beam propagates through a chopper, working at 0.5 kHz, establishing continuously the pump-on and pump-off operation. The pump pulse is focuses at the sample's position using a concave spherical mirror (S.M). A second B/S reflects ~10μJ of the 800nm fundamental, used for the generation of the probe pulses in the UV-Vis and NIR setups. After propagation through a motorized optical delay line (D.L) a third B/S (60:40 ratio), splits the beam between the UV-Vis and NIR setups. In the case of the UV-Vis setup the beam focuses on a 2mm thick calcium fluoride crystal (CaF_2), while in the NIR setup on a 4mm thick yttrium aluminum garnet crystal (YAG). In both cases, the WL generated (section 2.1.4) is re-collimated using parabolic mirrors (P.M). Afterwards the probe pulse focuses at sample's position using a P.M (UV-Vis setup) or using a concave mirror (NIR setup) as shown in the scheme. Finally, after re-collimation of the probe beam using a lens, the beam propagates and refocuses on the vertical slit of a spectrometer. In both cases, the probe beams are dispersed and imaged on CCD sensors (UV-Vis) or on 1D-diode array (NIR). To allow almost no loss of UV photons in detection, the role of the dispersive element in the UV-Vis spectrometer is played by a prism.

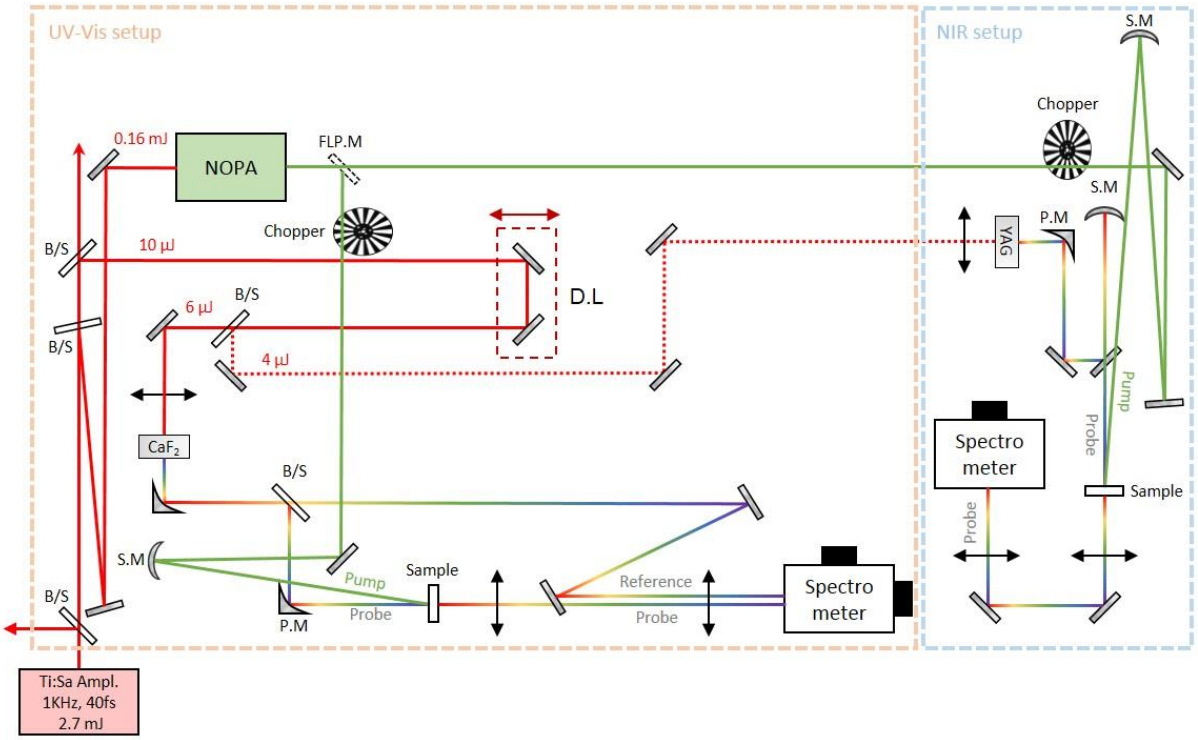

Fig. 9 : Scheme describing the transient absorption setups for UV-Visible (in orange dashed frame) and NIR range (in light blue frame)

2.2.3 Balanced detection – Sensitivity

The use of a CaF_2 crystal for WLG gives the opportunity to have probe photons in the UV region, but unlikely suffers due to thermal effects introduced by the intense focused beam. To avoid these effects, the crystal is mounted on a moving loudspeaker which allows vertical displacements ~1-2mm (at 1Hz frequency). In addition, to increase the WL stability referenced (balanced) detection is used. The reference beam is obtained by using a metallic neutral density filter OD=0.3 at 60°, which acts as a beam splitter producing an identical pulse such as the probe (intensity and spectrum). Then, this reference pulse is also focused on the slit of the spectrometer with a very small vertical angle with respect to the probe, imaged afterwards on a separate CCD sensor. In this way, correction for WL fluctuations is obtained, resulting in noise reduction during the measurement. The expression for ΔA(λ,t) is

$$\Delta A(\lambda,t) = -log_{10}\left(\frac{I_w(\lambda,t)}{I_{w/o}(\lambda,t)}\right)\left(\frac{I_{ref_{w/o}}(\lambda,t)}{I_{ref_w}(\lambda,t)}\right) \quad \text{eq. 26}$$

where the indices ref_w and $ref_{w/o}$ correspond to the reference intensity with and without pump. Referencing allows a flatter noise distribution along the probe wavelengths spanning from UV (320nm) to NIR (840nm) as shown in fig.10a. In the case of the UV-Vis setup the shot-noise (dashed-red line) is limited to $1.4x10^{-3}$ resulting from the use of two sensors for detection[13], with the pulse to pulse fluctuations (PtP) reaching the level of $2x10^{-3}$ for a sampling over 1000 pulses. An example which documents the sensitivity of the setup is shown in fig.10b, for a kinetic trace probed at 600nm. The signal at negative delays (orange line in the inset) has a standard deviation (Stdv) of $<20x10^{-6}$ for an average of 2500 differential spectra.

Supplementary, fig.10a shows the shot-noise and PtP rms noise for the NIR setup where referencing is not used (black dashed and solid lines). The shot-noise there is limited to $1x10^{-}$

^{3} while the PtP rms reaches 1.5x10^{-3} for 950nm. Even without referencing, is possible to have PtP rms < 4x10^{-3} for a 400nm range, spanning from 850nm-1250nm, which is the probing region of interest of the samples under study. Analogous to the UV-Vis setup, the sensitivity of this setup is demonstrated in fig.10b, showing similar statistics Stdv<20x10^{-6} for 910nm probing.

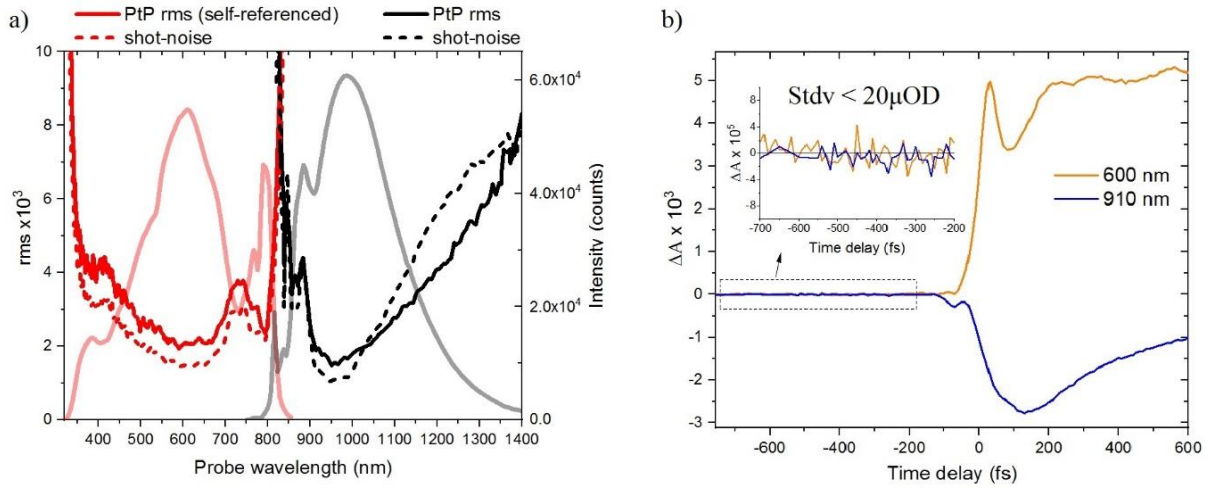

Fig. 10 : a) Balanced and unbalanced detection for UV-Vis and NIR setup respectively; Shot-noise is shown with dashed lines; PtP rms over 1000pulses shown with solid lines; WL for each probing region shown with transparent thick lines b) Kinetic traces at negative time delays demonstrate the sensitivity of the setups; kinetic traces from the UV-Vis (orange line) and NIR (blue line) setups respectively, show a Stdv <20x10^{-6} after an average of 2500 differential spectra (5s acquisition time)

2.2.4 Artefacts in TAS

After the collection of the raw experimental data, a treatment is needed to avoid unwanted contributions present due to the interaction of pump and probe pulses in the sample. Lorenc et al.[14] documented the latter, encoded in a form called "artefacts" in TAS. Here we will refer to two-photon absorption (TPA), stimulated Raman amplification (SRA) and cross-phase modulation (XPM) contributions.

The first artefact is observed when a photon from the pump and a photon from the probe are simultaneously absorbed, resulting in TPA. The amplitude the TPA signal is power dependent and is present mainly in organic solvents upon UV-Vis excitation (250nm-430nm). The second unwanted contribution is SRA present when the pump wavelength is located close to the probe's wavelength. In this case, the Raman amplification which is a nonlinear process, couples pump and probe beams at Stokes and anti-Stokes frequencies, through material excitation. As a result, an increase/decrease in the differential signal occurs shifted in energy according to the molecular oscillation energy in the medium. An example is shown in fig.11a, where the solvent used is water and the pump pulse is centred at 535nm. The –OH stretching mode of water leads to the appearance of an increased differential signal located at 453nm, 3435cm^{-1} shifted with respect to pump's energy, in line with –OH frequency. Finally, in the case where a broadband pulse is used for probing (such as a supercontinuum), the probe pulse experiences a time depended modulation of the refractive index of the medium (eq.5), due to the much higher intensity of the pump pulse. Thus, the spectral distribution of the probe pulse is modified and gives rise to unwanted signal around time zero eq.27, where L is the medium thickness, ω_0 the probe's central frequency and A(t) the amplitude of the pump pulse.

$$\Delta\omega(t) = -2\frac{n_2\omega_0 L}{c}\frac{\partial|A(t)|^2}{\partial t} \quad \text{eq. 27}$$

Each spectral component of the probe can be described by eq.28 where parameter β determines the linear chirp of the continuum components.

$$\omega_{probe}(t) = \omega_0 + \beta t + \Delta\omega(t) \quad \text{eq. 28}$$

The combination of group velocity delay (GVD) between the spectral components of the probe and the time dependent frequency modulation induced by the pump pulse (fig.11b) can be expressed in a global cross-phase modulation (XPM) term. An example of XPM is shown in fig.11a, where the probe's longer wavelengths arrive faster in the medium and interact with the pump leading in this way to a time delayed signal for longer wavelengths highlighted with a black dashed line. The frequency modulation is shown for three selected wavelengths in fig. 11b.

Correction of TPA, SRA and XPM will result in the data from which we can extract information concerning only the population dynamics of the sample.

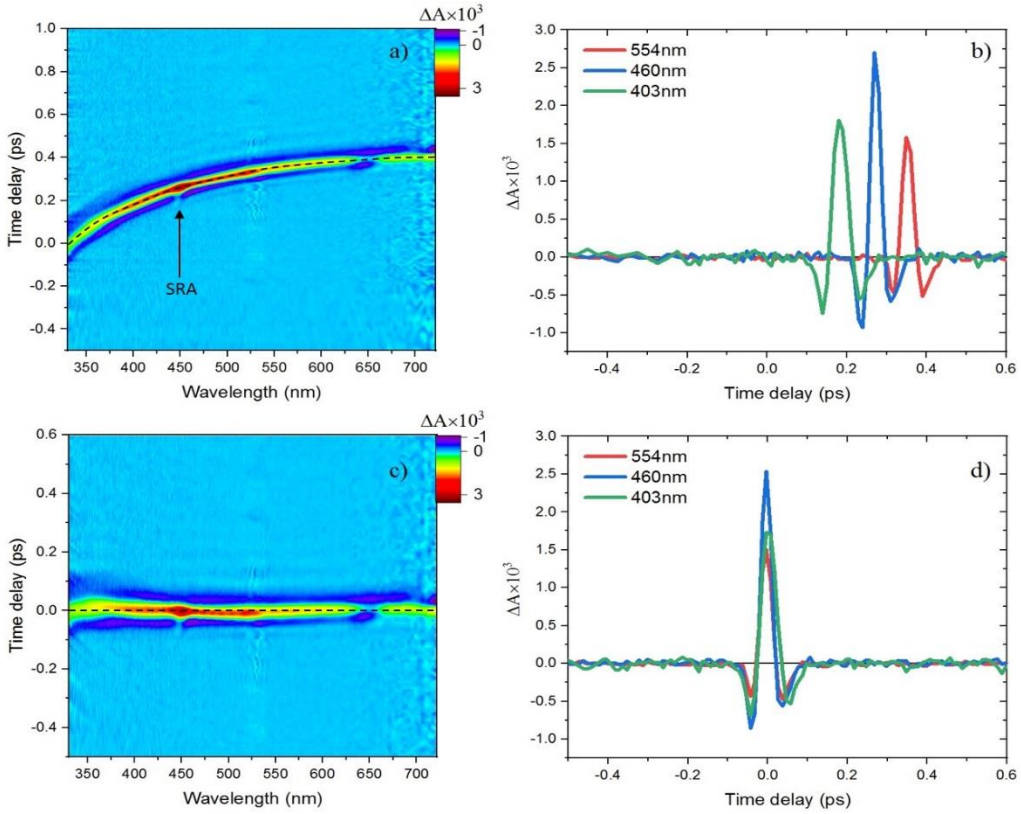

Fig. 11 : GVD correction in TAS data; a) 2D map of TAS data for water in 0.2mm flow cell; Black dashed line evidences GVD and black arrow the SRA signal b) Kinetic traces showing the XPM with a different time zero for each probe wavelength; 460nm kinetic trace includes SRA signal with the higher amplitude pronounced c) same 2D map as in a) after correction; Black dashed line defines time zero for each probe wavelength; d) same kinetic traces as in b) after applying correction; Time zero for each probe wavelength is the same

2.2.5 Data processing

Studying samples in condensed phase and particularly in liquid phase, suggests that the absorbing molecules will be dissolved in a solvent or buffer environment. The response of the solvent is present at early time delays <100fs in TAS (fig.12) where the "artefacts" are present.

A way to remove the unwanted contributions, is to record under the same experimental conditions, data for the molecule of interest and data for the solvent or buffer the molecule is dissolved in. Thus, the pure molecule's signature will be given by the subtraction of the two datasets by using an appropriate factor α as shown in eq.29. The factor α has a value smaller or equal than unity, as upon resonant excitation, the average intensity of the pump absorbed by the molecules in the excited volume is attenuating the solvent contribution in the data.

$$\Delta A(\lambda,t)_{molecule} = \Delta A(\lambda,t)_{molecule\ in\ solvent} - a\Delta A(\lambda,t)_{solvent} \quad \text{eq. 29}$$

For the proof of principle, the procedure applied for only one probe wavelength is shown in fig.12 using a factor α=0.9.

After removing the artefacts at early time delays the final step is to correct for group velocity dispersion (GVD) of the different probe wavelengths in the chirped WL. This is obtained by fitting the solvent data using a fifth order polynomial function, defining in this way the time zero for each spectral component of the probe within ±20fs accuracy. Thus, the result of the fit can be applied to the data previously corrected for artefacts. A demonstration of this procedure is shown in fig.11 where 11a and 11b correspond to the solvent data before treatment and figures 11c and 11d to the data after treatment. Fig.11c shows the 2D map for the time shifted solvent data with the black dash line depicting time zero. Three selected kinetic traces are shown in Fig.11d proving the validity of the method.

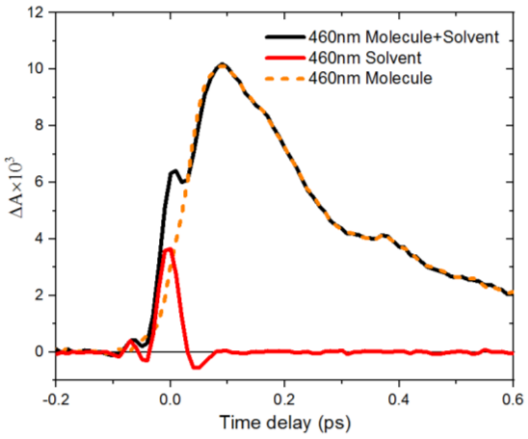

Fig. 12: Subtraction of solvent's contribution by using an appropriate factor; Molecule with solvent contribution (black solid line); Solvent contribution (red solid line); Pure molecules signature after subtraction (orange dashed line)

In order to avoid having so prominent the GVD in TAS measurements, we tent to use flow cells with short path length of 0.2mm and ultrathin windows (from Starna). Supplementary, the SRA contribution is used to ensure that the pulses are as short as possible (Fourier limited at samples position), while by adjusting the dispersion in the excitation pulse the amplitude of SRA signal gets higher when the pulse is shorter and the cross-correlation signal for the given probe wavelength shorter in duration. To reduce this signal, we either decrease the excitation

energy density, by increasing the diameter of the pump pulse at sample's position or by reducing the average intensity of the pump pulse.

2.2.6 Data Analysis for TAS

The extraction of information from the data (after the corrections) can be done in terms of spectrum and time. In our analysis, we assume that the different transitions involving the specific species "i" (see eq.25) are described by a series of concentrations with exponential decays and/or grows. The latter falls in the framework of rate equations description, with first order kinetics desribing the system under study. The concentration initially excited "Δc" by the pump, follows a climbing down ladder scheme starting from the excited state and reaching finally the ground state. In a very simple reaction model involving three states (simulation shown in fig.13a), each transition is represented by a rate "k" or a time constant "τ"=1/k. The rate constants k reflect the average time that population of species "i" need, in order to go from a state "m" to a state "n". Particularly in this example, two rates are used for the transitions from state 1→2 and from 2→0. The concentration in the different states as a function of time is given by the set of eq.30

$$C_1(t) = \Delta c \cdot e^{-k_{12}t} \;,\; C_2(t) = \frac{\Delta c\, k_{12}}{k_{12} - k_{20}} \cdot (e^{-k_{20}t} - e^{-k_{12}t}) \qquad eq.\,30$$

$$C_0(t) = \frac{\Delta c}{k_{12} - k_{20}} \cdot (k_{20}e^{-k_{12}t} - k_{12}e^{-k_{20}t}) + C_{tot}$$

A simulation of this simple three states model is shown in fig.13b. The total concentration C_{tot} is set as unity, with only 5% of the total concentration excited and with the rate constants corresponding to a 20ps and 80ps decays for 1→2 and 2→0 transitions respectively.

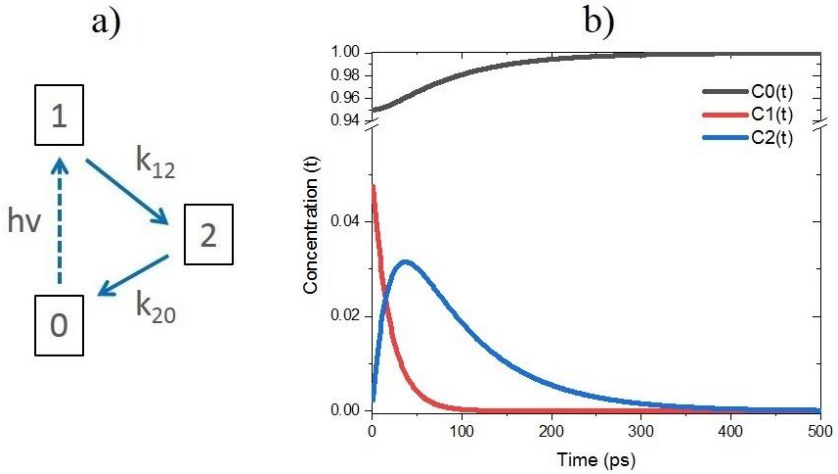

Fig. 13: Representation of a) three-level reaction model scheme with the appropriate rate constants describing population transitions between the different states b) Concentration of each state as a function of time assuming the total concentration as unity; Different coloured solid lines correspond to different states

In the general case, where "N" number of states are involved, by taking into account the extinction coefficient of each species at a certain probe wavelength and the flow cell path, the description is given by a sum of exponentials with appropriate amplitudes as in eq.31

$$\Delta A(\lambda, t) = \sum_{i=1}^{N} A_i e^{(-t/\tau_i)} \quad \text{eq. 31}$$

The acquired data will not be only a series of exponentials, as they are convolved with the instrument response function (IRF) of the setup. In our case the IRF is approximated by a Gaussian of a given standard deviation σ, defined in each case by the duration of the pump pulse. The fitting function used for deriving the different time constants "τ_i" accompanied with amplitudes "A_i" is shown in eq.32, where t_0 is a constant representing time zero of the fitted kinetic trace.

$$\Delta A(\lambda, t) = \sum_i A_i e^{-\frac{(t-t_0)}{\tau_i}} * \frac{1}{\sigma\sqrt{2\pi}} e^{-\frac{t^2}{\sigma^2}} \quad \text{eq. 32}$$

The validity of a fit is determined by the difference between the fitting curve and the experimental data, called residuals.

$$residuals = \Delta A_{exp}(\lambda, t) - \Delta A_{fit}(\lambda, t) \quad \text{eq. 33}$$

The meaningful fit is obtained when the least number of exponentials is used in order to bring the residuals amplitude close to the noise floor of the measurement (minimization of parameter χ^2). The noise level is defined for each probe wavelength by looking the signal at negative time delays

$$\chi^2 = \int \left| residuals|_{A_i, \tau_i, t_0, \sigma} \right|^2 dt \quad \text{eq. 34}$$

An example of a correct fit is shown in fig.14b.

2.2.7 Data Filtering and Global analysis

Beside the individual fits, which can be applied for each selected probe wavelength, a faster way of determining time constants is the global fit. In this case, a given number of probe wavelengths is fitted simultaneously using a number of shared time constants "N" as the associated transitions can be assumed to originate from the same state, but with different amplitudes according to eq.35.

$$\Delta A(\lambda_i, t_j) = \sum_{i,j} \sum_{a=1}^{N} A_{ia} \exp(-t_j/\tau_a) \quad \text{eq. 35}$$

The indices "i" correspond to the different wavelengths, indices "j" to the time points recorded and indices "a" to the number of time constants describing the excited population evolution (decay or rise). The application of this fitting procedure in a large dataset involves a huge amount of parameters (amplitudes). A way of further simplifying the fitting procedure is to apply a mathematical operation such as Singular Value Decomposition (SVD)[15].

By application of SVD, the TAS two-dimensional data (time components "j" and spectrum components "i") can be decomposed to three separated matrices U, S and V of given dimensions (eq.36). In this way time and wavelength variables are separated.

$$\Delta A(\lambda_i, t_j) = \sum_{m,n} U_{i \times m} S_{m \times n} V_{n \times j} \quad \text{eq. 36}$$

The diagonal matrix $S_{mxn}=\delta_{mn}s_n$ contains the s_n singular values (SV) sorted in descending order, starting from the most dominant ones. For m=n columns the U_{im} matrix will represent the "n" singular spectra (SS) associated to these SV and for j=n rows the V_{nj} matrix will

represent the "n" singular transients (ST) respectively. In this representation, SVs are the weight contribution of each transient-spectrum pair to the dataset, as shown in eq.37.

$$\Delta A(\lambda_i, t_j) = \sum_n U_n(\lambda_i) s_n V_n(t_j) \quad \text{eq. 37}$$

A limited number, e.g. n≤6 of SVs, is often enough to reconstruct the data, excluding in this way most of the noise contribution; selection according to the amplitude of the n highest s_n. The weighted singular transients (noticed with red dashed line in eq.37) can be expressed in a series of "N" exponential decays/rises and amplitudes, analogous to eq.35, where i=n.

$$\sum_n s_n V_n(t_j) = \sum_n \sum_{a=1}^{N} A_{na} \exp(-t_j/\tau_a) \quad \text{eq. 38}$$

By globally fitting these transients, it is possible to extract the different time constants and amplitudes associated with the spectral evolution of the excited species.

The information extracted for the moment is only in terms of time constants (τ_a) and amplitudes (A_{na}). A way of representing the species evolution in terms of time and spectra is by constructing the Decay Associated Differential Spectra (DADS) plot. In a DADS each time constant extracted from the global fit is associated to a characteristic spectrum (eq.39).

$$DAS_{ia} = \sum_n \sum_{a=1}^{N} U_{in} A_{na} = \sum_n \sum_{a=1}^{N} U_n(\lambda_i) A_{na} \quad \text{eq. 39}$$

Thus, the spectral signatures such as ESA, SE, GSB and PA will be decaying or rising with the time constants determined by the fitting procedure. Taking into account the sign (positive or negative) for each contribution, an equivalent sign in the DADS plot will represent a decay of that contribution. In the alternative case where the sign is opposite to what it should normally be, then the representation in DADS is a rise (formation) of that signature. An example of a DADS plot is shown in fig.14C.

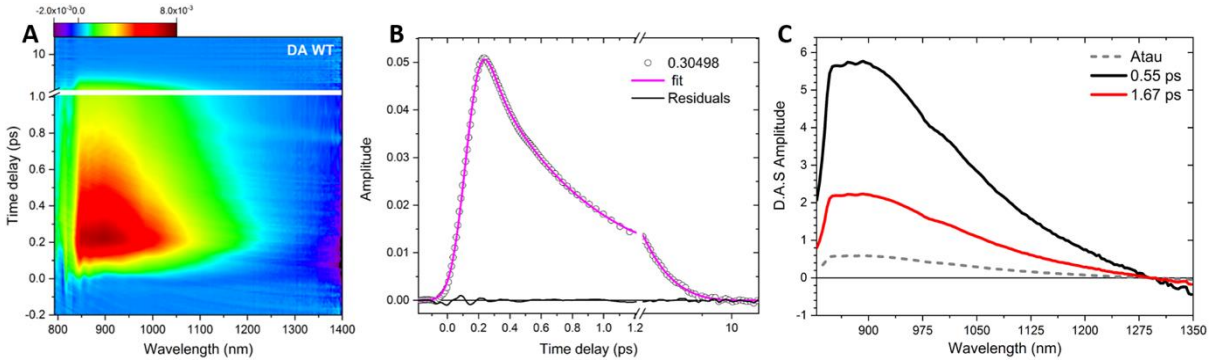

Fig. 14 : SVD and Global analysis A) 2D map for DA WT ASR probed in the NIR spectral range with inverted amplitude; the positive contribution spanning from (820-1230)nm corresponds to SE while in the range>1250nm a signature of an ESA is observed. The inverted signs in this dataset are due to opposite phase of the chopper; B) The dominant singular transient is shown with black circles while the fit and residuals are shown with magenta solid line and black solid line respectively. C) DADS result from the current analysis; Each time constant from the fit is associated with a characteristic spectrum with the bi-exponential decay (0.55ps and 1.67ps) of SE and ESA shown with solid lines while an initial unresolved component (Atau) is represented with dashed line.

2.3.1 Two-Dimensional Electronic Spectroscopy (2DES)

Since the last decade coherent two-dimensional spectroscopies (2DS) are widely used, as they can reveal molecular connections between transitions[16,17]. These transitions can be electronic or vibrational depending on the spectral range of application[18]. When this technique is applied in the infrared (2D-IR)[19], the vibrational couplings and vibrational

relaxation processes can be used to provide transient structural information of a system, in the sub-picosecond timescale. Upon application in the visible range, 2D-Vis or 2DES (Two-dimensional Electronic Spectroscopy) is possible to monitor electronic states and identify electronic couplings or energy transportation[20]. Recently, 2DES has been applied in the mid-UV range where it is known that DNA nucleobases and aminoacids have their lowest-frequency electronic resonances[21,22]. Spanning the whole spectral range from IR to mid-UV, 2DS is able to unravel the ultrafast photo-physics of many complex systems from semiconductors and organic materials to structurally/chemically heterogeneous biomolecular systems.

The advantage of this technique, is that it allows to retrieve information by resolving the excitation process spectrally. Analogous to TAS, 2DES measures the third order non-linear polarization of a system, emitted when using a sequence of three pulses (fig.15a). Initially the first pulse, which is resonant with the system's transitions (pump pulse), creates coherences between the ground and first excited states. After a certain time τ; called coherence time, a second pulse (replica of the first) arrives and creates population in the ground and first excited state. Then, a third pulse serving as the probe, arrives delayed by a time T relative to the first two and creates a second coherence in the sample. The three-field interaction with the sample results in the emission of the $P^{(3)}$ signal at time t after the arrival of the probe pulse; called detection time. The emitted signal can result in two contributions, called "rephasing or photon echo" ($P_R^{(3)}$) and "non-rephasing or virtual echo" $P_{NR}^{(3)}$, depending on the time ordering of the pump pulses[23].

As shown in the schematic of fig.15b, a 2DES interferogram can be derived for a certain waiting time T (called also population time), after scanning the coherence time τ and recording the emitted signal at time t. In this way an interferogram in the time domain S(τ,t;T) is obtained. Then, a two dimensional fourier transform (FT) of this interferogram, with respect to the detection time "t" and with respect to the coherence time "τ" will yield the 2D spectrum. The first Fourier transform with respect to time t results in a spectral domain interferogram s(τ,ω_t;T), with the emission axis ω_t obtained. Finally, a FT along time "τ" results in the 2D spectrum for a fixed waiting time T. The last FT, defines the excitation axis ω_τ, which gives the extra-dimension with respect to TAS. The spectral resolution along the excitation axis is defined by the scan range of the coherence time.

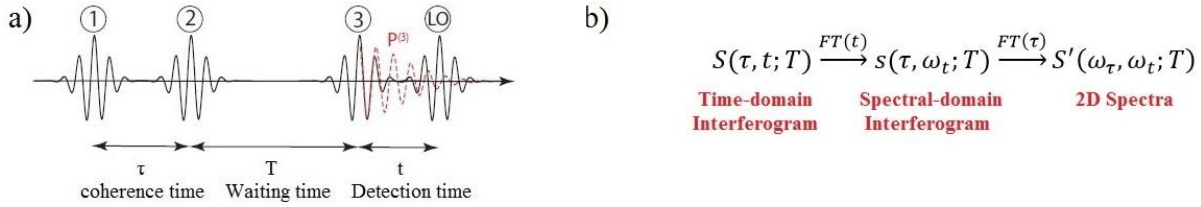

Fig. 15: a) pulse sequence in 2DS; the delay τ between the first two pulses (pump pulses) is called coherence time; the delay T between the pair of pumps and the third pulse (probe) is called waiting or population time; The sequence of the first three pulses results in the emission of a $P^{(3)}$signal at time t called detection time; A fourth pulse called local oscillator (LO) is used for heterodyning the emitted signal b) Description for derivation of a 2D spectrum at a given T; A 2D-FT along the coherence and detection time respectively yields the 2D spectrum .

The main geometrical configurations for performing 2DES experiments are the "boxcar" and "pump-probe" geometries[24] (fig.16a). In the boxcar geometry or fully non-collinear geometry, the three pulses are focused on the sample as shown fig.16b. The two pump pulses are shown with red and green colours, while the probe is represented with light blue colour.

Depending on the arrival timing of the two pump pulses, the phase matching conditions for rephasing and non-rephasing contributions is different. According to the scheme the rephasing signal $\bar{k}_{Sig}^{R}$ will be emitted in the $-\bar{k}_1 + \bar{k}_2 + \bar{k}_3$ direction after the sample, represented with violet colour, while the non-rephasing signal $\bar{k}_{Sig}^{NR}$ will be emitted in the $+\bar{k}_1 - \bar{k}_2 + \bar{k}_3$ direction represented with blue marine colour. The signal in each case has to be heterodyne detected, by using a fourth beam called local oscillator (LO).
In the alternative case of pump probe geometry, the two pumps are collinear and the probe beam is simultaneously heterodyning the signal emitted. As a following, the rephasing and non-rephasing contributions cannot be separated due to the phase matching conditions. The result is basically the sum of the two signals as shown in fig.16a. To be able to retrieve the two signals, then two separate measurements need to be done, with the phase difference between the two pump pulses equal 0 and π/2 respectively. Afterwards, using phase cycling; described by Hamm and Zanni[18], the pure rephasing and non-rephasing signals can be retrieved (fig.19).

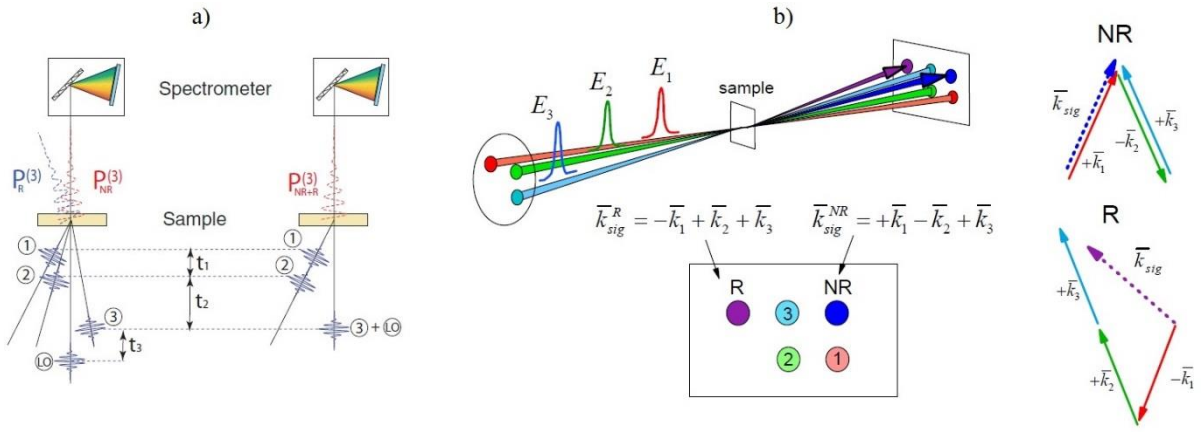

Fig. 16: a) "Boxcar" and "pump-probe" configuration for performing 2DS measurements (figure from ref.23); In the Boxcar geometry two signals can be recorded, rephasing $P_R^{(3)}$ and non-rephasing $P_{NR}^{(3)}$ contributions while in the pump-probe geometry the signal is the sum of the two and cannot be distinguished. B) Configuration for the beams in the Boxcar geometry (figure from Andrei Tokmakoff lectures notes, MIT); Violet and blue circles correspond to the directions where rephrasing $\bar{k}_{Sig}^{R}$ and non-rephasing $\bar{k}_{Sig}^{NR}$ signals are emitted. Circles with numbers 1 and 2 correspond to the two pump pulses while beam number 3 corresponds to the probe beam; The arrows in colour represent the phase matching conditions upon rephasing and non-rephasing cases.

2.3.2 2DES signals

Like in the case of TAS, the third order nonlinear polarization $P_{NL}^{(3)}$ is emitted after the three fields interact with the sample. Here we need to extend more the description for this signal in comparison with the didactic one already described in section 2.3.1, due to the complexity of selecting pathways by phase cycling. Particularly, in this description the electric fields are treated classically, while the system under study quantum mechanically. In condense phase the word "system" refers to both the molecule and the surrounding bath. A description of the system is given by a density matrix ρ[25], where the elements along the diagonal ρ_{ii} represent populations and the off diagonal elements ρ_{ij} $(i \neq j)$ represent coherences. The emitted signal for this three-field interaction scheme is given by the expectation value of the dipole operator μ (eq.40), (where N is the chromophore's density).

$$P^{(3)}(\boldsymbol{r},t) = NTr\left[\hat{\mu}\rho^{(3)}(\boldsymbol{r},t)\right] \quad \text{eq. 40}$$

The detailed description has been documented by Mukamel[26,27], by introducing the nonlinear response function $R^{(3)}$, being the convolution of the three electric fields (eq.41)

$$R^{(3)}(t_3,t_2,t_1) \propto -i\langle\hat{\mu}(t_3+t_2+t_1)[\hat{\mu}(t_2+t_1),[\hat{\mu}(t_1),[\hat{\mu}(0),\rho(\infty)]]]\rangle \quad \text{eq. 41}$$

Thus, the expression for $P^{(3)}(\boldsymbol{r},t)$ is given by eq.42.

$$P^{(3)}(\boldsymbol{r},t) \propto N\int_0^\infty dt_3\int_0^\infty dt_2\int_0^\infty dt_1\, E_3(\boldsymbol{r},t-t_3)E_2(\boldsymbol{r},t-t_3-t_2)E_1(\boldsymbol{r},t-t_3-t_2-t_1) * R^{(3)}(t_3,t_2,t_1) \quad \text{eq. 42}$$

where $E_n(t)$ stands for electric fields of the different laser pulses (see eq.43), arriving at time t_n.

$$E_n(t) = E'_n(t)\cos\left(\bar{k}\cdot\bar{r}-\omega t+\varphi\right)+c.c \quad \text{eq. 43}$$

In the boxcar geometry configuration, many other signals are emitted in all the possible phase matching directions, but we are interested only for the signals emitted in the rephasing and non-rephasing pathways (dominant signals). The different signal contributions in a 2D spectrum (GSB, SE, ESA, PA); for each pathway, are explained by the double-sided Feynman diagrams (fig.18).

In this kind of diagrams, the time is evolving from bottom (equilibrium) to top with the different times between the interactions being t_1, t_2 and t_3; which correspond to the coherence, population and detection time, respectively. The density matrix is represented with two vertical lines, where the left corresponds to the *ket* and the right to the *bra* of the density operator. The different interactions of the fields are represented via solid black arrows. In the interaction scheme, a pulse with $+\bar{k}_i$ direction is drawn as an arrow heading in the up-right direction, where the electric field is $E'_n(t)\cos(\bar{k}\cdot\bar{r}-\omega t)$. Additionally, for a pulse with $-\bar{k}_i$ direction the arrow drawn is heading the up-left direction and the electric field is $E'^{*}_n(t)\cos(-\bar{k}\cdot\bar{r}+\omega t)$. At time t_3; where the three interactions took place, the signal is emitted along the $+\bar{k}_s$ direction, represented with a wave-shaped arrow in the Feynman diagram (F.D). Each F.D carries a $(-1)^n$ sign where n is the number of interactions from the bra side of the diagram.

As time evolves, each interaction is represented with green or red arrows in a simple energy level diagram below the Feynman ones (the sequence starts from the left). The solid arrows correspond to the interaction with the bra of the density operator, while the dashed ones to the interaction with the ket. In fig.17 an illustration of the evolving density matrix is shown for the description of a two-level system; for the rephasing pathway[28]. The interaction scheme shows the system initially at equilibrium with only the ρ_{00} element of the density matrix describing the system. After the first pulse interaction, coherences are created, as expressed via the non-diagonal element ρ_{01}. Upon arrival of a second pulse at time t_1, populations are created, expressed via the diagonal elements ρ_{11} and ρ_{00}. After a certain time t_2 (population time), a third pulse creates coherences shown via the other off diagonal matrix element ρ_{10}. Finally, the signal is emitted after a time period t_3 (detection time).

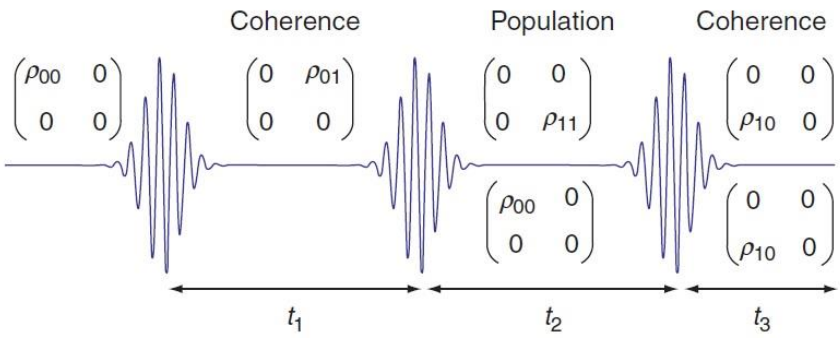

Fig. 17: Pulse sequence for the three-field interaction scheme with the evolution of the density matrix elements shown. The diagonal elements represent the population while the off diagonal elements represent the coherences (figure from ref.27).

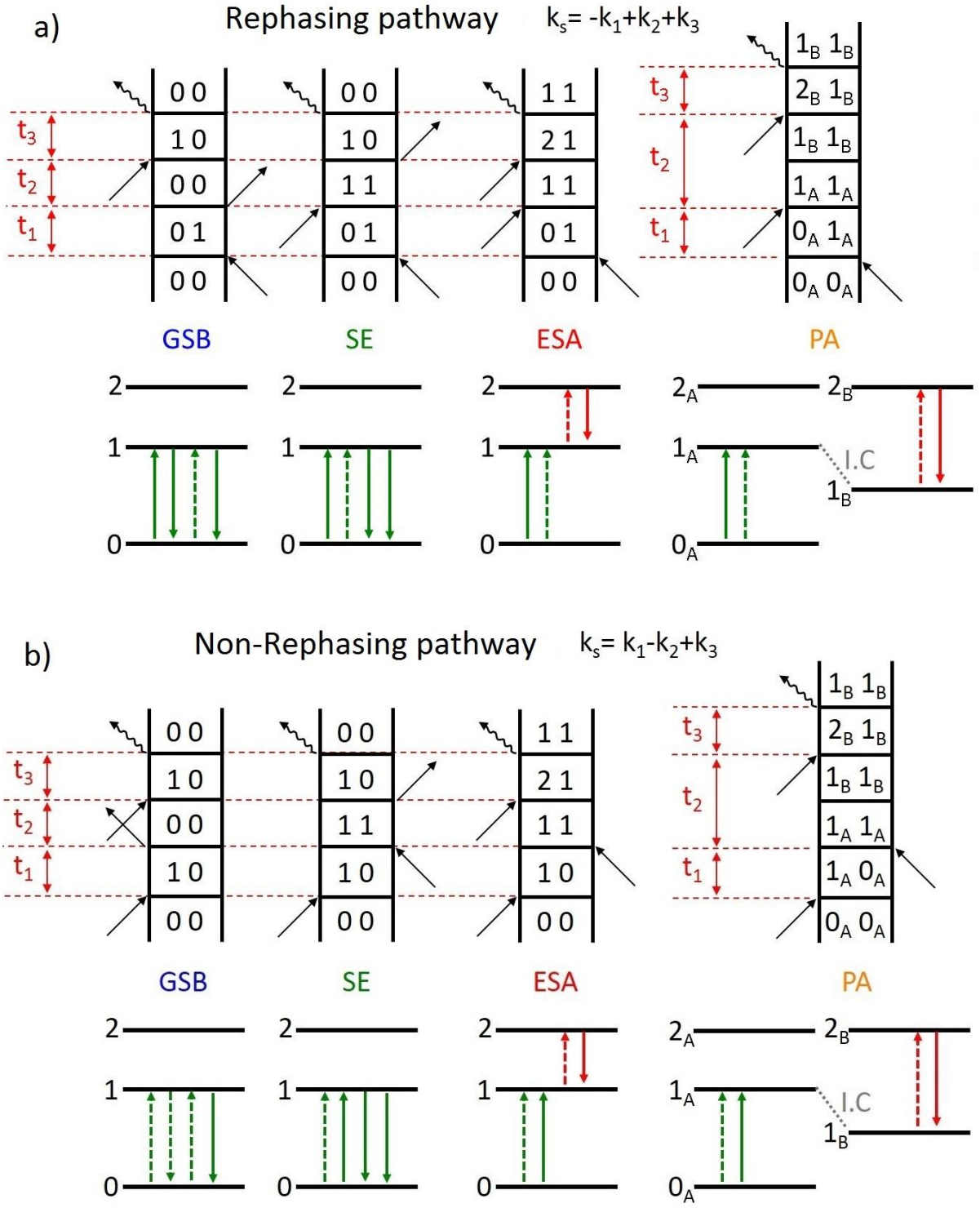

Fig. 18: Double sided Feynman diagrams representing the different signal contributions for a) rephasing and b) non-rephasing pathways (from Myers thesis); For each Feynman diagram the two vertical lines represent the density operator with the left line as the ket and the right line as the bra respectively. The time is evolving from bottom to top with t1, t2 and t3 corresponding to the coherence, population and detection time respectively. Each interaction is represented with a solid arrow line with the direction corresponding to the appropriate k_i vector direction. The wavy arrow corresponds to the signal emitted in the k_s direction for each pathway; For each diagram the different interactions are shown in a simplified energy level diagram (only the first three electronic levels are shown) with the dotted arrows (green or red) representing the pulses interactions for ket states and solid arrows for the bra respectively; In the case of photoproduct absorption PA, for a certain t_2 time, a conformational change takes place represented through an internal conversion process (I.C) in the scheme and thus the energy levels for the initial reactant and the conformer have different indices A and B.

The general goal, is to measure the purely absorptive 2DES spectra, where all the information concerning homogeneity of the spectral lineshape and electronic couplings is hidden. To retrieve this kind of 2DES maps, both rephasing and non-rephasing signals are necessary. The latter can be understood in terms of the different pathways for the different signals. Particularly, in the rephasing case, the system evolves at conjugate frequencies during the two coherence periods, which produces an "echo" signal at the end. Two paths of the rephasing contribution (see ref.28) lead to cross-peaks on the 2DES maps which are basically the couplings between the different electronic states and two paths to diagonal peaks. On the contrary, in the non-rephasing case, the system evolves at the same frequency during both coherence periods and thus no macroscopic rephasing is produced. Three of the paths lead to diagonal peaks, while only one leads to cross-peaks. Taking into account the two aspects the evolution of the system during the coherences for the rephasing and non-rephasing signals will lead to different locations of the peaks[28,29,30]. Eventually, the sum of the two contributions will contain all the information which can be extracted by 2DES.

Concerning the 2DES in pump-probe geometry, the last requirement of measuring both rephasing and non-rephasing contributions is overcome by the fact that both signals are emitted in the same direction. What is recorded in such an experiment is the spectral domain interferogram $S(\omega_3, t_2, t_1)$

$$S(\omega_3, t_2, t_1) \propto -Im\left[E_3^*(\omega_3) P_{S2D}^{(3)}(\omega_3, t_2, t_1)\right] \qquad \text{eq. 44}$$

$$\propto Re\left[E_3^*(\omega_3)\left\{R^{(R)}(\omega_3, t_2, t_1)e^{-i\varphi_{12}} + R^{(NR)}(\omega_3, t_2, t_1)e^{+i\varphi_{12}}\right\}\right]$$

The expression in eq.44 shows that the FFT over the detection time is already performed and no heterodyned detection is needed by using a LO. In contrary with "box-car" 2DES, where heterodyned detection is obtained by using a LO, the signal here is heterodyned by the probe pulse itself which serves as the LO. As a following of the latter, the FFT over the detection time t_3 is performed by the spectrometer itself which is already an additional advantage in comparison with the box-car geometry 2DES. Moreover, a FFT along the coherence time t_1 results directly in the purely absorptive 2D map (real part), as the measured signal is the sum of the two contributions.

In eq.44 the rephasing and non-rephasing signals are shown with the exponent indices *R* and *NR* respectively, while the phase difference between the two pump pulses is the term φ_{12}. As mentioned in section 2.5.1 is possible to record the rephasing and non-rephasing signals by setting the relative phase φ_{12} at 0 and π/2. The latter has been demonstrated by Myers et al.[31] using a pulse shaper, shown in fig.19.

From this point, we will refer only to the 2DES in pump-probe geometry, since the experimental setup which will be described in this thesis is operating in this configuration.

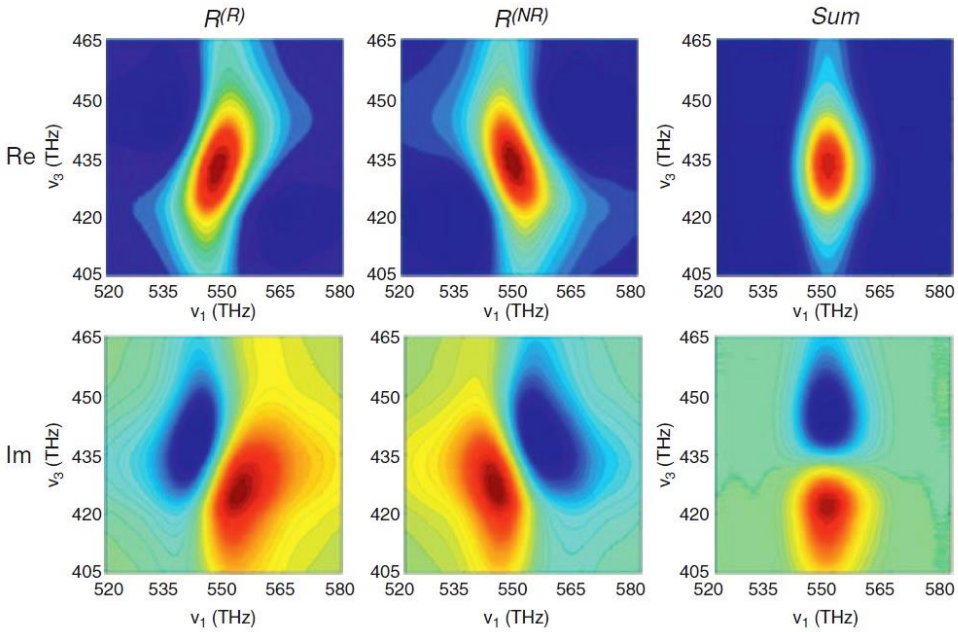

Fig. 19 : Rephasing and non-rephasing signals constructed by performing 2DES in pump probe geometry (from ref.31); The top raw of panels correspond to the real part of the 2DES maps for the two different signals, while the map on the right corresponds to the sum of the two, which consists a purely absorptive map; Bottom raw panels correspond to the imaginary part of the 2DES for both signals with the last map being the sum of the two (purely dispersive map).

2.3.3 2DES setup using TWINS

During my thesis, I have contributed to upgrading a pump-probe setup (see ref.12), previously used for Vibrational Coherence Spectroscopy (VCS), into a 2DES one operating in the UV-Vis spectral range. Part of my work concerned programming, experimental development and pulse characterization. The goal was the generation of a pair of sub-10fs pulses in the near UV-blue range 360-430nm where they could be used for performing 2DES on (bio)molecular systems that absorb in this spectral range. The challenges we had to overcome concerned mainly the phase stability of the pulses and the maintenance of short pulse duration (nearly Fourier limited).

In 2DES measurements, the relative phase φ_{12} between the pump pulses already mentioned in eq.44 has to remain constant (phase-locked pulses), while simultaneously the delay between the two (coherence time) varies. Due to the short wavelength of the pulses (centred at 400nm) the control of the coherence time has to be determined with interferometric precision ($<\lambda/100$). In addition, the generation of these pulses has to be achieved with minimum loss of pulse intensity. Thus, an interferometer based on passive optical elements should be favored with respect to one based on diffractive optics.

One way to overcome the interferometric stability issue is to generate two co-propagating copies of one single pulse, ensuring intrinsic relative phase locking. An original optical device named "TWINS", which was recently introduced[32,24] uses birefringent wedges to precisely control the time delay with attosecond precision between co-propagating pulses of orthogonal polarizations, resulting in a relative phase stability better than 30 mrad in the Vis[32] or in the UV range[33]. In our work, we incorporate a TWINS (Translating-Wedge-based Identical Pulses eNcoding System) device to generate sub-10 fs pump pulses in the 360-430nm range based on a hollow-core-fiber (HCF) compressor with a supercontinuum chirped

pulse serving as the probe; generated in CaF_2 crystal with the spectrum spanning in the 300nm-840nm range.

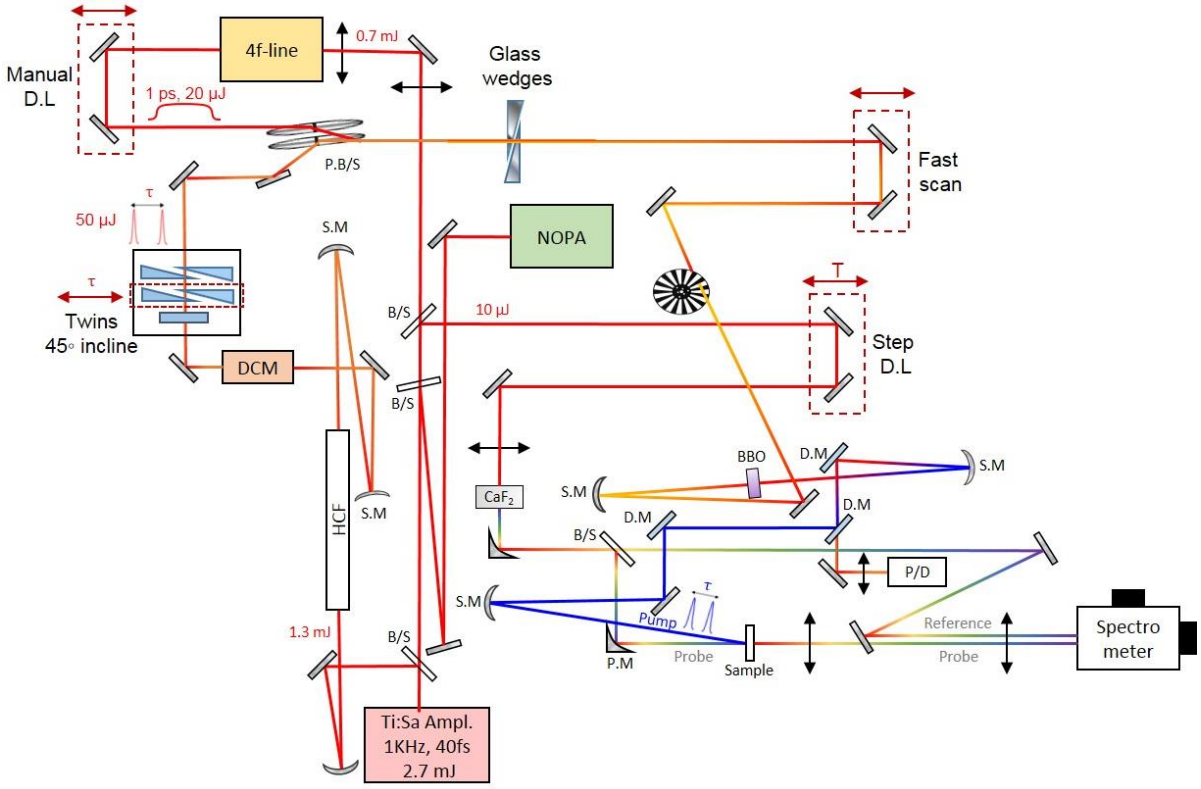

Fig. 20 : Scheme of the experimental setup (H.C.F.: hollow-core-fiber, CMs: Chirped Mirrors, D.L: Delay line, WLG: White Light Generation, P/D: Photodiode, SPECTR: Spectrometer).

The scheme of the experimental setup is shown in Fig.20. We use a 1-kHz Ti:Sapphire amplified system which delivers pulses of 2.7 mJ, 40 fs at 800 nm. About 1.3 mJ of this fundamental beam seeds a Neon gas filled H.C.F using a concave mirror, resulting in a broad Red-NIR pulse with a spectrum spanning from 600 to 930nm (see fig.21 with orange solid line) and low pulse-to-pulse energy fluctuations ~0.4%[34,35,36,37]. A pair of concave and convex mirrors placed after the HCF serves as a telescope, which is responsible for collimation and reduction of the beam size by a factor of 4. After several reflections on two pairs of dispersion compensating mirrors (DCM) the beam is sent into the TWINS device. At the output of the TWINS system, two collinear phase-locked replicas of the Red-NIR pulse are generated (50 µJ). Several reflections on the DCMs in front of the TWINS pre-compensate for the dispersion of TWINS wedges and for the dispersion the pulse experiences during the non-linear processes in the HCF. Thus, the two phase-locked replicas are recompressed down to ~7 fs duration.

Generation of the pair of pulses centred at 400nm, is obtained by collinear broadband sum frequency generation (Type II SFG) in a 80 µm thick β-BBO crystal of the two Red-IR replicas with a quasi-monochromatic 800nm pulse (fig.21 red solid line). The latter is produced by filtering spectrally the fundamental 800-nm pulse in a 4f-line (see section 2.2.6), thus generating a ~1 ps long pulse. The collinear co-propagation of the two Red-IR replicas and the quasi-monochromatic NIR pulses is established by using a custom polarized beam splitter (P.B/S), which reflects and transmits the p- and s-polarized beams respectively. The co-propagating beams are focused on the BBO crystal using a concave spherical mirror of

20cm focal length. Hence, a uniform up-conversion of the Red-NIR pulse pair is achieved for a sufficiently large range of delays between both replicas. The spectrum of each of the two blue pulses is displayed in Fig.21 with blue solid line. It covers the 360-430 nm range: more than 80% of the energy bandwidth of the Red-NIR 7-fs pulse is up-converted. In addition, this SFG scheme transfers the almost flat spectral phase of the original compressed Red-NIR pulses into the UV-Vis spectral range.

After re-collimation of the beam using a 30cm concave mirror, residuals of the Red-IR replicas are also present. Separation of the blue and Red-IR pulses is achieved by using low GDD dichroic mirrors (D.M). The reflected pair of near UV-Blue pulses reaches the sample's position after focusing via a 30cm concave mirror. By using two pairs of DCMs before the TWINS and a pair of variable-thickness glass wedges on the Red-NIR pulse before SFG, we are able to optimize the duration of each of the UV-blue phase-locked replicas to ~8.4 fs at the sample position (cf. § 2.4.4). Moreover, the transmitted pair of the residual Red-IR pulses are sent in a photodiode (P/D) in order to record their temporal autocorrelation during the experiments (cf. §2.3.5).

Finally, the supercontinuum probe pulse is generated as has been already described in sections 2.2.2-2.2.3. The waiting time variation is achieved by using a motorized delay line (D.L) by delaying the 800nm pulse prior WLG. In the experimental setup's scheme an alternative way of scanning the waiting time is shown commented as "fast scan" but we will not discuss it, as is not used in the 2DES measurements (see ref.13 for details).

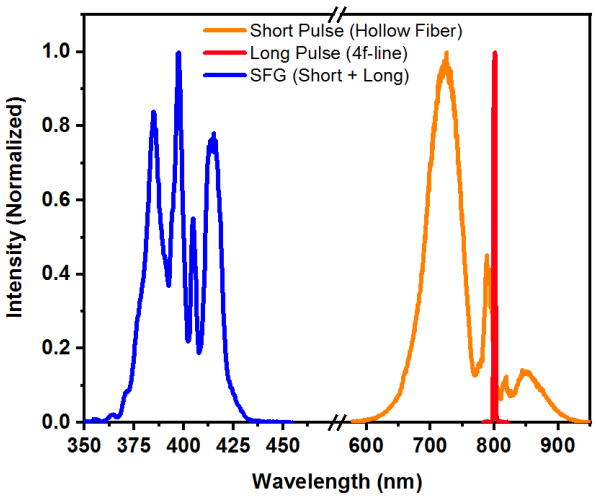

Fig. 21 : SFG in a 80μm thick BBO crystal (TypeII) between a spectrally broad NIR pulse (600nm-930nm) and a quasi-monochromatic 800nm pulse, results in a broad UV-blue pulse (360nm-430nm).

2.3.4 TWINS (Translating Wedge-based Identical Pulses eNcoding System) operation

As said above, the TWINS system allows to generate two collinear phase-locked replicas of the Red-NIR pulse, and, a consequence of the SFG, two phase-locked near-UV pulses. According to the design invented by Brida et al[32], the TWINS system is composed of three blocks (A, B, C as shown in fig.22) made of a-BBO material. This material is chosen due to its birefringence properties as in this type of negative uniaxial crystals, the ordinary refractive index (o) has higher values than the extra-ordinary one (e). In fig.23a, the n_o and n_e values are shown as a function of wavelength (300nm-1000nm).

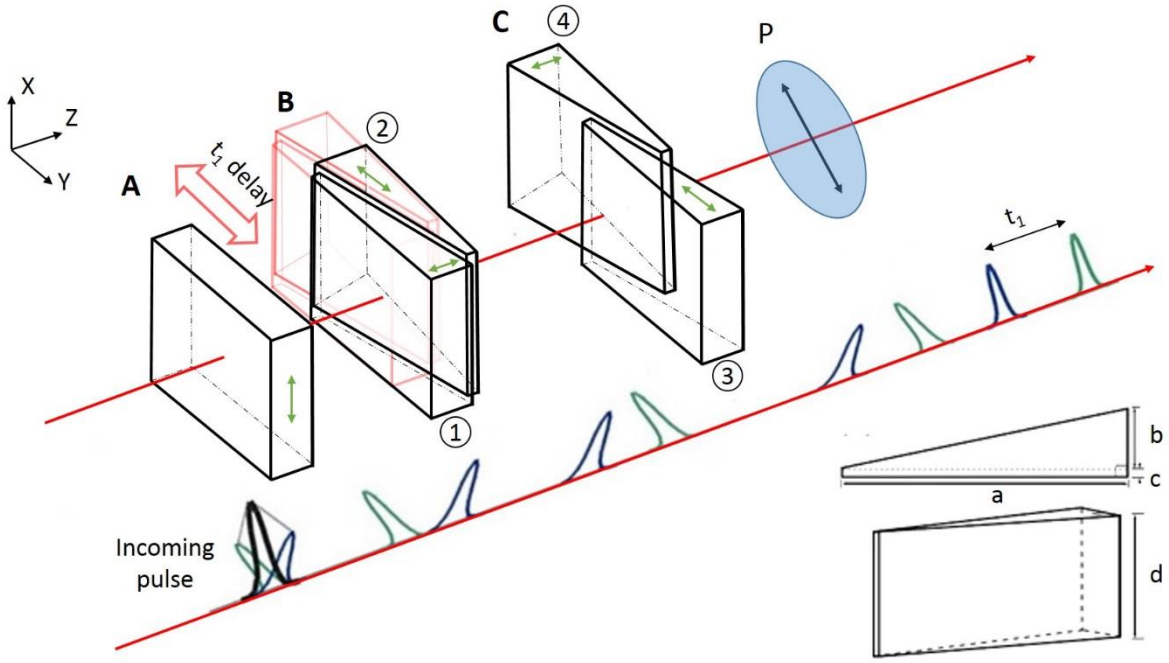

Fig. 22 : TWINS system composed of one a-BBO plate and four a-BBO wedges cut along different optical axis (figure adapted from ref.24); the optical axis for each optical element are indicated with green double sided arrows. Block A creates an initial negative delay between Y and X polarized pulses (2.4mm thickness). Block B is mounted on a motorized stage the translation of which, along the Y direction, changes the optical path for the Y polarized pulse introducing a delay between the pulses. Block C is used to correct for phase front tilt and slightly non-collinear direction of the pulses after exiting Block B. The polarizer P at the end of the sequence projects both pulses on a 45° tilted linear polarization axis. The wedges designed for the TWINS have dimensions a=25mm, b=3.1mm and c=0.5mm with an edge apex ~7°.

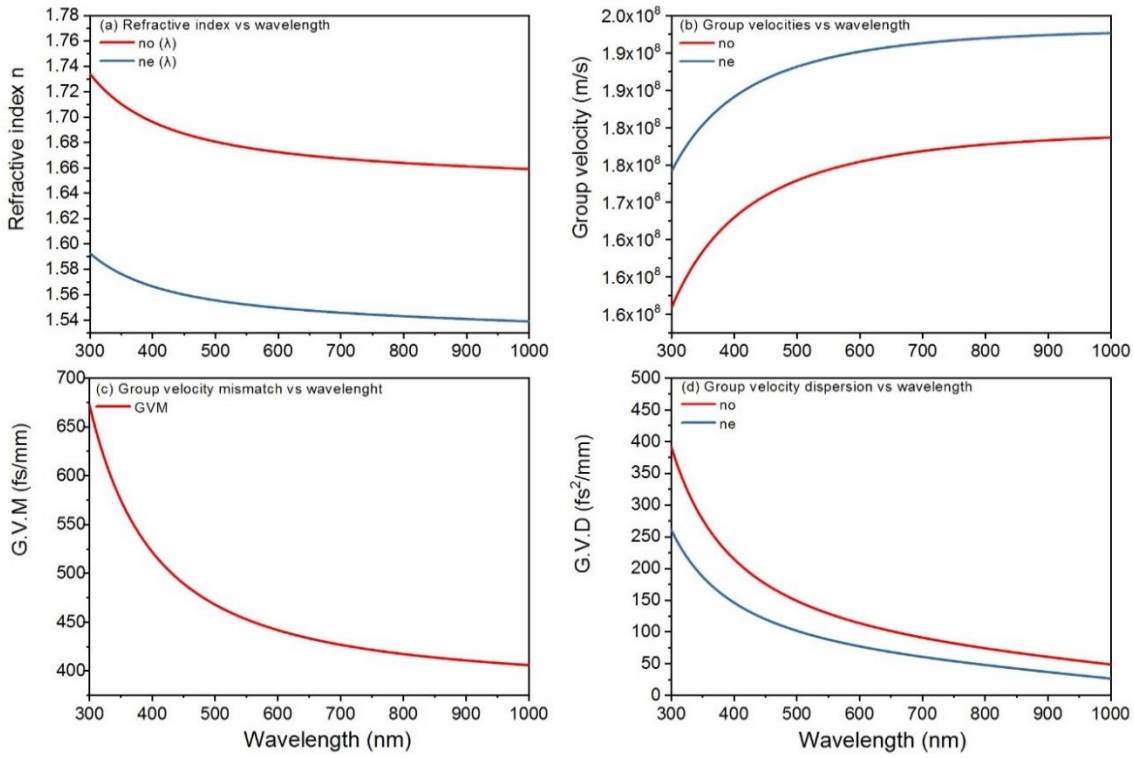

Fig. 23 : a) refractive indices as a function of wavelength b) Group velocities of two pulses polarized along no and ne axis c) Group velocity mismatch between two pulses that propagate along the two polarizations d) calculated group velocity dispersion for pulses propagating along the two polarizations

For our description, we refer to the X-Y-Z directions as defined in the scheme, with the beam Pointing vector in the Z-axis direction (red arrow) and the optical axes of the BBO wedges depicted with green double sided arrows.

The first block is a plate of a constant thickness with the optical axis along the X direction. The incident beam which arrives with a linear polarization of 45º is split in two pulses with perpendicular polarizations and same intensity (X and Y axis). The two pulses now propagate with different group velocities v_g (v_{go} and v_{ge} according to their polarization) as shown in fig.23b and table 1, with the pulse along the X axis traveling faster (v_{ge}) and creating an initial delay with respect to the one along the Y axis (v_{go}). This delay depends on the thickness of block A, which in our case is 2.4mm.

As can be understood, if the plate's thickness could vary, then a relative delay between the pulses can be achieved. The latter is obtained after implementation of block B, which is composed of a pair of wedges. The wedges 1 and 2 have their optical axis along Z and Y directions respectively and are both mounted on a Y-axis motorized stage (Physik Instrumente). The translation along the Y direction will increase or decrease the relative thickness of the one wedge with respect to the other, while simultaneously the total thickness of the two wedges is kept constant. Due to the wedge's optical axis, the X polarized pulse will see a constant optical path as the two wedges are geometrically identical and have their optical axis perpendicular to the pulses polarization. In contrary, the Y polarized pulse will see a different optical path and will travel with a v_{ge} group velocity in the wedge 2. Depending on the thickness of wedge 2 we insert in the beam's path, the latter pulse can arrive earlier than the X polarized one. The delay created between the two pulses depends on the Group velocity mismatch (GVM) between the two pulses; the GVM (eq.45) of the two polarized pulses is shown in fig.23c.

$$GVM = \frac{1}{v_{go}} - \frac{1}{v_{ge}} \quad \text{eq. 45}$$

One of the requirements upon performing 2DES experiments is that the delay between the probe pulse and the second pump pulse (fig.15a) has to remain constant (waiting/population time). This means that the one of the two pulses in the TWINS has to remain static and the other one should be able to be delayed relative to the first one. In our case, the pulse with the X polarization remains static and the one with Y polarization is moving. The latter requirement is established because of the wedges geometrical design which maintain a constant thickness for Block B upon scanning the t1 delay.

At the output of Block B, the two pulses are phase front tilted[1] and slightly non-collinear as they have experienced different refractive indices on wedge 2. To maintain that both pulses propagate collinearly in the same path, the implementation of Block C is mandatory. This Block is composed of another pair of static wedges, geometrically identical to the wedges pair in Block B. The wedge 3 and 4 have their optical axis along the Y and Z direction respectively. While imperfections on the wedges design can arise, wedge 3 is mounted on a goniometer (X,Y plane rotation) used to maintain that wedge 3 and 2 are parallel. To avoid lateral displacement of the two pulses, Block C is placed as closed as possible to Block B.

[1] Front tilt: the arrival time of the pulse varies along the beam's spatial profile (www.rp-photonics.com)

At the output of Block C, a polarizer set at 45° projects the two pulses to obtain the same polarization for both. However, the scheme for our case is slightly different. Indeed, in order to avoid implementation of a λ/2 plate before the TWINS and a polarizer at the output, we rather mount the whole device on a stage with 45° incline. Thus, we avoid introducing additional dispersion when using a λ/2 plate and a polarizer, while remaining in the frame of highest transmission.

Table 1 shows the refractive index that each pulse experiences along propagation through the three Blocks.

Table 1 : Refractive index that each pulse experiences along propagation through the three Blocks

Pulse polarization	Block A	Wedge 1	Wedge 2	Wedge 3	Wedge 4
X	n_e	n_o	n_o	n_o	n_o
Y	n_o	n_o	n_e	n_e	n_o

2.3.5 TWINS advantages and characteristics

The biggest advantage of using the TWINS arises from the fact that the pulses are collinear, both pulses see the same propagation path and so they are phase-locked. Supplementary, controlling the delay among the two pulses is a crucial point, as the precision has to be extremely high. In our case the precision for the t1 delay is outstanding, as the motorised stage used offers <10nm resolution, resulting in a minimum delay of <5as ($5 \cdot 10^{-18}$s). The maximum relative delay between the two pulses is given by eq.46 and can vary up to ~1ps, for d≈2.37mm.

$$t_1 max = GVM \cdot d \qquad \text{eq. 46}$$

When scanning the t1 delay, we set a constant velocity of the motor, with the acquisition based on the arrival time of each pulse (every 1ms). To keep the acquisition time as short as possible, we acquire data on forward and backward movement of the motor. While the acquisition of data is continuous, the motor's movement in the TWINS is not synchronised with the laser's repetition rate. To ensure that same delays are recorded for back and forward movement of the motor and avoid this time jitter between different scans; simultaneous recording of the pulse autocorrelation in order to correct is obligatory. The latest is achieved using a low GDD dichroic mirror just after SFG which allows transmission of the un-converted Red-NIR replicas and recording the autocorrelation by a photodiode (fig.24).

Moreover, the spectral resolution $\Delta\nu$ needed for performing each measurement is directly linked with the scanning range of the two Red-NIR replicas (see eq.47).

$$\Delta\nu = \frac{1}{t_1 max} \ , \ \Delta\lambda = \frac{\lambda^2 \Delta\nu}{c} \qquad \text{eq. 47}$$

Once we vary the delay for the Red-IR replicas, the same delay holds for the UV-Blue replicas. To be more precise, the desired spectral resolution we are interested in concerns the UV-blue pair. In table 2 the calculated values of spectral resolution as a function of different scanning ranges are shown. It can be understood that for electronic transitions in the UV-Vis spectral range, and depending on their linewidth, a 3-4nm spectral resolution is enough to reveal any couplings. The latter is achieved by not more than a 150fs scanning range for t1.

Table 2 : Expected values for the spectral resolution Δλ for the 400nm pulses as a function of t1 scanning range; the thickness variation of the wedge2 is shown for each scanning range; Calculated duration of the moving pulse according to the scanning range for using the TWINS in the Red-IR or on the UV-Blue pulse;

t1 scan range (fs)	d (mm)	Δλ (nm)	Red-IR duration (fs)	UV-Blue duration (fs)
50	0.118	10.67	7.03	8.64
100	0.237	5.33	7.41	9.87
150	0.355	3.56	8.01	11.62
250	0.591	2.13	9.67	15.96
400	0.946	1.33	12.85	23.41

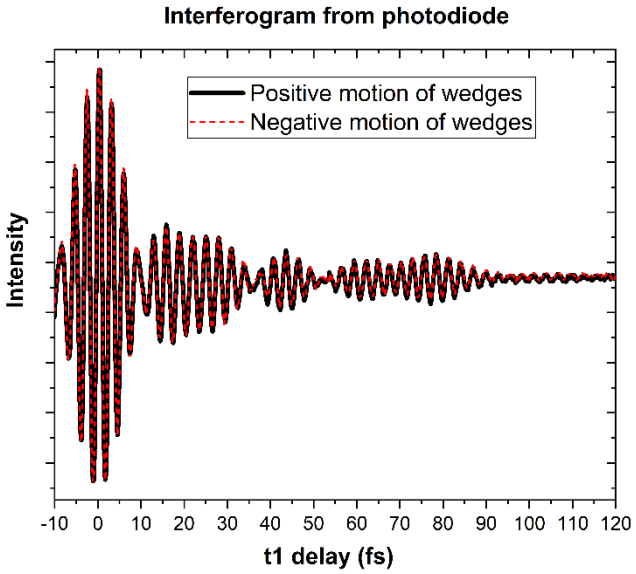

Fig. 24: Autocorrelation of the Red-IR replicas for forward (black solid line) and backward movement (red dashed line) of the TWINS recorded by a photodiode; this autocorrelation is used for precise determination of time zero between the two pulses and for phasing the 2DES data.

A concern that arises from the TWINS design is the maintenance of very short pulses, particularly in the sub-10fs regime, since the broad pulse spectra are prone to experience significant dispersion induced by the a-BBO wedges. Taking into account the group velocity dispersion for n_o and n_e refractive indices (see fig 23d) we can calculate the amount of dispersion that the pulses experience after propagation through the TWINS. For the wedges set at t1=0fs the positive dispersion is ~610fs^2 at 740nm (center wavelength of our pulse). This amount of dispersion can be compensated by using two pairs of chirp mirrors before the TWINS device (DCM9 from Laser Quantum). The latter DCMs allow a compensation of 50fs^2 for each pair of bounces. For fine tuning the pulse dispersion, we use a pair of Fused silica wedges after the TWINS (fig.20). For the pulse duration characterization we will refer in more detail in section 2.4.

Even though we take the advantage of birefringence to delay the one pulse with respect to the other, limitations can arise. One limitation is related to the different group velocity dispersion that the moving pulse experiences while the thickness of wedge 2 inserting the beam path increases. In fact, the moving pulse is changing its duration depending on the scanning range of t1 according to the difference in group velocity dispersion between the X and Y polarized pulses. This effect was previously reported by Réhault[24] concerning a pulse in the Visible range. Generally, the shorter the wavelength range of the pulses, the more pronounced the

effect will be. The effect in duration broadening of the moving pulse as a function of scanning ranges t1 is summarized in table 2. For our calculations, we assumed a ~7fs Fourier-limited (FL) pulse, representing the Red-IR pulse we use in the TWINS (eq.48), with the results showing an evident broadening upon scanning t1 delays >150fs. In eq.48, $\Delta\tau_{FL}$ and $\Delta\tau_{after}$ are the durations of the FL and the broadened pulses respectively, with φ_2 corresponding to the difference in GVD induced by the two different refractive indices corresponding to a certain t1 range.

$$\Delta\tau_{after} = \Delta\tau_{FL}\sqrt{1 + \left[\frac{4ln2\varphi_2}{(\Delta\tau_{FL})^2}\right]^2} \quad \text{eq. 48}$$

Particularly, for a scanning range of 400fs the pulses duration is almost doubled. On the other hand, a 150fs scanning range corresponds to a 3.54nm spectral resolution (for the UV-blue replicas) with a minor effect of ~1fs in the Red-IR pulse's duration. The idea of using the TWINS on the Red-IR pulse and not directly on the UV-Blue is obvious for two important reasons. Firstly, the amount of dispersion we had to compensate would have been huge, in the range of ~1500fs^2 which is almost triple the amount we have to compensate for the Red-IR one. Secondary but still important, is the effect on the duration of the moving pulse, which for a 150fs scan appears longer by ~40% (11.62fs from 8.2fs) and for a ~400fs range almost triples (23.41fs).

For the proof of principle, we have recorded a spectrally-resolved autocorrelation of the near-UV-Vis pulses recorded by varying the time delay between both Red-IR replicas with the TWINS device (fig.25). As shown in the figure, the structured pulse spectrum is encrypted on the autocorrelation traces map, with evidences for the constructive and destructive interferences when moving the TWINS motor. The latter proves clearly that we are able to produce two collinear replica of the UV-Blue pulse and delay the one with respect to the other. This kind of autocorrelation measurement is used in the calibration procedure prior to performing 2DES measurements (by having the two replica dispersed in the spectrometer) and thus we are able to retrieve the excitation axis.

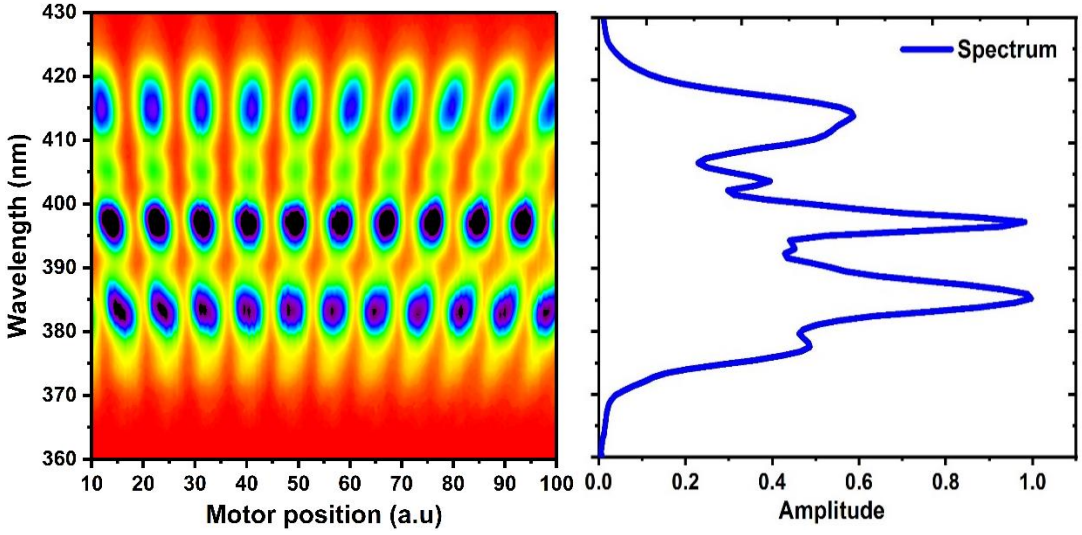

Fig. 25: Spectrally-resolved autocorrelation of the near-UV-Vis pulses recorded by varying the time delay between both Red-IR replicas with the TWINS device; on the right the spectrum of pulses at t1=0fs is shown for comparison

2.3.6 Calibration – Data phasing

During this thesis, the lack of time did not allow me to perform 2DES experiments using the near-UV-Blue replicas in our laboratory. However, in the framework of a funded project by "LaserLab Europe" I was given the opportunity to perform experiments at Politecnico di Milano, particularly in the group of Prof. Giulio Cerullo with the appropriate assistance by members of his team and from our group (Johanna Brazard and Youssef El-Khoury). The 2DES experiments based on the TWINS, were performed in the visible spectral range (525nm-725nm) for investigating a microbial retinal protein named ASR. In this section I will not comment on the results of these experiments but I will rather use the data to explain the Calibration procedure and the data analysis.

The calibration procedure as mentioned already in the previous section is the way to retrieve the excitation axis of the 2DES data. Usually the excitation axis is directly retrieved from the t_1 delay step which is constant; the step is known by the displacement of the motorized stage on the moving arm of the interferometer. Thus upon Fourier transforming the data, we pass from the Time domain to the Frequency domain with the data plotted along that excitation axis. Similarly in our case, we aim to pass from the TWINS motor position domain, to the optical frequency domain. The slight difference in our case is that depending on the scanning range and sampling of the data we want to achieve, we set a different velocity for the TWINS motor. This means that the step for t_1 delay changes according to the parameters of the acquisition we want to perform. An elegant way to get the excitation axis depending on each set of acquisition parameters, is to perform a spectrally resolved autocorrelation between the two pump pulses with identical conditions as those used for the actual 2DES measurement. The latter is done by simply sending only the two pump pulses inside the spectrometer and launch a unique t1 scan (fig26a, for a ≈8 fs pulse derived from a NOPA). On this kind of 2D map, each horizontal cut is an autocorrelation of the two pump pulses as a function of motor steps, which corresponds to a specific optical frequency (wavelength). An example of the latter is shown in fig.26e with the autocorrelation trace corresponding to ~598nm (501 THz). Afterwards, an FFT of the traces along the motor position axis will result in a single frequency peak as shown in fig.26d. Notice that the axis is in units of inverse motor steps, which is a pseudo-frequency axis. When this procedure is applied for all the traces of fig.26a, then it is possible to assign each pseudo-frequency to an optical frequency. A linear fit between the two (fig.26f) yields the excitation axis. To confirm that the procedure is reliable, we measure separately the spectrum of the two pumps at t1=0fs (red solid line in fig26c) and we compare it with the sum of the FFTs of each horizontal cut of fig.26a (black solid line). An alternative way, equivalent with the latter, is to record the autocorrelation between the two pumps in a photodiode (interferogram in fig.26b) and then apply an FFT scaled along the excitation axis obtained from the procedure described before. On a normal basis, and in order to have a better sampling of the data in the frequency domain, we apply "zero padding", addition of zero's, until the next power of 2 of the number of time steps in the time domain. For example, if the data in the time domain are acquired for 1310 steps, we add zeros at the end until reaching 2048.

After performing the calibration procedure and acquiring 2DES data we have to perform a phasing procedure. The latter is relevant with the determination of time zero between the two pump pulses for each consecutive scan, since the TWINS motor is not synchronized with the laser and a time jitter appears between the several scans. A way to correct for this time jitter

is to acquire 2DES data while simultaneously recording the interferences between the two pumps with a photodiode; as Helbing et al[38] did.

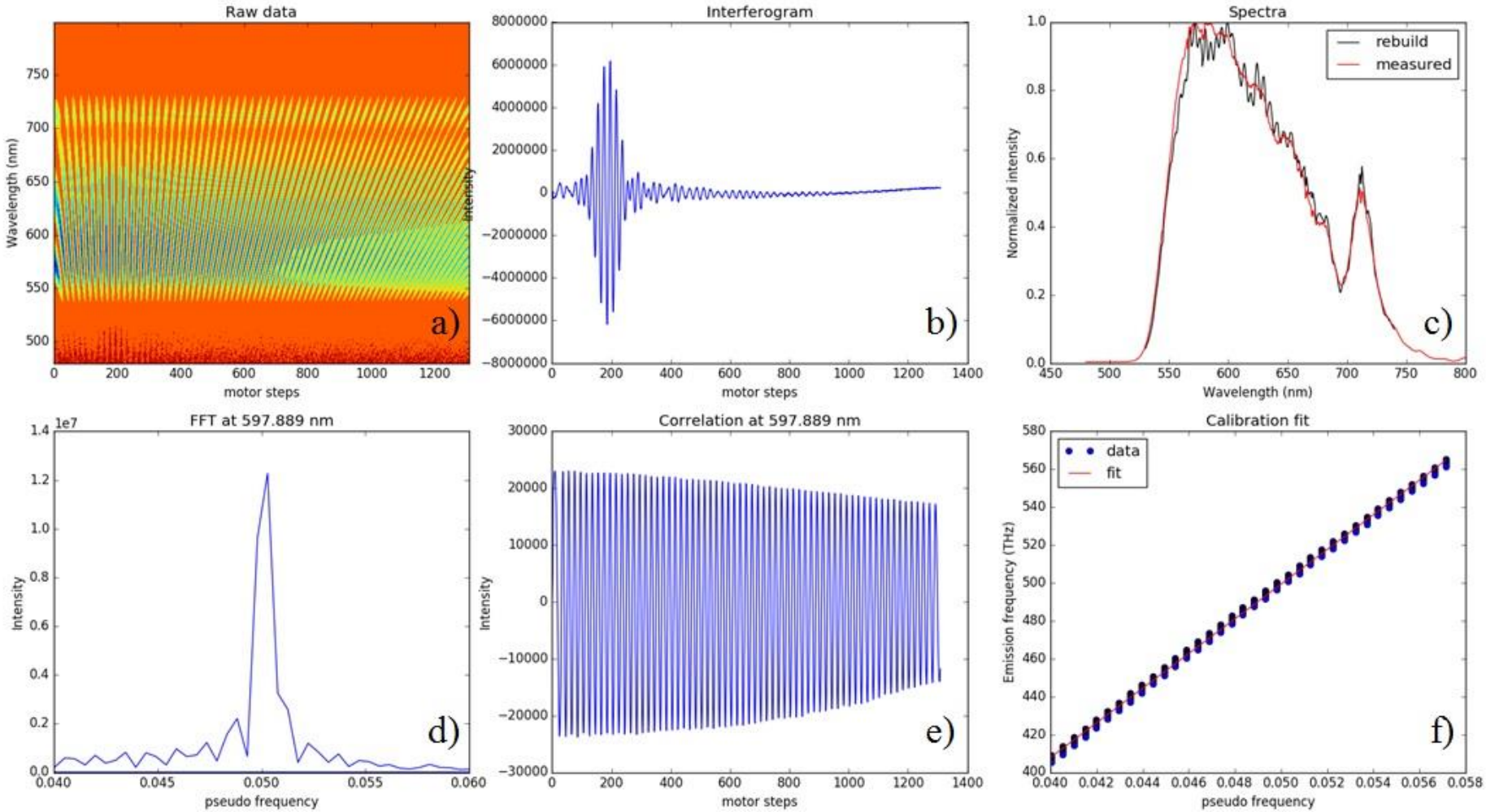

Fig. 26 Calibration procedure; a) spectrally resolved autocorrelation of the two pump pulses after dispersing them in the spectrometer d b) the same autocorrelation as in a) detected using a photodiode (used for having the time zero for each scan as the laser is not synchronised with the laser's repetition rate); c) comparison between the spectrum measured at t1=0fs (red solid line) and the one extracted after the calibration procedure (black solid line); e) an horizontal cut of a) showing an autocorrelation trace which corresponds to an optical frequency (wavelength=~598nm); d) the FFT of e) results in a unique peak scaled along a pseudo-frequencies axis (units are inverse of motor steps); f) assignment of each pseudo-frequencies to an optical frequency after a linear fit in the frequency domain (used to obtain the excitation axis)

Fig.27a shows an example of this kind of autocorrelation recorded upon 2DES measurement, with the data recorded in the spectrometer shown in fig.27c. Upon FFT of the photodiode's interferogram, it is possible to get the amplitude and phase of the pump pulse as shown in fig.27b; black and red solid lines correspond to the pulse's amplitude and phase respectively. The actual time zero between the pump pulses is given at the position where the interferogram is maximum (t1=0fs shown with vertical black line). Then a simple translation of the data prior to the time zero, to the end of the data is enough to phase the data. The latter procedure is shown in fig.27d with the phase now being flat for the whole range of the pulse spectrum (fig.27e). The translation of the data prior the defined zero, to the end is applied in an analogous way, for the data recorded in the spectrometer (fig.27f). Notice that the time zero (white horizontal line) in fig.27c is the same as the one in fig.27a. Both, in case of phasing the photodiode's data and the data from the spectrometer, we apply a zero padding in the next power of 2.

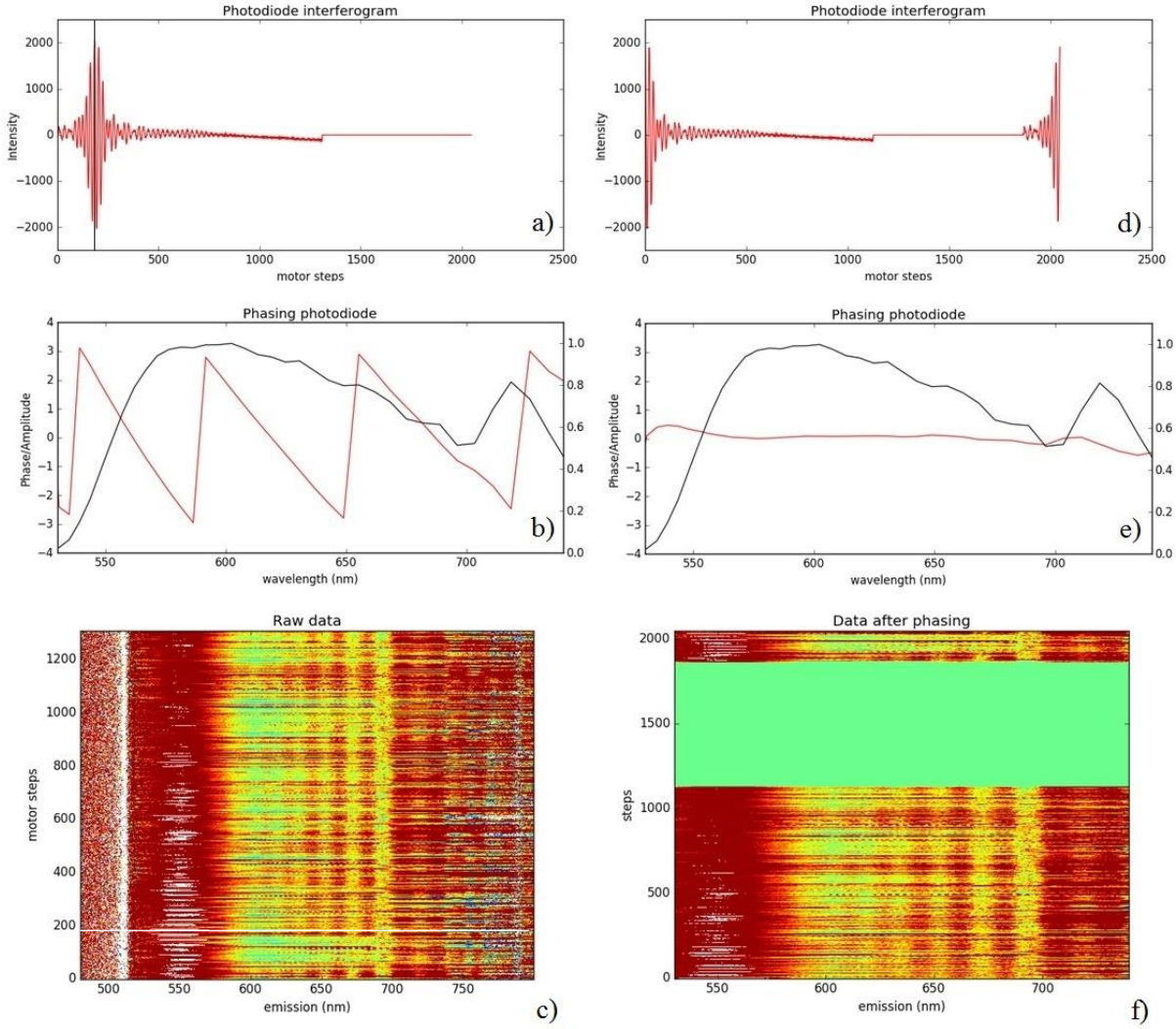

Fig. 27 : Phasing of the data by using a photodiode (determination of t1=0fs) a) the interferogram between the two pump pulses recorded simultaneously upon 2DES measurement (red solid line); the black vertical line is used to show the maximum intensity value which corresponds to the time zero b) amplitude (black) and phase (red) of the pump pulses after FFT of a); c) spectral domain interferogram $s(\tau,\omega_t;T)$ which is recorded in the spectrometer (probe pulse); d) same interferogram as in a) after defining the time zero and translating the negative time signal to the end; e) amplitude and phase of the pulse as in b) we notice that after this phasing procedure the phase is flat along the whole pulse spectrum in contrary with b); f) same spectral domain interferogram as in c) with the appropriate translation of the negative time data at the end analogous to d);

2.3.7 2DES Data filtering

After performing the calibration and completing the phasing procedure, is possible to average the interferograms recorded for each waiting time T separately. An FFT operation on the data along the motor step position, will result in the 2D spectra for a specific T. In this section, we will comment on the filtering procedure of the data, which is possible to be done either in the time or in the frequency domain. Here we refer explicitly to the time domain filtering and to the different windowing options.

The starting point is the averaged 2D spectral interferogram. To apply a specific filtering window we use the data from the spectral range with the higher signal which in our case is the one at 550nm (raw data at fig.28b). The raw data suggest that the coherences expressed through the oscillating signal are damped within ≈160 steps. Therefore the signal for steps longer than 200 should be only noise contributions. Here we test three different windowing options such as rectangular, exponential and Gaussian with the form shown in fig.28a. The windowed data are shown with different colored lines in fig.28b with the FFT of the windowed data shown in fig.28c. In fig.28c we can see directly the effect of each window on the intensity value. The highest intensity is observed for the case of rectangular filtering once the data up to 200 steps were weighted equally. In the case of Gaussian and Exponential windows, we observe gradually a decrease in intensity, which is relevant to the filtering form. Supplementary, the most Gaussian-shaped peak (no side wings) is observed for the case of Gaussian filtering. Even though, the highest intensity value is observed for the case of rectangular filtering some artifacts can appear. The latter is relevant with the shape of the window, once an FFT of a rectangular results in a sinc function. Indeed, the latter is reflected as an oscillation in the pseudo-frequency domain suggesting that unwanted contributions can also appear on the 2D map. The 2D maps corresponding to the different windows are shown in fig.28d. Two main peaks are presented, the one of GSB (centered at 550nm) and the ESA/PA (centered at 610nm) one. Beside some scattering contribution along the diagonal, the shape of the signals for Rectangular and Gaussian windows is quite similar. On the contrary, the broader shape of the GSB in the case of Exponential filtering is more meaningful as the absorption spectrum of the sample extends up to ~630nm. In addition, for the other 2 cases, a small but unexpected negative signal is observed for the excitation wavelength of 630nm. However, between the Gaussian and exponential windows, the latter seems more reliable while the ideal windowing could be achieved by using a super-Gaussian form. In this way, the data along the broader range of coherences could be equally weighted and we could avoid the sharp ending of the window (for example rectangular) analogous to the exponential case.

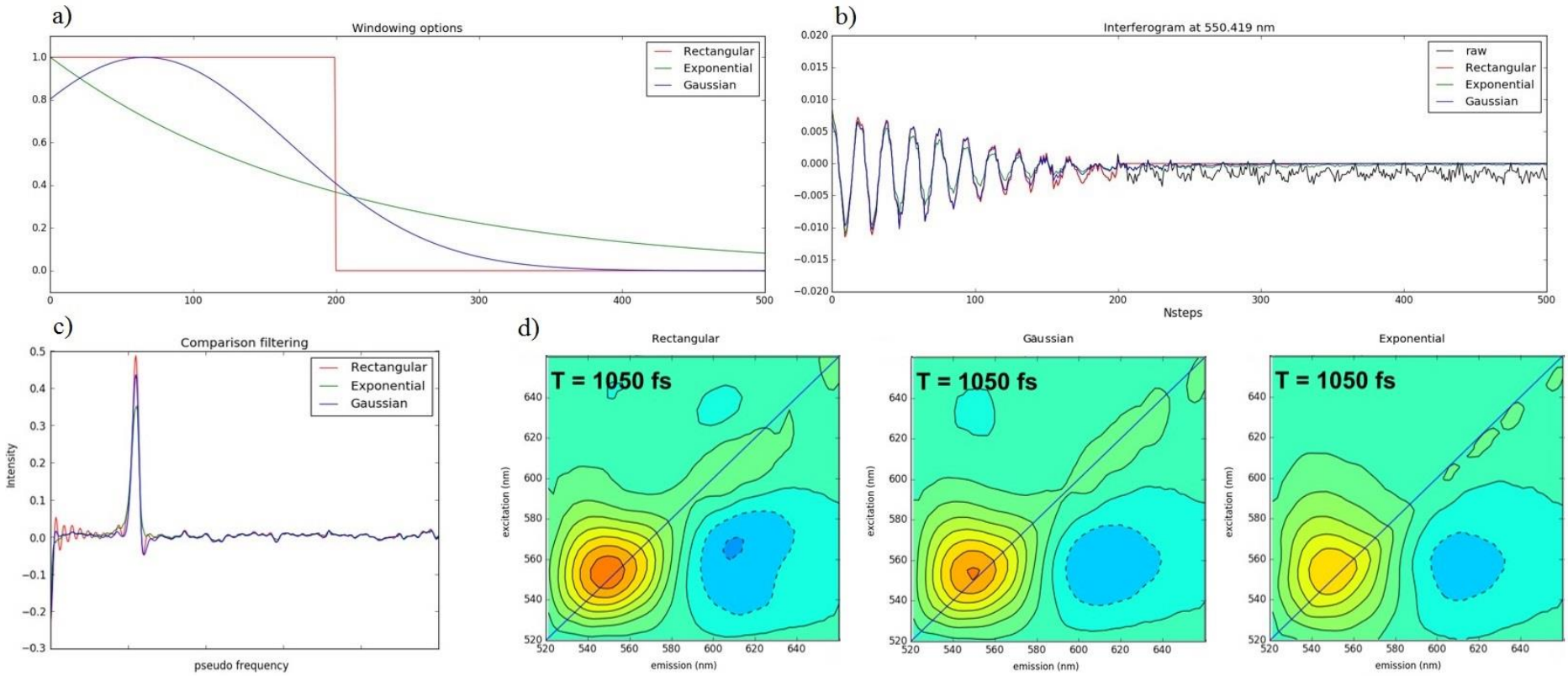

Fig. 28: Filtering of 2DES data in the time domain; a) different windows used shown with different coloured lines; b) Interferogram from spectrometer plotted for 550nm wavelength; Different coloured lines correspond to application of each windowing function shown in a); c) FFT of b); d) 2DES maps for T=1050fs for the different windows;

2.4.1 Two-dimensional Spectral Shearing Interferometry

The most frequently method for characterizing pulses with duration >15fs is by recording their 2nd order autocorrelation $G_2(\tau)$ by using an autocorrelator. In our case the $G_2(\tau)$ is obtained by SHG of two interfering replicas, of the pulse under study, in a BBO crystal. When it comes to very broad spectrally pulses (>40THz bandwidth); which is the case for the red-IR pulses and UV-blue pulse, the determination of the pulses duration is limited by the conversion bandwidth of frequency doubling in a non-linear crystal. To overcome the latter, we have to use a technique that takes advantage of the pulse's large bandwidth. Thus we use a technique which allows characterization of a few-cycles pulses, called two-dimensional spectral shearing interferometry (2DSI)[39–41]. The latter falls in the category of techniques related to amplitude-phase measurements, of the pulse's Electric field E(t). Particularly, using 2DSI, it is possible to measure the pulse's spectral phase φ(ω). The phase is encoded in an interference term between two up- (or down)-converted replica of a pulse; the generated replica can be described in the frequency domain as $A(\omega)e^{i\varphi(\omega)}$ and $A(\omega-\Omega)e^{i\varphi(\omega-\Omega)}$ respectively (eq.49).

$$I(\omega,\tau_{cw}) = |A(\omega)|^2 + |A(\omega-\Omega)|^2 + 2|A(\omega)A(\omega-\Omega)| \times \cos[\omega_{cw}\tau_{cw} + \varphi(\omega) - \varphi(\omega-\Omega)] \qquad \text{eq. 49}$$

The two up-converted replica are the product between two very long (in duration) auxiliary pulses (quasi-cw), with the pulse we would like to characterize. The quasi-cw pair is usually generated either by using a Michelson Interferometer (M.I); which includes a highly dispersive element (thick glass beam splitter), or by using a pulse shaper such as in the case of ref.41. In both cases, the generation of the two quasi-cw replica is accompanied with a relative frequency shift called "shear" (Ω). In the M.I case, the relative position of the interferometer's static arm with respect to the moving arm defines the shear frequency (τ_{CW} delay in fig.29). Complementary, in the pulse shaper's case (4f-line), it is possible to end up with a similar result by using a spectro-spatial mask at the Fourier Plane. However, the strategy is to create two pulses, which have the same spectral phase as the one we want to characterize and make them interfere. Both conditions are established upon up- (or down) converting the short pulse with the two long (but simultaneously frequency shifted) replicas in a birefringent N.L crystal.

The advantage of this technique over similar ones, such as the well-known SPIDER[42], is the additional dimension, introduced by scanning the relative phase $\omega_{CW}\tau_{CW}$ between the long replicas. In the SPIDER method, the pulse's spectral phase is encoded in a single fringe, while in 2DSI's case in a cosine fringe (eq.49). The variation of τ_{CW} delay (moving arm of MI) is giving the additional dimension yielding a two-dimensional map $I(\omega, \tau_{CW})$ as shown in fig.32a, which is independent of the setup properties (spectral resolution etc). The only requirement is the determination of the shear frequency Ω between the two up-converted replicas. What we actually measure is the phase difference between the two up-converted replica, which is the first order approximation for the pulse's group delay (τ_{GD}) multiplied by the shear frequency[39] (eq.50). The variation of τ_{CW} delay does not affect the measured spectral phase of the pulse, as it represents the scanning of the zeroth-order phase of the up-converted replica. The latter is likewise the phase of a plane wave component propagating with a velocity $u_\varphi(\omega_{CW})$ which does not carry any information for the pulse.

$$\varphi(\omega) - \varphi(\omega - \Omega) \cong \frac{d\varphi(\omega)}{d\omega}\Omega \cong \tau_{GD}(\omega)\Omega + O[\Omega^2] \quad \text{eq. 50}$$

The two up-converted replica are collinear, with the recorded signal expressed by three terms as shown in eq.49. When scanning the delay τ_{CW} within a short range, the first two terms represent a static contribution and can be removed; by recording the background upon having each MI arm path blocked. Thus, the remaining term upon performing a measurement is the one containing the cosine term. The latter contains all the valuable information, which is the difference in phase between the two replicas. For a shear $\Omega << \omega$ we can express this phase difference by the derivative of the pulse's spectral phase (eq.50).

In order to understand which terms of the spectral phase we measure, we write the spectral phase in a Taylor expansion around the central frequency ω_0 (eq.51). The zeroth order phase $\varphi_0^{(0)}$ represents the carrier envelope phase (CEP) which is not measured by 2DSI, as the derivative of this constant term is zero. Moreover, the $\varphi_0^{(1)}$ is a constant group delay term, which corresponds to a delay of the pulse with respect to an arbitrary origin of time[9]; this is a constant offset in the measurement. In contrary with the two previous terms, the most important one, responsible for a pulse duration increment, is $\varphi_0^{(2)}$ (quadratic phase). This term is called "chirp" and concerns the delay that each instantaneous frequency (within the pulse's spectrum) experiences. Particularly, a linear increment of this delay upon scanning the frequencies in acceding or descending order, will appear as negative or positive chirp respectively. As we measure the derivative of the phase we observe this term as a linear tilt on the recorded fringes, where the slope defines the amount of chirp the pulse is experiencing. Supplementary, the $\varphi_0^{(3)}$ term corresponds to a higher order dispersion (cubic phase), which appears as a quadratic term in the measurement. The effect of this kind of chirp is the presence of pre- or post-pulses. Any higher order of dispersion is neglected with the measured terms shown in the dashed red frame below.

$$\varphi(\omega) = \varphi_0^{(0)} + \boxed{\varphi_0^{(1)}(\omega - \omega_0) + \frac{1}{2}\varphi_0^{(2)}(\omega - \omega_0)^2 + \frac{1}{6}\varphi_0^{(3)}(\omega - \omega_0)^3} + \ldots + \frac{1}{n!}\varphi_0^{(n)}(\omega - \omega_0)^n$$

$$where \quad \varphi_0^{(0)} = \varphi(\omega_0), \varphi_0^{(n)} = \left.\frac{d^n\varphi}{d\omega^n}\right|_{\omega_0} \qquad \text{eq. 51}$$

2.4.2 2DSI setup

The overview of the experimental setup used in this thesis is shown in fig.29. Initially, the understudy pulse is split with a 10:90 (R:T) ratio using a wedge, with the transmitted portion sent in a M.I interferometer for production of the two quasi-cw replicas. As briefly described above, the M.I is based on a 3cm thick cubic BK7 B/S, which chirps the incoming pulse (>3000fs^2) and splits it with 50:50 ratio. The transmitted beam is located on the static arm of the interferometer, where a mirror mounted on a manual translation stage allows setting the time zero with respect to the moving arm's beam (τ_{SHEAR}). Complementary, the other part of the beam is located on the moving arm of the MI, where a piezo-electric stage is used for varying the τ_{CW} delay upon a measurement. At the output of the MI, both quasi-cw replicas (sheared) are collinear and propagate through a broadband $\lambda/2$ plate. In this way we are able to set the polarization of the long pulses perpendicular to the short's one; required for broadband type II phase matching conditions upon SFG on the BBO crystal. Both quasi-cw replicas and the short pulse are focused on a 50μm thick β-BBO crystal using a parabolic mirror. The time zero between the short pulse and the long pulses is obtained by using the

manual delay line (τ_{SFG}), placed on the short pulse optical path. Finally, the product of SFG, which are two UV replicas are collected and send in a fiber-based spectrometer using a lens and a bandpass filter.

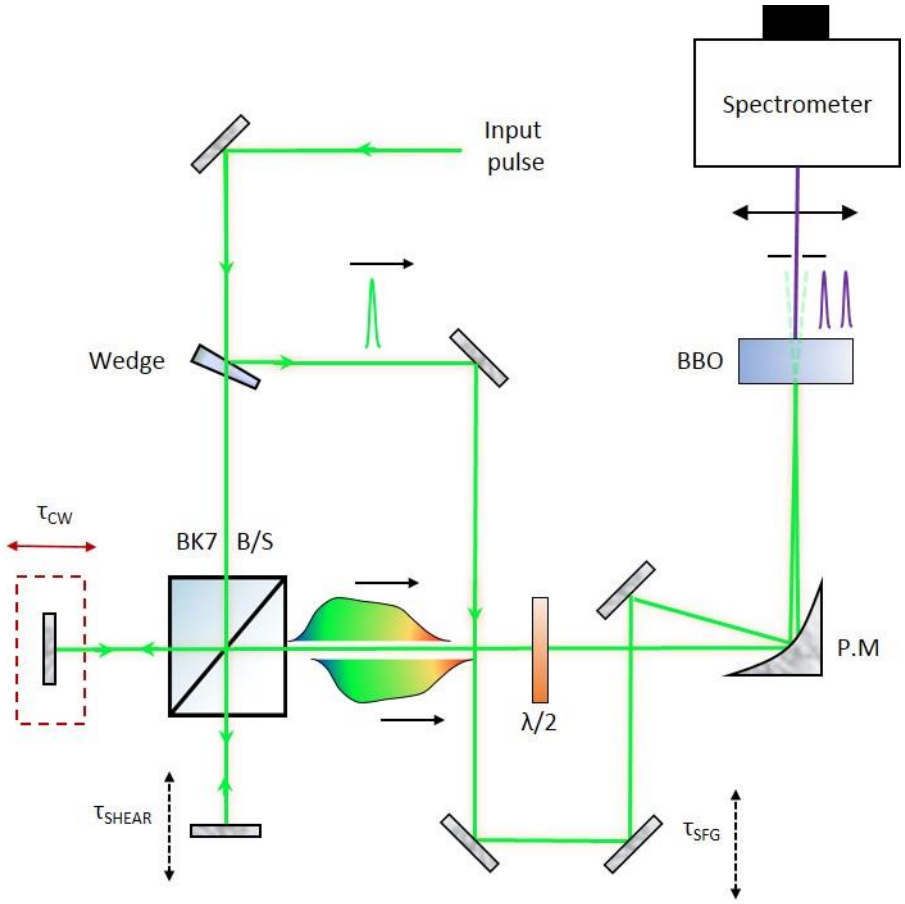

Fig. 29 : Overview of the 2DSI setup; the optical elements on the short pulse optical path are designed for low GDD (group delay dispersion) conditions.

According to Birge et al[43], the error on the pulse's duration δ_t in our measurements arises from the uncertainty on the τ_{CW} delay using the piezo-electric stage and the ratio between the bandwidth of the pulse $\Delta\omega$ and the shear frequency Ω eq.52.

$$\delta_t \approx \delta_{\tau_{CW}} \left(\frac{\Delta\omega}{\Omega}\right) \quad \text{eq. 52}$$

For a Gaussian shape pulse with a $\Delta\omega$ FWHM of ~(2π x 100)THz and for a shear frequency in the order of ~(2π x 10)THz, the ratio gives a factor of 10. Taking into account the uncertainty on our piezo-stage which is 18as (10^{-18}s), the uncertainty on the pulse duration is only ~0.2fs.

2.4.3 Determination of shear frequency Ω

The only requirement of calibration in a 2DSI measurement is the determination of the shear frequency between the two quasi-cw replicas. The latter we define it by performing a cross correlation of the up-converted spectra with the base spectrum by blocking the MI static arm optical path. An example of the "shear" determination is shown in fig.30a using the NOPA's green pulse. The maximum of the SF spectra shift with the variation of the piezo position is shown by a white dashed line. For direct comparison, we show the same data for the MI static arm (fig.30b) where clearly no shift is observed. A simple determination of the maximum wavelength of the SF spectrum for each piezo delay is enough to determine the shear frequency. A fit in the frequency domain between the maxima and the piezo position is shown in fig.30c. The slope corresponds to a shear gradient as shown in expression 53.

$$\Omega = Slope \times \langle piezo\ position \rangle \quad \text{eq. 53}$$

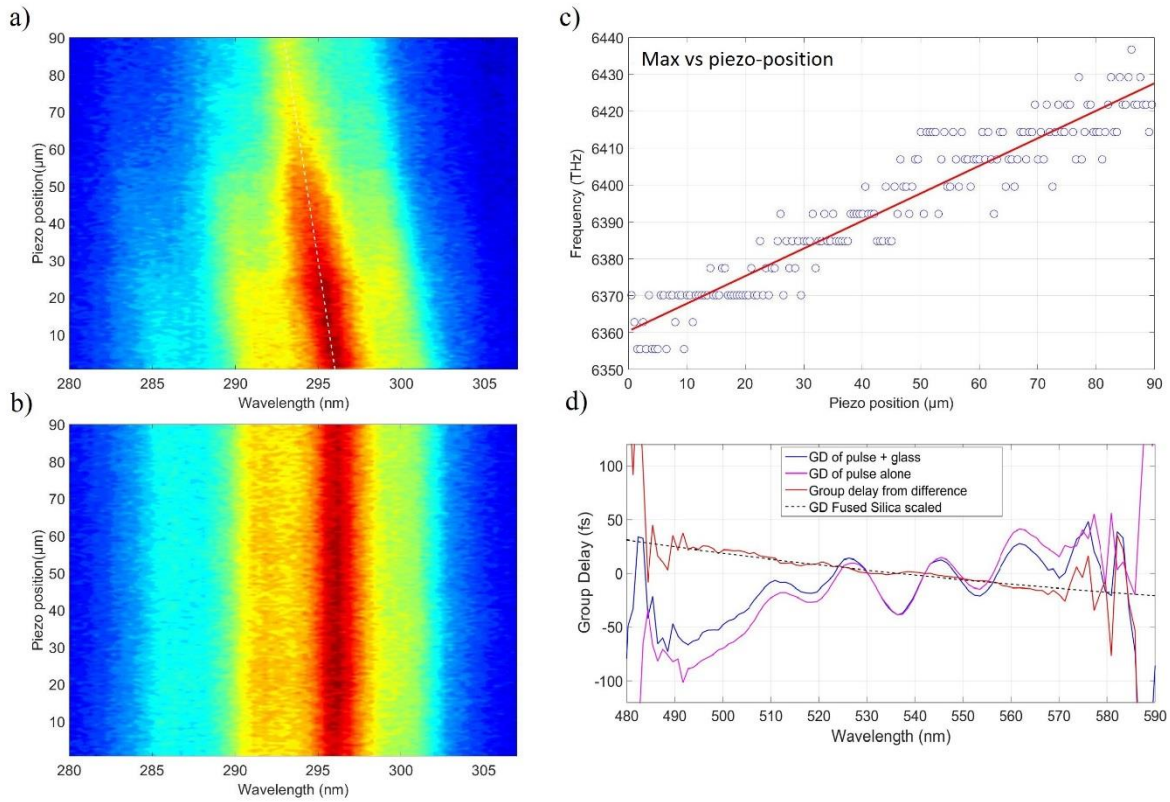

Fig. 30 : Determination of the shear frequency Ω; a)MI moving arm contribution from SFG with the short pulse - cross correlation of the up-converted replica by blocking the MI static's arm used for determination of the shear as show in in c); The SFG spectrum shifts according to the piezo position (white dashed line is used for guidance of the eye); b) Static arm contribution upon SFG with the short (moving's arm optical path is blocked); c) Procedure for determination of the shear frequency; Maxima of the SFG spectra (in ω) of a) vs piezo delay allows determination of a shear gradient (slope) d) alternative way for determination of the shear by measuring the pulses group delay by adding a glass of a known thickness; magenta and blue solid lines represent the group delay of the pulse alone and by adding a 1.08mm fused silica glass on the short pulse optical path respectively; red line shows the difference between the group delays with and without the glass; dashed black line represents the simulated group delay for the corresponding glass, where the scaling factor match the experimental data corresponding to a shear of Ω=37.1THz

In this case the slope corresponds to a 0.745 THz/μm value, with the actual measurement for the pulses duration performed in a (50-54) μm window. The mean piezo position is 52μm which corresponds to a shear of 38.7THz.

To demonstrate the accuracy of this method, we try to determine the shear frequency by performing two sequential measurements of the pulse alone and the pulse when a 1mm fused silica glass is inserted in its optical path as shown in fig.30d (magenta and blue lines respectively). The difference between the two will give the group delay of the given glass multiplied with the shear as shown below (eq.54).

$$\tau_{GD(pulse+glass)} \times \Omega - \tau_{GD(pulse\ alone)} \times \Omega = \tau_{GD(glass)} \times \Omega \quad \text{eq. 54}$$

Then if we simulate the expected the group delay (dashed black line) for the given glass thickness as a function of wavelength (or frequency), we can use it in order to fit the experimental data and extract the shear frequency. By using this procedure we have determined a shear of 37.2THz with a variation of ±1.5THz depending on the selection range of the data. The latter is expected as it depends on the scanning range during our measurement, suggesting that for higher shear gradient a shorter measurement window is required to have a nearly constant shear.

2.4.4 2DSI data treatment

After acquiring a set of data $I(x_{cw},\lambda)$ and with the determined shear frequency we start by extracting the group delay from a given number of fringes. We find the wavelength with the maximum signal and perform a FFT along the piezo-position axis. Then, we use the index which corresponds to the maximum amplitude from this FFT for this particular wavelength and we perform a phase unwrapping for the remaining wavelengths (after applying the same FFT before).
Thus we end up with the group delay with respect to wavelength of the sum frequency spectrum. To proceed on the extraction of the spectral phase we go into the frequency domain and we simply integrate (numerically) by using a finite dω step given by the spectrometer spectral resolution divided by the shear frequency. Once we have the spectral phase we can simply transfer this phase to the correct frequency axis of the pulse prior SFG. This can be done by matching the spectrum of the SF with the one of the pulses in the Vis or NIR range, by simulating the up-conversion of the latter with a quasi-monochromatic pulse. A summary of the phase extraction procedure is described in the scheme below.

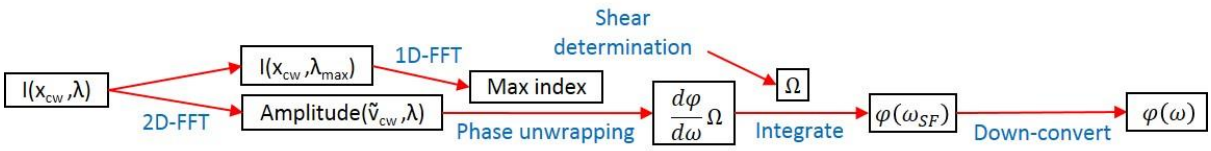

After down-converting the experimentally determined phase to the actual frequency axis, the only thing missing for constructing the pulse temporal profile, is the amplitude of the pulse. By recording its spectrum in the spectrometer we get the intensity S(ω) which is proportional to the squared amplitude $|A(\omega)|^2$. Thus the square root of the latter is the amplitude used for the reconstruction. Finally, a FFT along the optical frequencies results in the amplitude of the Electric field in the time domain E(t). Usually to avoid any kind of artefacts upon FFT we

take care in order to approach the tail of the pulses amplitude spectrum with exponential functions similar to the case of applying a super-Gaussian window.

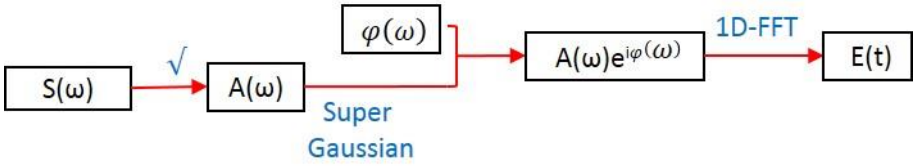

A demonstration of the procedure described above is done for the compressed broadband Red-IR generated in the hollow fiber (fig. 21) replicas to determine the pulses duration when the delay t1 is set at 0fs. For the 2DSI measurement we used a shear of 117.1THz (2π x18.65)THz with the scanning range of (50-53)μm using a 50nm step. The recorded data $I(x_{cw},\lambda)$ are shown in figure 32a with the SF spectrum integrated along the piezo positions shown (black line, fig.32b). For a direct comparison of the pulse bandwidth conversion upon SFG we show the actual spectrum up-converted with a quasi-monochromatic pulse centered at 768nm. The SF spectrum suggests that a conversion from 643-880nm was achieved. Having in mind that the full spectrum spans until 930nm the measurement will not provide any information for the phase in the >880nm wavelength range.

The treatment for getting the amplitude A(ω) from the pulse spectrum S(ω) is shown in fig.32c with the amplitude used in the Electric field's reconstruction shown as red dashed line. Moreover, the phase extracted from the data with the corresponding amplitude are shown in fig.32d. For a Fourier limited pulse, the spectral phase is expected to be flat (constant or zero) for the whole spectral range. However, according to Monmeyrant et. al[9] the sigmoidal shape of the phase suggests that our pulse experiences third order dispersion. The result concerning the temporal profile of the pulse (after FFT by applying a super-Gaussian window) is shown in fig.32e. The red solid line corresponds to the temporal profile of a F.L pulse (φ=0) and the black solid line to the reconstructed one. From a first look we can see that the measured profile is slightly broader and the central peak is shifted by 11fs. In addition, some smaller in amplitude satellite peaks (<3% of the main peak amplitude) are present. From a Gaussian fit the FWHM of the Fourier limited pulse is 7.0fs while the measured one is (9.7±0.1) fs. As can be understood, a temporal profile which is accompanied with satellite contributions will effectively have a longer duration than the value determined by its FWHM. Thus a more appropriate way of interpretation would be the Root-mean-square value (rms) which gives an effective value for the pulses duration[44]. For the Fourier limited pulse we get an rms value of 5.2fs while for the measured one 10.3fs with the resulting durations summarized in table 3. From this 2DSI measurement we understand that the amount of dispersion the pulses experience (TWINS+F.S wedges) cannot be totally compensated and results in a twice longer duration than what is ideally expected. To have an idea about the amount of dispersion on this pulse we have used a simulation program named LAB2[45]. We approached the experimental data by using a Gaussian spectrally pulse centred at 750nm with an expected FWHM duration of 7.0fs. Then we matched the phase extracted by the 2DSI measurement, by adding an appropriate amount of 1^{st},2^{nd} and 3^{rd} order dispersion. Thus, we concluded that the pulse experiences a $\varphi_0^{(1)}$=11fs , $\varphi_0^{(2)}$=-19fs^2 and $\varphi_0^{(3)}$=49fs^3. The $\varphi_0^{(1)}$ is simply a shift in time and the only important information arises from the two other terms. It seems our pulse was slightly over-compressed in terms of $\varphi_0^{(2)}$ as each pair of bounces on the DCM mirrors compensates for a dispersion of 50fs^2. Concerning the $\varphi_0^{(3)}$ term, the effect on

the pulse duration is not so pronounced as in the case of 2nd order dispersion. Assuming the same 7fs pulse which experiences a 49fs^3 dispersion, the pulse duration turns to be 7.45fs. Most probably, the day the measurement was performed we did not fine-tune the F.S glass wedges, as the amount of 19fs^2 could be easily added by inserting 0.45mm of glass.

Table 3 : FWHM and rms values for the Red-IR pulse's duration

	Fourier limit (fs)	Measurement (fs)
FWHM	7.0	9.7 ± 0.1
rms	5.2	10.3 ± 0.1

Figure 31 shows the analogous result obtained for the near-UV-Blue phase locked pulses when t1=0fs. The pulse used for producing the auxiliary pulses in this case, was the residual Red-IR pulse from the up-conversion procedure. The almost flat spectral phase shown in figure 31A suggests a duration close to FL. Indeed, from the temporal profile shown in fig.31B the measured pulse duration is 8.4fs FWHM, deviating only by 0.2fs from the FL. However, the profile shows temporal broadening due to the presence of "satellite wings" lower than 8% of the maximum amplitude. Thus a better representation is through the rms value, taking into account the satellite contributions. The rms value of the FL is 6.5fs, with the measured being 9.8fs. The latter, leads to the conclusion that we are able to generate a pair of phase-locked sub-10fs pulses in the near-UV-Vis spectral range.

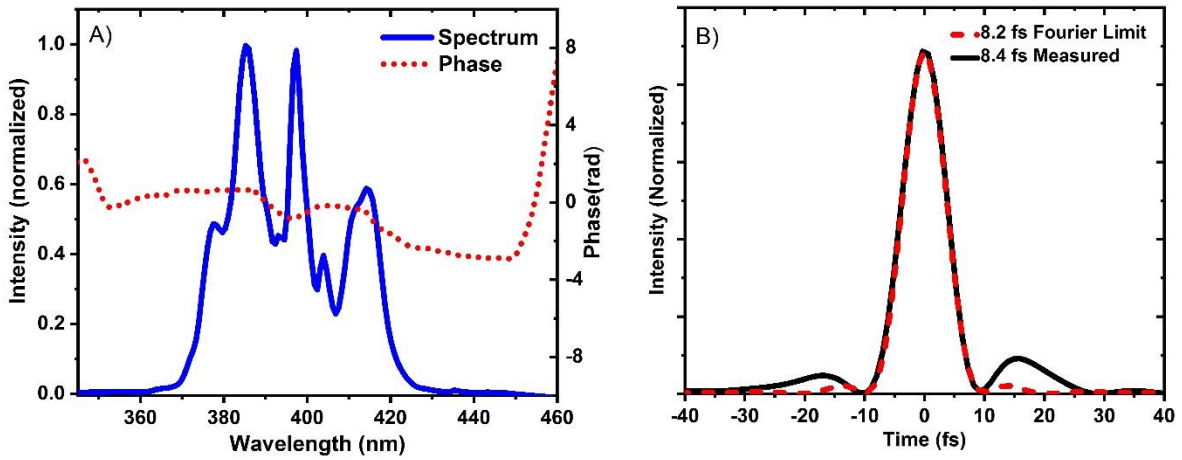

Fig. 31 : A) Normalized spectrum and measured phase of the near-UV-Blue pulses B) Normalized temporal profile of the expected FL pulse and the measured one.

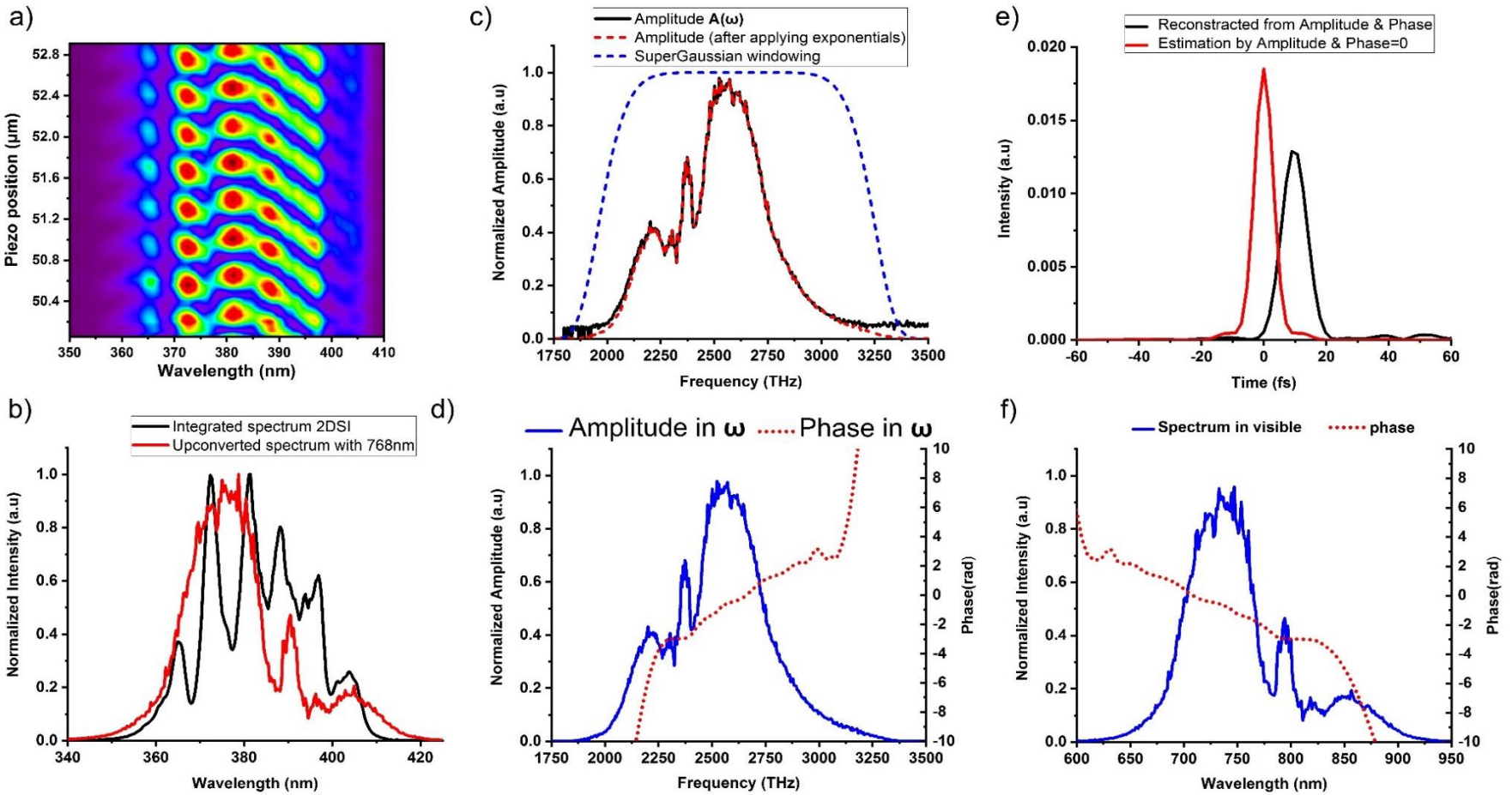

Fig. 32 : 2DSI measurement for Red-IR replicas at t1=0fs a) 2D map I(x_{cw},λ) from a 2DSI scan; b) Integration of spectra along the piezo positions (black) and up-converted spectrum of the actual Red-IR pulse with a quasi-monochromatic pulse centered at 768nm. c) Procedure for getting the amplitude A(ω) of the pulse; Black solid and red dashed lines represent the initial and processed spectra respectively. The windowing using a super-Gaussian before applying an FFT to result in the temporal profile is shown with blue dashed line. d) Amplitude and phase in the frequency domain used for determination of the pulse's duration. e) Temporal profile of the pulse; Red and black lines represent the Fourier limited and measured profile respectively. f) Spectrum and phase of the pulse in wavelength.

2.5 Summary

In this chapter, we described the experimental setups which were developed during this PhD work and we documented the data treatment and analysis procedure for TAS, 2DES and 2DSI data.

Particularly, we have upgraded a T.A spectrometer previously used for Vibrational Coherence Spectroscopy (VCS), into a 2DES one operating in the UV-Vis spectral range. The 2DES spectrometer uses a pair of phase-locked sub-10fs pulses in the near UV-blue range 360-430nm and can be used for performing 2DES on (bio)molecular systems that absorb in this spectral range. In addition we have developed a new T.A spectrometer, performing in the NIR spectral range (800-1400) nm. The setup sensitivity allows measuring signals $<10^{-3}$, with the level of noise down to $\sim 20 \times 10^{-6}$ upon 5s of acquisition time at 910nm.

References

(1) Butcher, P. N.; Cotter, D. *The Elements of Nonlinear Optics*; Cambridge University Press: Cambridge, 1990. https://doi.org/10.1017/CBO9781139167994.

(2) Tkachenko, N. V. Lasers for Spectroscopy Applications. In *Optical Spectroscopy*; Elsevier, 2006; pp 39–59. https://doi.org/10.1016/B978-044452126-2/50027-7.

(3) Smith, A. V.; Armstrong, D. J.; Alford, W. J. Increased Acceptance Bandwidths in Optical Frequency Conversion by Use of Multiple Walk-off-Compensating Nonlinear Crystals. *J. Opt. Soc. Am. B* **1998**, *15* (1), 122. https://doi.org/10.1364/JOSAB.15.000122.

(4) Bradler et Al. - 2009 - Femtosecond Continuum Generation in Bulk Laser Hos.Pdf.

(5) *The Supercontinuum Laser Source*; Alfano, R. R., Ed.; Springer-Verlag: New York, 2006. https://doi.org/10.1007/b106776.

(6) Cerullo, G.; Manzoni, C. Solid-State Ultrafast Optical Parametric Amplifiers. In *Solid-State Lasers and Applications*; Sennaroglu, A., Ed.; CRC Press, 2006; Vol. 119, pp 437–472. https://doi.org/10.1201/9781420005295.ch11.

(7) Cerullo, G.; De Silvestri, S. Ultrafast Optical Parametric Amplifiers. *Rev. Sci. Instrum.* **2003**, *74* (1), 1–18. https://doi.org/10.1063/1.1523642.

(8) Baltuška, A.; Fuji, T.; Kobayashi, T. Controlling the Carrier-Envelope Phase of Ultrashort Light Pulses with Optical Parametric Amplifiers. *Phys. Rev. Lett.* **2002**, *88* (13). https://doi.org/10.1103/PhysRevLett.88.133901.

(9) Monmayrant, A.; Weber, S.; Chatel, B. A Newcomer's Guide to Ultrashort Pulse Shaping and Characterization. *J. Phys. B At. Mol. Opt. Phys.* **2010**, *43* (10), 103001. https://doi.org/10.1088/0953-4075/43/10/103001.

(10) *Femtosecond Laser Pulses*; Rullière, C., Ed.; Advanced Texts in Physics; Springer New York: New York, NY, 2005. https://doi.org/10.1007/b137908.

(11) Pollard, W. T.; Lee, S.; Mathies, R. A. Wave Packet Theory of Dynamic Absorption Spectra in Femtosecond Pump–Probe Experiments. *J. Chem. Phys.* **1990**, *92* (7), 4012–4029. https://doi.org/10.1063/1.457815.

(12) Berera, R.; van Grondelle, R.; Kennis, J. T. M. Ultrafast Transient Absorption Spectroscopy: Principles and Application to Photosynthetic Systems. *Photosynth. Res.* **2009**, *101* (2–3), 105–118. https://doi.org/10.1007/s11120-009-9454-y.

(13) Gueye, M.; Nillon, J.; Crégut, O.; Léonard, J. Broadband UV-Vis Vibrational Coherence Spectrometer Based on a Hollow Fiber Compressor. *Rev. Sci. Instrum.* **2016**, *87* (9), 093109. https://doi.org/10.1063/1.4962699.

(14) Lorenc, M.; Ziolek, M.; Naskrecki, R.; Karolczak, J.; Kubicki, J.; Maciejewski, A. Artifacts in Femtosecond Transient Absorption Spectroscopy. *Appl. Phys. B Lasers Opt.* **2002**, *74* (1), 19–27. https://doi.org/10.1007/s003400100750.

(15) Chen, W.-G.; Braiman, M. S. KINETIC ANALYSIS OF TIME-RESOLVED INFRARED DIFFERENCE SPECTRA OF THE L and M INTERMEDIATES OF BACTERIORHODOPSIN. *Photochem. Photobiol.* **1991**, *54* (6), 905–910. https://doi.org/10.1111/j.1751-1097.1991.tb02110.x.

(16) Jonas, D. M. TWO-DIMENSIONAL FEMTOSECOND SPECTROSCOPY. *Annu. Rev. Phys. Chem.* **2003**, *54* (1), 425–463. https://doi.org/10.1146/annurev.physchem.54.011002.103907.

(17) Hochstrasser, R. M. Two-Dimensional Spectroscopy at Infrared and Optical Frequencies. *Proc. Natl. Acad. Sci.* **2007**, *104* (36), 14190–14196. https://doi.org/10.1073/pnas.0704079104.

(18) Cho, M. Coherent Two-Dimensional Optical Spectroscopy. *Chem. Rev.* **2008**, *108* (4), 1331–1418. https://doi.org/10.1021/cr078377b.
(19) Hamm, P.; Zanni, M. *Concepts and Methods of 2D Infrared Spectroscopy*; Cambridge University Press: Cambridge, 2011. https://doi.org/10.1017/CBO9780511675935.
(20) Brixner, T.; Stenger, J.; Vaswani, H. M.; Cho, M.; Blankenship, R. E.; Fleming, G. R. Two-Dimensional Spectroscopy of Electronic Couplings in Photosynthesis. *Nature* **2005**, *434* (7033), 625–628. https://doi.org/10.1038/nature03429.
(21) West, B. A.; Moran, A. M. Two-Dimensional Electronic Spectroscopy in the Ultraviolet Wavelength Range. *J. Phys. Chem. Lett.* **2012**, *3* (18), 2575–2581. https://doi.org/10.1021/jz301048n.
(22) Prokhorenko, V. I.; Picchiotti, A.; Pola, M.; Dijkstra, A. G.; Miller, R. J. D. New Insights into the Photophysics of DNA Nucleobases. *J. Phys. Chem. Lett.* **2016**, *7* (22), 4445–4450. https://doi.org/10.1021/acs.jpclett.6b02085.
(23) Khalil, M.; Demirdöven, N.; Tokmakoff, A. Obtaining Absorptive Line Shapes in Two-Dimensional Infrared Vibrational Correlation Spectra. *Phys. Rev. Lett.* **2003**, *90* (4). https://doi.org/10.1103/PhysRevLett.90.047401.
(24) Réhault, J.; Maiuri, M.; Oriana, A.; Cerullo, G. Two-Dimensional Electronic Spectroscopy with Birefringent Wedges. *Rev. Sci. Instrum.* **2014**, *85* (12), 123107. https://doi.org/10.1063/1.4902938.
(25) *Progress in Atomic Spectroscopy*; Hanle, W., Kleinpoppen, H., Eds.; Springer US: Boston, MA, 1978. https://doi.org/10.1007/978-1-4615-7688-4.
(26) Mukamel, S. *Principles of Nonlinear Optical Spectroscopy*; Oxford series in optical and imaging sciences; Oxford Univ. Press: New York, 2009.
(27) Mukamel, S.; Loring, R. F. Nonlinear Response Function for Time-Domain and Frequency-Domain Four-Wave Mixing. *J. Opt. Soc. Am. B* **1986**, *3* (4), 595. https://doi.org/10.1364/JOSAB.3.000595.
(28) Ogilvie, J. P.; Kubarych, K. J. Chapter 5 Multidimensional Electronic and Vibrational Spectroscopy. In *Advances In Atomic, Molecular, and Optical Physics*; Elsevier, 2009; Vol. 57, pp 249–321. https://doi.org/10.1016/S1049-250X(09)57005-X.
(29) Khalil, M.; Demirdöven, N.; Tokmakoff, A. Vibrational Coherence Transfer Characterized with Fourier-Transform 2D IR Spectroscopy. *J. Chem. Phys.* **2004**, *121* (1), 362. https://doi.org/10.1063/1.1756870.
(30) Nee, M. J.; Baiz, C. R.; Anna, J. M.; McCanne, R.; Kubarych, K. J. Multilevel Vibrational Coherence Transfer and Wavepacket Dynamics Probed with Multidimensional IR Spectroscopy. *J. Chem. Phys.* **2008**, *129* (8), 084503. https://doi.org/10.1063/1.2969900.
(31) Myers, J. A.; Lewis, K. L.; Tekavec, P. F.; Ogilvie, J. P. Two-Color Two-Dimensional Fourier Transform Electronic Spectroscopy with a Pulse-Shaper. *Opt. Express* **2008**, *16* (22), 17420. https://doi.org/10.1364/OE.16.017420.
(32) Brida, D.; Manzoni, C.; Cerullo, G. Phase-Locked Pulses for Two-Dimensional Spectroscopy by a Birefringent Delay Line. 3.
(33) Borrego-Varillas, R.; Oriana, A.; Ganzer, L.; Trifonov, A.; Buchvarov, I.; Manzoni, C.; Cerullo, G. Two-Dimensional Electronic Spectroscopy in the Ultraviolet by a Birefringent Delay Line. *Opt. Express* **2016**, *24* (25), 28491. https://doi.org/10.1364/OE.24.028491.
(34) Matsubara, E.; Yamane, K.; Sekikawa, T.; Yamashita, M. Generation of 26 Fs Optical Pulses Using Induced-Phase Modulation in a Gas-Filled Hollow Fiber. *J. Opt. Soc. Am. B* **2007**, *24* (4), 985. https://doi.org/10.1364/JOSAB.24.000985.

(35) Chen, X.; Jullien, A.; Malvache, A.; Canova, L.; Borot, A.; Trisorio, A.; Durfee, C. G.; Lopez-Martens, R. Generation of 43 Fs, 1 MJ Laser Pulses via Compression of Circularly Polarized Pulses in a Gas-Filled Hollow-Core Fiber. *Opt. Lett.* **2009**, *34* (10), 1588. https://doi.org/10.1364/OL.34.001588.
(36) Nisoli, M.; De Silvestri, S.; Svelto, O.; Szipöcs, R.; Ferencz, K.; Spielmann, C.; Sartania, S.; Krausz, F. Compression of High-Energy Laser Pulses below 5 Fs. *Opt. Lett.* **1997**, *22* (8), 522. https://doi.org/10.1364/OL.22.000522.
(37) Nisoli, M.; De Silvestri, S.; Svelto, O. Generation of High Energy 10 Fs Pulses by a New Pulse Compression Technique. *Appl. Phys. Lett.* **1996**, *68* (20), 2793–2795. https://doi.org/10.1063/1.116609.
(38) Helbing, J.; Hamm, P. Compact Implementation of Fourier Transform Two-Dimensional IR Spectroscopy without Phase Ambiguity. *J. Opt. Soc. Am. B* **2011**, *28* (1), 171. https://doi.org/10.1364/JOSAB.28.000171.
(39) Birge, J. R.; Ell, R.; Kärtner, F. X. Two-Dimensional Spectral Shearing Interferometry for Few-Cycle Pulse Characterization. *Opt. Lett.* **2006**, *31* (13), 2063. https://doi.org/10.1364/OL.31.002063.
(40) Birge, J. R.; Crespo, H. M.; Kärtner, F. X. Theory and Design of Two-Dimensional Spectral Shearing Interferometry for Few-Cycle Pulse Measurement. *J. Opt. Soc. Am. B* **2010**, *27* (6), 1165. https://doi.org/10.1364/JOSAB.27.001165.
(41) Borrego-Varillas, R.; Oriana, A.; Branchi, F.; De Silvestri, S.; Cerullo, G.; Manzoni, C. Optimized Ancillae Generation for Ultra-Broadband Two-Dimensional Spectral-Shearing Interferometry. *J. Opt. Soc. Am. B* **2015**, *32* (9), 1851. https://doi.org/10.1364/JOSAB.32.001851.
(42) Iaconis, C.; Walmsley, I. A. Self-Referencing Spectral Interferometry for Measuring Ultrashort Optical Pulses. *IEEE J. QUANTUM Electron.* **1999**, *35* (4), 9.
(43) Birge, J. R.; Kärtner, F. X. Analysis and Mitigation of Systematic Errors in Spectral Shearing Interferometry of Pulses Approaching the Single-Cycle Limit [Invited]. *J. Opt. Soc. Am. B* **2008**, *25* (6), A111. https://doi.org/10.1364/JOSAB.25.00A111.
(44) Sorokin, E.; Tempea, G.; Brabec, T. Measurement of the Root-Mean-Square Width and the Root-Mean-Square Chirp in Ultrafast Optics. *J. Opt. Soc. Am. B* **2000**, *17* (1), 146. https://doi.org/10.1364/JOSAB.17.000146.
(45) Schmidt, B.; Hacker, M.; Stobrawa, G.; Feurer, T. LAB2-A Virtual Femtosecond and Laser Lab. Http://Www.Lab2.De.

Part III

Ultrafast photo-isomerization of retinal proteins: Anabaena Sensory Rhodopsin

3.1 Ultrafast photo-isomerisation in Retinal Proteins

Retinal proteins (RPs) are a category of transmembrane photoreceptor proteins which are supplied with a vitamin A aldehyde (retinal chromophore) bound to the protein through a protonated Schiff base (PSB). They are found in living organisms from mammals to archea, with many features common to the visual pigment rhodopsin. In addition to rhodopsin pigment they include four additional protein pigments located in the plasma membrane of Halobacterium salinarium[1]. According to their differences and biological function they can be distinguished to three large families of retinal-binding ion transporters, light-gated channels and membrane-embedded photosensors etc[2]. Examples of several well-known RPs are shown in fig.33.

Since 1990's the X-ray crystallographic structure of many of these RP's including the visual Rhodopsin (Bovine Rhodopsin) and the bacterial rhodopsin named Bacteriorhodopsin (BR) are known; with striking similarities observed. The proteins consist of ~300 amino-acids which fold in space to form seven transmembrane α-helices, referred in literature as "opsin". Those helices have their carboxyl terminal ends exposed to the cytoplasm, due to their hydrophobic properties, while their amino terminal ends are exposed extracellularly[3]. In both cases, the retinal cofactor is linked to the opsin with a lysine sidechain, forming the protonated Schiff base of the retinal (PSBR, fig. 35b). In bovine Rhodopsin, the PSBR bears the 11-cis ground state conformation, while in the BR it is possible to have all-trans or both all-trans and 13-cis forms in the ground state, depending on external light adaptations conditions. Interestingly, the property of having two different conformers in the ground state simultaneously, is observed uniquely in microbial rhodopsins. Furthermore, the selectivity of the reactant's conformation (trans/cis) and along which C-C double bond the cis form is found, depends on the opsin.

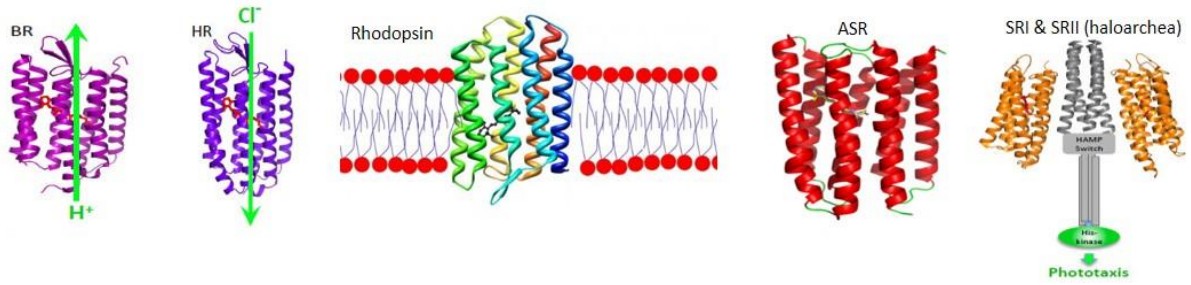

Fig. 33: Structures of several retinal proteins extracted from X-ray diffraction measurements; Structures from left to right correspond to the RPs of Bacteriorhodopsin (BR), Halorhodopsin (HR), Rhodopsin (Rho), Anabaena Sensory Rhodopsin (ASR) and Sensory Rhodopsins I & II respectively.

The general interest around RPs arises from their ability to convert sunlight into chemical energy, be able to store it and use it at a further step for the execution of a specific biological function[4]. The primary process associated with this energy conversion is called isomerisation, during which the retinal's chromophore twist around a specific C-C double bond occurs. After this first reaction takes place observed by the decay of an excited state called "I"-state or "fluorescent state", a cascade-like reaction scheme follows up, during which several meta-stable states are formed (J-K-L-M-N-O) with the whole photocycle completing usually within ~10-100ms.

Intrinsically, the ability of RPs to absorb light in the 350- 700 nm range is related to retinal, which is found in the form of a protonated Schiff base (PSBR), formed through the covalent link of the C15 carbon with the nitrogen of a lysine of helix G (K 216, in the case of bR), and protonated by near-by acid side chains of amino acids. In addition, the electrostatic interactions with the side chains of the amino acids of the "protein's binding pocket" and slight distortions of the PSBR backbone determine the wavelength of maximum absorption (color tuning). In literature, there are many examples where the electrostatic interactions and steric hindrance translate in a big change of the PSBR properties. Wang et al[5] showed that upon opsin's mutations the absorption maxima of the PSBR in the visible can shift up to 200nm (425-644nm), evidencing the huge impact of the opsin environment. The protein-chromophore interaction effects are most obvious, when comparing the PSBR in the protein environment with the PSBR in solution (methanol, hexane etc). There, tremendous differences appear, having as a starting point the absorption maximum, located in those cases <450nm.

Beside the steady state properties (absorbance and fluorescence), a lot of information was retrieved also from time resolved spectroscopic studies. The C-C double bond isomerization reaction attracted the interest of a lot of research groups who wanted to determine the speed and yield of that process, as it was believed to occur in the sub-ps timescale. Since the early 1980, as soon as sub-femtosecond laser sources were available, initial time resolved experiments on BR concluded that isomerization occurs within ~500fs[6–8] with a high quantum yield of ~0.65[9–11]. Later on, a similar study on bovine Rhodopsin by Schoenlein et al[12] revealed that isomerization takes place within ~200fs[13], while exhibiting a similar quantum yield of ~0.65[14] for the latter process. Even more surprisingly, Kim et al[15] documented a quantum yield dependency according to the excitation wavelength (within ±5%), which is still undebated.

Despite the minor differences of the opsin, the increase of the isomerization speed by a factor of ~2.5 for Rhodopsin's case points to possible effects induced by the PSBR conformations, and by the protein-chromophore interactions. The latter effect is most pronounced for the case of PSBR in solution where studies showed that isomerization takes place on the ps timescale[16]. Bassolino et al[17] demonstrated that the all-trans reactant leads to the production of 9-cis and 11-cis isomerized products, expressed by a an average time constant of ~4ps . Surprisingly, the one order of magnitude difference in isomerization speed with respect to BR and Rhodopsin, is accompanied by an almost ~50% decrease of the quantum yield. The absolute values reported for 11-cis and 9-cis products were 0.16 and 0.05 respectively. Earlier investigations on PSBR in solution are in agreement with these significantly low values[18–20]. In the same framework of environment-chromophore interactions, Mukai et al[19] documented the impact of solvent polarity and Schiff's base protonation on the isomerization yield. The results revealed an increment of the quantum yield up to a factor of ~3 when the Schiff base was protonated, while the solvent polarity appeared to have minor effects.

Moreover, experiments on other retinal proteins such as Isorhodopsin[21], Sensory Rhodopsin I & II (SRI & SRII)[22–24] appeared to been in line with a claim for correlation between isomerization speed and yield. Particularly, it was believed that faster isomerization speeds are accompanied with higher yield for the process. The latter statement was misleading as

later on experiments on other RPs and Rhodopsin-like biomimetic photo-switches did not show any correlation between speed and yield[25–27].

Other aspects concerning the effect of the environment on the isomerization reaction were reported for different pH values. In some cases, such as the SRI system, at pH 6 resulted in an extension of the excited state lifetime by exhibiting a bi-exponential decay with 5ps and 33ps[24]. The latter effect was due to the protonation of Asp-76 residue. Later experiments on Anabaena Sensory Rhodopsin (ASR) showed that the pH can change the isomeric composition for the all-trans and 13-cis reactants but with the dynamics staying almost unaffected by the pH changes[28].

The understanding of the protein-chromophore interactions on the atomic level involves the change on either the protein or the chromophore. Experiments performed on BR loaded with "locked", i.e. non-isomerizing forms of PSBR were reported by Ye[29,30] and Haacke[31,32]. Complementary, numerous examples concerning mutated proteins have been reported until today with the aim of pinpointing the role of specific amino acids on the increased isomerisation speed and reaction quantum yields, as compared to the case of PSBR in solution. In most cases, the isomerization reaction is slowed down with respect to the native proteins [33], but the opposite is also reported in some cases[34,35]. In this thesis we will refer to the effect of point mutations on the PSBR isomerization reaction in ASR.

3.2 Isomerization Reaction Scheme - Conical Intersection

The usual scheme used for describing the isomerization reaction is based on a three state model represented by the corresponding potential energy surfaces (PES), with the reaction evolving along the molecular coordinates (stretching, torsion etc)[36,37]. An example of the latter scheme is shown in fig.34[38]

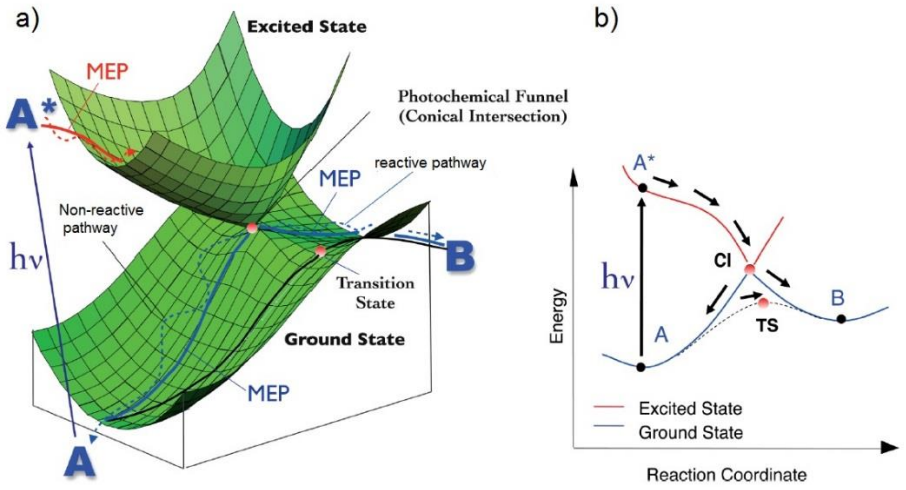

Fig. 34 : Isomerization reaction scheme (from ref.38) a) PES formed by the presence of three states; dashed lines represent the two pathways (reactive and non-reactive) along which the species evolve after reaching the Conical Intersection; MEM stands for the minimum energy paths. B) Simplified scheme of A) represented in a two dimensional picture;

In this scheme, initial excitation of the absorbing species (A on fig.34) leads to the formation of excited state population (C_0^*) in the Franc-Condon region (A*). A first relaxation process

takes place within ~50fs (red dashed line) involving the C-C double bond stretching mode of the PSBR. During this ultrafast process, bond length alternation (BLA) occurs along the π-conjugated system, leading afterwards to the unlocking of a specific C-C double bond along where the isomerization will take place. The excited state has a charge transfer character (CT) as charge is partially translocated from the Schiff base towards the β-ionone head of the retinal. According to Schenkl et al[39] the latter charge translocation induces a dipole moment which reaches up to 30D. Then the population reaches a crossing point which is between the excited state surface and the ground state one called Conical Intersection (CI). At that point the decision of the following pathway is defined by a combination of at least two vibrational modes (phase and vector) out of 3N-6 allowed by symmetry. The hopping of the excited species from a higher PES to a lower one will result in two reaction paths called reactive and non-reactive pathways.

The reactive pathway is associated with the formation of a photoproduct state (B in fig.34) and is accompanied with a 90° torsion change of the PSBR around a specific C-C double bond. The evolution of the excited species towards the CI has been described theoretically by the mechanism of asynchronous double bicycle-pedal deformation of the C10-..-C14=N moiety of PSBR[40]. On the other hand, the percentage of the initial excited species that unsuccessfully didn't follow that reactive pathway will return back to the initial GS (A), following a non-reactive path. Moreover, the isomerized species evolve further by thermal relaxation with the environment's bath (vibrational cooling) and lead to the formation of other meta-stable states as described briefly in the previous section. The percentage of the population which led to the photoproduct formation with respect to the one initially excited defines the quantum yield of isomerization Φ.

The slope of the excited state's PES is representative of the timescale of the isomerization process. Thus, a steeper slope will result in a faster isomerization, while a more flat energy profile will lead to a slower isomerization. The species evolution on a barrier-less excited state PES is expressed through a vibrationaly coherent motion of the latter, from the Franck-Condon region towards the CI, with the coherences surviving even after the isomerization occurs. The latter can be understood in terms of a vibrational wavepacket initially formed in the excited state with a coherence time longer than the reaction timescale. Upon evolution through the CI some vibrational modes are coupled, maintaining their phase relation, and are present in photoproduct's state. These coherences are usually damped within the ps timescale due to interaction with the surrounding phonon bath. On the contrary a barrier-like excited state PES leads to a stochastic reaction where the isomerization reaction is expressed through an average rate constant, without any coherences surviving after passing the CI. Since the 90's the community believed that the quantities of isomerization speed and yield are connected following the Landau-Zener theory[41,42] and that a vibrationally coherent isomerization process will result in a high quantum yield[21,43]. Nevertheless, experimental observations showed that the two quantities are independent[25,27,44] with a recent statement by Schnedermann et al[45] claiming the QY is connected, for rhodopsin, with the phase of specific vibrational modes; particularly hydrogen out of plane modes (HOOP).

3.3 Anabaena Sensory Rhodopsin (ASR) - Motivation

Anabaena Sensory Rhodopsin is the first sensory rhodopsin observed in freshwater cyanobacterium Anabaena (Nostoc)[46,47]. The membrane opsin protein consists of 261 residues (26kDa) and is co-expressed with a smaller 14kDa protein transducer (fig.35a). ASR is believed to function as light intensity sensor due to its ability of transmitting signal to other integral membrane proteins through the transducer in contrast with other sensory rhodopsins (i.e SRI, SRII).

In ASR, the protonated Schiff base of retinal (PSBR) adopts two different conformations in the ground state, the all-trans,15-anti (AT) and 13-cis, 15-syn (13C) (fig.35b). The isomer ratio depends on external illumination conditions (intensity and wavelength) reaching a photostationary, so-called light adapted (LA) state. Interestingly, upon incubation in the dark at room temperature, the AT population exceeds 97%, defining the so-called dark-adapted (DA) state. AT and 13C undergo two distinct photo-cycles interconverting on a millisecond time scale[48,49](fig.35c).

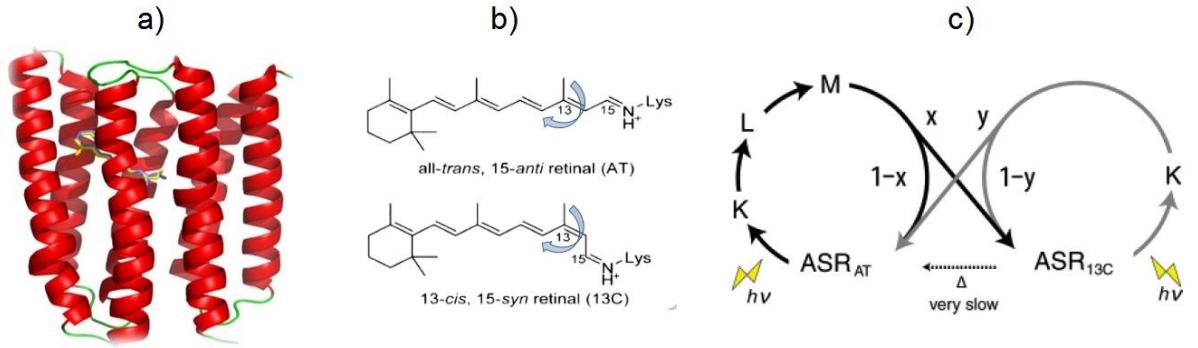

Fig. 35: a) ASR x-ray crystallographic structure plotted using PyMol platform (data used from RCSB protein bank, library:1XIO); b) all-trans,15-anti (AT) and 13-cis, 15-syn (13C) are the ground state conformations of the PSBR; light blue arrows are pointing the C-C bond at which the isomerization occurs. c) scheme from ref.48 showing the two distinct photo-cycles occurring for the two ground state conformers; Capital letters represent the different intermediate states formed in each photocycle while x and y represent the branching ratios for AT and 13C isomers.

The interest of studying the primary steps of retinal protein's photo-cycle (GS to K-intermediate transition) via femtosecond spectroscopy originates from a long-standing question, on how the protein environment tunes and optimizes the photoisomerization reaction speed and yield. In this context, ASR is a particularly suitable model system, since it allows to study the photoreaction of both conformers in the same protein environment at the same time. In particular, the excited state lifetime (ESL) is representative of the photoisomerization speed. In the wild-type protein (WT-ASR), it is only 150fs for 13C, and ~5 times longer for AT (750fs). The results are supported also by advanced quantum mechanics/molecular mechanics simulations which predict the presence of a small energy barrier (~few kcal/mol) in the S1 PES, explaining in this way the longer isomerization time observed for the AT case.

The relative isomerization quantum yield (Φ) is 2.7 times higher for the AT isomer[25,44]. However, the absolute Φ values are the lowest ever reported for retinal proteins (< 25%)

demanding an extended study on point mutated proteins for a deeper understanding. The effect of point mutations on the PSBR isomerization dynamics is discussed in chapter 4.

3.4 Photochromism of ASR

The photochromism properties of ASR are expressed through its ability of interconversion between the two isomers. The scheme in fig.35c represents the two distinct photo-cycles initiated upon absorption of a photon. In the case of the *all-trans,15-anti* (AT) isomer the thermal relaxation processes following the isomerization process (formation of K species), leads sequentially to the formation of the L (>1ns) and M intermediate states with the latter step being the conversion to the *13-cis,15-syn* (13C) isomer. Steady state absorbance experiments at 170K and 277K revealed that the branching ratio x is unity[48]. The latter is due to the thermal isomerization process upon M state's decay, which occurs on the C15=N bond making possible in this way the conversion to the 13C conformer. The same observation holds also for the *13-cis,15-syn* (13C) isomer with a branching ratio y being also unity. However, the latter process occurs after the K state's decay, once L and M states are not formed in this photocycle.

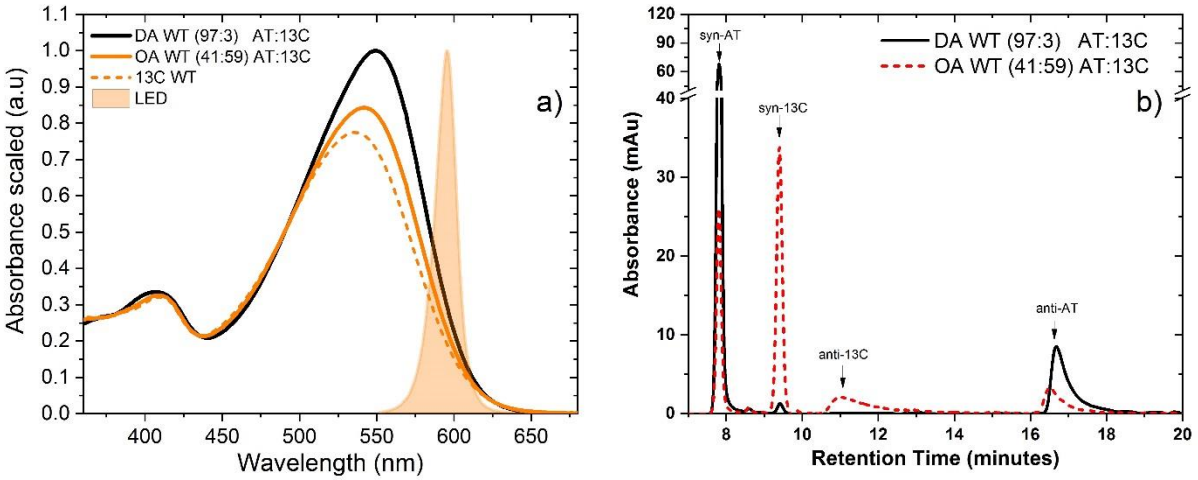

Fig. 36: Steady state absorption a) and HPLC measurement b) of the photostationary ground states of WT-ASR; a) Black and orange solid lines represent the Dark and Light adapted states respectively with the isomeric containt shown in brackets (from HPLC performed just after the measurement); dashed orange line represents the pure 13C contribution retrieved using the values from HPLC (details in next section; Orange shade represents the spectrum of the orange LED used for light adaptation) b) Black solid and dashed red lines represent the absorbance of the retinal oxime derivatives for DA and OA states. The area under each peak is used for defining the isomeric ratio AT:13C in each state (see in Annexe A.I)

As mentioned in section 3.3 we study the two photostationary states of ASR, meaning the isomeric ratio AT:13C remains constant in these states. Fig.36a shows the dark (DA) and orange (OA) adapted state states of ASR where the isomeric content of AT isomers was 97% and 41% respectively (fig.36b). The OA is reached upon illumination with an orange LED) for 30 minutes (spectrum in fig.36). Thus, we create a constant mixture with the dominant 13C isomer, whose percentage ranges between 59% up to 65% depending on the flux illuminating the sample etc. The procedure of reaching the DA state lasts very long, usually more than 12hours where the sample is kept in dark and at room temperature.

3.5 Disentanglement of AT & 13C ground and excited state signatures

Retrieving the pure isomers signatures (GS and ES) is possible if the understudy photostationary states are linear combinations of the first. The validity of this assumption can be established by studying the protein's structure (i.e X-ray diffraction) and confirming that the opsin structure, in particular the relative distances of PSBR and amino acids forming the retinal binding pocket, remain unchanged after the light adaptation procedure. In this way, the differences will arise only due to the isomer's conformation (AT/13C) associated with a specific spectroscopic signature (spectrum).

Assuming the statement holds, the absorption spectra of DA and OA proteins are linear combinations of AT and 13C absorbances according to eq.55

$$\begin{bmatrix} \mathrm{AT} \\ \mathrm{13C} \end{bmatrix} = \mathrm{R}^{-1} \times \begin{bmatrix} \mathrm{A_{DA}} \\ \mathrm{A_{LA}} \end{bmatrix} \quad \text{with} \quad \mathrm{R} = \begin{bmatrix} \mathrm{r_{DA}^{AT}} & \mathrm{r_{DA}^{13C}} \\ \mathrm{r_{LA}^{AT}} & \mathrm{r_{LA}^{13C}} \end{bmatrix} \quad \text{eq. 55}$$

The numbers of matrix "R" are basically the percentage "$\mathrm{r}_{\mathrm{state}}^{\mathrm{isomer}}$" of each isomer (exponent index) in each state (lower index) derived by HPLC (detailed description in Annexe A.I). The application of the latter procedure is shown in Fig.36a for WT-ASR.

While the AT's absorbance is overlapped with the DA one (97% AT); central peak located at 550nm, the OA state which is dominated by the 13C isomer and appears ~8nm blue shifted (max at 542nm). In addition a relative reduction in absorbance by a factor of ~1.2 is observed with respect to AT, which is an indication for the smaller extinction coefficient of 13C isomer (43500 $\mathrm{L{\cdot}mol^{-1}{\cdot}cm^{-1}}$ from ref.25). The pure spectrum of the 13C isomer appears to have ~1.3 times smaller absorbance with respect to the AT one with the main absorption peak located at 537nm.

When it comes to applying the same procedure for disentangling the ES species from T.A datasets, then we have to take into account the percentage of the excited concentration of each isomer, in each photostationary state. Thus, we have to define a new "R^{*}" matrix using the percentage of the excited AT and 13C species ($\mathrm{r}_{\mathrm{state}}^{*isomer}$) in each state. The procedure has been previously described by Gueye[50] and Cheminal[51] and holds only upon acquiring T.A datasets for both states under identical experimental conditions.

Initially, we calculate the number of excited molecules N^{*}, according to the characteristics of the excitation source (pulse energy $\mathrm{E_p}$ and central wavelength λ_{exc}) and to the absorbance of the sample $\mathrm{A}(\lambda)$ at the given wavelength (eq.56).

$$N^{*} = \frac{E_p \lambda_{exc}}{hcN_A}\left[1 - 10^{-A(\lambda_{exc})}\right] \quad \text{eq. 56}$$

The division of N^{*} by the volume of excitation $\mathrm{V_0}$ defines the excitation probability ($\Delta c_i/c_i$). This is a valuable quantity, as we use it to set a limit to avoid multiphoton excitation of the molecules. This limit is kept lower than 10%, establishing in this way that we work in the linear regime of excitation.

Moreover, we determine the percentage of the excited of AT-PSBR and 13C-PSBR molecules in each photostationary state. To do so, we define a cross section for each isomer according to the value of molar absorptivity at the given excitation wavelength $\varepsilon_{isomer}(\lambda_{exc})$

and the ground state contribution in the particular photostationary state (r_{state}^{isomer}). To define a percentage of $n^{*isomer}_{state}$ we multiply with the total number of molecules excited (eq.57).

$$n^{*13C}_{DA} = N^* \times \frac{r^{13C}_{DA}\varepsilon_{13C}(\lambda_{exc})}{r^{13C}_{DA}\varepsilon_{13C}(\lambda_{exc}) + r^{AT}_{DA}\varepsilon_{AT}(\lambda_{exc})} \quad , \quad n^{*13C}_{LA} = N^* \times \frac{r^{13C}_{LA}\varepsilon_{13C}(\lambda_{exc})}{r^{13C}_{LA}\varepsilon_{13C}(\lambda_{exc}) + r^{AT}_{LA}\varepsilon_{AT}(\lambda_{exc})} \quad \text{eq. 57}$$

Despite the fact that the experimental conditions are the same upon performing T.A experiments, the absorbance of the sample changes upon different the light adaptation conditions. Thus, a division of $n^{*isomer}_{state}$ with the absorbance of each state has to be taken into account (eq.58).

$$r^{*13C}_{DA} = \frac{n^{*13C}_{DA}}{1-10^{-A_{DA}(\lambda_{exc})}} \quad , \quad r^{*13C}_{LA} = \frac{n^{*13C}_{LA}}{1-10^{-A_{LA}(\lambda_{exc})}} \quad \text{eq. 58}$$

Equation 58 corresponds to the percentage of 13C-PSBR in each photostationary state. Complementary, the values for AT-PSBR are determined by the subtraction from unity.

As an example we applied the procedure described for extraction of the 13C-PSBR in WT-ASR. A laser pulse centered at 565nm (27nJ) was used for excitation, yielding an ES percentage for 13C isomer of 2% and 57% in DA and OA states respectively (fig.37A,B). Using the values from eq.58 to eq.55 results in the pure 13C-PSBR map as shown in fig.39.

3.6 Photochemistry of WT-ASR

While the steady state absorption spectra show that both isomers have their ground state spectra overlapped along the UV-Vis range (up to 650nm), here we use T.A spectroscopy to capture the excited state dynamics of both PSBR. Particularly, we follow spectrally and temporally the GS to K-state transition, where the isomerization takes place and we aim at determining the excited state lifetime (ESL) of each isomer. As described in section 2.3.2, in our studies we use sub-50fs pulses for excitation (NOPA) and broadband white light pulses for probing. Thus, we are able to have a temporal resolution of sub-60fs and sub-120fs for the UV-Vis and NIR probing regions respectively. In addition, to have better control of the experimental conditions we need to know precisely the ground state isomeric content in each sample. For this reason, we perform HPLC measurements before each experiment.

The pump pulse used for excitation of DA and OA proteins was tuned at 565nm (12nm FWHM) which lies on the low energy side of both isomers absorption bands. The energy of excitation was kept at 27nJ in order to be in the linear regime of excitation within a factor of ~2. The latter is established also by the low excitation probability which is in the range of ~4%. A flow-cell with ultrathin windows (Starna) with 0.2mm path length was used for the UV-Vis probing region in order to minimize the chirp effect on the probe pulse, while a 0.5mm cell was use for the NIR probing region instead. The optical density at the excitation wavelength was ~0.1 and ~0.25 for UV-Vis and NIR regions respectively. The polarization angle between pump and probe pulses was set at magic angle (54.7º) to exclude any contributions from rotational diffusion processes. A peristaltic pump was used for circulation of the sample and to establish that the volume excited was refreshed between two excitation pulses. Experiments on the DA proteins were carried out under the absence of light. Inspection of the dynamics between consecutive scans ensured if light adaptation due to the excitation laser occured. Supplementary, experiments on LA proteins were carried out under

constant illumination of the samples reservoir by an LED. The latter ensured that the isomeric ratio in this state doesn't change during the T.A experiment.

The T.A maps of both DA and OA states are shown in fig.37A and 37B, for delays between pump and probe up to 150ps. Vertical brakes correspond to the wavelength at which the UV-Vis and NIR datasets where combined using a scaling factor in order to match. A horizontal brake at 1ps delay is used to emphasize the initial evolution of the excited species, during which the isomerization reaction occurs. The species evolution after the brake (>1ps) corresponds mainly to ground state relaxation processes.

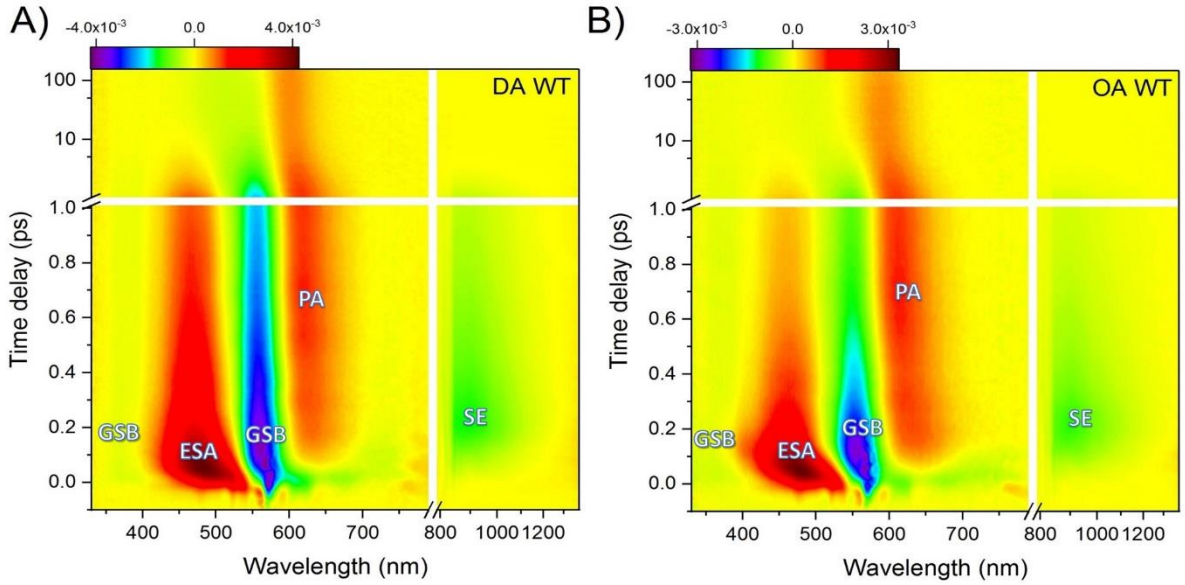

Fig. 37: Transient absorption maps of DA (A) and OA (B) proteins of WT-ASR after data treatment described in section 2.2.1; The excited state fraction of 13C isomer is 2%, 57% for maps of A) and B) respectively. Brakes at 790nm are used for defining the two probing windows upon acquisition of the data in the UV-Vis and NIR spectral region. The signatures of ESA,GSB,PA and SE are indicated in the figures; The colour bar on top of each map shows the scale for ΔA magnitude.

The UV-Vis probing range includes the signatures of ESA, GSB and PA, while the NIR region is dominated by the SE signature. Particularly, GSB (ΔA<0) is located in the 330-600nm range, while an ESA (ΔA>0) appears in the 400-510nm range, splitting in this way the GSB. In addition, the PA (ΔA>0) band associated with the isomerized species is located in the 580-700nm region, while SE (ΔA<0) covers the 700-1300nm range. A weak signal of ESA appears at 750-790nm and >1300nm and as a result cancels out the SE signal at specific wavelengths. For delays above 50ps we observe only the remaining signals of GSB and PA.

The different reactions occurring can be described by looking at the spectral evolution of the different signatures as a function of pump-probe delay as displayed in figure 38. In the following description, we will refer to DA WT which is dominated by AT-PBSR (98%) and compare it afterwards with the OA WT where 57% contribution is from 13C-PSBR.

By looking at the short time delay window (<250fs) in panel A, excitation of PSBR leads to population of the Franck-Condon region. This is observed by the formation of GSB (~370nm and 560nm) and ESA (~485nm) within 40fs (IRF). Simultaneously, the SE signature is observed in the 650-1100nm range competing with ESA (positive signal). The latter is concluded for the fact that positive features overcome SE at 775nm and >1200nm (see

Annexe III). In the usual reaction scheme within our IRF, we have populated the I-state (fluorescent state) of the PSBR.

In the 40-250fs time scale, an initial relaxation occurs. The ESA band (485nm) is blue-shifting by ~15nm, narrowing and simultaneously decaying by ~35% of the initial amplitude. In the region >600nm, SE is red-shifting to the NIR and forms fully at ~850-900nm. The red-shift of SE, reveals an ESA (640nm) which is simultaneously blue-shifting (by ~15nm). Considering the magnitude of spectral shift the origin of this ESA is the same as the one observed in the <510mn range. The described spectral relaxation observed is most likely due to C=C bond length alternation and intramolecular vibrational relaxation (IVR). An indication for our assignment of this relaxation is the minor recovery on the GSB signal (~12%) which is located at ~550nm and the fact that SE has not decreased in amplitude.

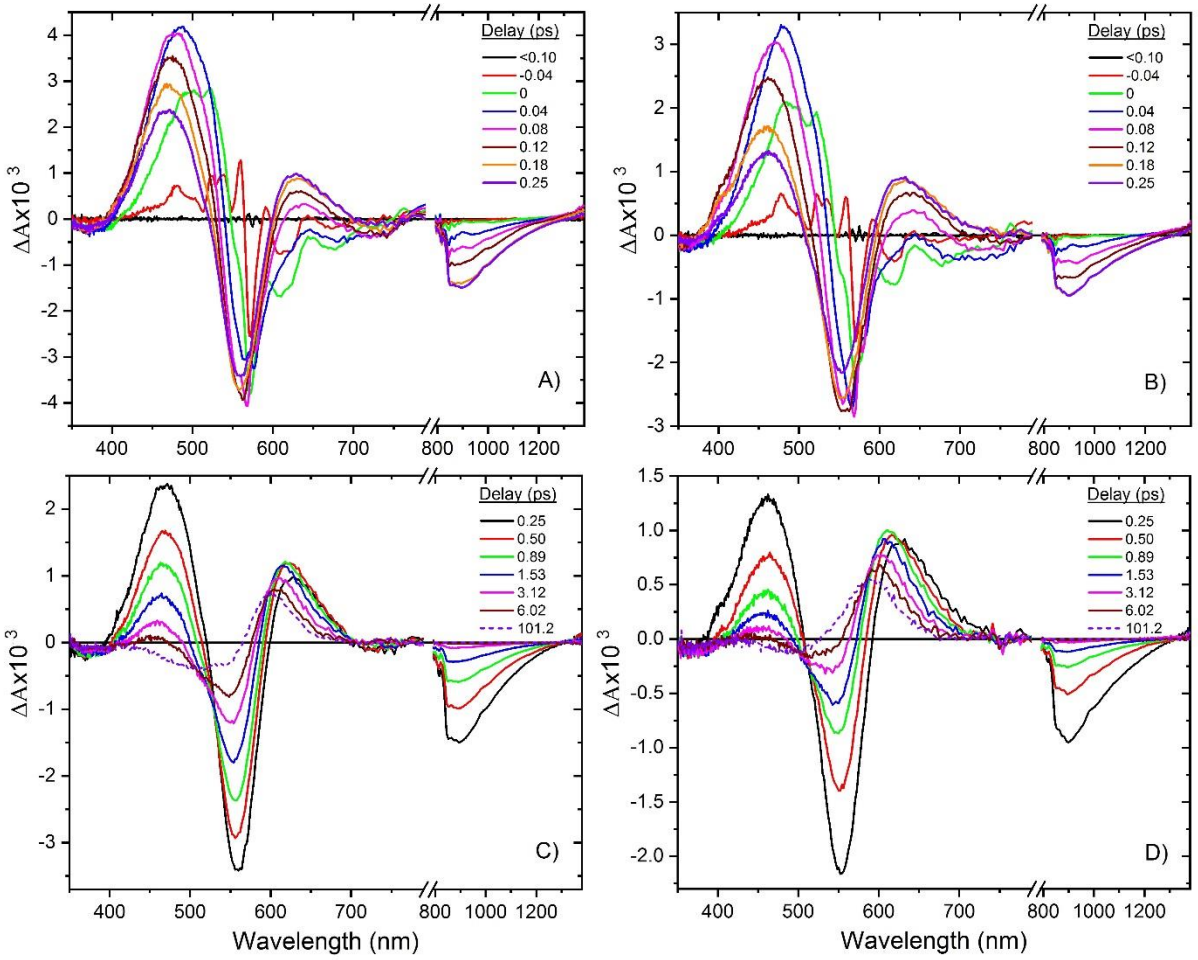

Fig. 38: Spectral evolution for DA and OA proteins of WT-ASR; A break at 790nmis used for defining the two probing windows upon acquisition of the data in the UV-Vis and NIR spectral region. A) DA WT <0.25ps B) OA WT <0.25ps C) DA WT >0.25ps D) OA WT >0.25ps; The long differential spectra which correspond to the formed K-species are shown with violet dashed line in figures C) and D) for DA and OA states respectively.

Panel C shows the spectral evolution at delays longer than >0.25ps. By approximately ~0.9ps the ESA (470nm) and SE (>800nm) have decayed by 70% and 60% of their initial amplitude respectively. From the latter observation we have the evidence for AT-PSBR's excited state lifetime, which should be in the order of ~0.9ps. Moreover, GSB has recovered by 40% from its initial amplitude, while a positive feature at ~620nm previously assigned to ESA further

increases and reaches a plateau, and slightly blue-shifts (0.5-1.5 ps). The plateau suggests that the ESA observed at <0.25ps at the specific region has been succeeded and superimposed by the photoproduct signature. The formation of the species that undergo isomerization and are vibrationally hot are expressed through the initially formed PA band. These species are assigned to the J-intermediate state and correspond to the percentage of the initially excited species that followed the reactive pathway upon reaching the conical intersection point.

At the delay of ~6ps, the SE signal has decayed fully while a spurious positive signal at the ESA (455nm) region is still present. Supplementary, the PA band seems to blue shift (~10nm) and decay (by 35%) in comparison with the previous plateau and GSB signal recovers further (reaching 20% of the initial amplitude). The spectral shift of the PA is an indication for vibrational cooling of the J-species and transition to the K-intermediate formation in several ps. Considering the full decay of SE by 6ps, we are led to the conclusion that the positive feature located at 455nm is a residual signal of PA, as the latter is in competition with GSB in the particular range. Finally, the spectrum at ~100ps is the long-delay, fully relaxed differential spectrum corresponding to the percentage of the excited species which successfully isomerized. The latter is confirmed because of the unchanged shape and amplitude of the spectrum up to the ns time scale (not shown).

From a comparison with OA WT (panel B), the general scheme is similar but with the processes progressing faster. Particularly, in the <0.25ps time window ESA decays to 40% of the initial amplitude within 250fs, while GSB has recovered by 25%. Supplementary, the spectral shifts occurring in the UV-Vis window reveal a higher amplitude for the ESA located in the 620-700nm range. On the NIR range, SE is formed within 180fs, slightly faster than for the DA WT.

In the >0.25ps time window the changes are more obvious, as ESA (470nm) and SE decay faster than DA WT. For the same time delay of 0.89ps, ESA and SE reached the 14% and 30% of their initial amplitude suggesting that the ESL for the 13C-PSBR (~56% percentage of contribution in OA state) is shorter than the AT-PSBR one. This is supported also by the total decay of the shorter wavelengths of ESA (<425nm). Supplementary, GSB has recovered to 40% of its initial amplitude for the 0.89ps delay. Moreover, a careful look at the PA formation we observe that a plateau is reached within ~0.7ps suggesting that while the AT-PSBR photoproduct is still forming the photoproduct of 13C isomer has already been formed.

By ~6ps, ESA and SE have decayed fully, with the cooling of the J-species taking place. The reduction of the GSB amplitude is the same level with the ~100ps differential spectrum is an indication that the J to K transition occurs on a faster time scale in comparison with DA WT. The shape of the final spectrum (~100ps) is different than the one of DA WT with obvious differences in the remaining GSB amplitude. The latter is an indication that the K-species spectra for both isomers are different.

Application of the procedure described in section 3.1.5 allows to retrieve the T.A map for 13C-PSBR isomer as shown in figure 39. From a first look on the 2D map we can see that ESA and SE bands last shorter in comparison with DA and OA data, while the GSB band is blue-shifted as expected from the steady state spectrum of 13C isomer.

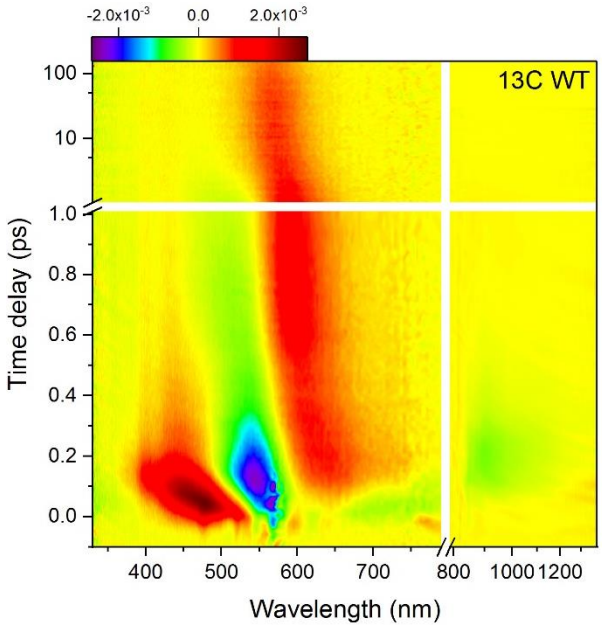

Fig. 39 : Transient absorption maps of 13C-PSBR of WT-ASR; The map is retrieved after applying the procedure described in section 3.1.5. Breaks at 790nm are used for defining the two probing windows upon acquisition of the data in the UV-Vis and NIR spectral region.

Analogous to DA and OA datasets, the spectral evolution for the two time windows is shown in figure 40A and 40B. By looking at the early time evolution we see that ESA is dynamically blue-shifting (~40nm) and decaying to 30% of her initial amplitude within 250fs. Contrary to DA and OA, SE contribution here starts decaying since the ~200fs delay.

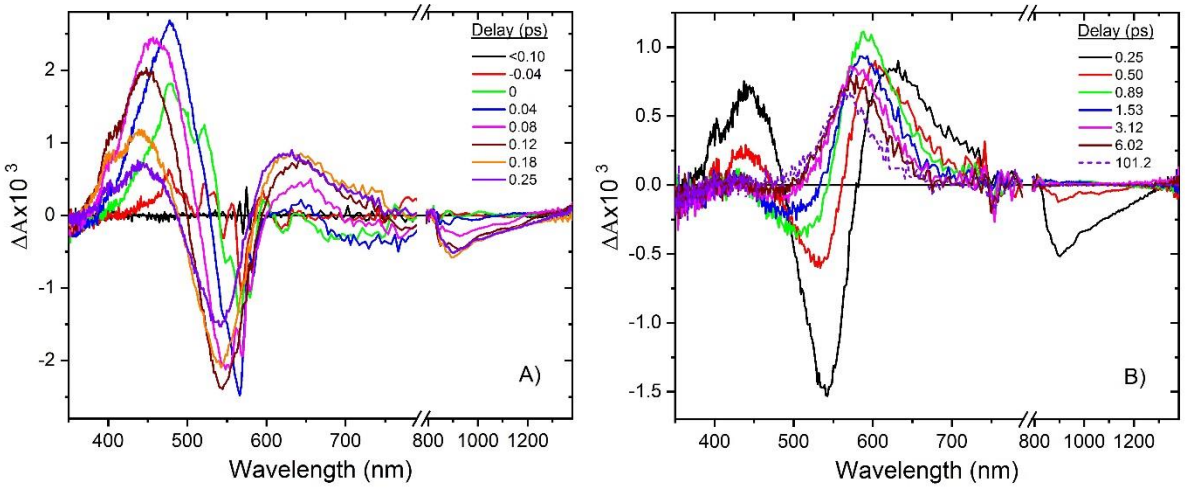

Fig. 40 : Spectral evolution for 13C-PSBR of WT-ASR; A) spectral evolution <0.25ps B) spectral evolution >0.25ps; The long-time differential spectra which correspond to the formed K-species is shown with violet dashed line in figure B)

The evolution on the longer timescale (panel B) shows that within 0.5ps SE has decayed to ~25% of the initial amplitude with the photoproduct forming (600nm) by 75%. The same holds for GSB which has recovered to 25% of the initial amplitude. The latter observation leads to the conclusion that the ESL of this isomer is in the sub-400fs timescale. For delays above ~0.9ps we see only the cooling of J-species with the final spectrum being only a

positive signal located at 570nm. This indicates that the extinction molar coefficient of the K-species of this isomer is higher than the GS one.

In order to have a general dynamic overview of the data, figure 41 shows DA, OA, and 13C-PSBR kinetic traces from ESA, GSB, PA and SE contributions, at selected wavelengths.

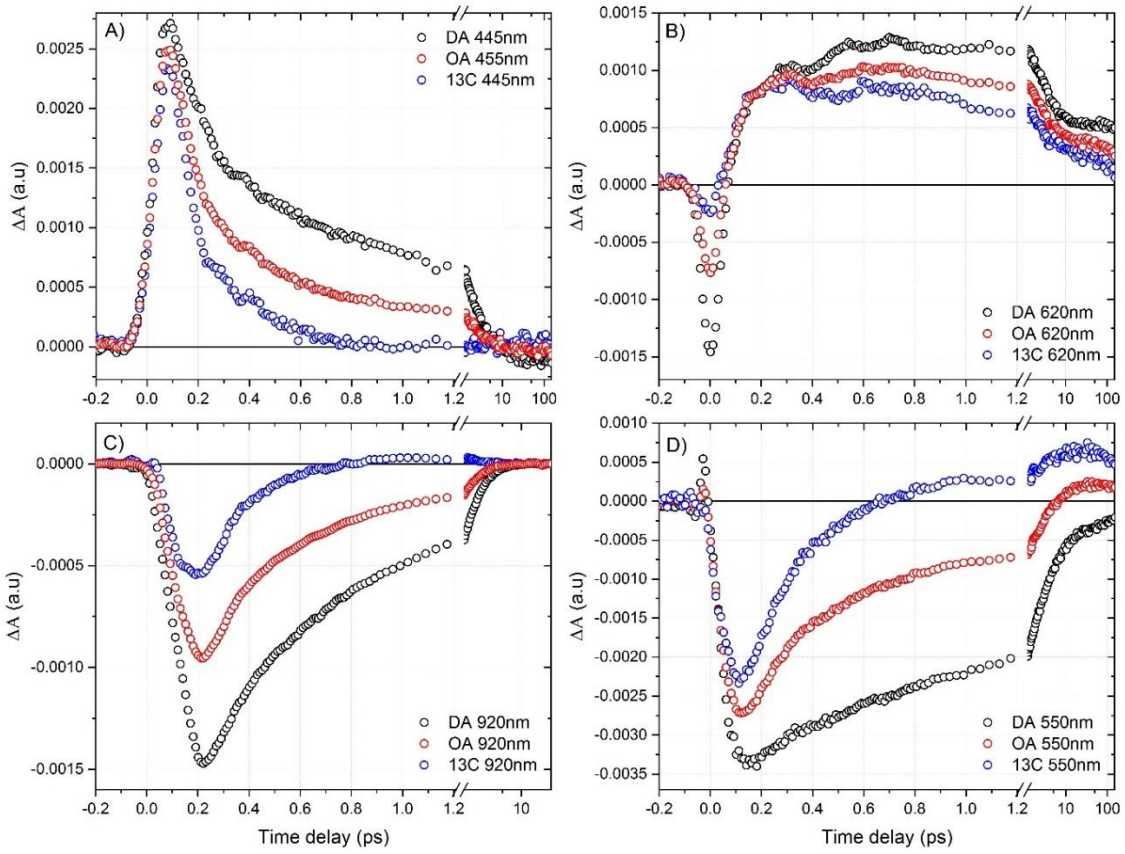

Fig. 41: Kinetic traces for DA (black),OA (red) and 13C isomer (blue) of WT ASR. A) ESA at 445nm B) PA at 620nm C) SE at 920nm D) GSB at 550nm

As anticipated above, slower dynamics are observed for the AT-PSBR (DA WT) with respect to 13C-PSBR. An intermediate behaviour is observed for the case of the mixture in the OA state (57% of 13C). Ideally, SE and ESA kinetic traces should decay with the same time constants as they originate from the excited state. However, in our case ESA is overlapped with PA contributions, resulting in additional time constants (in the ≈3ps range) due to vibrational cooling of the J-species and with a constant contribution at delays after 10ps corresponding to the final spectrum of the K-species. For this reason, the only background free spectral region used for providing the ESL is SE (discussed in section 3.7). Application of a global fit in the UV-Vis spectral range gives erroneous results as a consequence of the large dynamic spectral shifts, due to excited and ground state vibrational relation. Thus our interpretation will be based on individual fits of specific probe wavelengths for the UV-Vis range and global fits of the SE contribution in the NIR region. The description will hold only for the pure isomers.

3.7 Excited state lifetime of AT-PSBR and 13C- PSBR in WT ASR

The stimulated emission contribution is able to screen the evolution of the excited population from FC zone to a relaxed configuration on the S1 PES, before isomerization through CI occurs. Indeed, the spectral evolution showed that dynamic shifts occur in an initial ~250fs window, SE is formed and decays globally without any shape changes (figs. 38A and 40A).

The global analysis for AT-PSBR for the spectral region of 850nm-1100nm is shown in figure 42. The reason of selecting this range is because SE traces show identical dynamics for the particular range, while at shorter and longer probing wavelengths dynamic shifts occur (see Annexe). The SVD decomposition resulted in a dominant singular transient as shown in Panel A. A use of a double-exponential with 0.19ps and 0.95ps fails to capture the longer time-delays; shown in Annexe (IV). However, a <50fs component is needed in addition to the two exponentials in order to obtain a correct fit, leading to a fit with longer time constants. While our temporal resolution doesn't allow the discrimination of such a short time constant we used an Atau component which includes the un-resolved time constants hidden in the IRF. The latter resulted in a (0.53±0.04)ps and (1.64±0.2)ps time constants with a ratio of 72:28 between them. Thus, the ESL for AT-PSBR is expressed by the weighted average of both with (0.83±0.05)ps.

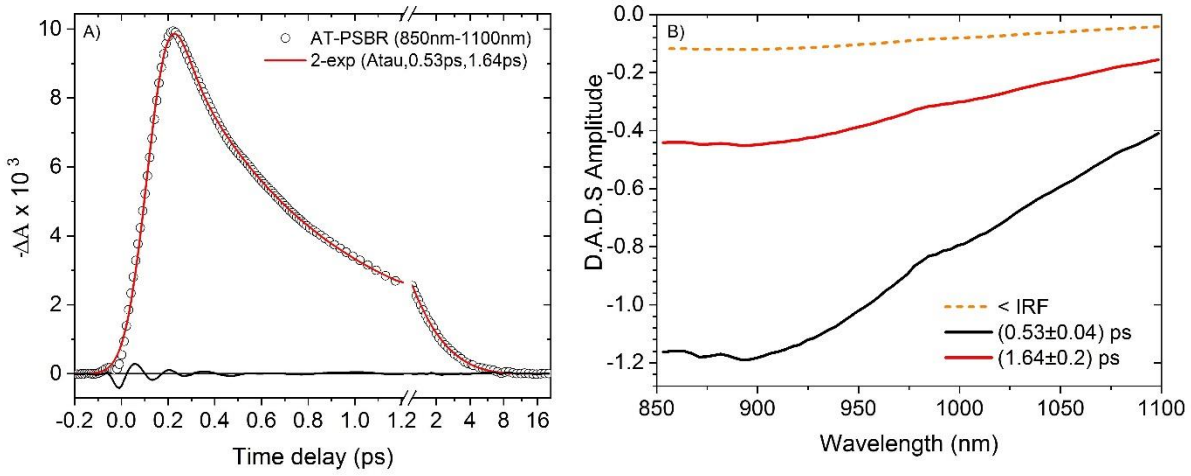

Fig. 42 : Global fit A) and DADS B) from inverted sign SE (850nm-1100nm) of AT-PSBR; A) 2-exponential fit with an additional un-resolved constant shorter than our IRF; Black circles correspond to the dominant singular value after SVD decomposition, Red solid line corresponds to the fit and black solid line to the residuals; B) Black and red solid lines correspond to the associated spectra with time constants of 0.53ps and 1.64ps respectively. The spectrum corresponding to the initial Atau (un-resolved) component is shown with orange dashed line.

The same procedure applied for 13C-PSBR results in a bi-exponential fit with (0.19±0.04)ps and (1.82±0.5)ps time constants (figure 43). The short constant with a 94% amplitude corresponds to the ESL of 13C isomer, while the 1.8ps constant has a negative amplitude and is most likely an artefact of the AT/13C subtraction procedure. However, a similar behaviour for SE data of 13C isomer was observed also by Wand[44] and Cheminal[25].

The resulting ESL's for AT and 13C PSBRs are in agreement with previously reported results, supporting a ratio $AT_{ESL}/13C_{ESL}$ of ~4.5. In the same description as the one described in fig 34b, the potential energy surfaces in a simplified two-dimensional scheme can be drawn as in figure 44.

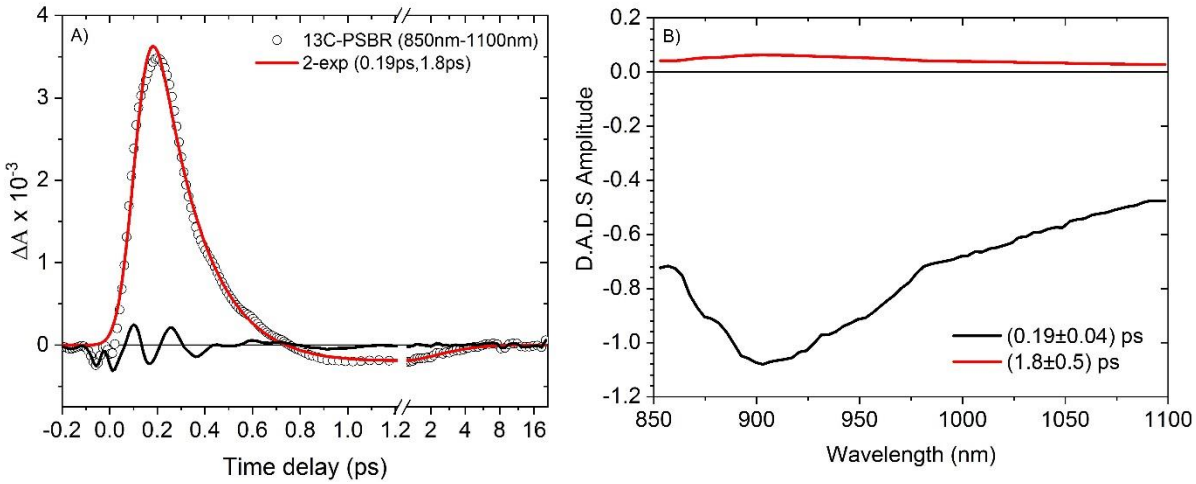

Fig. 43 : Global fit A) and DADS B) from inverted-sign SE (850nm-1100nm) of 13-PSBR; A) 2-exponential fit with an additional un-resolved constant shorter than our IRF; Black circles correspond to the dominant singular value after SVD decomposition, Red solid line corresponds to the fit and black solid line to the residuals; B) Black and red solid lines correspond to the associated spectra with time constants of 0.19ps and 1.8ps respectively.

The slope of 13C-PSBR S1 PES is steeper in comparison with the AT's one with the excited state population moving towards the CI characterised in a ballistic fashion. On the contrary, the shape of AT S1 PES is flatter (represented by a plateau) and the motion of population towards the CI can be characterized as non-coherent. The latter results are also supported by theoretical calculations[52,53].

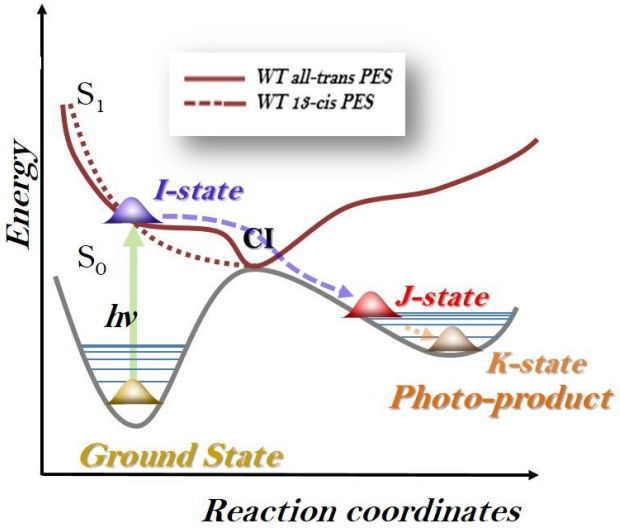

Fig. 44 : PES for AT- and 13C-PSBR; The vertical axis corresponds to the energy of each PES while the horizontal axis to the reaction coordinates; CI is the intersection between S1 and S0 PES's corresponding to 90 degrees torsion on the C13=C14 bond. The green vertical arrow corresponds to the excitation of ground state species (populating the Franck-Condon region); Purple dotted arrow represents the pathway for J-species formation while the orange one to the cooled K-species. Solid brown line corresponds to the S1 PES of AT-PSBR (flat) while the dotted brown line to the S1 PES of 13C-PSBR.

3.8 Isomerized Species formation

While in the previous section we have determined the ESL for both isomers by monitoring the S1→S0 transition (SE), here we try to extract information for the pathway the initially excited species followed. Particularly, it is possible to get this information by monitoring the depletion of ground state (S0→S1 transition) and the formation of the isomerized species (Sproduct→Sn transition). The first transition is represented by GSB and the second one by PA. Figure 45 shows the GSB and PA dynamics of selected probing wavelengths for each isomer. Note the strong wavelength dependencies due to rapid spectral shifts of SE and ESA (<0.2 ps), and slower ground state vibrational relaxation (3-10 ps).

From a visual inspection of the GSB contributions we clearly see an obvious difference in the sub-ps time window. The AT-PSBR (panel A) exhibits a slower recovery than 13C-PSBR (panel C) with the fits suggesting a 1ps (black) to 1.5ps (red) time constant. In the 13C case, GSB recovers with a dominant ~0.2ps time constant. This initial recovery is in agreement with the ESL determined from SE. In addition, in the longer timescale we find a ~6ps and ~2ps for AT and 13C isomer respectively which is representative of the J→K species transition. In both cases, an additional >200ps constant is needed to capture the long-time differential spectrum.

Furthermore, the formation of the J-species should appear as a rise time in the PA dynamics, but as pointed out above, ESA contributions are also present in the first 0.25 ps and for λ> 600nm (fig. 38), in addition to an exponential rising with the PA formation time (eq.31 in chap. 2). Therefore, we discuss qualitatively the time scale for occurrence of a signal level plateau, characteristic for ≈2-3 times the formation times. At 600nm, this PA initial plateau is reached within 0.65ps for 13C isomer case, while for the AT case this formation is still progressing up to ~1-1.2ps. In the case of PA contribution a preliminary ESA and SE contributions are present within the initial 100fs captured with 40-50fs constant. The fitting procedure on the >100fs range resulted in two exponentials and an infinite constant for both cases. For the AT isomer we obtained a short constant in the range of (0.27-0.37)ps and a long one in the range of (3-4)ps. Supplementary, for the 13C we obtained a (0.24-0.28)ps and a longer in the range of (1.3-1.7)ps. Here the result is unclear once the time constants in the ~ps range are smeared out from the J-species cooling. While the photoproduct formation is expressed through a negative amplitude, the J-species cooling carry a positive sign.

However, further information concerning the timescale of the photoproduct formation cannot be extracted from our data. The resulting time constants from the individual fits are summarised in Table 4.

Time constants	**GSB**	DA	13C	**PA**	DA	13C
τ1 (ps)		**(-) 1.1-1.5**	**(-) 0.19-0.20**		**(-) 0.27-0.37**	**(-) 0.24-0.28**
τ2 (ps)		**(-) 5.8-6.2**	**(-) 1.9-2.1**		**(+) 3.1-4.1**	**(+) 1.3-1.7**
τ3 (ps)		**>200**	**>200**		∞	∞

Table 4: Time constants extracted from fitting procedure for kinetic traces shown in Fig.45

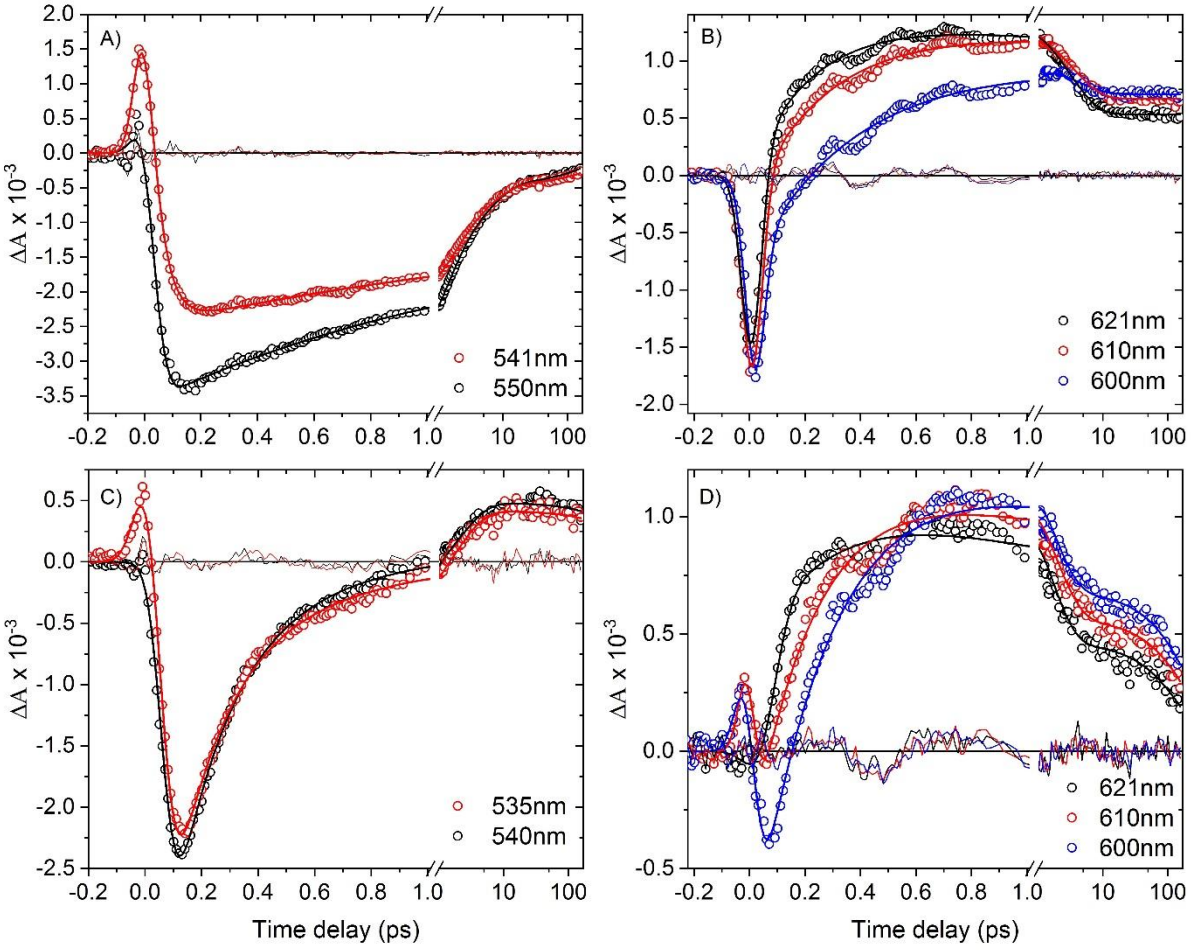

Fig. 45 : GSB dynamics for AT (A) and 13C (C); PA dynamics for AT (B) and 13C (D); Data for each probe wavelength are shown with circles while the fits with thick solid lines; The residuals are shown with thin solid lines.

3.9 Quantum Yield of isomerization

At the beginning of this chapter it was mentioned that we want to reveal the time-scale of processes taking place in the GS→K-intermediate transition of the two photo-cycles. Thus, the combination of the ESLs and the timescale of the J→K transition are used for designing the reactive pathway scheme for both isomers (shown in figure 46).

$$AT_{PSBR} \xrightarrow[h\nu]{<IRF} AT^{*}_{PSBR}(I_{AT}) \xrightarrow{\sim 0.83ps} CI \begin{cases} \xrightarrow{\Phi_{AT}} J_{AT} \xrightarrow{\sim 3ps-6ps} K_{AT} \rightarrow \cdots \rightarrow 13C_{PSBR} \\ \xrightarrow{1-\Phi_{AT}} AT_{PSBR} \end{cases}$$

$$13C_{PSBR} \xrightarrow[h\nu]{<IRF} 13C^{*}_{PSBR}(I_{13C}) \xrightarrow{\sim 0.2ps} CI \begin{cases} \xrightarrow{\Phi_{13C}} J_{13C} \xrightarrow{\sim 1.3ps-2ps} K_{13C} \rightarrow \cdots \rightarrow AT_{PSBR} \\ \xrightarrow{1-\Phi_{13C}} 13C_{PSBR} \end{cases}$$

Fig. 46 : Reactive pathway scheme for the initial GS→K transition of the AT- and 13-C PSBRs photo-cycle.

On this scheme the only unknown quantity is the efficiency of the isomerization process mentioned as quantum yield Φ. The latter corresponds to the percentage of the initially excited population which followed the reactive pathway and managed to form the isomerized species. In our data, the percentage of this population is translated in a constant differential spectrum after the cooling of J-species has completed (delays ~100ps); see figure 47A for a pump-probe delay of 150ps. This spectrum consists of a negative and positive feature. The negative part is the contribution of the non-recovered excited species (GSB in the 400nm-550nm range for DA) and the positive part corresponds to the relaxed K-species (PA in the 570nm-670nm range for DA). The shape of this spectrum is defined by the difference in molar absorption coefficient of the K-species with respect to GS-species, with the K- and GS-spectra shown in figure 47B. Note that these spectra were obtained from data measured at 130K[48] and by extrapolating them to 300 K (ref. 25). Analogous to section 3.5, the final spectrum will be a linear combination of both isomers K- minus GS- spectra with each spectrum scaled by the fraction of the excited concentration $n^{*isomer}_{state}$, the cuvette thickness l and the quantum yield for each isomer Φ_{isomer} (eq.59).

$$\Delta A_{state}(\lambda, t_\infty) = lC_0^* \times \{n^{*AT}_{state}(\epsilon_{KAT}(\lambda) - \epsilon_{GSAT}(\lambda))\Phi_{AT\to 13C} + n^{*13C}_{state}(\epsilon_{K13C}(\lambda) - \epsilon_{GS13C}(\lambda))\Phi_{13C\to AT}\}$$

eq. 59

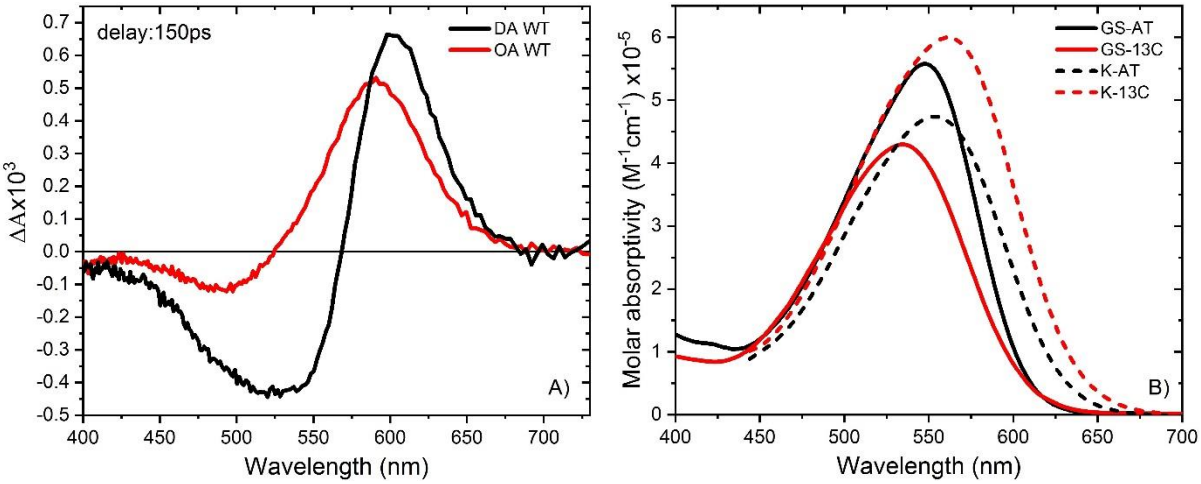

Fig. 47: A) Differential spectrum for DA (black) and OA (red) at 150ps delay B) Molar extinction coefficient of AT- (black) and 13C PSBR (red) ground state (GS) and K-species (K) at room temperature; The spectra shown in B)are taken from ref.25

The C_0^* quantity is basically the number of excited molecules N^* divided by the excitation volume V_0.

$$C_0^* = \frac{E_p \lambda_{exc}}{V_0 hcN_A}\left[1 - 10^{-A(\lambda_{exc})}\right] \quad \text{eq. 60}$$

Calculating E_p and thus C_0*, which are average values for the probed volume, bears a number of uncertainties, as recognised in Ref. 25. From an experimental point of view, a more accurate way will be to define this value relative to a known reference sample with a well characterised Φ. For the latter purpose, we have recorded the long differential spectrum of light adapted Bacteriorhodopsin (>95% AT-PSBR) under identical excitation conditions. BR has a well-known quantum yield for AT-PSBR equal to ~0.65[11] and by using it as reference we can eliminate any errors on determination of the excitation volume (e.g beam diameter, pump volume probed etc). Complementary to the ASR case, the K- and GS- spectra of

extinction coefficients, used for this analysis were already available at room temperature[54]. Thus, the only unknown parameter in eq.59 (for AT→13C isomerisation only) is the excited state concentration for the specific excitation wavelength. An example for the case of OA BR is shown in figure 48 for two different excitation wavelengths. In the case of 540nm excitation the data are overlapped very well with the scaled K- minus GS- spectrum with a small deviation at the pump wavelength region. For the case of 565nm excitation, the data need to be shifted by 5nnm in order to match the previous data in the >575nm region. However, the data located at shorter probe wavelengths are different. For our calculations we rely on the values which reproduce the positive feature from the differential spectrum.

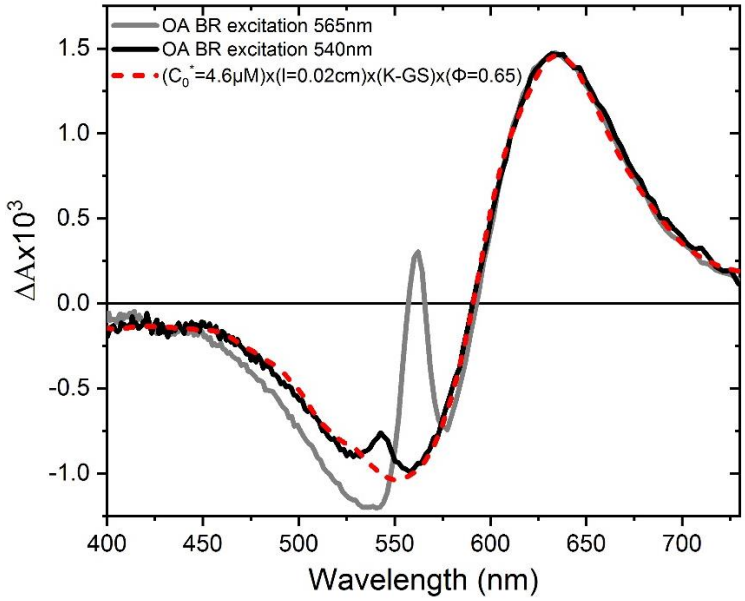

Fig. 48: Differential spectrum of OA BR at 250ps delay for excitation at 565nm (grey) and 540nm (black); Red dashed line corresponds to application of eq.59 for AT-PSBR; In the case of 565nm excitation the data were shifted by 5nm towards shorter wavelengths to match the positive feature at ~630nm (calibration).

With the known differential ext. coefficient, and the QY=0.65, the excited concentration C_0^* for BR case is determined at 4.6μM, at λ= 565 nm. Since experimentally the same pump laser excitation density is used, this corresponds to 3μM and 2.23μM for the case of DA WT-ASR and OA WT-ASR, respectively, due to the lower extinction coefficients, as compared to bR. In the case of DA WT-ASR, we assumed that the sample is purely AT-PSBR, while for the OA WT a percentage of 57% is due to the 13C-PSBR. The spectrum of K-species for the AT case was leading to erroneous results (quantum yield of ~1) with the K- minus GS- spectrum not matching our experimental data (see Annexe A.V). Having in mind that the analogous spectrum of BR was fitting well our experimental data, we concluded that the long differential spectrum depends on small experimental details that I was not able to clarify.

Particularly, the main peak of BR's K-spectrum is 29nm red-shifted in comparison with the GS one. A similar amount of shift is observed for the case of K-spectrum for 13C-PSBR in ASR. On the contrary the AT-PSBR in ASR, a 6nm shift (fig. 47B) gave good agreement with the experimental spectra published in Ref.25 and the PhD thesis of A. Cheminal[51]. However, the DA spectra reported here, even though for the same protein in the same conditions, are different from the ones reported previously by our team. The reasons for this

difference are unclear at the present stage, in particular since this kind of experiment was performed repeatedly in course of both thesis projects. However, by simply shifting the K-spectrum of AT-PSBR in WT-ASR towards longer wavelengths in order to reach this ~30nm shift we are able to reproduce the final spectrum (fig. 49). The latter results in a $\Phi_{AT\rightarrow 13C}$=0.36±0.04 with the error bars defined by an uncertainty of ±0.3μM (10%) on the determination of C_0^*. The determination of $\Phi_{13C\rightarrow AT}$ is determined by application of eq.59 on the OA WT, yielding a quantum yield of 0.43±0.04. The scaled K- minus GS spectra which give the latter values are shown in figure 49.

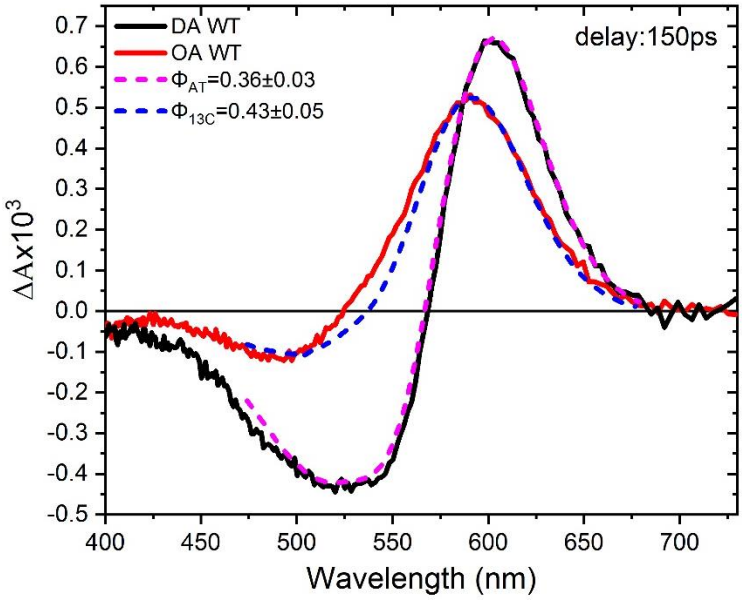

Fig. 49 : Differential spectrum of DA and OA WT at 150ps with dashed magenta and blue lines corresponding to the scaled K- minus GS spectra of each isomer.

These results appear to be different from what was previously reported in ref.25. In particular, we find a relative $\Phi_{AT\rightarrow 13C}/\Phi_{13C\rightarrow AT}$ = 0.8±0.2, while this ratio was found to be 2.7 before. We note that $\Phi_{AT\rightarrow 13C}/\Phi_{13C\rightarrow AT}$ must be larger than one, otherwise 13C concentrations > 50% would not be possible, as is reported even for broadband VIS sources[47], and which is the molecular basis for the light intensity sensing function of the protein.

In summary, we find for AT wt-ASR a long-time difference spectra with different shapes than those reported in Ref. 25. As a consequence the reaction QY is different (larger). We find a higher QY for 13C→AT than for the reverse process, which is at odds with all previously published results. This point requires further investigation.

3.10 Vibrational coherences in WT ASR

In section 3.8 a comparison between GSB and PA dynamics was made with the residuals from the fits suggesting the presence of low frequency oscillatory features. The latter is noticeable even by visual inspection of the raw data, when compared with the negative delay signal (defining the noise floor due to white-light fluctuations). In the present section, we try to compare DA and OA WT oscillatory signals and try to understand if some of these oscillatory features are shared between AT- and 13C-PSBR. For this task, we have performed

a pump probe measurement on DA and OA WT by using a ~25fs pump pulse, centered at 550nm and white light probing (350-700nm). The step used was set at 10fs.

An example of the data treatment is show in figure 50. Panel A shows a kinetic trace for DA WT at 590nm, fitted with a bi-exponential function (red-line). The residuals shown with blue color reveal the existence of at least two periods of oscillations, a slow one with ~400fs period and faster one with ~100fs; notice that the amplitude of these oscillatory features is at least a factor of ~3 above the noise floor. A FFT of the residuals (up to 1200fs) results in the amplitude spectrum shown in panel B. Each peak in this spectrum can be attributed to a vibrational mode (central frequency labelled on each peak). The way to define if a peak corresponds to a real oscillation in our data and not to noise, we define the noise floor in this procedure as the amplitude of modes >1100cm^{-1}. The selection of this value is based on the duration of our pump pulse which is shorter than 30fs (corresponds to 1100cm^{-1}).

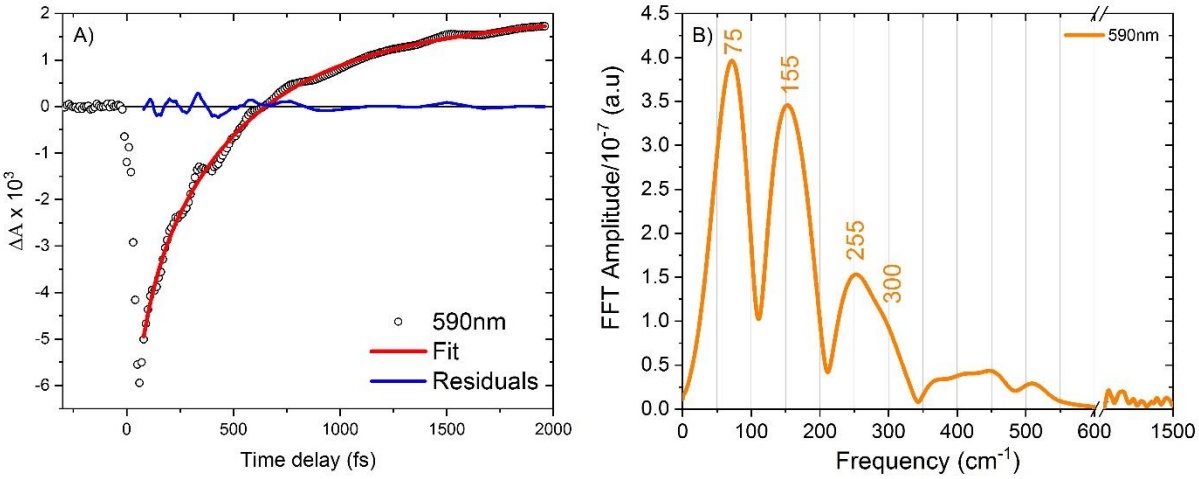

Fig. 50: Procedure for extracting oscillations from a specific probe wavelength. A) Kinetic trace at 590nm of DA WT-ASR; Black circles correspond to the experimental data while red and blue solid lines to fit and residuals respectively. B) FFT of residuals determined from A).The orange curve corresponds to the amplitude of the FFT, expressed through several peaks attributed to a specific frequency of a vibrational mode. Each peak central frequency is labelled. A break is used to show the defined noise floor, which here is the amplitude of peaks >1100cm^{-1}.

The results of this analysis are summarised in figure 51 for specific probing regions (ESA, ESA/GSB, GSB/PA, PA). To get a more accurate result, the FFT is applied on the averaged residuals over 2-5nm range around the central probe wavelength, which apart from noise are identical (same vibrational pattern). The observed vibrational modes lie in the <400cm^{-1} frequency range. The dominant contribution is from modes ranging between 65-90cm^{-1}, while modes observed at higher frequencies (130-460cm^{-1}) seems to increase their amplitude depending on the detection range.

The 65-90cm^{-1} (370fs-520fs periods) mode observed in all contributions is related to the skeletal torsion of the polyene as has been shown from resonant Raman and far-Infrared experiments on rhodopsin and all-trans retinal[55,56]. Alternatively, and in some cases, they could also arise as the beating frequency of higher energy modes. In the ESA probing region (450nm and 470nm), we see the presence of modes at 150-160cm^{-1}, 210-220cm^{-1} and 280-320cm^{-1}, assigned in previous reports to excited state vibrations [57,58]. The latter assignment is due to the presence of these modes also in SE signature as reported by Wand et al[57].

Complementary, from a Rhodopsin study at low and room temperatures Kim et al[59] commented on modes located between 130cm^{-1} - 320cm^{-1} assigning them to skeletal delocalised torsions. In the observation region of ESA/GSB (520nm and 530nm) we see the appearance of modes at 135-140cm^{-1}, 235cm^{-1} and 460cm^{-1} (particularly for OA WT). The situation with respect to the previous is different here, once the dominant modes are the 210-235cm^{-1} ones (140-160fs periods). For detection at longer wavelengths (region of GSB/PA at 590nm), we see the dominant mode shifting in frequency located now at 65-75cm^{-1}. Finally at 612nm and 627nm probing, the 65cm^{-1} mode is dominating the modes in the range of 155-170cm^{-1} succeeded by a 135cm^{-1} and 280cm^{-1}.

While DA and OA proteins appear to have similar vibrational mode activity at least for the low-frequency range, a shift of the central frequency of each mode is observed in the case of the mixture (OA state), arising mainly from the different conformation of 13C-PSBR.

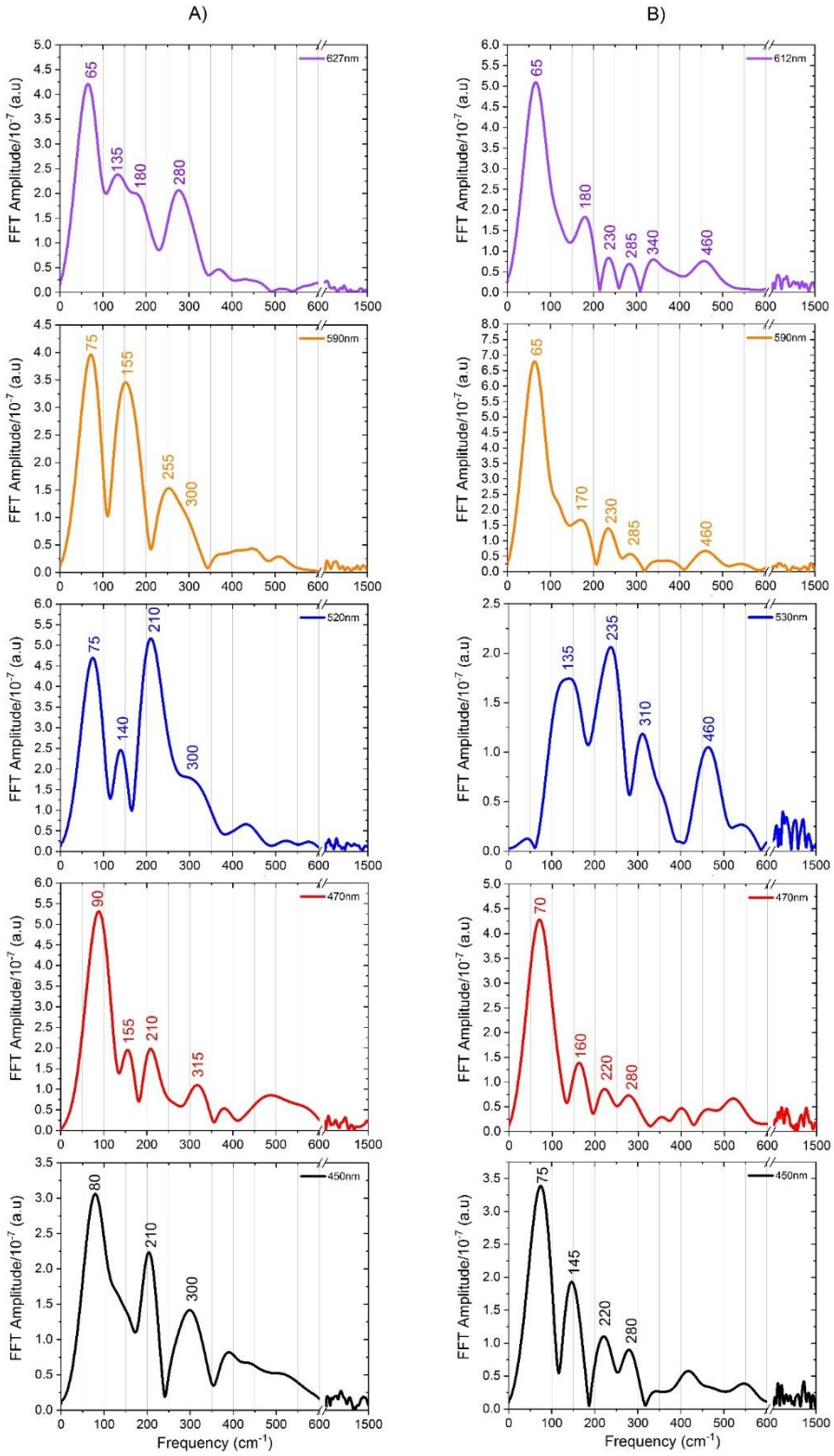

Fig. 51: FFT amplitude spectra of residuals at specific probe wavelength shown for DA WT (A) and OA WT (B) ASR; Different colours are representing the spectral regions of ESA (450nm,470nm), ESA/GSB (520nm,530nm), GSB/PA (590nm) and PA (612nm,627nm). The central frequency of each peak is indicted; The residuals used were an average over 2-5nm around the central probe wavelength;

3.11 Summary

From our studies on WT-ASR, we provided T.A data for DA and LA proteins revealing the spectroscopic signatures in the (330-1400) nm spectral range. From our analysis, the ESL of both isomers was determined confirming previous reports on WT ASR with the ESL for AT and 13C isomers being 0.83ps and 0.2ps respectively.

Moreover, we attempted to determine the isomerization Q.Y values for both isomers with discrepancies arising concerning the final K-GS spectra shape measured. Particularly, the K-species spectra for AT-PSBR didn't match our experimental data and approximations were made. The values obtained gave a relative quantum yield between the two isomers of $\Phi_{AT\rightarrow 13C}/\Phi_{13C\rightarrow AT}$ = 0.8±0.2, with the absolute values being $\Phi_{AT\rightarrow 13C}$=0.36±0.03 and $\Phi_{13C\rightarrow AT}$ 0.43±0.05 respectively. The contradiction with previously published results suggests a deeper investigation and clarification of the parameters determining the shape of the final K-GS spectra.

In addition to the ESL and QY, we provided information concerning the vibrational activity of low in frequency modes (<400cm^{-1} range). The performed experiments for DA and LA proteins, resulted in four low frequency modes presented for both DA and OA WT proteins ranging between 60cm^{-1} - 400cm^{-1}. The latter results was previously reported in literature for other retinal proteins, attributing these modes to the chromophore's skeletal delocalized torsions.

References

(1) Hong, F. T. Interfacial Photochemistry of Retinal Proteins P. *Prog. Surf. Sci.* **1999**, 237.

(2) Harris, A.; Ljumovic, M.; Bondar, A.-N.; Shibata, Y.; Ito, S.; Inoue, K.; Kandori, H.; Brown, L. S. A New Group of Eubacterial Light-Driven Retinal-Binding Proton Pumps with an Unusual Cytoplasmic Proton Donor. *Biochim. Biophys. Acta BBA - Bioenerg.* **2015**, *1847* (12), 1518–1529. https://doi.org/10.1016/j.bbabio.2015.08.003.

(3) *Biomembranes: A Multi-Volume Treatise*; Lee, A. G., Ed.; JAI Press: Greenwich, Conn, 1995.

(4) Diller, R. Primary Reactions in Retinal Proteins. In *Ultrashort Laser Pulses in Biology and Medicine*; Braun, M., Gilch, P., Zinth, W., Eds.; Springer Berlin Heidelberg: Berlin, Heidelberg, 2008; pp 243–277. https://doi.org/10.1007/978-3-540-73566-3_10.

(5) Wang, W.; Nossoni, Z.; Berbasova, T.; Watson, C. T.; Yapici, I.; Lee, K. S. S.; Vasileiou, C.; Geiger, J. H.; Borhan, B. Tuning the Electronic Absorption of Protein-Embedded All-Trans-Retinal. *Science* **2012**, *338* (6112), 1340–1343. https://doi.org/10.1126/science.1226135.

(6) Kaiser, W.; Kglling, E.; Oesterhelt, D. CYCLE- IN BACTEFUORHODOPSIN. *Chem. Phys. Lett.* **1985**, *117* (1), 7.

(7) Hasson, K. C.; Gai, F.; Anfinrud, P. A. The Photoisomerization of Retinal in Bacteriorhodopsin: Experimental Evidence for a Three-State Model. *Proc. Natl. Acad. Sci.* **1996**, *93* (26), 15124–15129. https://doi.org/10.1073/pnas.93.26.15124.

(8) Mathies, Ri. A.; Cruz, C. H. B.; PoLARD, W. T.; Shank, C. V. Direct Observation of the Femtosecond Excited-State Cis-Trans Isomerization in Bacteriorhodopsin. 4.

(9) Tittor, J.; Oesterhelt, D. The Quantum Yield of Bacteriorhodopsin. *FEBS Lett.* **1990**, *263* (2), 269–273. https://doi.org/10.1016/0014-5793(90)81390-A.

(10) Schneider, G.; Diller, R.; Stockburger, M. Photochemical Quantum Yield of Bacteriorhodopsin from Resonance Raman Scattering as a Probe for Photolysis. *Chem. Phys.* **1989**, *131* (1), 17–29. https://doi.org/10.1016/0301-0104(89)87078-8.

(11) Logunov, S. L.; El-Sayed, M. A. Redetermination of the Quantum Yield of Photoisomerization and Energy Content in the K-Intermediate of Bacteriorhodopsin Photocycle and Its Mutants by the Photoacoustic Technique. *J. Phys. Chem. B* **1997**, *101* (33), 6629–6633. https://doi.org/10.1021/jp970955c.

(12) Schoenlein, R.; Peteanu, L.; Mathies, R.; Shank, C. The First Step in Vision: Femtosecond Isomerization of Rhodopsin. *Science* **1991**, *254* (5030), 412–415. https://doi.org/10.1126/science.1925597.

(13) Polli, D.; Altoè, P.; Weingart, O.; Spillane, K. M.; Manzoni, C.; Brida, D.; Tomasello, G.; Orlandi, G.; Kukura, P.; Mathies, R. A.; et al. Conical Intersection Dynamics of the Primary Photoisomerization Event in Vision. *Nature* **2010**, *467* (7314), 440–443. https://doi.org/10.1038/nature09346.

(14) Dartnall, H. J. A. The Photosensitivities of Visual Pigments in the Presence of Hydroxylamine. *Vision Res.* **1968**, *8* (4), 339–358. https://doi.org/10.1016/0042-6989(68)90104-1.

(15) Kim, J. E.; Tauber, M. J.; Mathies, R. A. Wavelength Dependent Cis-Trans Isomerization in Vision †. *Biochemistry* **2001**, *40* (46), 13774–13778. https://doi.org/10.1021/bi0116137.

(16) Loevsky, B.; Wand, A.; Bismuth, O.; Friedman, N.; Sheves, M.; Ruhman, S. A New Spectral Window on Retinal Protein Photochemistry. *J. Am. Chem. Soc.* **2011**, *133* (6), 1626–1629. https://doi.org/10.1021/ja1087387.

(17) Bassolino, G.; Sovdat, T.; Liebel, M.; Schnedermann, C.; Odell, B.; Claridge, T. D. W.; Kukura, P.; Fletcher, S. P. Synthetic Control of Retinal Photochemistry and Photophysics in Solution. *J. Am. Chem. Soc.* **2014**, *136* (6), 2650–2658. https://doi.org/10.1021/ja4121814.
(18) Hamm, P.; Zurek, M.; Röschinger, T.; Patzelt, H.; Oesterhelt, D.; Zinth, W. Femtosecond Spectroscopy of the Photoisomerisation of the Protonated Schiff Base of All-Trans Retinal. *Chem. Phys. Lett.* **1996**, *263* (5), 613–621. https://doi.org/10.1016/S0009-2614(96)01269-9.
(19) Mukai, Y.; Imahori, T.; Koyama, Y. COMPARISON OF THE PATHWAYS AND QUANTUM YIELDS OF DIRECT PHOTOISOMERIZATION OF UNPROTONATED AND PROTONATED N-BUTYLAMINE SCHIFF BASES OF ISOMERIC RETINYLIDENEACETALDEHYDE WITH THOSE OF SCHIFF BASES OF ISOMERIC RETINAL: RATIONALIZATION OF THE SELECTION OF THE RETINYLIDENE CHROMOPHORE BY RETINOCHROME. *Photochem. Photobiol.* **1992**, *56* (6), 965–975. https://doi.org/10.1111/j.1751-1097.1992.tb09719.x.
(20) Freedman, K. A.; Becker, R. S. Comparative Investigation of the Photoisomerization of the Protonated and Unprotonated N-Butylamine Schiff Bases of 9-Cis-, 11-Cis-, 13-Cis-, and All-Trans-Retinals. *J. Am. Chem. Soc.* **1986**, *108* (6), 1245–1251. https://doi.org/10.1021/ja00266a020.
(21) Schoenlein, R. W. Femtosecond Dynamics of Cis- Trans Isomerization in a Visual Pigment Analog: Isorbodopsin. 6.
(22) Losi, A.; Braslavsky, S. E.; Gärtner, W.; Spudich, J. L. Time-Resolved Absorption and Photothermal Measurements with Sensory Rhodopsin I from Halobacterium Salinarum. *Biophys. J.* **1999**, *76* (4), 2183–2191. https://doi.org/10.1016/S0006-3495(99)77373-X.
(23) Losi, A.; Wegener, A. A.; Engelhard, M.; Gärtner, W.; Braslavsky, S. E. Time-Resolved Absorption and Photothermal Measurements with Recombinant Sensory Rhodopsin II from Natronobacterium Pharaonis. *Biophys. J.* **1999**, *77* (6), 3277–3286. https://doi.org/10.1016/S0006-3495(99)77158-4.
(24) Lutz, I.; Sieg, A.; Wegener, A. A.; Engelhard, M.; Boche, I.; Otsuka, M.; Oesterhelt, D.; Wachtveitl, J.; Zinth, W. Primary Reactions of Sensory Rhodopsins. 6.
(25) Cheminal, A.; Léonard, J.; Kim, S.-Y.; Jung, K.-H.; Kandori, H.; Haacke, S. 100 Fs Photo-Isomerization with Vibrational Coherences but Low Quantum Yield in Anabaena Sensory Rhodopsin. *Phys. Chem. Chem. Phys.* **2015**, *17* (38), 25429–25439. https://doi.org/10.1039/C5CP04353K.
(26) Briand, J.; Bräm, O.; Réhault, J.; Léonard, J.; Cannizzo, A.; Chergui, M.; Zanirato, V.; Olivucci, M.; Helbing, J.; Haacke, S. Coherent Ultrafast Torsional Motion and Isomerization of a Biomimetic Dipolar Photoswitch. *Phys. Chem. Chem. Phys.* **2010**, *12* (13), 3178. https://doi.org/10.1039/b918603d.
(27) Léonard, J.; Briand, J.; Fusi, S.; Zanirato, V.; Olivucci, M.; Haacke, S. Isomer-Dependent Vibrational Coherence in Ultrafast Photoisomerization. *New J. Phys.* **2013**, *15* (10), 105022. https://doi.org/10.1088/1367-2630/15/10/105022.
(28) Rozin, R.; Wand, A.; Jung, K.-H.; Ruhman, S.; Sheves, M. PH Dependence of Anabaena Sensory Rhodopsin: Retinal Isomer Composition, Rate of Dark Adaptation, and Photochemistry. *J. Phys. Chem. B* **2014**, *118* (30), 8995–9006. https://doi.org/10.1021/jp504688y.
(29) Ye, T.; Friedman, N.; Gat, Y.; Atkinson, G. H.; Sheves, M.; Ottolenghi, M.; Ruhman, S. On the Nature of the Primary Light-Induced Events in Bacteriorhodopsin: Ultrafast

Spectroscopy of Native and C $_{13}$ =C $_{14}$ Locked Pigments. *J. Phys. Chem. B* **1999**, *103* (24), 5122–5130. https://doi.org/10.1021/jp9846227.
(30) Ye, T.; Gershgoren, E.; Friedman, N.; Ottolenghi, M.; Sheves, M.; Ruhman, S. Resolving the Primary Dynamics of Bacteriorhodopsin, and of a `C13□C14 Locked' Analog, in the Reactive Excited State. *Chem. Phys. Lett.* **1999**, *314* (5–6), 429–434. https://doi.org/10.1016/S0009-2614(99)01125-2.
(31) Haacke, S.; Vinzani, S.; Schenkl, S.; Chergui, M. Spectral and Kinetic Fluorescence Properties of Native and Nonisomerizing Retinal in Bacteriorhodopsin. *ChemPhysChem* **2001**, *2* (5), 310–315. https://doi.org/10.1002/1439-7641(20010518)2:5<310::AID-CPHC310>3.0.CO;2-C.
(32) Haacke, S.; Schenkl, S.; Vinzani, S.; Chergui, M. Femtosecond and Picosecond Fluorescence of Native Bacteriorhodopsin and a Nonisomerizing Analog. *Biopolymers* **2002**, *67* (4–5), 306–309. https://doi.org/10.1002/bip.10092.
(33) Song, L.; El-Sayed, M. A.; Lanyi, J. K. Protein Catalysis of the Retinal Subpicosecond Photoisomerization in the Primary Process of Bacteriorhodopsin Photosynthesis. *Science* **1993**, *261* (5123), 891–894. https://doi.org/10.1126/science.261.5123.891.
(34) Briand, J.; Léonard, J.; Haacke, S. Ultrafast Photo-Induced Reaction Dynamics in Bacteriorhodopsin and Its Trp Mutants. *J. Opt.* **2010**, *12* (8), 084004. https://doi.org/10.1088/2040-8978/12/8/084004.
(35) Agathangelou, D.; Orozco-Gonzalez, Y.; del Carmen Marín, M.; Roy, P. P.; Brazard, J.; Kandori, H.; Jung, K.-H.; Léonard, J.; Buckup, T.; Ferré, N.; et al. Effect of Point Mutations on the Ultrafast Photo-Isomerization of Anabaena Sensory Rhodopsin. *Faraday Discuss.* **2018**, *207*, 55–75. https://doi.org/10.1039/C7FD00200A.
(36) Gonzalez-Luque, R.; Garavelli, M.; Bernardi, F.; Merchan, M.; Robb, M. A.; Olivucci, M. Computational Evidence in Favor of a Two-State, Two-Mode Model of the Retinal Chromophore Photoisomerization. *Proc. Natl. Acad. Sci.* **2000**, *97* (17), 9379–9384. https://doi.org/10.1073/pnas.97.17.9379.
(37) Cembran, A.; Bernardi, F.; Olivucci, M.; Garavelli, M. The Retinal Chromophorechloride Ion Pair: Structure of the Photoisomerization Path and Interplay of Charge Transfer and Covalent States. 6.
(38) Schapiro, I.; Melaccio, F.; Laricheva, E. N.; Olivucci, M. Using the Computer to Understand the Chemistry of Conical Intersections. *Photochem. Photobiol. Sci.* **2011**, *10* (6), 867. https://doi.org/10.1039/c0pp00290a.
(39) Schenkl, S. Probing the Ultrafast Charge Translocation of Photoexcited Retinal in Bacteriorhodopsin. *Science* **2005**, *309* (5736), 917–920. https://doi.org/10.1126/science.1111482.
(40) Altoe, P.; Cembran, A.; Olivucci, M.; Garavelli, M. Aborted Double Bicycle-Pedal Isomerization with Hydrogen Bond Breaking Is the Primary Event of Bacteriorhodopsin Proton Pumping. *Proc. Natl. Acad. Sci.* **2010**, *107* (47), 20172–20177. https://doi.org/10.1073/pnas.1007000107.
(41) Zener, C. Non-Adiabatic Crossing of Energy Levels. *Proc. R. Soc. Math. Phys. Eng. Sci.* **1932**, *137* (833), 696–702. https://doi.org/10.1098/rspa.1932.0165.
(42) Nikitin, E. E. N ONADIABATIC T RANSITIONS : What We Learned from Old Masters and How Much We Owe Them. *Annu. Rev. Phys. Chem.* **1999**, *50* (1), 1–21. https://doi.org/10.1146/annurev.physchem.50.1.1.
(43) Kochendoerfer, G. G. Spontaneous Emission Study of the Femtosecond Isomerization Dynamics of Rhodopsin. 7.

(44) Wand, A.; Rozin, R.; Eliash, T.; Jung, K.-H.; Sheves, M.; Ruhman, S. Asymmetric Toggling of a Natural Photoswitch: Ultrafast Spectroscopy of Anabaena Sensory Rhodopsin. *J. Am. Chem. Soc.* **2011**, *133* (51), 20922–20932. https://doi.org/10.1021/ja208371g.
(45) Schnedermann, C.; Yang, X.; Liebel, M.; Spillane, K. M.; Lugtenburg, J.; Fernández, I.; Valentini, A.; Schapiro, I.; Olivucci, M.; Kukura, P.; et al. Evidence for a Vibrational Phase-Dependent Isotope Effect on the Photochemistry of Vision. *Nat. Chem.* **2018**, *10* (4), 449–455. https://doi.org/10.1038/s41557-018-0014-y.
(46) Jung, K.-H.; Trivedi, V. D.; Spudich, J. L. Demonstration of a Sensory Rhodopsin in Eubacteria: Sensory Rhodopsin in Eubacteria. *Mol. Microbiol.* **2003**, *47* (6), 1513–1522. https://doi.org/10.1046/j.1365-2958.2003.03395.x.
(47) Sineshchekov, O. A.; Trivedi, V. D.; Sasaki, J.; Spudich, J. L. Photochromicity of *Anabaena* Sensory Rhodopsin, an Atypical Microbial Receptor with a *Cis* -Retinal Light-Adapted Form. *J. Biol. Chem.* **2005**, *280* (15), 14663–14668. https://doi.org/10.1074/jbc.M501416200.
(48) Kawanabe, A.; Furutani, Y.; Jung, K.-H.; Kandori, H. Photochromism of *Anabaena* Sensory Rhodopsin. *J. Am. Chem. Soc.* **2007**, *129* (27), 8644–8649. https://doi.org/10.1021/ja072085a.
(49) Kawanabe, A.; Kandori, H. Photoreactions and Structural Changes of Anabaena Sensory Rhodopsin. *Sensors* **2009**, *9* (12), 9741–9804. https://doi.org/10.3390/s91209741.
(50) Gueye, M. Optomechanical Energy Conversion and Vibrational Coherence in Biomimetic Molecular Photoswitches, University of Strasbourg, 2016.
(51) Cheminal, A. Processus de Conversion d'´energie Ultra-Rapide Dans Des Prot´eines Photo-Sensibles et Nanostructures Organiques `a Vis´ee Photovolta¨ıque, University of Strasbourg, 2015.
(52) Strambi, A.; Durbeej, B.; Ferre, N.; Olivucci, M. Anabaena Sensory Rhodopsin Is a Light-Driven Unidirectional Rotor. *Proc. Natl. Acad. Sci.* **2010**, *107* (50), 21322–21326. https://doi.org/10.1073/pnas.1015085107.
(53) Schapiro, I.; Ruhman, S. Ultrafast Photochemistry of Anabaena Sensory Rhodopsin: Experiment and Theory. *Biochim. Biophys. Acta BBA - Bioenerg.* **2014**, *1837* (5), 589–597. https://doi.org/10.1016/j.bbabio.2013.09.014.
(54) Birge, R. R.; Gillespie, N. B.; Izaguirre, E. W.; Kusnetzow, A.; Lawrence, A. F.; Singh, D.; Song, Q. W.; Schmidt, E.; Stuart, J. A.; Seetharaman, S.; et al. Biomolecular Electronics: Protein-Based Associative Processors and Volumetric Memories. *J. Phys. Chem. B* **1999**, *103* (49), 10746–10766. https://doi.org/10.1021/jp991883n.
(55) Lin, S. W.; Groesbeek, M.; van der Hoef, I.; Verdegem, P.; Lugtenburg, J.; Mathies, R. A. Vibrational Assignment of Torsional Normal Modes of Rhodopsin: Probing Excited-State Isomerization Dynamics along the Reactive C_{11} C_{12} Torsion Coordinate. *J. Phys. Chem. B* **1998**, *102* (15), 2787–2806. https://doi.org/10.1021/jp972752u.
(56) Gervasio, F. L.; Cardini, G.; Salvi, P. R.; Schettino, V. Low-Frequency Vibrations of *All - Trans* -Retinal: Far-Infrared and Raman Spectra and Density Functional Calculations. *J. Phys. Chem. A* **1998**, *102* (12), 2131–2136. https://doi.org/10.1021/jp9724636.
(57) Wand, A.; Loevsky, B.; Friedman, N.; Sheves, M.; Ruhman, S. Probing Ultrafast Photochemistry of Retinal Proteins in the Near-IR: Bacteriorhodopsin and Anabaena Sensory Rhodopsin vs Retinal Protonated Schiff Base in Solution. *J. Phys. Chem. B* **2013**, *117* (16), 4670–4679. https://doi.org/10.1021/jp309189y.

(58) Kraack, J. P.; Buckup, T.; Hampp, N.; Motzkus, M. Ground- and Excited-State Vibrational Coherence Dynamics in Bacteriorhodopsin Probed With Degenerate Four-Wave-Mixing Experiments. *ChemPhysChem* **2011**, *12* (10), 1851–1859. https://doi.org/10.1002/cphc.201100032.
(59) Kim, J. E.; Mathies, R. A. Anti-Stokes Raman Study of Vibrational Cooling Dynamics in the Primary Photochemistry of Rhodopsin. *J. Phys. Chem. A* **2002**, *106* (37), 8508–8515. https://doi.org/10.1021/jp021069r.

Part IV

ASR mutants

4.1 Point mutations on RP's environment - Motivation

In the previous chapter, our study on WT ASR revealed significant differences between the two PSBR conformers (AT- and 13C-) in terms of ESL and isomerization yield. The origin of those differences is most probably associated with the electrostatic and steric interactions between the chromophore-protein pair, but the torsional twist of 13C in the ground state was also invoked[1], in analogy to the ultrafast ESL afforded by 11-cis PSBR in rhodopsin. In this chapter, our study is focused on point mutated proteins, where the variable is the environment of the surrounding protein. Our assumption here is that a single residue replacement in the binding pocket will not have an effect on the whole protein's structure but the effect will be local, in the vicinity of PSBR. The latter effect will be coordinated by the residue's electrostatic or steric hindrance.

Similar studies on mutated BR[2,3] have shown significant differences holding both for GS and ES properties. Particularly, a shift of the absorption maxima by ~40nm was observed accompanied with a ~20 fold increase of the ESL[2]. It was shown that the differences are enhanced when a replacement of polar residues with neutral ones takes place, making the point that electrostatic interactions are responsible both for increasing the ESL and for tuning the absorption maximum.

Concerning ASR, there are at least ~10 mutants where modifications in the binding pocket leads to an almost ~40nm blue-shift of the absorption maximum (for AT-PSBR). Computational work addressing the origin of these shifts has been already reported[4,5] and, apart from a systematic protein-independent overestimation of the computed transition energies, a very good agreement of the computed and observed values was found. This proves the adequacy and accuracy of the combined CASSCF/CASPT2 methods employed by our partners (M. Olivucci and N. Ferré). Hence, in this section we will refer on three particular mutants for providing more information concerning the ESL for both isomers. Part of our study concerning the W76F, V112N and L83Q mutants has already been reported[6]. Here we show an extended version analogous to the case of WT-ASR where we try to retrieve GS information for both isomers using S.S absorption and HPLC and the ES information in terms of lifetime by T.A spectroscopy (monitoring the SE contribution).

4.2 Steady State information of ASR mutants

The ground state absorption spectra for DA and LA states of WT-ASR, W76F, V112N and L83Q mutants are shown in figure 52. The DA spectra are normalized to 1.0, since the extinction molar coefficients were not available, and the LA spectra are plotted with the experimental relative reduction in absorbance. The light adaptation of the proteins was carried out using an orange or a blue LED, in order to retain the highest 13C ratio in the particular state. Table 5 summarizes the wavelengths of absorption maxima, the isomer composition, as well as the absorption maxima of the isomer specific spectra (shown in Annex.B.I) obtained after linear decomposition (see section 3.5).

The data show a blue-shift of the absorption maxima of all mutants with respect to the DA and OA states of WT-ASR. Particularly, the DA states where the AT-PSBR is purely present (>97%), this blue shift reaches up to ~33nm for the case of L83Q mutant. The analogous shift in the case of W76F and V112N is ~21nm and ~18nm respectively. Supplementary, the LA states where 13C isomer contribution is dominant (>56%), we observe shifts relative to the DA states reaching up to ~8nm for the case of W76F in the most extreme case. The shift for the other two cases is less pronounced, with a ~2nm shift for V112N and ~3nm one for the L83Q mutant, surprisingly towards longer wavelengths. While in the case of WT-ASR the relative shift of the absorption maxima between AT and 13C isomers is ~ 13nm, in the case of the mutants only W76F shows a similar behavior with ~15nm. Complementary, V112N and L83Q exhibit a ~5nm and ~6nm shift respectively.

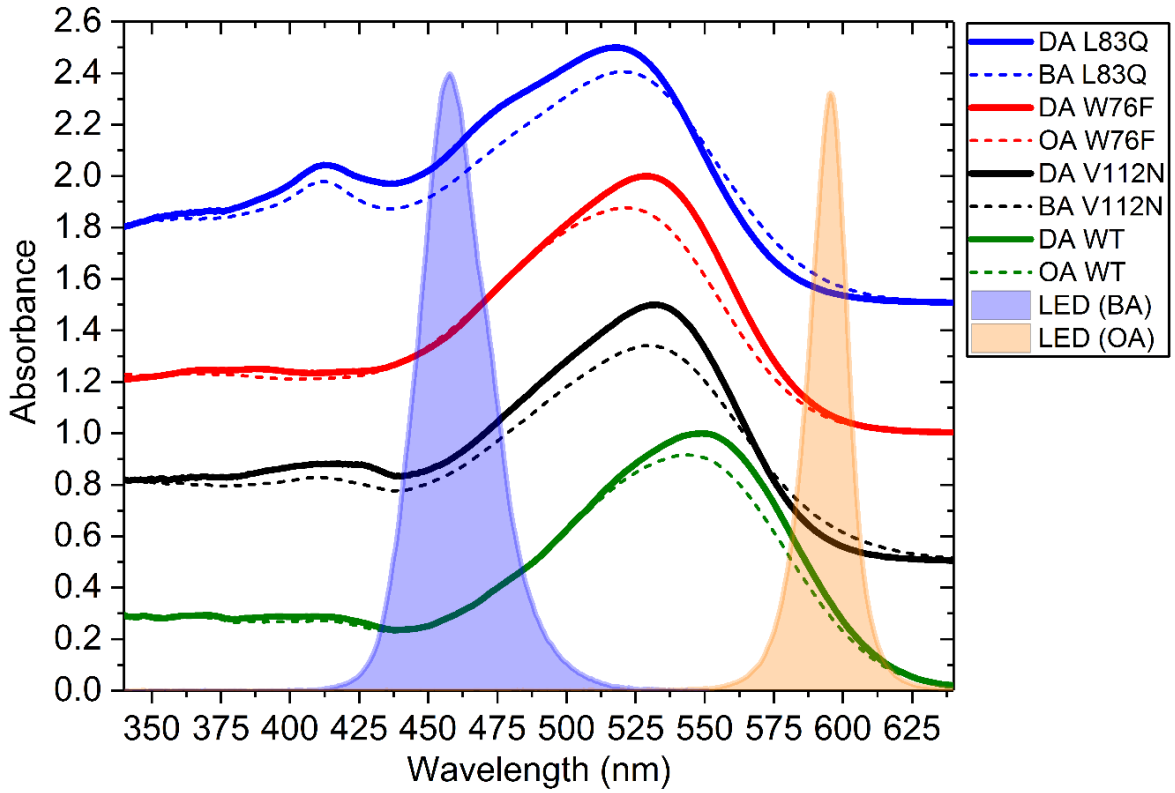

Fig. 52: Normalized ground state absorption spectra of light- and dark-adapted WT-ASR (green) and the three mutants W76F (red), V112N (black) and L83Q (blue). Spectra are vertically shifted by multiples of 0.5 units; Solid and dashed lines correspond to the DA and OA states respectively; The spectral intensity distributions of the OA and BA LED's used for light adaptation are displayed in orange and blue respectively.

Table 5: Ground state isomeric composition for ASR samples and absorption maxima

Sample	State	AT (%)	13C (%)	Abs max (nm)	Calculated Abs max (nm)
WT	DA	97±1	3±1	550±1	
	OA	41±1	59±1	543±1	
	AT			550±1	544
	13C			537±1	525
W76F	DA	97±1	3±1	529±1	
	OA	42±1	58±1	521±1	
	AT			529±1	510
	13C			514±1	499
V112N	DA	98±1	2±1	532±1	
	BA	42±1	58±1	530±1	
	AT			532±1	513
	13C			527±1	512
L83Q	DA	98±1	2±1	517±1	
	BA	44±1	56±1	520±1	
	AT			517±1	509
	13C			523±1	518

In order to understand the origin of the observed shifts at the atomic level we need support from the theoretical point of view. In this framework, we collaborate with the group of Prof. Massimo Olivucci who designed the QM/MM models of ASR and computed the corresponding S_0-S_1 transition energies of the PSBR for WT-ASR and the mutants (work of M. del Carmen Marín and Y. Orozco-Gonzalez). The semi-automatic ARM[7] protocol used employs the multi-configurational complete active space self-consistent field (CASSCF) method to obtain the ground state geometries. Then the excitation energies are computed using multi-configurational second-order perturbation theory (CASPT2) to recover the missing dynamical electron correlation associated with the CASSCF description.

The distribution of positive charge in S_0 and S_1 are shown in figure 53 top, according to calculation from the group of M. Olivucci and others[6]. In S_0 the PSB moiety is protonated, while in the S_1 case the positive charge is partially distributed along the chromophore's backbone and towards the β-ionone ring. The latter induces a large dipole moment change (~10-30D[8]) leading to the S1 state being characterised as a charge transfer state (CTS). Moreover, the structure of AT-PSBR with the corresponding residues upon mutation are displayed from A-D. A direct comparison of the mutants with WT-ASR, helps to understand the effect of the dipole moment introduced by the mutated residues, particularly whether it corresponds to a red or blue shift of the absorption maximum.

It was shown in Ref. 6 that the spectral shift of the S0→S1 transition is largely dominated by electrostatic interactions. In wild-type ASR (A), the positions 76, 83 and 112 correspond to the hydrophobic residues of Tryptophan, Leucine and Valine. While Valine and Leucine do not carry any dipole moment; meaning that the electrostatic effect on the PSBR is small, Tryptophan has a small dipole moment. The absorption maximum of WT AT-PSBR, located at 550nm, is the result of the interaction of the modified retinal binding pocket with the charged PSB moiety (S_0) and the S_1 dipole moment change. The replacement of Tryptophan

with the Phenylalanine residue (B) shifts the absorption maximum to 529nm (W76F). Phenylalanine residue removes a dipole moment vector which in WT ASR was stabilizing S_1 with respect to S_0. The latter leads to a blue shift with respect to WT ASR. Moving now to the case where the mutation is in the vicinity of the β-ionone ring, Asparagine (C) which is a polar residue, introduced a dipole moment in an orientation that blue shifts the absorption maximum by 18nm. Using the crystallographic structure of WT-ASR we can estimate the distance of the polar side chain of Asparagine with respect to the positive charge located at the SB and with respect to the β-ionone ring. Particularly, we estimate a ~4Å distance with respect to the ionone head and ~15Å with respect to the SB (figure in Annexe IV). Finally, in the case where Leucine is replaced by Glutamine (polar), the mutation is in the vicinity of the SB (~5Å with respect to the sidechain). The O-H has its negative end pointing towards the protonated SB nitrogen, stabilizing in this way S_0 and generating a ~33nm blue shift with respect to WT ASR.

The calculated values for the S0-S1 transitions for WT ASR and the mutants are summarised in Table 5. The trend for the absorption maxima is reproduced with a small overestimation of the absolute values, which is a systematic error in this kind of calculations. A figure comparing the computed and experimentally determined values of the absorption maxima is shown in Annexe.B.I.

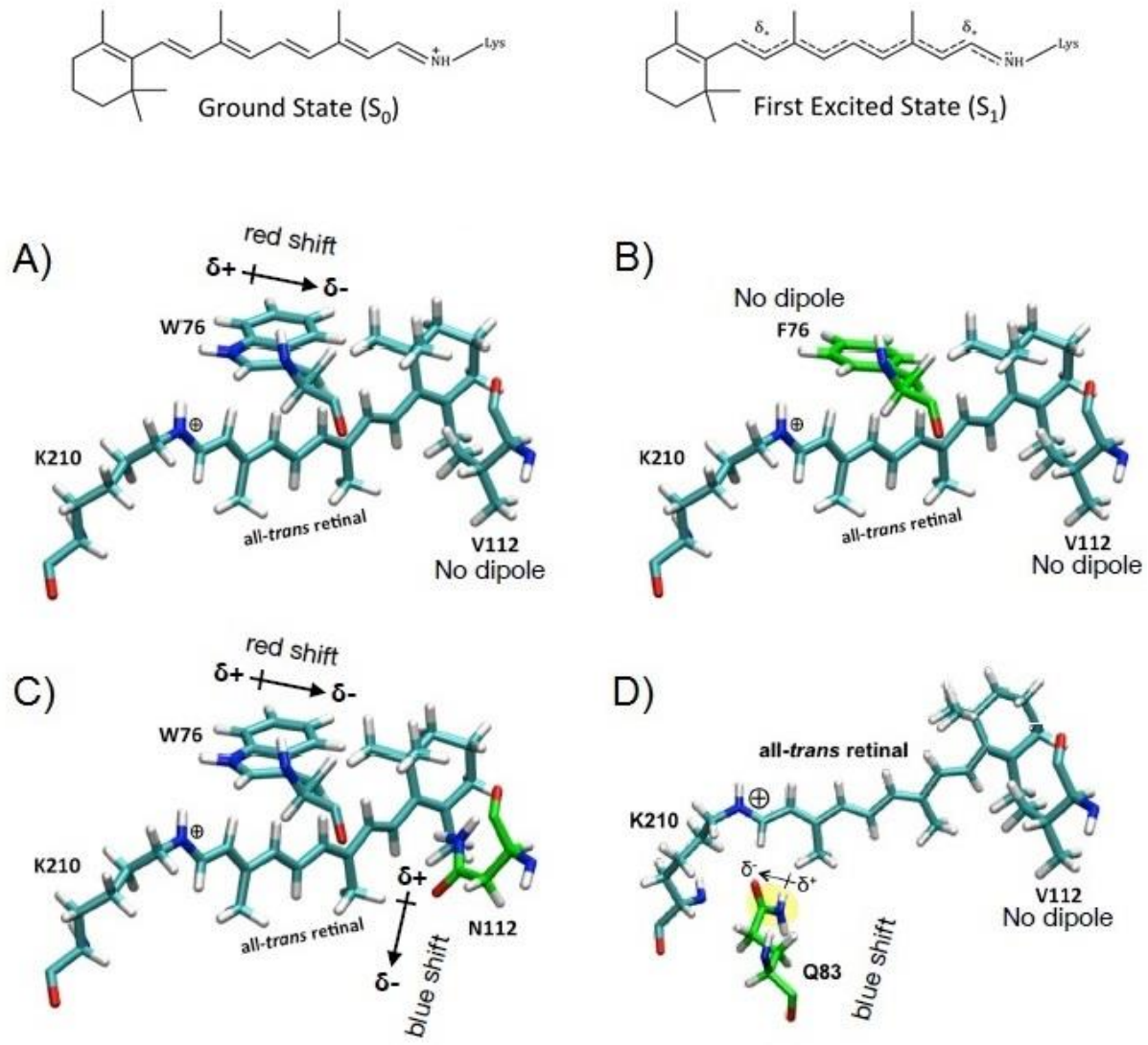

Fig. 53: Orientation of the dipole moments induced by the replacing residues upon mutation responsible for the shifts of the absorption maxima in the case of AT-PSBR for the case of WT (A), W76F (B), V112N (C) and L83Q (D); The mutations are shown highlighted in each case with the appropriate dipole moment induced and the corresponding effect of shift (red or blue). The electronic distribution of the S0 and S1 are shown on the top of figure; In S0, the PSB linkage of Lysine residue and the retinal chromophore is protonated. Photo-excitation in S1, and the subsequent C=C bond length alternation leads to a partial charge transfer of the positive charge towards the β-ionone ring.

4.3 Determination of ESL of AT-PSBR in ASR mutants

We have carried out several TAS experiments on these three mutants probing in the 330-800 nm range. The characteristic lifetimes derived were reported in Ref. 6 and in several contributions to conferences (Ultrafast Phenomena proceedings). Similar to wt-ASR, prominent dynamics spectral shifts as well as overlapping bands (e.g. ESA/GSB and ESA/PA) are observed. Hence, the determination of ESL is best done by recording the "pure" SE contributions appearing in the NIR spectral range (820nm-1400nm). Here we have performed a series of T.A experiments on DA and LA mutant proteins of ASR to see the effect of the environment on the reaction dynamics of PSBR.

In each case the excitation wavelength was adjusted to be on the low energy side of the absorption maxima, i.e 540nm for L83Q, 545nm for W76F and 548nm for V112N. The

excitation energy used in these experiments was not exceeding 50nJ (150μm spot size), maintaining our experiment in the linear excitation regime. This was cross-checked by running a couple of acquisitions with a pump intensity attenuated by a factor of ~4 (OD filter of 0.6), with the normalized dynamics being overlapped.

To have a direct comparison between the different mutants we show individual wavelength kinetic traces for the DA state of WT ASR and mutants, where the AT-PSBR exceeds 97% (figure 54). The fitting procedure yields two exponential decays for all cases ranging from (0.28-0.53) ps for the short constant and (1.1-2.0) ps for the longer one. The amplitude of the short constant has a dominant >70% contribution for all cases. Moreover, the ESL is determined as the weighted average of the two time constants. A summary of the results obtained from global fit is presented in table 6.

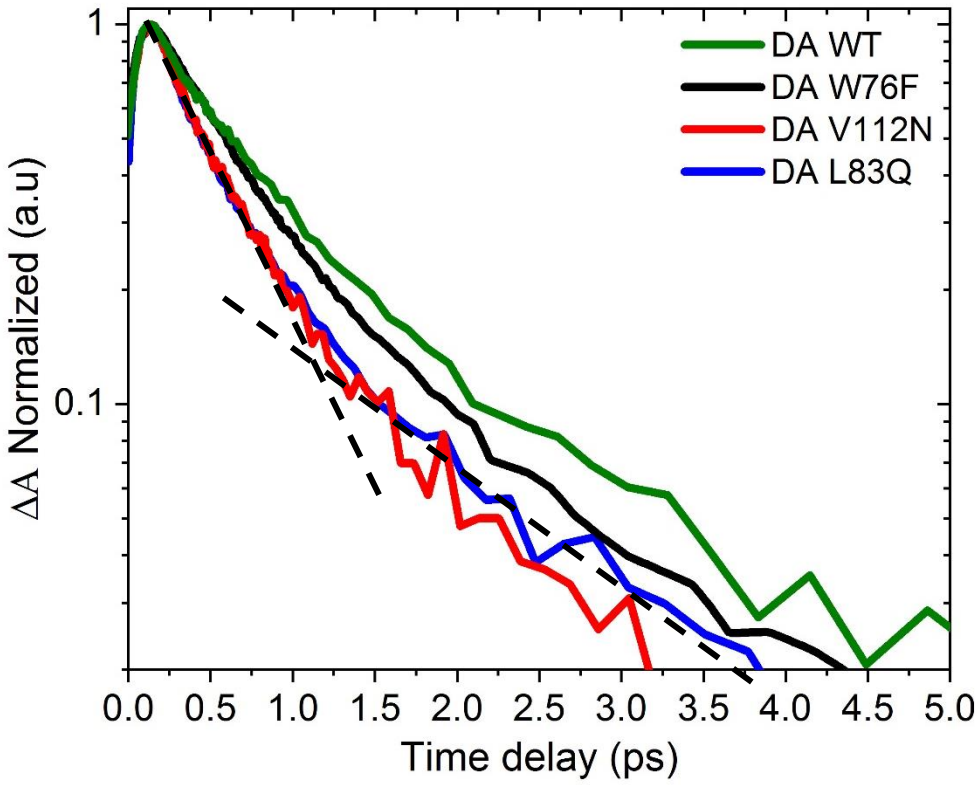

Fig. 54: Normalized kinetic traces from individual wavelengths of SE for DA WT ASR and mutants. The semi-log plot directly shows the ESL shortening due to the point mutations and highlights the bi-exponential character of the SE decay (see grey dashed lines).

The semi-logarithmic plot shown in figure 54 shows that the slowest population decay from the first excited state belongs to WT-ASR case while the fastest one to L83Q mutant. An equivalent fast decay is observed for the case of V112N mutant defined within the error bar of the measurements. In addition, W76F shows an intermediate behaviour with a behaviour closer to WT's rather than the other two mutants. The determined ESL values are 0.83ps, 0.70ps, 0.52ps and 0.48ps for WT, W76F, V112N and L83Q respectively.

This ~2 fold reduction in ESL observed for AT- L83Q with respect to AT-WT is a clear sign that the protein environment modifies the shape of the PSBR potential energy surfaces. One explanation for the latter result is based on the S1/S2 electronic mixing, resulting in a faster

or slower isomerization reaction. The following theoretical description of the photochemical reaction has been provided by Prof. Olivucci (work of M. del Carmen Marín and Y. Orozco-Gonzalez).

Table 6: Summary of global fit parameters for DA WT ASR and mutants

Sample	a1 (%)	τ1 (ps)	a2 (%)	τ2 (ps)	ESL (ps)
DA WT	72	0.53	28	1.64	0.83
DA W76F	86	0.50	14	1.86	0.70
DA V112N	80	0.34	20	1.27	0.52
DA L83Q	79	0.28	21	1.26	0.48
error		±0.04		±0.2	±0.05

4.4 Tuning of isomerization reaction according to S1/S2 electronic mixing

The explanation concerning the S1/S2 electronic mixing is based on the electronic structure of the polyene chain of the retinal chromophore featuring 5 conjugated double bonds (PSB5) as shown in figure 55A. It shows the diabatic states associated with the electronic characters (1Ag, 1Bu and 2Ag) dominating the S_0, S_1 and S_2 equilibrium structures of PSB5. The corresponding charge distribution associated with the –CH-CH-CH-CH-NH_2 moiety on the S_0, S_1 and S_2 is shown on the right. In addition, the bond length distance for each C-C pair is given in Å.

Starting from 1Ag (historic labelling, even though PSBR does not have C_{2v} symmetry), which corresponds to S_0, we observe that the positive charge is mainly located on the –C=NH_2 moiety, meaning the proton is localized on the N, as expected. On contrary, in ^1B_u the positive charge is spread over the conjugated chain; only 49% of positive charge is located on the -NH_2 half). In addition, in the $1B_u$ the bond length alternation (BLA) is almost complete, i.e. the C13-C14 bond has a single bond character (1.46Å with respect to 1.38Å in 1Ag case) allowing in this way the isomerization to occur. Thus 1Bu has a reactive character in terms of isomerization. Moreover, 2Ag appears to show a charge distribution similar with 1Ag, with the charge mainly located on the –C=NH_2 terminal and the C13-C14 bond appearing with an only slightly reduced double bond character. From the latter, we understand that 2Ag has a non-reactive character and is not connected with the isomerization reaction but is rather associated with a diradical. Depending on the mixing between the reactive character of 1Bu and the non-reactive character of 2Ag, as a function of torsion or dihedral angle changes leading to isomerization (e.g. concerted and aborted bicycle pedal motion) the S1 PES can be modified accordingly with the presence or not of an energy barrier.

Figure 55B shows two opposite cases where the S1 is dominated by a 1Bu character (left) and one where 1Bu/2Ag mixing occurs in such a way that a barrier is formed (right, dashed lines corresponding to diabatic states). In the case described on the left the S1 PES is barrier-less allowing the isomerization to occur faster with respect to the case on the right where the presence of the barrier will slow down the process.

As detailed QM/MM calculations showed, the first one suits the case for AT-PSBR in L83Q while the second one the AT-PSBR behavior in WT-ASR.

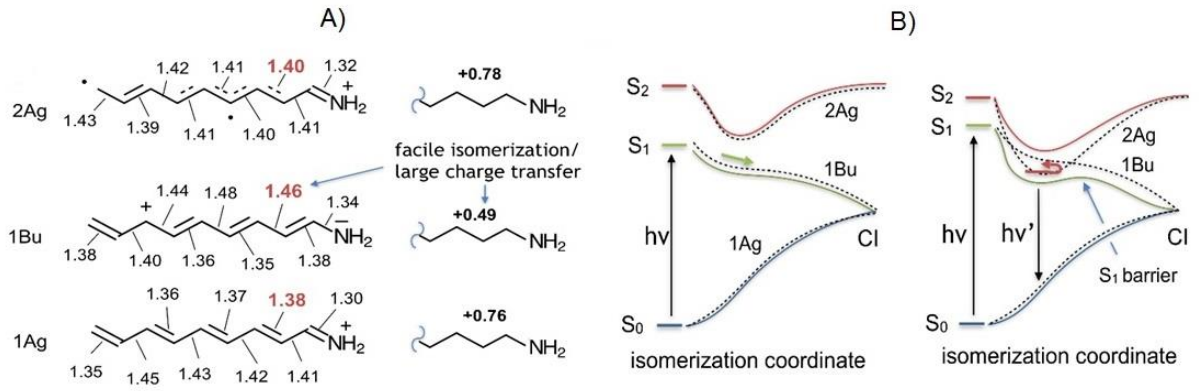

Fig. 55 : A) Electronic and bonding structure of the retinal chromophore. Left. Resonance formula associated with the electronic characters (1Ag, 1Bu and 2Ag) dominating the S_0, S_1 and S_2 equilibrium structures of PSB5. The bond lengths are given in Å. Right. Total positive charge located on the $-CH-CH-CH-CH-NH_2$ moiety on the S_0, S_1 and S_2. B) Schematic S_0, S_1 and S_2 energy profiles along the S_1 PES path driving the chromophore S_1 isomerization. An S_1 PES dominated by a 1Bu character (left) is associated with a barrier-less path while a mixed 1Bu/2Ag character (right) is associated with the presence of a barrier along the path. The dashed energy profiles represent the energy of diabatic states corresponding to "pure" 1Bu and 2Ag electronic characters.

Indeed, figure 56 shows Franck-Condon semi-classical trajectories starting 15fs after the initial relaxation, which describe the scenario for L83Q (fig.56A) and WT (fig.56B) cases. Particularly, in the L83Q trajectory we see that after BLA occurs until the 50fs, S_1 and S_2 start to separate with S_1 downshifting and reaching the CI within 110fs. The glutamine residue at position 83 is responsible for the latter dynamical S1 decrease in energy, as it stabilizes an increment of charge transfer character in the S1 state. Indeed, details retrieved from the simulations show that the motion associated with the PSBR dihedral angle changes and dynamic reorientation of Q83 stabilize energetically a situation with a reduced positive charge on the Schiff base. This dynamic structural change inverts the situation with respect to the unexcited ground state situation, for which we invoked that the attractive interaction of the Schiff base with the neg. carboxylate end induces the blue-shift of absorption.

On the contrary, in WT ASR the result is different as the L83 residue does not appear to have the same effect. The S1/S2 mixing remains until the end of the 200fs simulation time resulting in an isomerization on a longer time scale as previously described by the experimental results. In other words, there is no discrimination in terms of potential energies for the different charge distributions of S_1 and S_2.

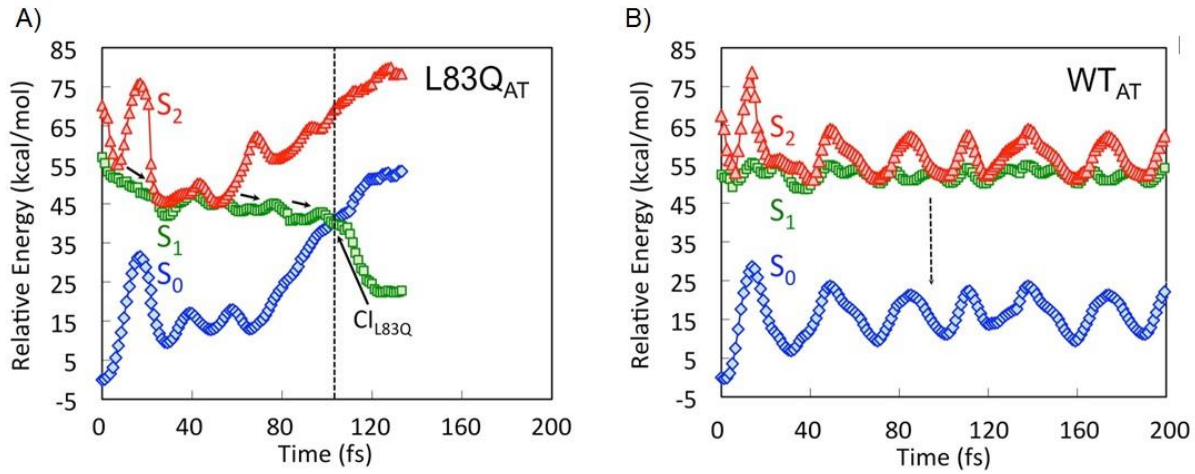

Fig. 56: Trajectory computation on S_1. (A) and (B) QM/MM FC trajectories of L83Q and WT ASR, computed at two-root state-averaged-CASSCF/AMBER level of theory and corrected at the CASPT2 level. S_0 (blue diamonds), S_1 (green squares) and S_2 (red triangles) CASPT2/CASSCF/AMBER energy profiles along the Franck-Condon trajectories.

4.5 Determination of excited state lifetime of 13C-PSBR of ASR mutants

The disentanglement procedure used for retrieving the pure 13C-PSBR in each experiment was the same as described in the previous chapter for WT-ASR. The HPLC measurements for the precise ground state isomeric content in each sample used for this procedure is shown in Annexe B.II.

Figure 57 shows the normalized SE dynamics (903nm) for DA, OA and 13C-PSBR of W76F mutant. From a direct comparison between DA and OA states we observe differences in the >0.5ps timescale with the OA dynamics becoming slower. Indeed, the presence of this longer component leads to slower dynamics for 13C-PSBR as can be seen from the dotted blue curve. This is the opposite behavior from what we observed for WT-ASR where the 13C isomer appeared to have ~5x shorter ESL with respect to AT.

The result from the fitting procedure (shown in Annexe B.IV) supports the presence of three exponential components for 13C dynamics. Particularly, a 0.18ps, 2.48ps and a longer 18.8ps components reproduce the experimental data with the amplitudes being 53%, 42% and 5% respectively. The determination of the longer time constant lies within a ±5ps range since the data are recorded only until 16ps. However, the ESL from the weighted average results in a (2.1±0.3)ps value for the ESL, which is ~3 times longer than the AT case. We see that the replacement of the tryptophan residue at position 76 with phenylalanine has the opposite effect for 13C than for AT-PSBR in WT. It reduces the portion of 13C molecules able to isomerize within < 0.2 ps and enables most probably a 13C configuration, which appears to be sterically hindered.

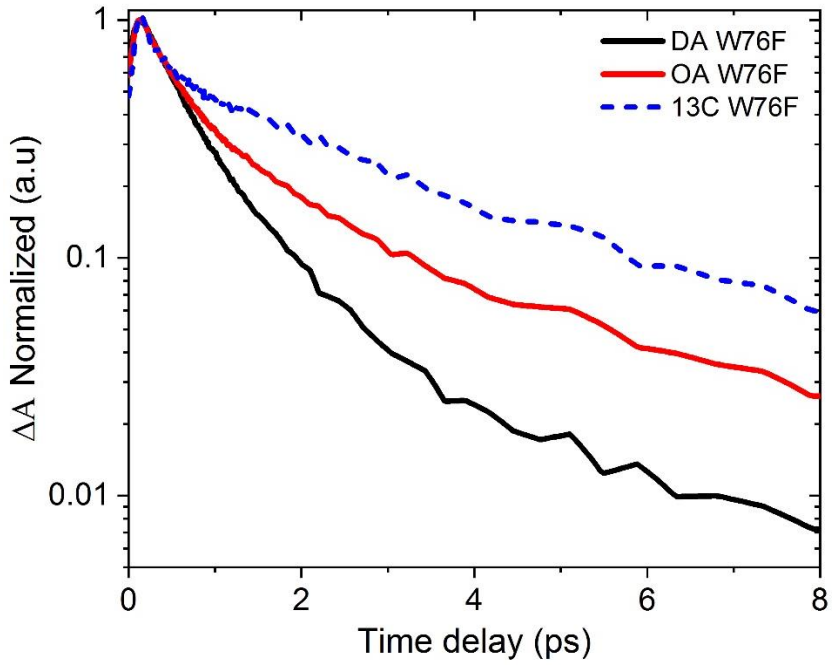

Fig. 57: DA (black), OA (red) and 13C-PSBR dynamics of W76F mutant probed at 903nm. The dynamical behaviour in the OA data supports that 13C-PBSR will have a longer ESL than the AT-PSBR. The recoding window of 16ps was not enough to follow the full decay for 13C case. The semi-log plot highlights the amplitude of the ~2.5ps time constant in the OA and 13C-PSBR dynamics.

Figure 58A shows the dynamic behavior of DA, BA states and 13C-PSBR of V112N mutant. Here the situation is different than in W76F case, as the presence of 13C isomer in the BA state results in faster dynamics with respect to the DA state. The pure 13C contribution shows an even faster decay with the global fit resulting in two exponential decays with 0.23ps and 1.17ps time constants. The amplitude on the short constant is accompanied with a ~80% amplitude yielding a 0.41ps value for the ESL. The latter corresponds to a ~20% decrease in comparison with the AT isomers ESL, suggesting that asparagine residue at position 112 implies a similar effect on 13C isomer's reaction dynamics as does for the AT case.

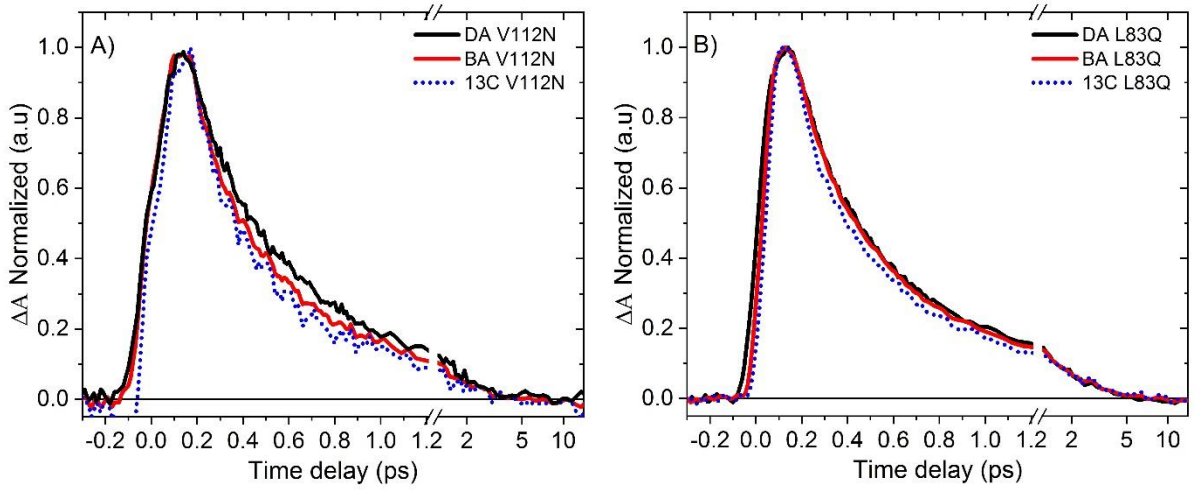

Fig. 58 : DA (black), BA (red) and 13C-PSBR dynamics of V112N A) and L83Q B) mutants probed at 921nm. The dynamical behaviour in the BA data supports that 13C-PBSR in V112N and L83Q will have a slightly shorter ESL than the AT-PSBR.

Analogous to the previous, figure 58B shows the T.A data for the L83Q mutant. The dynamics of the BA state are almost overlapped with those of DA state. The disentanglement procedure reveals the 13C contribution, which appears to have slightly faster dynamics, with the effect being even less pronounced than in the case of V112N mutant. From the fit we obtain a 0.28 and a 1.5ps constants with an 80% amplitude on the short time constant. The latter results in the weighted average 0.52ps constant for the ESL. The ESL for 13C mutant is the same as the one of AT, within the error bars (±0.05). Similarly to the case of V112N, the mutation does not have a significant effect on the dynamics of 13C as compared to AT. However, it is more likely that the replacement of Leucine's residue with Glutamine does not enhance further the reactive character of S1 state.

Figure 59 shows the 13C-PSBR dynamics for WT ASR and the three mutants. In contradiction with DA dynamics (AT-PSBR), the fastest decay is found for WT ASR expressed through an ESL of 0.19ps. Surprisingly, the W76F mutant appears to have the slowest dynamic behavior with an ESL increase reaching up to 1 order of magnitude (2.1ps), as compared to WT ASR. In addition, V112N and L83Q mutants show an intermediate-similar behavior, with the ESLs corresponding to 0.41ps and 0.52ps respectively. A summary of the global fit results concerning the 13C-PSBR of WT ASR and the three mutants is shown in table 7.

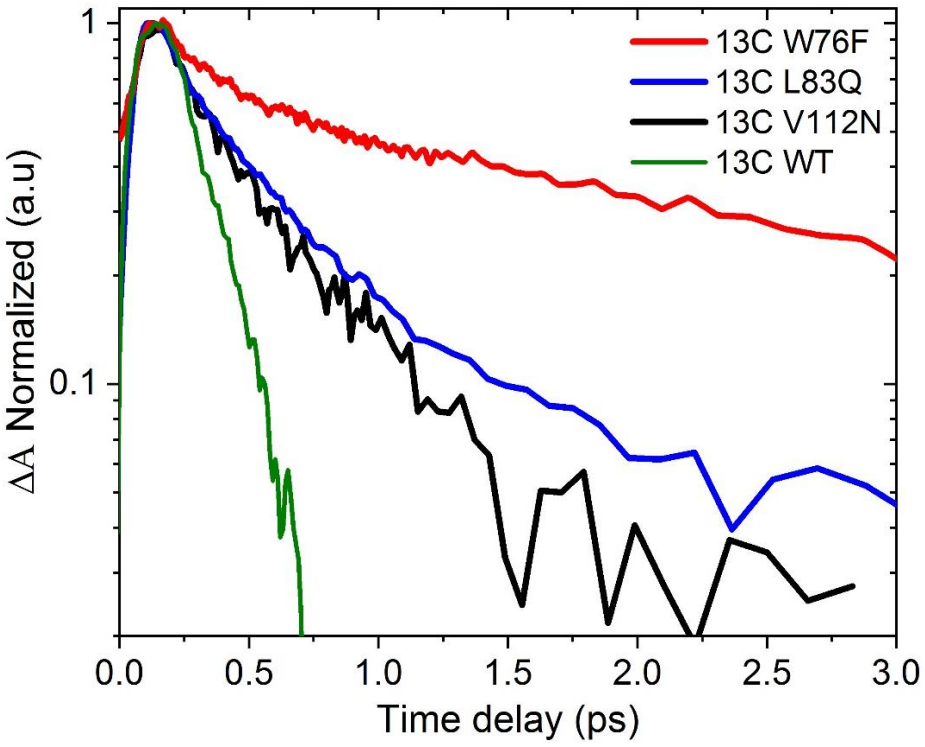

Fig. 59 : Normalized kinetic traces from individual wavelength of SE for 13C-PSBR in WT ASR and mutants

Table 7: Summary of global fit parameters for 13C-PSBR for WT ASR and mutants

Sample	a1 (%)	τ1 (ps)	a2 (%)	τ2 (ps)	a3 (%)	τ3 (ps)	ESL (ps)
13C WT	100	0.19	-	-	-	-	0.19**
13C V112N	80	0.23	20	1.17			0.41
13C L83Q	81	0.28	19	1.50			0.52
13C W76F	53	0.18	42	2.48	5	19	2.1*
error		±0.04		±0.2		±5	±0.05

* the error for this constant is ±0.3ps

** the fit yielded an additional 1.9ps constant with opposite amplitude, which was neglected

4.6 UV-Vis TAS data of DA mutants

In this section we comment on the reaction kinetics of the all-trans species on the DA mutants for the UV-Vis spectral range. Figure 60 shows the TAS 2D maps for W76F (A) and L83Q (B) where the ESA, GSB, PA and SE contributions are present. The signatures presented in this spectral region are similar to what was presented in chapter 3 for WT-ASR, but with a relative shift blue shift according to the shifted GS absorbance (section 4.2).

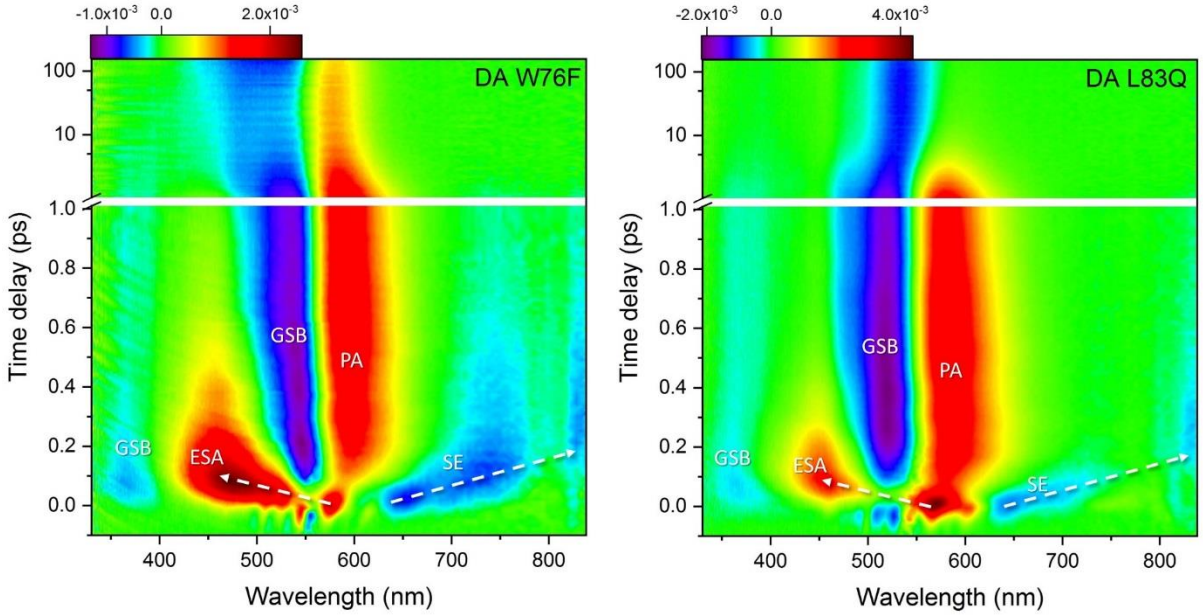

Fig. 60 : Transient absorption maps of DA states of W76F (A) and L83Q (B) proteins. The excited state fraction of ATC isomer is >97% in both cases. The signatures of ESA,GSB, PA and SE are indicated in the figures; White dashed-lines show the prominent blue and red shift of ESA and SE respectively within 200fs window; The colour bar on top of each map shows the scale for ΔA magnitude.

Selected time-resolved spectra for delays between 40 fs and 1.0 ps, and longer than 140 ps are presented in figure 61. Until 100–150 fs, the spectra show a prominent ESA in the range

from 420 to 620 nm, and SE beyond 630 nm. Complementary, an ESA appearing in the 740nm-810nm range, splits the broad SE. During this early time period, significant dynamic spectral shifts are observed redistributing the ESA spectral intensity to shorter wavelengths, and allowing for the ground state bleach (GSB) to show up progressively as a trough in the ESA). Simultaneously, the SE red-shifts towards NIR as high-lighted in figure 60 by dashed arrows. This initial phase of relaxation (<0.1 ps) is attributed to excited state relaxation, most likely due to C=C bond length alternation and IVR. GSB is observed at all delay times at wavelengths shorter than 400 nm. After 100 fs, the ESA and SE globally decay in amplitude, indicating excited state decay due to isomerization. In contrast, the spectral range between 570 and 670 nm, now displays an increasing differential absorption, consistent with the formation of the J_{AT} photo-product, as reported for WT-ASR[1,9].

The high-energy part of ESA, 400–500 nm, continues decaying and slightly blue-shifting until 1.0 ps. It is not clear, whether the remaining amplitude at 430–450 nm is ESA or part of the GS-J_{AT} difference spectrum, slowly decaying on a ps timescale. The spectral overlap of ESA and J_{AT}, throughout the entire 420–620 nm range, makes difficult our attempt for determination of the ESL. For the latter, we relied on the SE data recorded in the NIR region (section 4.3). Nevertheless, a careful analysis of the TAS transients for the determination of the isomerization reaction time (IRT) can be obtained, by looking at the photoproduct formation. The photoproduct rise has to be consistent with the ESL determined from SE contributions.

After the vibrational cooling occurs (spectra not shown) in the ps time scale the long differential spectrum is formed. The latter corresponds to the K-GS transition and is represented by the >140ps differential spectrum in figure 61. Likewise the case of WT-ASR, it can be used for determination of the isomerization quantum yield. However, the extinction molar coefficients for the GS and K species are not provided and thus we do not discuss it further in this thesis.

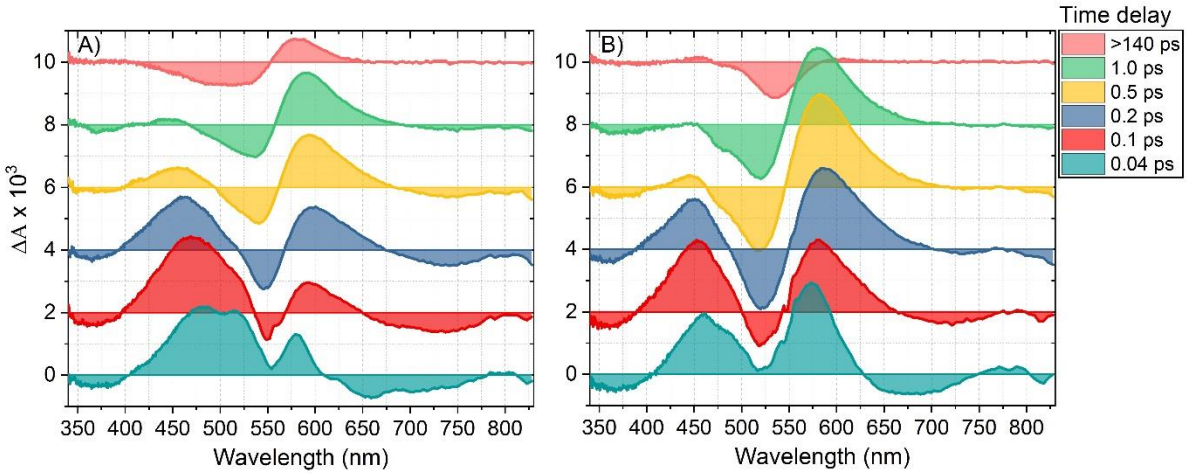

Fig. 61: Time-resolved TAS spectra for DA states of W76F (A) and L83Q (B) for high-lighting delays up to 1ps and a long-time, 140ps, GS-K difference spectrum. Note the prominent spectral shifts of ESA, GSB and SE in the first 200fs.

4.7 Vibrational coherences in mutated proteins

In chapter 3 where WT's data were presented, we observed low frequency oscillations superposed on the electronic dynamics. These oscillations correspond to specific vibrational modes present in both isomers dynamics but with the central frequencies shifted by 5-15cm^{-1} in the case of light-adapted proteins. Here we want to identify vibrational modes present in DA and LA mutated proteins and see differences or similarities between them. For this purpose, we have performed T.A spectroscopy with detection in the UV-Vis spectral range using sub-50fs excitation pulses. The pulses were centered at 545nm for V112N and 540nm for L83Q and W76F respectively.

An example of the data treatment is shown in figure 62. Panel A shows a kinetic trace of DA W76F (circles) fitted using a bi-exponential (red); the residuals of the fit are shown as a blue line. Panel B shows the FFT of the residuals, where each peak corresponds to the activity of a certain vibrational mode. Our interest is focused on low frequency modes <400cm^{-1} and thus any kind of noise on our data will appear as high frequency contribution on the FFT plot. To cancel out this noise we fit individually a series of kinetic traces around the central probe wavelength (fig.62C) and by averaging the noise is reduced. Then we apply an FFT on the averaged residuals as shown in fig.62D.

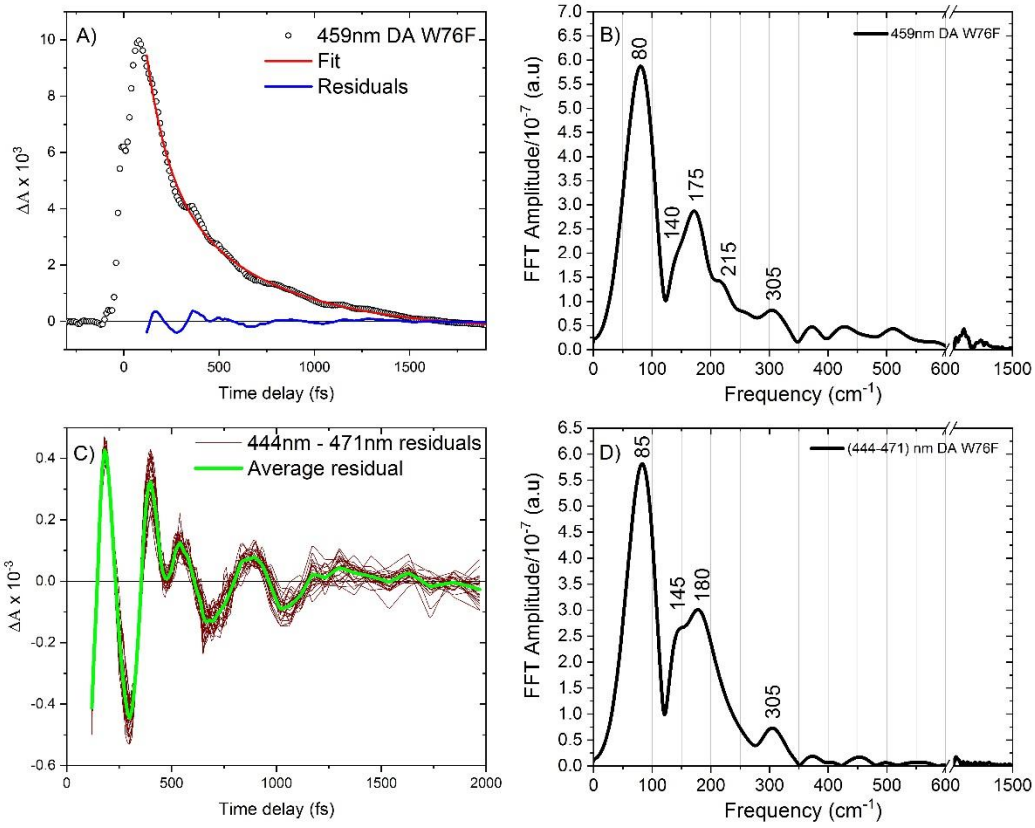

Fig. 62: Procedure for extracting oscillations from T.A data. A) Kinetic trace at 459nm of DA W76F; Black circles correspond to the experimental data while red and blue solid lines to fit and residuals respectively. B) FFT of residuals determined from A). C) Residuals of kinetics traces in the range of 441nm-471nm (lines with wine color) and average (light green). D) FFT of residuals average from C). A break is used to show the defined noise floor which here is the amplitude of peaks >1100cm^{-1}.

We start our discussion by comparing the results of W76F DA and OA proteins, shown in figure 63. Panels A and C correspond to the FFT spectra from the fit residuals of the ESA contribution. For the case of DA proteins we identify four main peaks located at 85cm^{-1}, 145cm^{-1},180cm^{-1} and 305cm^{-1}. The latter frequencies were also presented in DA WT's data attributed to skeletal torsion of the polyene (85cm^{-1}) and delocalized torsions (100cm^{-1} - 320cm^{-1}). The same plot for OA proteins (panel C) shows small differences, with the 180cm^{-1} and 305cm^{-1} modes becoming 190cm^{-1} and the 295cm^{-1} respectively. The presence of a small in amplitude mode located at 250cm^{-1} is not present in DA data, who is most likely hidden under the much higher and broader 180cm^{-1} peak. Analogous to the ESA, the results for ESA/PA region are shown in panels B and D for DA and OA proteins. While in the case of DA we observe the 145cm^{-1} and 180cm^{-1} modes; presented also in ESA, the lowest frequency mode shifts by ~20cm^{-1} resulting to a 65-70cm^{-1} (~450-500fs period). The highest frequency mode is now located at 290cm^{-1} (~120fs period). In addition, the data for OA case, suggest the presence of a mode at 275cm^{-1}, ~15cm^{-1} redshifted with respect to DA case. Beside the 70cm^{-1} no further information can be extracted due to the lower quality of the data (evidenced by the peak ~1000cm^{-1}).

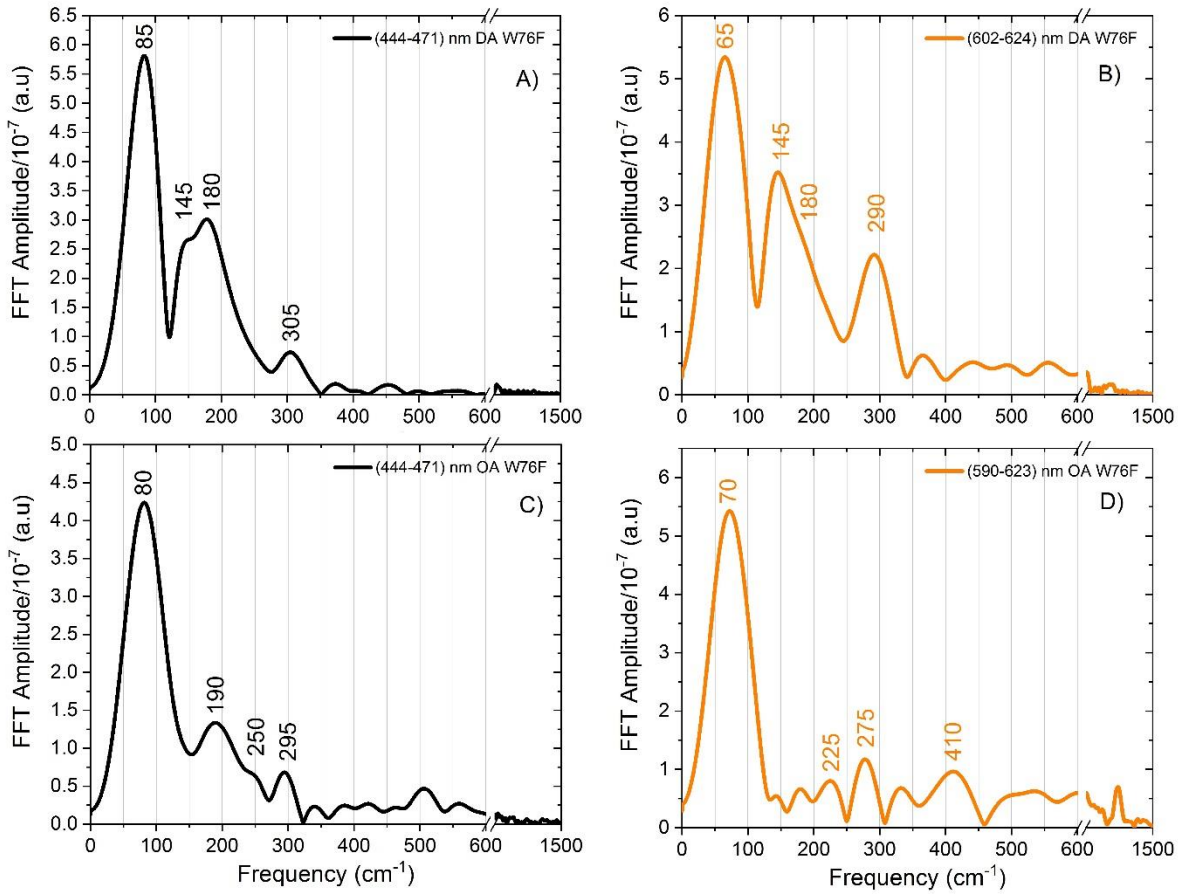

Fig. 63 : FFT-Amplitude of residuals from ESA (440nm-470nm) and PA (590nm-624nm) bands for DA (A,B) and OA (C,D) W76F mutant.

Analogous to W76F mutant the ESA and ESA/PA contributions of L83Q mutant are shown in figure 64. Panel A shows that ESA contribution in DA proteins is dominated by a ~60cm^{-1} and 150cm^{-1} modes, while a lower in amplitude 210cm^{-1} mode is also present. In the case of the mixture (panel C), modes in the 300cm^{-1} - 420cm^{-1} range are present with the lowest in frequency mode blue shifted by ~20cm^{-1} (~77cm^{-1}). The situation for PA contribution is almost identical to what was observed for WT ASR and W76F. Particularly for DA data, the 70cm^{-1}, 140cm^{-1}, 175cm^{-1} and 290cm^{-1} frequencies are present, while for OA proteins the 140cm^{-1} mode is absent. In addition, the 290cm^{-1} mode blue shifts towards 310cm^{-1}. Detection at shorter and longer wavelength of PA from those presented here show that the mode at 175cm^{-1} and 290cm^{-1} shifts within a ~15cm^{-1} range (Annexe B.V). Moreover, peaks at 230cm^{-1} and 360cm^{-1} modes are also present likewise for the ESA case.

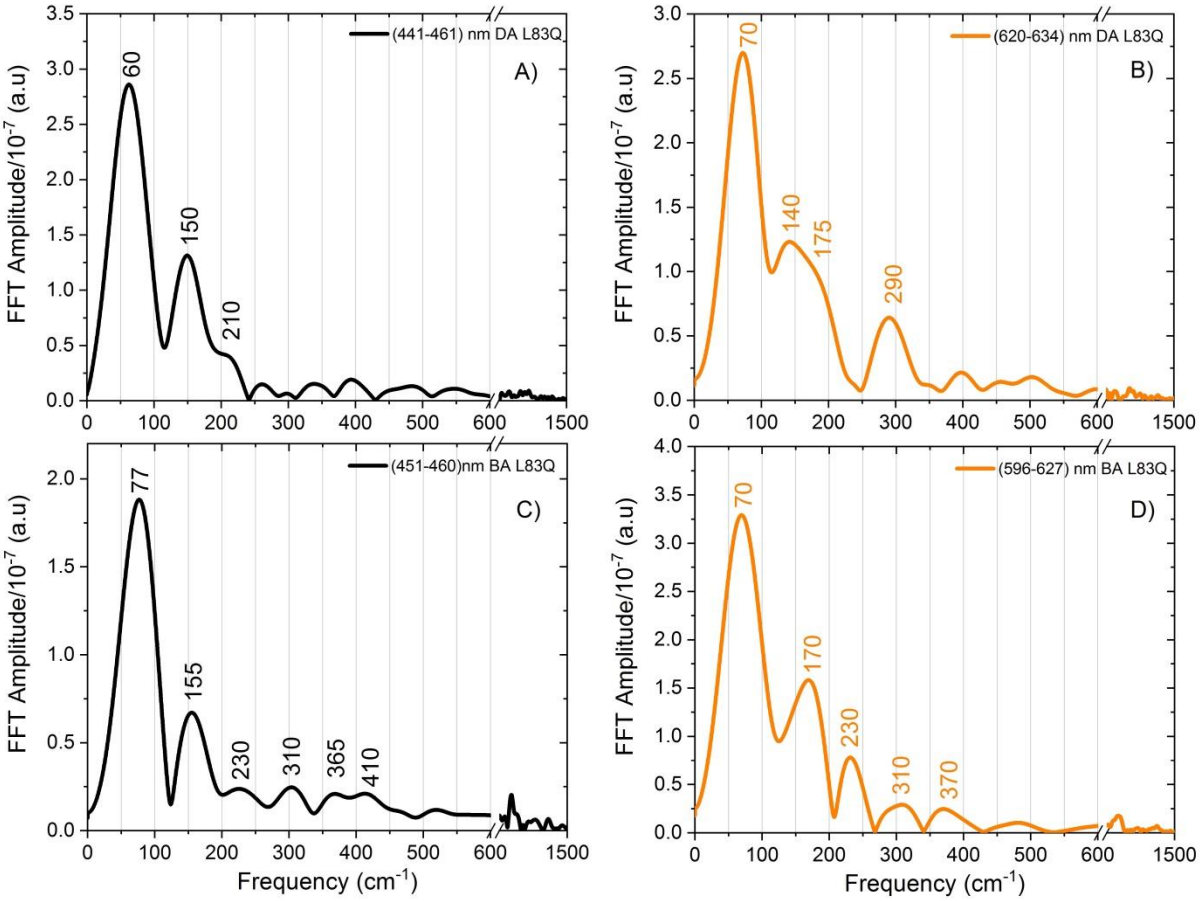

Fig. 64 : FFT-Amplitude of residuals from ESA (451nm-461nm) and PA (596nm-634nm) bands for DA (A,B) and OA (C,D) W76F mutant.

The analysis for V112N mutant is shown in Annexe B.V with similar results obtained as for the other mutants. The general result out of this analysis is that vibrational modes located at (70±20)cm^{-1}, (160±20)cm^{-1}, (210±20)cm^{-1} and (300±20) cm^{-1} are present in all mutants and WT ASR. The modes >160cm^{-1} origin from the excited state, while the lower in frequency one ranging between 60-70cm^{-1} and detected at PA region corresponds to ground oscillations. The blue/red shifts in frequency of each mode occurs within ±20cm^{-1}, depending on the protein and the detection range.

4.8 Isomerization reaction time

Kinetic traces from the high-energy part of PA of DA mutants are shown in figure 65. In all cases, the primary ultrafast ESA contribution precedes and decays before the photoproduct rises. From a visual inspection of the data, we assign the slower photoproduct rise to W76F mutant (A) and the faster one to L83Q (C). In addition, V112N appears to have a similar behavior as L83Q. The global fitting procedure yielded three exponentials with an exception for L83Q where an additional one was used.

The first constant corresponds to the photoproduct formation, the second one to the J→K cooling process the last one which is infinite to the final K-GS differential spectrum (~1ns). In detail for W76F we obtained a 0.36ps, 2.3ps and an infinite constant, while for L83Q a 0.28ps, 1.4ps, 6.5ps and an infinite one. Moreover, for V112N we obtained a 0.29ps, 1.8ps and the infinite one. The results from the fits are summarized in table 8.

The time constants obtained for the photoproduct rise are different than the dominant ones obtained from SE contribution. Particularly, the 0.36ps rise time of W76F mutant appears as a 0.5ps in the SE decay, while for V112N the 0.29ps of the photoproduct rise as a 0.34ps from SE data, but this deviation falls within the error bars of our analysis. Finally, for L83Q mutant we find the same result both for SE decay and for PA rise.

While SE decay is bi-exponential, the longer component ranging between 1.3-2 ps (15-20% amplitude), should appear as a rise contribution in the PA contribution. However, the photoproduct rise is mono-exponential meaning that the second SE component is smeared out due to the J-species cooling process, occurring on a same timescale. Particularly, in all cases the second component of PA has a positive sign, corresponding to a decay and not to a rise. This is relevant to a PA blue-shift, expressed through a faster decay of the longer PA wavelengths on a 1.5-6ps timescale.

Table 8 : Time constants from global fitting procedure for determination of IRT

Sample	τ1 (ps)	τ2 (ps)	τ3 (ps)	τ4 (ps)
DA W76F	**0.36**	**2.3**	**-**	**1000**
DA V112N	**0.29**	**1.8**	**-**	**1000**
DA L83Q	**0.28**	**1.40**	**6.5**	**1000**
error	**±0.02**	**±0.2**	**±1**	**fixed**

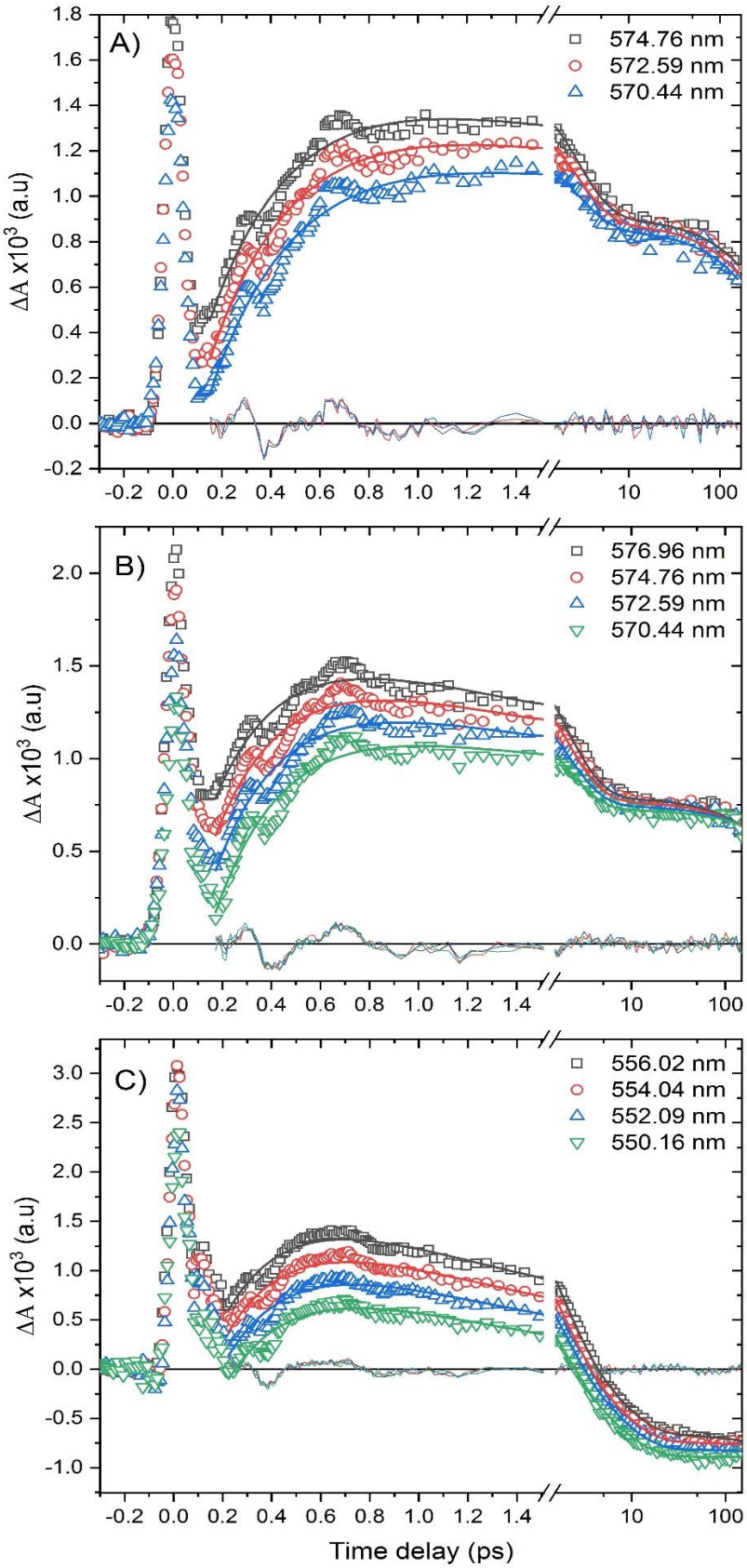

Fig. 65 : Photoproduct formation dynamics for DA W76F (A), V112N (B) and L83Q (C) mutants. Global fit allows determination of the IRTs corresponding to the photoproduct rise time.

4.9 Summary

From the experiments performed on DA and LA ASR mutants we have determined the ESL of both isomers and identified low frequency vibrational modes (<400cm^{-1}) superposed to the electronic dynamics.

The effect of the environment introduced by point mutations in the binding pocket, resulted in a ~2 fold reduction in ESL for the case of AT-PSBR (L83Q). The reduction in ESL is accompanied by a blue-shifted GS absorption of the mutants (figure 66). Moreover, the effect on 13C-PSBR is expressed through an increase of the ESL. Surprisingly, for the case of W76F mutant an ESL differing by an order of magnitude is observed. By mapping the results obtained for 13C-PSBR we see that the blue shift in absorption is accompanied by an increase of the ESL in contrary with AT's case.

Our attempt for determining vibrational modes in DA and LA proteins, resulted in four low frequency modes presented for all mutants and WT-ASR ranging between 60cm^{-1} - 400cm^{-1}. The latter results was previously reported in literature for Rhodopsin proteins and biomimetic rhodopsin analogues, attributing these modes to the chromophore's skeletal delocalized torsions.

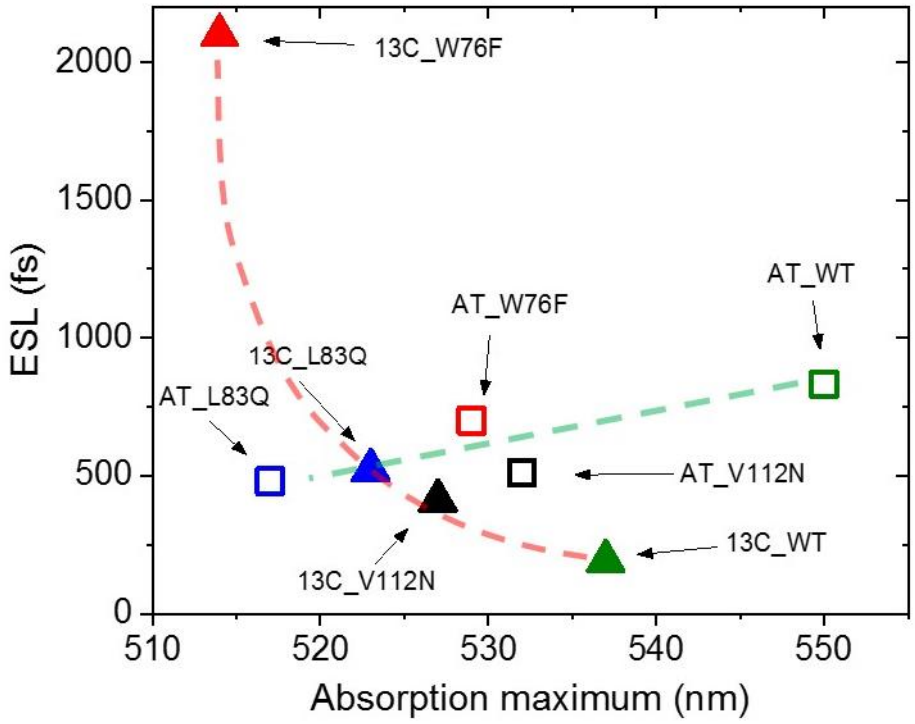

Fig. 66 : ESL with respect to absorption maxima of AT (open squares) and 13C isomers (triangles) in WT-ASR and the three mutants. Dashed green and red lines are guides for the eye, showing the trend for AT- and 13C- PSBR respectively.

References

(1) Wand, A.; Rozin, R.; Eliash, T.; Jung, K.-H.; Sheves, M.; Ruhman, S. Asymmetric Toggling of a Natural Photoswitch: Ultrafast Spectroscopy of Anabaena Sensory Rhodopsin. *J. Am. Chem. Soc.* **2011**, *133* (51), 20922–20932. https://doi.org/10.1021/ja208371g.

(2) Song, L.; El-Sayed, M. A.; Lanyi, J. K. Protein Catalysis of the Retinal Subpicosecond Photoisomerization in the Primary Process of Bacteriorhodopsin Photosynthesis. *Science* **1993**, *261* (5123), 891–894. https://doi.org/10.1126/science.261.5123.891.

(3) Briand, J.; Léonard, J.; Haacke, S. Ultrafast Photo-Induced Reaction Dynamics in Bacteriorhodopsin and Its Trp Mutants. *J. Opt.* **2010**, *12* (8), 084004. https://doi.org/10.1088/2040-8978/12/8/084004.

(4) Melaccio, F.; Ferré, N.; Olivucci, M. Quantum Chemical Modeling of Rhodopsin Mutants Displaying Switchable Colors. *Phys. Chem. Chem. Phys.* **2012**, *14* (36), 12485. https://doi.org/10.1039/c2cp40940b.

(5) Orozco-Gonzalez, Y.; Manathunga, M.; Marín, M. del C.; Agathangelou, D.; Jung, K.-H.; Melaccio, F.; Ferré, N.; Haacke, S.; Coutinho, K.; Canuto, S.; et al. An Average Solvent Electrostatic Configuration Protocol for QM/MM Free Energy Optimization: Implementation and Application to Rhodopsin Systems. *J. Chem. Theory Comput.* **2017**, *13* (12), 6391–6404. https://doi.org/10.1021/acs.jctc.7b00860.

(6) Agathangelou, D.; Orozco-Gonzalez, Y.; del Carmen Marín, M.; Roy, P. P.; Brazard, J.; Kandori, H.; Jung, K.-H.; Léonard, J.; Buckup, T.; Ferré, N.; et al. Effect of Point Mutations on the Ultrafast Photo-Isomerization of Anabaena Sensory Rhodopsin. *Faraday Discuss.* **2018**, *207*, 55–75. https://doi.org/10.1039/C7FD00200A.

(7) Melaccio, F.; del Carmen Marín, M.; Valentini, A.; Montisci, F.; Rinaldi, S.; Cherubini, M.; Yang, X.; Kato, Y.; Stenrup, M.; Orozco-Gonzalez, Y.; et al. Toward Automatic Rhodopsin Modeling as a Tool for High-Throughput Computational Photobiology. *J. Chem. Theory Comput.* **2016**, *12* (12), 6020–6034. https://doi.org/10.1021/acs.jctc.6b00367.

(8) Leonard, J.; Portuondo-Campa, E.; Cannizzo, A.; Mourik, F. v.; van der Zwan, G.; Tittor, J.; Haacke, S.; Chergui, M. Functional Electric Field Changes in Photoactivated Proteins Revealed by Ultrafast Stark Spectroscopy of the Trp Residues. *Proc. Natl. Acad. Sci.* **2009**, *106* (19), 7718–7723. https://doi.org/10.1073/pnas.0812877106.

(9) Cheminal, A.; Léonard, J.; Kim, S.-Y.; Jung, K.-H.; Kandori, H.; Haacke, S. 100 Fs Photo-Isomerization with Vibrational Coherences but Low Quantum Yield in Anabaena Sensory Rhodopsin. *Phys. Chem. Chem. Phys.* **2015**, *17* (38), 25429–25439. https://doi.org/10.1039/C5CP04353K.

Part V

Fluorescence enhancement in ASR mutants

5. Fluorescence enhancement in ASR mutants

The use of microbial rhodopsins in the field of optogenetics is a very interesting topic, as they can be employed to visualize action potentials in neurons with space and temporal resolution[5,7-10]. However, one of the requirements for such an application is the ability to exhibit fluorescence. Generally, microbial rhodopsins show a fluorescence quantum yield in the order of 10^{-4}, with a representative example the well-known BR which shows a Fl. QY of $2.5x10^{-4}$. On the contrary, Archaerhodopsin 3, is a system that is currently used for the described purpose of application, with a Fl. Q.Ys in the order of 10^{-3}. Towards the direction of improving the fluorescence quantum yield in microbial rhodopsins, engineering of these systems exhibiting enhanced fluorescence properties is a must.

In the submitted manuscript below, we show a combination of experimental and theoretical work, on WT-ASR, L83Q and W76S/Y179F mutants of ASR, which show opposite fluorescence behaviours. The purpose of this work is to address the mechanisms leading to fluorescence enhancement in rhodopsin systems.

JACS
JOURNAL OF THE AMERICAN CHEMICAL SOCIETY
Article
Cite This: J. Am. Chem. Soc. 2019, 141, 262−271
pubs.acs.org/JACS

Fluorescence Enhancement of a Microbial Rhodopsin via Electronic Reprogramming

María del Carmen Marín,[†,‡,◆] Damianos Agathangelou,[§,◆] Yoelvis Orozco-Gonzalez,[‡,∥] Alessio Valentini,[⊥] Yoshitaka Kato,[#] Rei Abe-Yoshizumi,[#,▽] Hideki Kandori,[#,▽] Ahreum Choi,[○] Kwang-Hwan Jung,[○] Stefan Haacke,[*,§] and Massimo Olivucci[*,†,‡,∥]

[†]Biotechnology, Pharmacy and Chemistry Department, University of Siena, Siena 53100, Italy
[‡]Chemistry Department, Bowling Green State University, Bowling Green, Ohio 43403, United States
[§]University of Strasbourg−CNRS, Institute of Physics and Chemistry of Materials of Strasbourg, 67034 Strasbourg, France
[∥]Université de Strasbourg, USIAS Institut d'Études Avancées, 67083 Strasbourg, France
[⊥]Theoretical Physical Chemistry, UR Molsys, University of Liège, Liège, Belgium
[#]Department of Life Science and Applied Chemistry, Nagoya Institute of Technology, Showa-ku, Nagoya 466-8555, Japan
[▽]OptoBioTechnology Research Center, Nagoya Institute of Technology, Showa-ku, Nagoya 466-8555, Japan
[○]Department of Life Science and Institute of Biological Interfaces, Sogang University, Sogang 04107, South Korea

Supporting Information

ABSTRACT: The engineering of microbial rhodopsins with enhanced fluorescence is of great importance in the expanding field of optogenetics. Here we report the discovery of two mutants (W76S/Y179F and L83Q) of a sensory rhodopsin from the cyanobacterium *Anabaena* PCC7120 with opposite fluorescence behavior. In fact, while W76S/Y179F displays, with respect to the wild-type protein, a nearly 10-fold increase in red-light emission, the second is not emissive. Thus, the W76S/Y179F, L83Q pair offers an unprecedented opportunity for the investigation of fluorescence enhancement in microbial rhodopsins, which is pursued by combining transient absorption spectroscopy and multiconfigurational quantum chemistry. The results of such an investigation point to an isomerization-blocking electronic effect as the direct cause of instantaneous (subpicosecond) fluorescence enhancement.

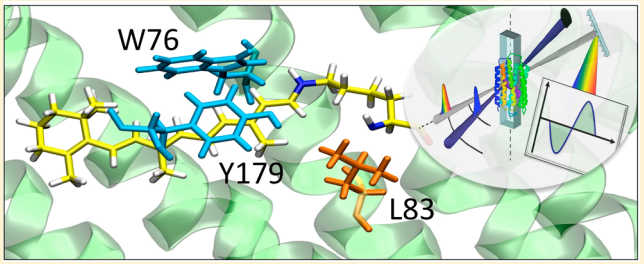

INTRODUCTION

Microbial rhodopsins have been instrumental for the development of optogenetics. In fact, when certain rhodopsins are expressed in neurons, light can be used to activate, inhibit, and even visualize neuronal activity.[1] Indeed, few rhodopsins have been reported to exhibit a weak fluorescence,[2−4] a property that is being harnessed to develop superior action potential visualization techniques.[2,3,5] The understanding of the factors determining rhodopsin fluorescence is the target of the present work as a high fluorescence intensity is a prerequisite for the development of voltage sensors.[2,4,6]

Archaerhodopsin 3 (Arch3)[2] from the dead sea archaebacterium *Halorubrum Sodomense*, is a fluorescent microbial rhodopsin that is currently employed to visualize action potentials in neurons with space and temporal resolution.[5,7−10] However, its fluorescence is very dim (ca. 0.001 quantum yield), and three photons must be absorbed to generate one emitted photon. Furthermore, since the emission is not due to the dark adapted (DA) state but to a photocycle intermediate formed only milliseconds after photoexcitation, Arch3 has a limited temporal resolution. Finally, Arch3 proton pumping activity partially silences the action potential signal.[9]

In order to overcome the limitations outlined above, one could look for Arch3 variants[5,8,10] or for variants of other microbial rhodopsins[4,7,11] displaying enhanced fluorescence intensity. The first approach has yielded, for instance, QuasAr1,[8] QuasAr2,[8] Archer,[7] and Archon1[12] with the first displaying a remarkable 19-fold fluorescence increase generated by a one-photon process. The second approach has instead been applied to a rhodopsin from *Gleobacter violaceous* and yielded a mutant displaying a ca. 0.01 fluorescence quantum yield.[11] A third approach involves the use of cyanine-based chromophore analogues, but it has the disadvantage of not using the natural chromophore.[13] In spite of this progress, obtained through random or systematic mutagenesis, no attempt to unveil the mechanism behind emission enhancement has been reported. As a consequence, our ability to

Received: September 1, 2018
Published: December 11, 2018

DOI: 10.1021/jacs.8b09311
J. Am. Chem. Soc. 2019, 141, 262−271

search rationally for highly fluorescent rhodopsins remains impaired.

In the present combined experimental and theoretical study, we consider the second approach by focusing on Anabaena Sensory Rhodopsin (ASR), a light sensor from the fresh water eubacterium *Anabaena*.[14−16] ASR exhibits a dim fluorescence[17] similar to Arch3 but has only a weak (inverse) proton pumping activity. Furthermore, ASR exists in two forms; all-*trans* ASR (ASR_{AT}) and 13-*cis* ASR (ASR_{13C}), which can be interconverted with light of different wavelengths. Such bistability (i.e., photochromism) is an attractive feature as it provides the basis for engineering photoswitchable fluorescent probes.[18] Finally, the X-ray crystallographic structure of ASR is available,[16] making possible the construction of realistic computer models of both wild type (WT) forms, their isomers, and their mutants.

Below we report on the accidental discovery of two ASR mutants featuring, with respect to WT, DA states with opposite fluorescence variations. In fact, W76S/Y179F displays an almost one order of magnitude enhanced fluorescence, while L83Q displays a fluorescence slightly larger than the WT but a shorter excited state lifetime (ESL). By using transient absorption spectroscopy (TAS) and quantum mechanics/molecular mechanics (QM/MM) models based on multiconfigurational quantum chemistry (MCQC), we show that the ESL and, likely, the fluorescence intensity, is controlled by the changes in the electronic character along the first singlet excited state (S_1) potential energy surface (PES) of ASR. Indeed, the models show that the increased mixing between charge transfer and diradical characters along the S_1 isomerization path is responsible for the increase in fluorescence of W76S/Y179F. The same models show that the ESL decrease of L83Q originates from a dramatic decrease of such mixing. The QM/MM model analysis shows that specific electrostatic and steric interactions control the charge transfer/diradical mixing opening a path to the rational engineering of highly fluorescent rhodopsins.

METHODS

Sample Preparation and Spectroscopy. ASR proteins were expressed in *E. coli*, prepared according to the reported protocol[19] and solubilized in buffer (200 mM NaCl, 25 mM Tris-HCl, 0.02% DDM, pH 7.0). The steady state absorption spectra of the DA and light-adapted (LA) proteins were recorded by using a PerkinElmer "Lambda 950" UV/vis spectrometer. DA samples were prepared by incubation in the dark for at least 12 h at room temperature, while the LA samples, orange-adapted (OA) or green-adapted (GA), were exposed to light illumination for 30 min using Luxeon LEDs "LXHL-PL01" (590 ± 10 nm) or "LXHL-NE98" (500 ± 15 nm), respectively.

The fluorescence emission spectra for DA, OA, and GA states were recorded by using a homemade static fluorescence setup.[15] Replacement of the excited volume, required for preserving the DA state, was achieved by circulation of the sample, using a peristaltic pump through a close circuit consisting of a 0.5 mm path length flow cell and a 2 mL vial serving as sample reservoir. A nitrogen cooled CCD (−120 °C, PyLoN, Princeton Instr.) mounted on an imaging spectrometer (SP-2300i, Princeton Instr.) was used for detection of the signal covering the 550−1050 nm spectral range with 4 nm resolution. See the SI for more details.

TAS was carried out with sub-80 fs temporal resolution at 1 kHz repetition rate (system described elsewhere[20]). A homemade noncollinear parametric amplifier was used for delivering sub-60 fs excitation pulses at the wavelength of interest, while a NIR broad band probe pulse (850−1400 nm) was produced by focusing ∼0.7 μJ of the 800 nm fundamental beam in a 4 mm thick YAG crystal.[21] The probe beam was dispersed in an Acton "SP2156" spectrograph, and the single pulse spectra at 1 kHz were recorded by a Hamamatsu IR head sensor (G11608−256).

Determination of the LA-dependent isomer content was done after retinal oxime extraction, by performing High Performance Liquid Chromatography.[19] Retinal oximes were resolved using a Dionex UltiMate 3000 System, equipped with a Zorbax SIL 70 Å 4.6 × 250 mm−5 μm column (see detailed protocol in the SI).

Computations. The QM/MM models were built using the Automatic Rhodopsin Modeling (ARM) protocol[22] (see Figure 1A and the SI for details). ARM employs the complete active space self-consistent field (CASSCF)[23] MCQC method combined with the Amber molecular mechanics force field to obtain ground state (S_0) QM/MM models of rhodopsins semiautomatically in a standardized fashion. Vertical excitation energies are then computed using multiconfigurational second-order perturbation theory (CASPT2)[24] to recover the dynamic electron correlation missing by the CASSCF wave function.

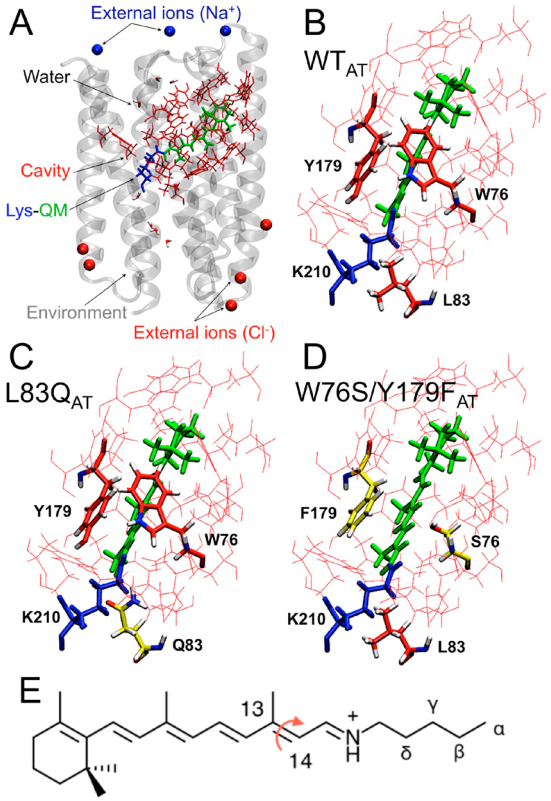

Figure 1. QM/MM models. (A) General structure of the ASR model. The protein environment is colored in gray with external counterions in blue (Na^+) and red (Cl^-). The region hosting of the retinal chromophore is colored in red with the Lys210-chromophore system in blue-green. Chromophore hosting region for the all-*trans* isomers of (B) WT (ASR_{AT}), (C) L83Q, and (D) W76S/Y179F. The variable cavity residues 76, 83, and 179 are shown in tube representation. (E) All-*trans* retinal chromophore. The curly arrow indicates the C_{13}═C_{14} isomerizing double bond, and the greek letters are the atoms of the Lys210 side chain.

Excited state reaction paths are documented by computing relaxed scans driven by the C_{12}−C_{13}═C_{14}−C_{15} dihedral angle of the rhodopsin chromophore (Figure 1E). The S_1 dynamics is instead investigated by computing semiclassical Franck−Condon (FC) trajectories, namely, deterministic surface-hop trajectories released on S_1 PES starting from the S_0 equilibrium structure with zero initial velocities. All QM/MM energy, gradient, relaxed scan, and FC trajectory calculations were carried out using interfaced Molcas[25]

DOI: 10.1021/jacs.8b09311
J. Am. Chem. Soc. 2019, 141, 262−271

quantum chemistry and Tinker[26] molecular mechanics/dynamics packages.[27]

RESULTS AND DISCUSSION

Bonding in the Excited Electronic State. Here we introduce the theoretical framework necessary to discuss the results presented below. Since a detailed discussion can be found in recent publications,[28,29] we limit ourselves to a summary of the properties of the first three PESs of a gas-phase model of the rhodopsin chromophore featuring five conjugating double-bonds (PSB5).[17,29] Scheme 1A shows the electronic characters dominating the S_0, S_1, and S_2 equilibrium structures of PSB5 when this is subject to a planarity constraint. These are labeled 1Ag, 1Bu, and 2Ag (consistent with the electronic terms of a homologous all-*trans* polyene with C_{2h} symmetry).[28,30] S_1 has a 1Bu character characterized by a positive charge spread (i.e., transferred) toward the $H_2C{=}CH-$ end of the PSB5 framework. This is qualitatively different from the 1Ag character of S_0, which has the positive charge localized on the $-C{=}NH_2$ terminal moiety. In contrast, the second singlet excited state (S_2) has 2Ag character associated with a diradical, rather than charge transfer, structure, and features, similar to S_0, a positive charge mostly located on the $-C{=}NH_2$ moiety.

Scheme 1. Electronic and Bonding Structure of the Retinal Chromophore[a]

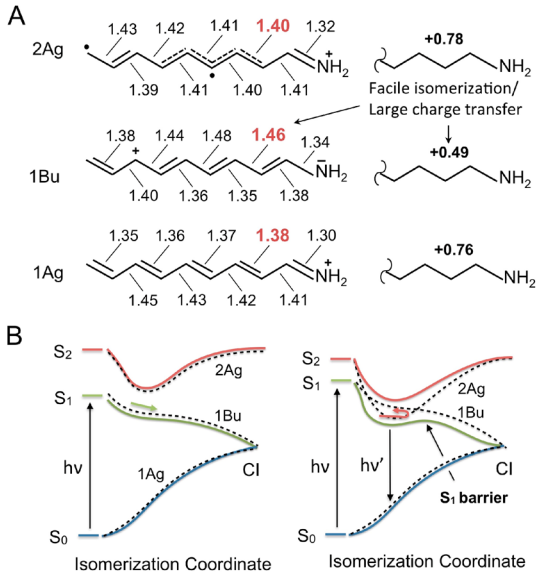

[a](A) Left. Resonance formula associated to the electronic characters (1Ag, 1Bu, and 2Ag) dominating the S_0, S_1, and S_2 equilibrium structures of PSB5. The bond lengths are given in Å (see left part), and the total charge of the displayed moiety (see right part) is indicated in bold. (B) Schematic S_0, S_1, and S_2 energy profiles along the S_1 PES path driving the chromophore S_1 isomerization. An S_1 PES dominated by a 1Bu character (left) is associated with a barrierless path, while a mixed 1Bu/2Ag character (right) is associated with the presence of a barrier along the path. The dashed energy profiles represent the energy of diabatic states corresponding to "pure" 1Bu and 2Ag electronic characters.

In the present work, we take the 1Ag, 1Bu, and 2Ag charge distributions as a reference to follow how the electronic character changes along the S_1 PESs (e.g., along a reaction path or trajectory). To do so, we compute the charge of a suitable chromophore moiety and track its variations along the PES. For example, as shown in the right part of Scheme 1A and consistently with the resonance formulas, the $-CH{=}CH{-}CH{=}CH{-}NH_2$ moiety has a large positive charge (ca. + 0.8) in regions with dominating 1Ag and 2Ag characters but a smaller charge (ca. + 0.5) when the 1Bu charge transfer character is dominating. Second, the same charge provides information on the nature of the π-bonding along the path. This is shown in Scheme 1A where we report the bond lengths of the equilibrium reference structures. A structure dominated by a 1Bu character displays inverted double and single bond lengths facilitating double bond isomerization (see values in red). In contrast, in a structure with 2Ag character, the double bonds are only weakened (i.e., partially broken) and thus feature a residual torsional energy barrier restraining double bond isomerization. Third, one can use the charge distribution to track the electronic coupling between two PESs. For instance, the fact that along a trajectory the S_1 and S_2 charges of the $-CH{=}CH{-}CH{=}CH{-}NH_2$ moiety change in a mirror-image like fashion[29,31] indicates that the S_1 and S_2 PESs are electronically coupled. In other words, the PESs exchange 1Bu (reactive) and 2Ag (nonreactive) character. This occurs in the presence of an avoided crossing region as the one illustrated in Scheme 1B. In such a scheme, the 1Bu and 2Ag electronic characters are regarded as diabatic states (i.e., states with pure characters), which mix to generate the S_1 and S_2 adiabatic states. In the left diagram, the S_2 and S_1 PESs remain dominated by the same diabatic state. In contrast, the right diagram displays a situation where the diabatic states cross twice and, therefore, the S_1 PES shows regions dominated by a 2Ag character. The electronic states driving the photoisomerization of model retinal chromophores have originally been described by Josef Michl and Vlasta Bonačić Koutecky.[30,32]

Below we assume that the ESL is determined by the chromophore S_1 reactivity. In other words, the isomerization motion on S_1, leading to fast nonradiative decay through a CI between the S_1 and S_0PESs, is held responsible for the subpicosecond ESL and the low fluorescence quantum yield (QY). Consistently, the presence of an energy barrier along the S_1 isomerization path would increase the ESL and QY proportionally to the barrier magnitude.

Spectroscopy and Reactivity Studies. The observed absorption spectra of the DA, OA, and GA states of ASR are reported in Figure 2A for the WT and W76S/Y179F and L83Q[33] mutants. As shown in Figure 2B, the observed trend in absorption maxima (λ^a_{max}) is reproduced by using all-*trans* QM/MM models to compute the corresponding vertical excitation energies for the $S_0 \rightarrow S_1$ transition (ΔE_{S1-S0}). The blue-shifted λ^a_{max} of W76S/Y179F and L83Q (6 and 4 kcal/mol, respectively, in terms of ΔE_{S1-S0}) must originate from changes in the interactions between protein and chromophore (see Figure 1B–D). More specifically, the change from leucine (L) to glutamine (Q) in L83Q and the change from tryptophan (W) to serine (S) and tyrosine (Y) to phenylalanine (F) in W76S/Y179F must destabilize S_1 with respect S_0 (or stabilize S_0 with respect to S_1).

In Figure 2C we also report the fluorescence spectra of DA WT, L83Q, and W76S/Y179F. Also GA and OA spectra are shown for the W76S/Y179F mutant. Experimental spectra are rescaled in order to correct for the sample-dependent absorbance values. The integrated fluorescence intensity is thus proportional to the fluorescence QY (see SI). Remarkably,

DOI: 10.1021/jacs.8b09311
J. Am. Chem. Soc. 2019, 141, 262−271

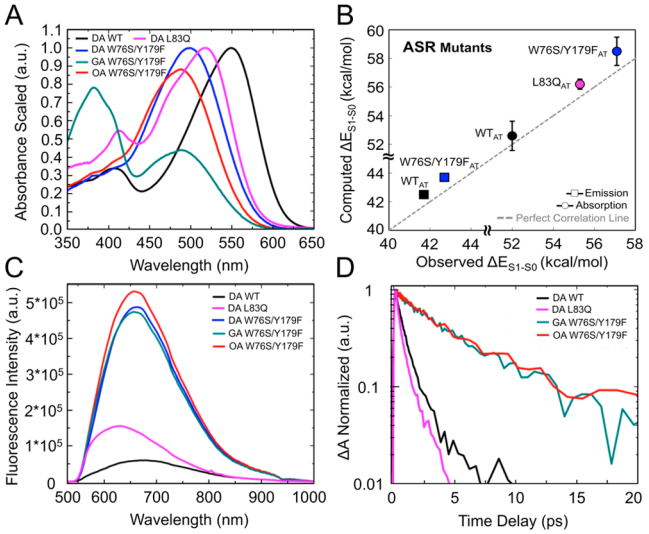

Figure 2. Steady state spectra and excited states dynamics. (A) Scaled absorption spectra of light-adapted (OA and GA) W76S/Y179F mutant and dark-adapted (DA)WT, W76S/Y179F, and L83Q mutants of ASR. Light-adaptation was carried out either with an orange or green LED. (B) Comparison between simulated all-*trans* and observed λ^{a}_{max} (circles) and λ^{f}_{max} (squares) values for the DA state. Deviation bars for the computed excitation energy values are shown as black segments. The excitation energy errors fall in the 0.5−1.5 kcal/mol range typical of ARM.[22] (C) Steady state emission of DA WT ASR, DA L83Q ASR, DA, OA, and GA W76S/Y179F mutant of ASR. (D) Comparison of the SE kinetic traces of WT (black trace), L83Q (pink trace), and W76S/Y179F (GA green trace and OA red trace).

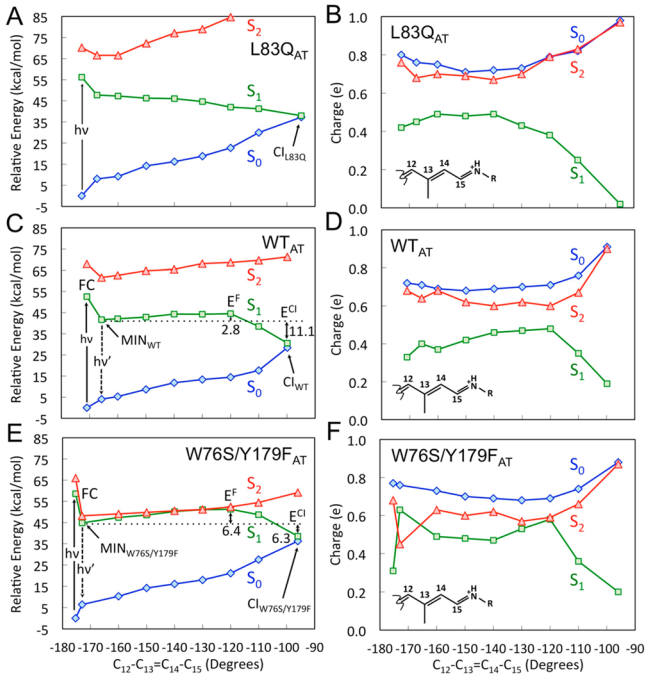

Figure 3. C_{13}=C_{14} isomerization path on S_1. (A,C,E) CASPT2//CASSCF/AMBER energy profiles along S_1 (green squares) isomerization path of L83Q, WT, and W76S/Y179F, respectively. S_0 (blue diamonds) and S_2 (red triangles) profiles along the S_1 path are also given. The S_1 is computed in terms of a relaxed scan along C_{12}−C_{13}=C_{14}−C_{15} dihedral angle. The corresponding, computed oscillator strengths are given in Figure S3. (B,D,F) Corresponding Mulliken charge variation of the −CH−CH−CH−CH−NH_2 moiety of the chromophore of L83Q, WT, and W76S/Y179F, respectively.

the data show that the QY of W76S/Y179F is ca. one order of magnitude higher than that of WT and, therefore, not far from that of certain improved Arch3 mutants.[7,8] In Figure 2B we show that the same all-*trans* QM/MM models reproduce the observed trend in emission maxima (λ^{f}_{max}). In fact, the ΔE_{S1-S0} (see Table S3) computed at the corresponding S_1 equilibrium structure (see MIN_{WT} and $MIN_{W76S/Y179F}$ in Figure 3C,E) yield a λ^{f}_{max} of 758 nm for WT and 744 nm for W76S/Y179F. However, these values do not account for the kinetic energy of the molecule. To do so, we compute the average ΔE_{S1-S0} values along the FC trajectories of Figure 4C,E starting 15 fs after the initial relaxation. The computed λ^{f}_{max} values of 672 nm for WT and 654 nm for W76S/Y179F are closer to the observed values of 674 nm for WT and 658 nm for W76S/Y179F.

As displayed in Figure 2D and Table 1, the ESL values are critically dependent on the mutations, as determined from the stimulated emission (SE) decay traces. We find values of 0.48, 0.86, and 5.7 ps for L83Q, WT, and W76S/Y179F, respectively (global fit of the entire SE data set, see SI). Comparing W76S/Y179F and WT, the measured and spectrally integrated steady-state emission intensities (see SI for details) are almost proportional to the average ESLs, as expected since the fluorescence QY is Φ = ESL*k_r, with k_r being the radiative rate. L83Q shows a larger QY despite an almost 2-fold reduction of the ESL, indicating that L83Q has a higher radiative rate than WT (see SI for details).

A complication arises for W76S/Y179F, which presents a light-adaptation-dependent isomer content, including the noncanonical 9-*cis* or 7-*cis* isomers, with a relative amount comparable to all-*trans*. Importantly, in the GA state a relative amount of 54% of the pair 9-*cis* and 7-*cis* isomers accumulates in S_0 absorption and was used for comparison with the OA state where the all-*trans* isomer is the dominant one (39%, see SI). For both the TAS and steady-state fluorescence experiments, the excitation wavelength was tuned to the lower energy tail of ground state absorption for selective excitation of all-*trans* isomer since its λ^{a}_{max} was calculated to be largest among all isomers. We find indeed that 9-*cis* and 7-*cis* isomers rather absorb in the 350−420 nm range (see Figure S12 in the SI). The SE dynamics are identical for both OA and GA light-adaptation states, even though the amount of 9-*cis* and 7-*cis* isomers almost doubles in GA. We thus conclude that in the present conditions, the ESL and the increased fluorescence emission comes mainly from the all-*trans* isomer.

In the following, we will show that the above all-*trans* QM/MM models reproduce the trends in ESLs and fluorescence intensities when they are probed via reaction paths and 200 fs FC trajectory computations.

The photochemical reactivity of WT, L83Q, and W76S/Y179F has been initially investigated by computing the all-*trans* to 13-*cis* relaxed scans connecting the FC point to the S_1/S_0 CI along the C_{13}=C_{14} twisting describing the isomerization. The resulting energy profiles are reported in Figure 3A,C,E. It is apparent that the steep S_1 potential energy profile of L83Q would accelerate the S_1 population toward the CI more effectively than the flatter WT and W76S/Y179F PESs. The results appear to be consistent with the measured ESLs, fluorescence intensities, and quantum yields (see Table 1 and panels C,D). More specifically, WT and W76S/Y179F display S_1 energy profiles (see Figure 3C,E) featuring a ca. 3 and 6

DOI: 10.1021/jacs.8b09311
J. Am. Chem. Soc. 2019, 141, 262−271

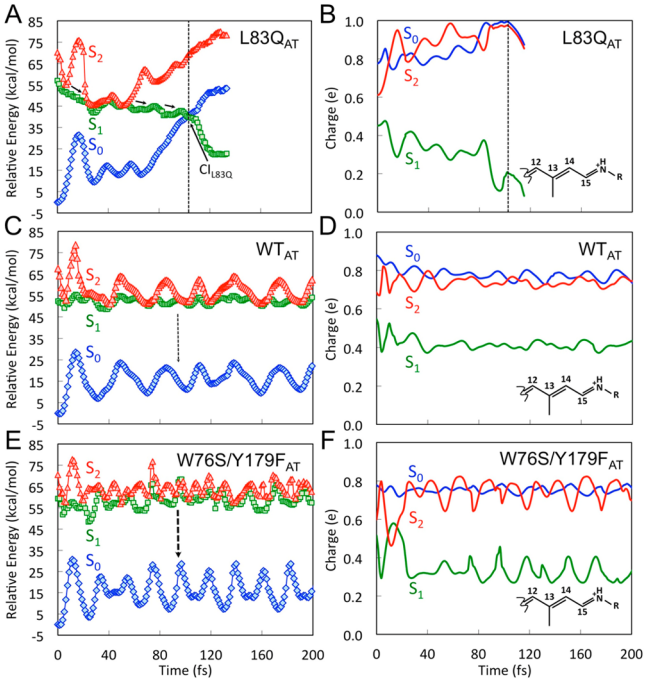

Figure 4. Trajectory computation on S_1. (A,C,E) QM/MM FC trajectories (see main text) of L83Q, WT, and W76S/Y179F, computed at two-root state-averaged-CASSCF/AMBER level of theory and corrected at the CASPT2 level. S_0 (blue diamonds), S_1 (green squares), and S_2 (red triangles) CASPT2/CASSCF/AMBER energy profiles along the FC trajectories. The corresponding, computed oscillator strengths are given in Figure S6. (B,D,F) Corresponding Mulliken charge variation of the −CH−CH−CH−CH−NH_2 moiety of the chromophore of L83Q, WT, and W76S/Y179F, respectively. To test the robustness of the W76S/Y179F results, the data of panels E and F have been recomputed at the 5-root-state-average level (see Figure S10).

Table 1. Time Constants and Amplitudes from the Bi-exponential Decay of SE, Average ESLs, and Experimentally Determined Fluorescence QYs (Φ) with Respect to That of Bacteriorhodopsin (Φ_{bR}), Determined from the Spectrally Integrated Fluorescence Intensities[a]

sample	A_1	t_1 (ps)	A_2	t_2 (ps)	ESL (ps)	Φ/Φ_{bR}
DA L83Q	0.78	0.27 ± 0.05	0.22	1.2 ± 0.2	0.48	2.4
DA WT	0.72	0.55 ± 0.05	0.28	1.7 ± 0.2	0.86	1.1
OA W76S/Y179F	0.60	2.8 ± 0.3	0.40	10 ± 0.8	5.7	8.7
GA W76S/Y179F	0.40	2.1 ± 0.4	0.60	8 ± 0.7	5.7	7.6

[a]The fluorescence QY's are determined with bacteriorhodopsin as a reference sample (see SI). However, we refrain from quoting absolute values since the only available experimentally determined value for bacteriorhodopsin appears to be excessively high, most probably due to contributions from later photocycle intermediates.[34]

kcal/mol isomerization barriers, respectively, leading to an increased ESL for the double mutant.

The results of 200 fs FC trajectory calculations for the all-*trans* models of L83Q, WT, and W76S/Y179F are given in Figure 4A,C,E, respectively. In all cases, we assume that during such a short time the trajectories describe the average evolution of population on the lowest excited states (S_1 and S_2).[35] As shown in Figure 4A, L83Q reaches the photochemically relevant S_1/S_0 CI and decays to S_0 in ca. 100 fs consistently with the dominant 270 fs decay (Table 1) as well as the S_1 potential energy slope of Figure 3A (notice that FC trajectories usually decay earlier with respect to the population investigated experimentally; see Figure 9 in ref 35) In contrast, Figure 4C,E show that WT and W76S/Y179F do not reach the CI within the simulation time, consistently with the observed shortest decay time, which is, in both cases, above 500 fs and with the computed S_1 barriers in Figure 3C,E.

The computational results above are based on all-*trans* QM/MM models. Such models do not take into account the effect of mutations on the isomer composition of the DA state, which may be altered in the mutants. In fact, as said above, in contrast with WT and L83Q, whose DA states are dominated by the all-*trans* chromophore, W76S/Y179 has a more complex isomer composition (see Figure S11 and Table S4). However, as explained above, the OA and GA steady-state absorption together with the isomer compositions for both OA and GA show that the 7-*cis* and 9-*cis* isomers do not contribute to the absorption band at 490 nm. Thus, the presence of these isomers does not alter the conclusions for W76S/Y179 based on the all-*trans* model exclusively.

Structure and Dynamics of the Emissive Excited State Species. In the present subsection we use the all-*trans* QM/MM models to investigate the mechanisms at the basis of the observed and simulated fluorescence enhancement. More specifically, we provide evidence that the increase in mixing between the reactive 1Bu and nonreactive 2Ag characters introduced above correlates with the observed L83Q < WT < W76S/Y179F trend in S_1 ESL. In other words, we provide support for a structure of the L83Q and W76S/Y179F PESs and related dynamics consistent with the left and right diagram of Scheme 1B, respectively.[29]

The comparison of panels A,C,E shows that the average S_2-S_1 energy gap along the S_1 path decreases in the order L83Q > WT > W76S/Y179F. As apparent from panels B,D,F, such changes are accompanied by changes in the positive charge distribution and, in turn, 1Bu character (see discussion). Thus, in W76S/Y179F the population moving out of the FC point, where one has a 1Bu character (i.e., the S_1 charge of the −CH−CH−CH−CH−NH_2 fragment is less than in S_0 and S_2), transits along regions where the 2Ag character of the S_1 PES increases ($MIN_{W76S/Y179F}$ in Figure 3E) indicating character mixing and then reaches regions (ca. −120° in panel F) where the 1Bu and 2Ag characters have close weights (similar charge in S_1 and S_2). This happens at a lesser extent in WT featuring a larger 1Bu weight in S_1 and at an even lesser extent in L83Q where the charge becomes less than +0.2 and the 1Bu character is retained. This appears to be also consistent with the larger S_2-S_1 gap along the energy profiles of panel C, which is brought to a periodic degeneracy (see Figure 4C) only when the chromophore acquires kinetic energy.

The magnitude of the S_1 barrier (E^F in Figures 3C and 3E), and in turn, the ESL, appears to increase with the mixed 1Bu/2Ag character at the ca. −120° twisted structure (see Figures 3B,D,F), which approximates the S_1 transition state. This suggests that, in contrast to L83Q, in W76S/Y179F the S_1 and S_2 PESs are generated via avoided crossings between 2Ag and 1Bu diabatic states as illustrated in Scheme 1B left. In other words, the S_1 energy barrier at −120° would be a result of such crossing.

DOI: 10.1021/jacs.8b09311
J. Am. Chem. Soc. 2019, 141, 262−271

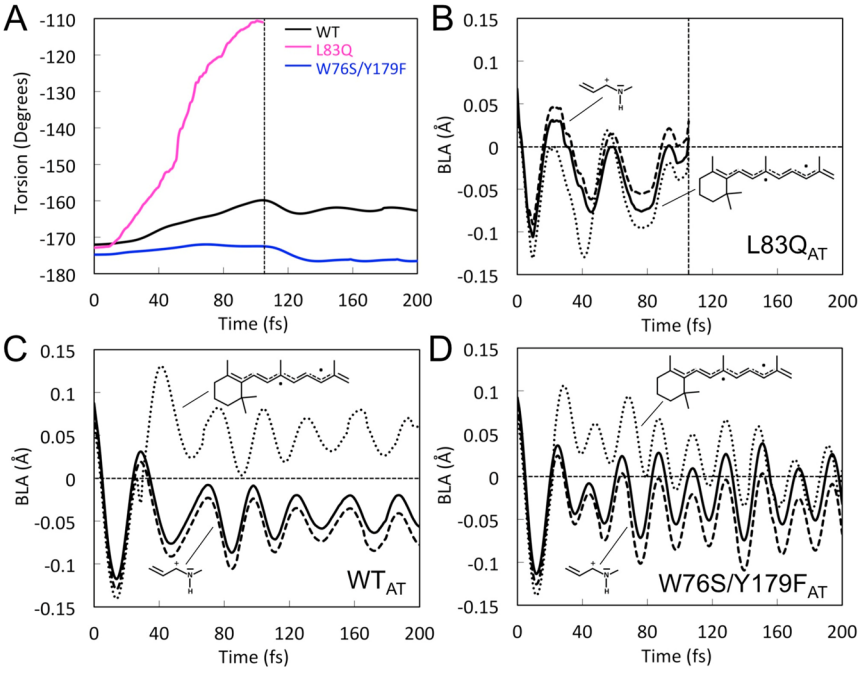

Figure 5. Geometrical variation along the L83Q, WT, and W76S/Y179F FC trajectories. (A) Evolution of the $C_{12}-C_{13}=C_{14}-C_{15}$ dihedral angle along the FC trajectories of all-*trans* ASR L83Q (purple), WT (black), and W76S/Y179F (blue) representing the $C_{13}=C_{14}$ isomerization. (B–D) Evolution of the total BLA (full line) and of the BLA of two specific moieties (dotted and dashed lines) for L83Q, WT, and W76S/Y179F, respectively.

The increasing 2Ag character along the S_1 energy profile in W76S/Y179F must have important consequences on the excited state dynamics. 2Ag being less reactive than 1Bu as demonstrated by the documented E^F barrier, the molecular population will be temporarily trapped in S_1 causing an increase in ESL with respect, for instance, to L83Q where the 1Bu character dominates and the S_1 PES has no barrier. However, since the reaction paths of Figure 3 do not consider kinetic energy effects, we have confirmed the above conclusion via FC trajectory calculations. Consistently with literature data,[28] initially all trajectories relax along a bond-length-alternation (BLA) stretching mode where the single bonds shrink and the double bonds expand. During BLA relaxation, which occurs within 30 fs, L83Q, WT, and W76S/Y179F enter a S_2/S_1 near degeneracy region, which is associated with the emissive species (sometimes called fluorescent state). Such region shall eventually be left to follow the C13=C14 isomerization coordinate. As anticipated above, we find that only L83Q exits such a region within the 200 fs simulation time supporting the mechanistic interpretation provided by the reaction paths (see Figure 5A).

The FC trajectories provide a detailed dynamic description of the S_1 trapping process due to the change in electronic character. In fact, in the reactive L83Q case (Figure 4A,B), the S_2 energy profile only crosses the S_1 energy profile in the 20 to 50 fs time segment and then becomes destabilized. Thus, as shown in Figure 4B, the system remains dominated by a 1Bu reactive character and it is not trapped in S_1. However, the trapping occurs in WT and W76S/Y179F (for WT see also our previous report[29]). In these cases, the S_2 and S_1 profiles cross (or couple) periodically generating "islands" with increased nonreactive 2Ag character. These islands are characterized by BLA oscillations (see also Figure 5), which modulate the S_1 and S_2 gap and the associated 1Bu/2Ag character mixing. This is confirmed by the $S_0 \rightarrow S_1$ oscillator strength progression (Figure S6) showing oscillations of a lower magnitude in WT than in W76S/Y179F. The described behavior is supported by the fact that the S_2 and S_1 positive charge on the reference $C_{12}-C_{13}=C_{14}-C_{15}=NH_2$ fragment display mirror-image variations (see Figure 4D,F).[29] As a consequence, due to the change in the corresponding electronic/bonding characters such motion hampers the unlocking of the $C_{13}=C_{14}$ double bond and, as a consequence, the reactivity of the S_1 chromophore. The frequency and depth of such crossing-recrossing events is larger for W76S/Y179F, and this is attributed to the S_2/S_1 degeneracy, which is already accomplished at the reaction path level (compare Figure 3C,E). Consistently, in W76S/Y179F the S_2 state becomes more stable than S_1 periodically each 30 fs. This does not happen in WT where the S_2 state only "touches" the S_1 energy profile with about the same frequency.

The formation of unreactive "islands" can also be documented structurally. For instance, in Figure 5A we report the evolution along the dihedral angle describing the isomerization of the $C_{13}=C_{14}$ double bond. The dihedral reaches the typical −110° value of a CI exclusively for L83Q. However, the generation of unlocked double bonds prone to isomerize (i.e., via double-bond-single-bond inversion) can be tracked by plotting the BLA value of specific chromophore fragment. Accordingly, in Figures 5B–D we report the evolution of the BLA value of a suitable β-ionone containing fragment. It oscillates about a completely inverted BLA value in L83Q (i.e., negative average BLA values) but not in WT and W76S/Y179F (i.e., positive average BLA values). As mentioned above, the DA state of the fluorescent ASR mutant W76S/Y179F is not dominated by a single all-*trans* isomer, which, in fact, only accounts for 30% of the total population. Such state also contains 15% of 13-*cis* and 18% of 11-*cis* isomers and 36% of a mixture of 9-*cis* and 7-*cis* isomers (see Table S4). As said above, the latter can be disregarded since

DOI: 10.1021/jacs.8b09311
J. Am. Chem. Soc. 2019, 141, 262–271

they are not excited in both the steady-state fluorescence and TAS experiments (see SI), but the contribution of 13-*cis* and 11-*cis* isomers needs to be discussed. We have used the same type of QM/MM model to investigate their photoisomerization dynamics via FC trajectory calculations. As shown in Figure S9, the 13-*cis* and 11-*cis* isomer reach a CI within 200 fs, a component that is not observed in the SE decay since the pump wavelength favors all-*trans* excitation. Since, the fluorescence spectra were recorded with the same excitation wavelength, and the increase in fluorescence quantum yield matches the ESL increase of W76S/Y179F with respect to WT, we conclude that these isomers do not contribute to the observed fluorescence. However, the 9-*cis* and, most likely, the 7-*cis* isomers would contribute with the same mechanism operating in the all-*trans* isomer (see the SI).

However, again, the steady state absorption spectra of OA and GA states strongly suggest that both isomers absorb in the region between 350 and 400 nm, are not excited, and are not presented in the TAS and static fluorescence measurements (see SI).

Residue-Level Modulation of Excited State Emission. We now provide information on how emissive PES regions (i.e., the islands described above) get stabilized (or destabilized) via electrostatic and/or steric interactions with specific residues. The L83Q, WT, and W76S/Y179F models indicate that the increase in ESL is due to the appearance of an S_1 energy barrier at ca. −120° twisting whose magnitude increases with the 1Bu/2Ag mixing developing along the S_1 PES. However, it is unclear if such variations are caused by changes in the electrostatic field acting on the chromophore or by changes in the chromophore geometrical progression (i.e., in the isomerization coordinate). To investigate the electrostatic effect we recomputed the energy profile of Figure 3A (i.e., for L83Q) for the isolated (i.e., *in vacuo*) chromophore taken with its protein geometry. The comparison between Figures 6A and 3A (or the dashed lines in Figure 6A) demonstrates that the change in protein electrostatics is fully responsible for the absence of a barrier in L83Q. Indeed, in the absence of protein electrostatic effects, the energy profile of L83Q appears to be very similar to the one detected along the WT and W76S/Y179F S_1 PESs when the protein is present. This behavior must be connected with the charge evolution of Figure 6B, which shows a marked difference when plotted in the presence and absence of the protein. In fact, it can be seen that between −140° and −120° the S_1 charge evolution displays a fast increase of 1Bu/2Ag mixed character in the isolated chromophore.

Remarkably, the same L83Q barrier induction effect is seen in the presence of a protein environment where the charges of the Q residue in position 83 are set to zero (see Figure S4). This is also consistent with the fact that it is sufficient to replace the polar Q residue with the apolar L residue (or with a "residue" with zero charges) to create the barrier akin to ASR_{AT}, which may, in part, be due to the relocation of the remaining cavity charges.

The removal of the S_1 barrier at the −120° twisted transition state can thus be directly connected to the interaction between the chromophore orientation, its torsion-induced charge translocation, and the Q83 side chain. While we cannot presently provide a quantitative analysis, our computations reveal two effects. First (see Figure 7A), there is an evident reorientation of the π-conjugated chain along the reaction path and the side-chain of the Q83 residue (compare the torsional

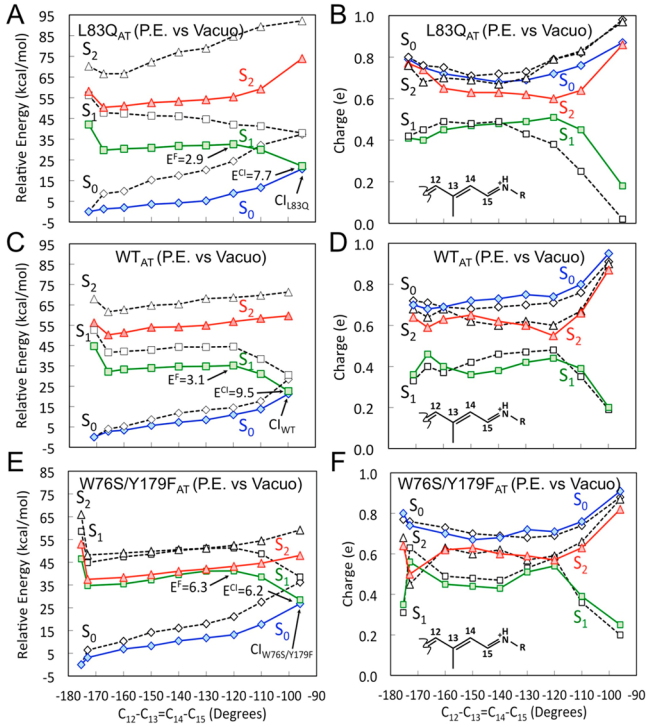

Figure 6. Energy profiles along the S_1 isomerization paths of Figure 3 for the chromophore *in vacuo*. (A,C,E) CASPT2//CASSCF/AMBER energy profiles for the S_1 state (green squares) of L83Q, WT, and W76S/Y179F, respectively. S_0 (blue diamonds) and S_2 (red triangles) profiles along the same path. (B,D,F) Corresponding Mulliken charge variation of the −CH−CH−CH−CH−NH_2 moiety of the chromophore of L83Q, WT, and W76S/Y179F, respectively. In all panels, the dashed energy profiles represent the corresponding energy profiles of the entire protein models (i.e., from Figure 3).

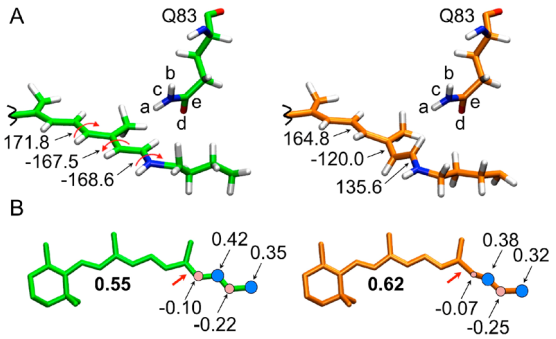

Figure 7. Geometrical and charge distribution variations along the S_1 isomerization path of L83Q (see Figure 3A). (A) Geometrical variation documented by three critical dihedral angles (curly arrows). The left structure corresponds to the second point along the energy profile of Figure 3A (i.e., the point corresponding to MIN_{WT} and $MIN_{W76S/Y179}$), while the right structure is the "transition state" structure featuring a −120 °C_{12}−C_{13}=C_{14}−C_{15} dihedral angle. (B) Charge distribution data for the same two structures.

deformation of the left structure corresponding to the second point along the path of Figure 3A with the "transition state" structure featuring a −120° twisted C_{13}=C_{14} double bond). Second (see Figure 7B), the charge transfer character is increasing along the path thereby enhancing the intensity of the interaction between chromophore and the dipolar Q83 side-chain. Our results suggest that, in the presence of the Q83 side-chain charges, the "transition state structure" gets

DOI: 10.1021/jacs.8b09311
J. Am. Chem. Soc. 2019, 141, 262−271

stabilized on S_1 with respect to the earlier structures along the path, and this leads to the disappearance of the S_1 barrier. However, such electrostatic stabilization is not an obvious effect as it depends on the exact reorientation of the chromophore during the isomerization and on the change in 1Bu character.

In Figure 6C–E, we report the same *in vacuo* analysis for WT and W76S/Y179F. Remarkably, in both cases there are no qualitative changes in the energy profiles indicating that the S_1 barrier is not associated to electrostatic interaction but that it is an intrinsic feature of the chromophore geometrical changes along the two paths. This conclusion is also valid for the S_2/S_1 degeneracy region of W76S/Y179F, which is maintained after removal of the protein electrostatic field. Furthermore, as we show in the SI, it is possible to transform the WT S_2, S_1, and S_0 energy profiles into W76S/Y179F-like energy profiles by simply changing the backbone dihedral angles along the WT reaction coordinate to the corresponding W76S/Y179F values. This is remarkable because those are limited changes that indicate the fluorescent tuning in rhodopsins might be achieved also through subtle geometrical effects.

CONCLUSIONS

Above we have looked at the origin of experimentally observed fluorescence QY and ESL variations in the DA state of ASR. While mutants of other microbial rhodopsins (e.g., bacteriorhodopsin and proteorhodopsin)[36] display an ESL increase, in our study we have reported on an electronic state mixing mechanism for ESL and fluorescence QY enhancement. In order to do so, the stationary and transient spectral parameters for WT and for L83Q and W76S/Y179 have been measured. Remarkably, while both mutants display, with respect to WT, blue-shifted absorption maxima, the measurements reveal opposite ESL changes. Indeed, while it is found that the W76S/Y179F mutant has a picosecond lifetime with a fluorescence QY not too far from the improved Arch3 mutants applied in optogenetics, L83Q fluoresces very weakly and undergoes all-*trans* to 13-*cis* isomerization on a ca. 200 fs time scale.

By using the ASR_{AT} isomer as a DA state model, we show that MCQC-based QM/MM models are capable to reproduce the observed trends in absorption, emission, and ESL indicating their suitability for mechanistic studies. Accordingly, reaction path and trajectory computations show, consistently, that the observed change in ESL is due to an opposite change in charge transfer character of the S_1 state of the molecule. Such changes that can be described as an increase in unreactive 2Ag diradical character along the L83Q, WT, and W76S/Y179F series do not regard the FC region but a critical segment of the reaction path or trajectory where the rhodopsin chromophore is significantly twisted. This mechanism is different from others that have been proposed for ESL increase in microbial rhodopsins.[37] Notice that a 2Ag/1Bu degeneracy has been reported for the retinal chromophore in solution in both computational[38] and experimental[39] studies.

While the nature of the electronic character variation causing the fluorescence enhancement is found to be consistently the same, QM/MM model analysis points to very different residue-level mechanisms responsible for such variations. In other words, the residue replacements in L83Q and W76S/Y179F appear to operate via dramatically different effects. The L83Q to WT variation is dominated by an electrostatic effect, while the WT to W76S/Y179F variation is controlled by steric effects: a change in the details of the isomerization coordinate.

Even if two mutants form a limited set, the consistency of the experimentally observed and simulated quantities confer a high significance to the described findings, which have a direct impact in the design of highly fluorescent rhodopsins. The most significant of these finding is the undeniable intrinsic complexity of the regulation of a basic spectroscopic property such as light emission. In the presented examples, such complexity shows up dramatically even upon a one–two residue replacement and discourages the extraction of simple "rules-of-thumb", which are sometimes introduced, in our opinion inappropriately, in the context of color tuning. However, our study suggests that the extension of the present study to an entire array of mutants may reveal if a rapidly computable structure such as the −120° TS located above, and the actual S_1/S_2 degree of mixing, can be used for practical *in silico* screening of fluorescent mutants.

As stressed above, the increase in ESL is a factor necessary for employing rhodopsins as fluorescence reporters. Another factor is the sensitivity to voltage changes across the membrane. While a robust study of voltage sensitivity of the ASR_{AT} W76S/Y179F mutant goes beyond the scope of the present work, in the SI we report the result of a preliminary computational investigation. In such study, we have probed the sensitivity of the λ^{f}_{max} and oscillator strength values of the ASR_{AT} W76S/Y179F QM/MM model to an increase/decrease in the number of external ions in the inner/outer surfaces of the protein (see Figure 1A). The result indicates that the λ^{f}_{max} is sensitive to the change in external ion concentration, which is assumed to provide a suitable model for voltage variation. Accordingly, ASR_{AT} W76S/Y179F or its variants may lead to promising voltage reporters for observing either the change in fluorescence intensity at a specific wavelength or the change in λ^{f}_{max} as a function of time.

ASSOCIATED CONTENT

Supporting Information

The Supporting Information is available free of charge on the ACS Publications website at DOI: 10.1021/jacs.8b09311.

QM/MM model, computation and experimental details, and voltage sensitivity (PDF)

QM/MM ground state optimized structures of ASR WT (PDB), L83Q (PDB) and W76S/Y179F mutants (PDB)

AUTHOR INFORMATION

Corresponding Authors

*molivuc@bgsu.edu

*stefan.haacke@ipcms.unistra.fr

ORCID

Hideki Kandori: 0000-0002-4922-1344

Massimo Olivucci: 0000-0002-8247-209X

Author Contributions

◆María del Carmen Marín and Damianos Agathangelou contributed equally.

Notes

The authors declare no competing financial interest.

ACKNOWLEDGMENTS

The research has been supported by the following grants NSF CHE-CLP-1710191 and NIH GM126627 01. M.O. is grateful

DOI: 10.1021/jacs.8b09311
J. Am. Chem. Soc. 2019, 141, 262–271

for a USIAS 2015 grant. S.H. is grateful for support by the French-German ANR-DFG grant Femto-ASR (ANR-14-CE35-0015-01), by the Labex NIE (ANR-11-LABX- 0058_NIE), and by "région Alsace" (Ph.D. grant D.A.). The France-Korea collaboration is supported by CNRS in the framework of the "LIA NanoFunc". H.K. is grateful for support from MEXT (Japan) and CREST-JST (Japan). K.H.J. is grateful for grant NRF-2016R1A6A3A11934084 (South Korea). We thank Dr. Luca De Vico for technical help with the computations and for valuable discussions. We thank Mr. Shinya Sugita and Ms. Aki Nemoto for their help with sample preparation. USIAS (University of Strasbourg), NSF, NIH, MEXT, CREST-JST, NRF.

REFERENCES

(1) Berndt, A.; Lee, S. Y.; Ramakrishnan, C.; Deisseroth, K. Structure-guided transformation of channelrhodopsin into a light-activated chloride channel. *Science* **2014**, *344*, 420−424.
(2) Kralj, J. M.; Douglass, A. D.; Hochbaum, D. R.; Maclaurin, D.; Cohen, A. E. Optical recording of action potentials in mammalian neurons using a microbial rhodopsin. *Nat. Methods* **2012**, *9*, 90−95.
(3) Gong, Y.; Wagner, M. J.; Li, J. Z.; Schnitzer, M. J. Imaging neural spiking in brain tissue using FRET-opsin protein voltage sensors. *Nat. Commun.* **2014**, *5*, 3674.
(4) Kralj, J. M.; Hochbaum, D. R.; Douglass, A. D.; Cohen, A. E. Electrical Spiking in Escherichia coli Probed with a Fluorescent Voltage-Indicating Protein. *Science* **2011**, *333*, 345−348.
(5) Gong, Y.; Li, J. Z.; Schnitzer, M. J. Enhanced Archaerhodopsin Fluorescent Protein Voltage Indicators. *PLoS One* **2013**, *8*, No. e66959.
(6) Looger, L. L.; Griesbeck, O. Genetically encoded neural activity indicators. *Curr. Opin. Neurobiol.* **2012**, *22*, 18−23. Looger, L. L. Running in reverse: rhodopsins sense voltage. *Nat. Methods* **2012**, *9*, 43. Mutoh, H.; Akemann, W.; Knöpfel, T. Genetically engineered fluorescent voltage reporters. *ACS Chem. Neurosci.* **2012**, *3*, 585−592. McIsaac, R. S.; Engqvist, M. K. M.; Wannier, T.; Rosenthal, A. Z.; Herwig, L.; Flytzanis, N. C.; Imasheva, E. S.; Lanyi, J. K.; Balashov, S. P.; Gradinaru, V.; Arnold, F. H. Directed evolution of a far-red fluorescent rhodopsin. *Proc. Natl. Acad. Sci. U. S. A.* **2014**, *111*, 13034−13039.
(7) Flytzanis, N. C.; Bedbrook, C. N.; Chiu, H.; Engqvist, M. K. M.; Xiao, C.; Chan, K. Y.; Sternberg, P. W.; Arnold, F. H.; Gradinaru, V. Archaerhodopsin variants with enhanced voltage-sensitive fluorescence in mammalian and Caenorhabditis elegans neurons. *Nat. Commun.* **2014**, *5*, 4894.
(8) Hochbaum, D. R.; Zhao, Y.; Farhi, S. L.; Klapoetke, N.; Werley, C. A.; Kapoor, V.; Zou, P.; Kralj, J. M.; Maclaurin, D.; Smedemark-Margulies, N.; Saulnier, J. L.; Boulting, G. L.; Straub, C.; Cho, Y. K.; Melkonian, M.; Wong, G. K.-S.; Harrison, D. J.; Murthy, V. N.; Sabatini, B. L.; Boyden, E. S.; Campbell, R. E.; Cohen, A. E. All-optical electrophysiology in mammalian neurons using engineered microbial rhodopsins. *Nat. Methods* **2014**, *11*, 825−833.
(9) Maclaurin, D.; Venkatachalam, V.; Lee, H.; Cohen, A. E. Mechanism of voltage-sensitive fluorescence in a microbial rhodopsin. *Proc. Natl. Acad. Sci. U. S. A.* **2013**, *110*, 5939−5944.
(10) Hou, J. H.; Venkatachalam, V.; Cohen, A. E. Temporal Dynamics of Microbial Rhodopsin Fluorescence Reports Absolute Membrane Voltage. *Biophys. J.* **2014**, *106*, 639−648.
(11) Engqvist, M. K. M.; McIsaac, R. S.; Dollinger, P.; Flytzanis, N. C.; Abrams, M.; Schor, S.; Arnold, F. H. Directed Evolution of Gloeobacter violaceus Rhodopsin Spectral Properties. *J. Mol. Biol.* **2015**, *427*, 205−220.
(12) Piatkevich, K. D.; Jung, E. E.; Straub, C.; Linghu, C.; Park, D.; Suk, H.-J.; Hochbaum, D. R.; Goodwin, D.; Pnevmatikakis, E.; Pak, N. A robotic multidimensional directed evolution approach applied to fluorescent voltage reporters. *Nat. Chem. Biol.* **2018**, *14*, 352.
(13) Herwig, L.; Rice, A. J.; Bedbrook, C. N.; Zhang, R. K.; Lignell, A.; Cahn, J. K. B.; Renata, H.; Dodani, S. C.; Cho, I.; Cai, L.; Gradinaru, V.; Arnold, F. H. Directed Evolution of a Bright Near-Infrared Fluorescent Rhodopsin Using a Synthetic Chromophore. *Cell Chem. Biol.* **2017**, *24*, 415−425. Hontani, Y.; Ganapathy, S.; Frehan, S.; Kloz, M.; DeGrip, W. J.; Kennis, J. T. M. Strong pH-Dependent Near-Infrared Fluorescence in a Microbial Rhodopsin Reconstituted with a Red-Shifting Retinal Analogue. *J. Phys. Chem. Lett.* **2018**, *9*, 6469.
(14) Kawanabe, A.; Furutani, Y.; Jung, K. H.; Kandori, H. Photochromism of Anabaena sensory rhodopsin. *J. Am. Chem. Soc.* **2007**, *129*, 8644−8649.
(15) Cheminal, A.; Léonard, J.; Kim, S. Y.; Jung, K.-H.; Kandori, H.; Haacke, S. Steady state emission of the fluorescent intermediate of Anabaena Sensory Rhodopsin as a function of light adaptation conditions. *Chem. Phys. Lett.* **2013**, *587*, 75−80.
(16) Vogeley, L.; Sineshchekov, O. A.; Trivedi, V. D.; Sasaki, J.; Spudich, J. L.; Luecke, H. Anabaena sensory rhodopsin: a photochromic color sensor at 2.0 A. *Science* **2004**, *306*, 1390−1393.
(17) Luk, H. L.; Melaccio, F.; Rinaldi, S.; Gozem, S.; Olivucci, M. Molecular bases for the selection of the chromophore of animal rhodopsins. *Proc. Natl. Acad. Sci. U. S. A.* **2015**, *112*, 15297−15302.
(18) McIsaac, R. S.; Bedbrook, C. N.; Arnold, F. H. Recent Advances in Engineering Microbial Rhodopsins for Optogenetics. *Curr. Opin. Struct. Biol.* **2015**, *33*, 8−15. Deisseroth, K. Optogenetics. *Nat. Methods* **2011**, *8*, 26−29.
(19) Jung, K.-H.; Trivedi, V. D.; Spudich, J. L. Demonstration of a sensory rhodopsin in eubacteria: Sensory rhodopsin in eubacteria. *Mol. Microbiol.* **2003**, *47*, 1513−1522. Choi, A. R.; Kim, S. Y.; Yoon, S. R.; Bae, K.; Jung, K.-H. Substitution of Pro206 and Ser86 residues in the retinal binding pocket of Anabaena sensory rhodopsin is not sufficient for proton pumping function. *J. Microbiol. Biotechnol.* **2007**, *17*, 138−145.
(20) Gueye, M.; Nillon, J.; Crégut, O.; Léonard, J. Broadband UV-Vis vibrational coherence spectrometer based on a hollow fiber compressor. *Rev. Sci. Instrum.* **2016**, *87*, 093109.
(21) Bradler, M.; Baum, P.; Riedle, E. Femtosecond continuum generation in bulk laser host materials with sub-μJ pump pulses. *Appl. Phys. B: Lasers Opt.* **2009**, *97*, 561−574.
(22) Melaccio, F.; del Carmen Marín, M.; Valentini, A.; Montisci, F.; Rinaldi, S.; Cherubini, M.; Yang, X.; Kato, Y.; Stenrup, M.; Orozco-Gonzalez, Y.; Ferré, N.; Luk, H. L.; Kandori, H.; Olivucci, M. Toward Automatic Rhodopsin Modeling as a Tool for High-Throughput Computational Photobiology. *J. Chem. Theory Comput.* **2016**, *12*, 6020−6034.
(23) Roos, B. O. In *Ab Initio Methods in Quantum Chemistry II*; Lawley, K. P., Ed.; Wiley & Sons: Chichester, 1987; pp 399−445.
(24) Andersson, K.; Malmqvist, P. A.; Roos, B. O.; Sadlej, A. J.; Wolinski, K. Second-order perturbation theory with a CASSCF reference function. *J. Phys. Chem.* **1990**, *94*, 5483−5488.
(25) Aquilante, F.; Autschbach, J.; Carlson, R. K.; Chibotaru, L. F.; Delcey, M. G.; De Vico, L.; Fernandez Galván, I.; Ferré, N.; Frutos, L. M.; Gagliardi, L.; Garavelli, M.; Giussani, A.; Hoyer, C. E.; Li Manni, G.; Lischka, H.; Ma, D.; Malmqvist, P.-Å.; Müller, T.; Nenov, A.; Olivucci, M.; Pedersen, T. B.; Peng, D.; Plasser, F.; Pritchard, B.; Reiher, M.; Rivalta, I.; Schapiro, I.; Segarra-Martì, J.; Stenrup, M.; Truhlar, D. G.; Ungur, L.; Valentini, A.; Vancoillie, S.; Veryazov, V.; Vysotskiy, V. P.; Weingart, O.; Zapata, F.; Lindh, R. Molcas 8: New capabilities for multiconfigurational quantum chemical calculations across the periodic table. *J. Comput. Chem.* **2016**, *37*, 506−541.
(26) Ponder, J. W.; Richards, F. M. An efficient newton-like method for molecular mechanics energy minimization of large molecules. *J. Comput. Chem.* **1987**, *8*, 1016−1024.
(27) Ferré, N.; Olivucci, M. Probing the Rhodopsin Cavity with Reduced Retinal Models at the CASPT2//CASSCF/AMBER Level of Theory. *J. Am. Chem. Soc.* **2003**, *125*, 6868−6869. Ferré, N.; Cembran, A.; Garavelli, M.; Olivucci, M. Complete-active-space self-consistent-field/Amber parameterization of the Lys296-retinal-

DOI: 10.1021/jacs.8b09311
J. Am. Chem. Soc. 2019, 141, 262−271

Glu113 rhodopsin chromophore-counterion system. *Theor. Chem. Acc.* **2004**, *112*, 335−341.
(28) Gozem, S.; Luk, H. L.; Schapiro, I.; Olivucci, M. Theory and Simulation of the Ultrafast Double-Bond Isomerization of Biological Chromophores. *Chem. Rev.* **2017**, *117*, 13502−13565.
(29) Manathunga, M.; Yang, X.; Orozco-Gonzalez, Y.; Olivucci, M. Impact of Electronic State Mixing on the Photoisomerization Timescale of the Retinal Chromophore. *J. Phys. Chem. Lett.* **2017**, *8*, 5222−5227.
(30) Michl, J.; Bonačić-Koutecký, V. *Electronic Aspects of Organic Photochemistry*; Wiley: New York, 1990.
(31) Manathunga, M.; Yang, X.; Olivucci, M. Electronic State Mixing Controls the Photoreactivity of a Rhodopsin with All-trans Chromophore Analogues. *J. Phys. Chem. Lett.* **2018**, *9*, 6350−6355.
(32) Bonačić-Koutecký, V.; Schöffel, K.; Michl, J. Critically heterosymmetric biradicaloid geometries of of protonated Schiff bases. *Theor. Chim. Acta* **1987**, *72*, 459−474.
(33) Agathangelou, D.; Orozco-Gonzalez, Y.; del Carmen Marín, M.; Roy, P. P.; Brazard, J.; Kandori, H.; Jung, K.-H.; Léonard, J.; Buckup, T.; Ferré, N.; Olivucci, M.; Haacke, S. Effect of point mutations on the ultrafast photo-isomerization of Anabaena sensory rhodopsin. *Faraday Discuss.* **2018**, *207*, 55−75.
(34) Kouyama, T.; Kinosita, K.; Ikegami, A. Excited-state dynamics of bacteriorhodopsin. *Biophys. J.* **1985**, *47*, 43−54.
(35) Manathunga, M.; Yang, X.; Luk, H. L.; Gozem, S.; Frutos, L. M.; Valentini, A.; Ferré, N.; Olivucci, M. Probing the Photodynamics of Rhodopsins with Reduced Retinal Chromophores. *J. Chem. Theory Comput.* **2016**, *12*, 839−850.
(36) Song, L.; El-Sayed, M. A.; Lanyi, J. K. Protein catalysis of the retinal subpicosecond photoisomerization in the primary process of bacteriorhodopsin photosynthesis. *Science* **1993**, *261*, 891−894. Kennis, J. T. M.; Larsen, D. S.; Ohta, K.; Facciotti, M. T.; Glaeser, R. M.; Fleming, G. R. Ultrafast protein dynamics of bacteriorhodopsin probed by photon echo and transient absorption spectroscopy. *J. Phys. Chem. B* **2002**, *106*, 6067−6080. Van Stokkum, I. H. M.; Gobets, B.; Gensch, T.; van Mourik, F.; Hellingwerf, K. J.; van Grondelle, R.; Kennis, J. T. M. (Sub)-picosecond spectral evolution of fluorescence in photoactive proteins studied with a synchroscan streak camera system. *Photochem. Photobiol.* **2006**, *82*, 380−388.
(37) Tahara, S.; Takeuchi, S.; Abe-Yoshizumi, R.; Inoue, K.; Ohtani, H.; Kandori, H.; Tahara, T. Origin of the Reactive and Nonreactive Excited States in the Primary Reaction of Rhodopsins: pH Dependence of Femtosecond Absorption of Light-Driven Sodium Ion Pump Rhodopsin KR2. *J. Phys. Chem. B* **2018**, *122*, 4784−4792. Hontani, Y.; Marazzi, M.; Stehfest, K.; Mathes, T.; Stokkum, I. H. M.; Elstner, M.; Hegemann, P.; Kennis, J. T. M. Reaction dynamics of the chimeric channelrhodopsin C1C2. *Sci. Rep.* **2017**, *7*, 7217. Dokukina, I.; Weingart, O. Spectral properties and isomerisation path of retinal in C1C2 channelrhodopsin. *Phys. Chem. Chem. Phys.* **2015**, *17*, 25142.
(38) Muñoz-Losa, A.; Fdez Galván, I.; Aguilar, M. A.; Martín, M. E. Retinal models: comparison of electronic absorption spectra in the gas phase and in methanol solution. *J. Phys. Chem. B* **2008**, *112*, 8815−8823. Demoulin, B.; Altavilla, S. F.; Rivalta, I.; Garavelli, M. Fine Tuning of Retinal Photoinduced Decay in Solution. *J. Phys. Chem. Lett.* **2017**, *8*, 4407−4412. Munoz-Losa, A.; Ignacio, I.; Aguilar, M. A.; Martín, M. E. Simultaneous Solvent and Counterion Effects on the Absorption Properties of a Model of the Rhodopsin Chromophore. *J. Chem. Theory Comput.* **2013**, *9*, 1548−1556.
(39) Nielsen, I. B.; Lammich, L.; Andersen, L. H. S1 andS2 Excited States of Gas-Phase Schiff-Base Retinal Chromophores. *Phys. Rev. Lett.* **2006**, *96*, 018304.

DOI: 10.1021/jacs.8b09311
J. Am. Chem. Soc. 2019, 141, 262−271

SUPPORTING INFORMATION

Fluorescence enhancement of a microbial rhodopsin via electronic reprogramming

María del Carmen Marín[†,¶], Damianos Agathangelou[§], Yoelvis Orozco-Gonzalez[¶,‡], Alessio Valentini[#], Yoshitaka Kato[¶¶], Rei Abe-Yoshizumi[¶¶,¶¶¶], Hideki Kandori[¶¶,¶¶¶], Ahreum Choi[§§], Kwang-Hwan Jung[§§], Stefan Haacke[§,*], and Massimo Olivucci[†,¶,‡,*]

[†]Biotechnology, Pharmacy and Chemistry Department, University of Siena, Siena, Italy, 53100. [¶]Chemistry Department, Bowling Green State University, Ohio, 43403. [§]University of Strasbourg–CNRS, Institute of Physics and Chemistry of Materials of Strasbourg, 67034 Strasbourg, France. [‡]Université de Strasbourg, USIAS Institut d'Études Avanceés, 67083 Strasbourg, France, [#]Theoretical Physical Chemistry, UR Molsys, University of Liège, Liège, Belgium. [¶¶]Department of Life Science and Applied Chemistry, Nagoya Institute of Technology, Showa-ku, Nagoya, Japan, 466-8555. [¶¶¶]OptoBioTechnology Research Center, Nagoya Institute of Technology, Showa-ku, Nagoya, Japan, 466-8555. [§§]Department of Life Science and Institute of Biological Interfaces, Sogang University, Sogang, South Korea, 04107.

Contents

1. QM/MM models

1.1. Model Construction: Automatic Rhodopsin Modeling (ARM) protocol

Here we report on the detailed workflow for the construction of the selected quantum/molecular mechanics (QM/MM) models of wild-type *Anabaena Sensory Rhodopsin* all-*trans* chromophore (ASR) and its blue-shifted mutants L83Q and W76S/Y179F, discussed in the main text. For the QM/MM, models we employed the Automatic Rhodopsin Modelling (ARM)[1]. This ARM protocol is based on a potential energy minimization of the energy of the cavity, which is a good approximation since the size of this is small enough to consider that the average representation of the environment is properly described by the X-ray crystallographic (or homology model) structure of the rest of the protein. Our target is to construct QM/MM models that can reproduce all the relevant observed spectroscopic data, so that they can be employed to study the molecular mechanics presented in the main text.

The QM/MM models constructed by ARM are gas-phase and globally uncharged monomer models. The model is divided into the three systems called environment, cavity and Lys-QM. The environment has backbone and side-chain atoms fixed at the crystallographic (or homology) structure, and, incorporates suitable placed external counterions also kept fixed at computed positions. ARM models do not incorporate the environment provided by the complex hydrated membrane. The effect of the protein environment is indirectly incorporated with the introduction of Cl^- and Na^+ counterions, which generated a model with neutral (zero charge) inner and outer surfaces. The cavity, which includes the Lys-QM system, also features fixed backbone atoms but its side-chain atoms are free to relax. The Lys-QM system comprises the atoms of the Lysine side-chain in contact (thought C_δ) with the QM/MM frontier and the entire QM subsystem, which corresponds to a N-methylated retinal chromophore. All Lys-QM atoms are free to relax. The environment, cavity and Lysine side-chain form the MM subsystem[2–5]. ARM models feature a fixed environment system and are conservative in the sense that they ensure that the information from the X-Ray crystallographic structure is retained in the final QM/MM model.

ARM employs the multi-configurational complete active space self-consistent field (CASSCF)[6,7] method to obtain ground state geometries (single-root CASSCF(12,12)/6-31G*/AMBER optimization). Excitation energies are then computed using multi-configurational second-order perturbation theory (CASPT2)[8–11] to recover the missing dynamical electron correlation associated with the CASSCF description (three-roots stage average single point CASPT2/6-31G*/AMBER calculation, taking a three-roots stage average (SA) CASSCF(12,12)/6-31G* wave function as a reference). All QM/MM calculations were performed with TINKER 6.3[12], GROMACS 4.5.4[13] and MOLCAS 8.1[14].

To compute the vertical excitation energies of each rhodopsin, with the aim of comparing them with the experimental absorption spectra, we run in parallel, consistently with the ARM protocol, N molecular dynamics (N=10) each run being 1 ns long, on the whole protein structure. From these ten runs, we have ten equilibrium structures, from each of which, after a QM/MM optimization of the chromophore, we compute the vertical excitation energy, again in a QM/MM fashion. This gives ten values of each vertical excitation energy for each rhodopsin, and we calculate the average of these ten values to obtain the computed value to compare to the experimental one. Since we have ten QM/MM models in each ARM cycle, the model employed to compute the Franck-Condon trajectories and to start relaxed scans correspond with the representative structure defined as the one with the vertical excitation energy closest to the value averaged over all ten vertical excitation energies.

The ASR all-*trans* models were prepared starting from the PDB crystallographic structure 1XIO (resolution 2.5Å)[15], which show a mixture of the 13-*cis* and all-*trans* chromophores. Membrane lipids at

the protein surface were not included, while all the crystallographic water molecules were maintained. Amino acid ionization states were determined with PROPKA 3.0[16] and visual inspection. Consequently Asp217, His8, His69 and His219 were protonated (His8 and His219 on the δ nitrogen; His69 on the ε nitrogen). CASTp[17] was used to get the list of cavity residues.

1.2. Trajectory Computations

Excited state (S_1) trajectories were calculated using Molcas module Dynamix which is described in more details in reference[18]. The trajectories were calculated at two-root state-averaged CASSCF/6-31G*/AMBER level followed by three-root state-average CASPT2 corrections (also used to scale the CASSCF energy profiles). Since we are only interested in the evolution on S_1 from the Franck-Condon (FC) point to the Conical Intersection (CI) region, all trajectories were propagated until entering the region of a S_1/S_0 CI, according with the energy and wave function criteria implemented in Dynamix module[18] or until research 200 fs time threshold. The ultrafast lifetime of these processes should ensure that the FC trajectory (i.e. trajectory starting from the Frank-Condon point with zero initial velocities) describes the average evolution of the corresponding S_1 population as discussed in the main text.

Trajectory calculations were always performed using two, rather than three, state-averaged roots as best compromise for the quality of the S_1 CASSCF wave function. In fact, while a charge-transfer character dominates S_1 state and S_0 has a covalent (closed shell) character, the third root (S_2) has a covalent (diradical) character. We found in the literature[19] that the three-root wave function has a far to high covalent character. This may lead to an S_1 gradient, which may significantly deviate, from the correct one as the system progress towards the S_1/S_0 (or S_2/S_1) conical intersections. Hence, all trajectories were performed at two state-averaged roots to maintain a more balanced description of the charge transfer character and covalent character in the S_1 wave function. Actually, to account for the effect of the S_2 state on the energy profiles correctly, we went beyond the CASSCF representation and corrected the energy profiles and oscillator strengths at the CASPT2 level using, as zeroth order wave functions, three state-averaged CASSCF wave functions.

2. Computational Details

2.1. Excitation Energies

Table S1. Observed vs computed vertical excitation energies $\Delta E_{S1\text{-}S0}$ (kcal/mol) and maximum absorption wavelengths (λ^a_{max}) (nm) for ASR wild-type (WT) and its mutants L83Q and W76S/Y179F ARM models, computed at CASPT2/CASSCF(12,12)/6-31G*/AMBER level of theory. Oscillator strength (f_{Osc}) and standard deviation (DEV.ST) are also shown.

Sample	Observed $\Delta E_{S1\text{-}S0}$ (λ^a_{max})	Computed $\Delta E_{S1\text{-}S0}$ (λ^a_{max})	Error	DEV.ST	f_{Osc}
WT_{AT}	52.0 (549)	52.6 (543)	0.6	1.0218	1.14
WT_{13C}	53.3 (536)	54.5 (524)	1.2	0.6748	0.98
$L83Q_{AT}$	55.3 (517)	56.2 (508)	0.7	0.3503	1.17
$L83Q_{13C}$	54.6 (526)	55.2 (518)	0.6	0.1619	1.10
$W76S/Y179F_{AT}$	58.6 (488)*	58.5 (488)	-0.1	0.9982	0.99
$W76S/Y179F_{13C}$	---	59.2 (482)	0.5	1.0293	1.05

*From OA sample where the all-*trans* is the dominant)

2.2. Electrostatic Effects

We focus on the differences between ASR_{AT} WT model and L83Q and W76S/Y179F mutant models. Mutants are challenging to model due to the smaller changes observed in ΔE_{S1-S0} values and the absence of crystallographic data. The mutants studied show significant blue-shifts with respect to the WT reference, as we carefully describe in the main text. We have computationally disentangled the electrostatic and steric effects causing the total blue-shifts by computing the ΔE_{S1-S0} values of the three chromophores in the gas phase (keeping the chromophore geometries fixed at their optimized protein structure). By comparing the electrostatic and steric effects of the different chromophore cavities (Fig. S1), we show that the electrostatic effect is the dominant in L83Q mutant (Table S2). However, in the case of W76S/Y179F mutant, the effects in the energy gaps presented in the protein environment, (Table S2) remain also in Vacuo, i.e. the changes in the chromophore geometry are the dominating in the double mutant.

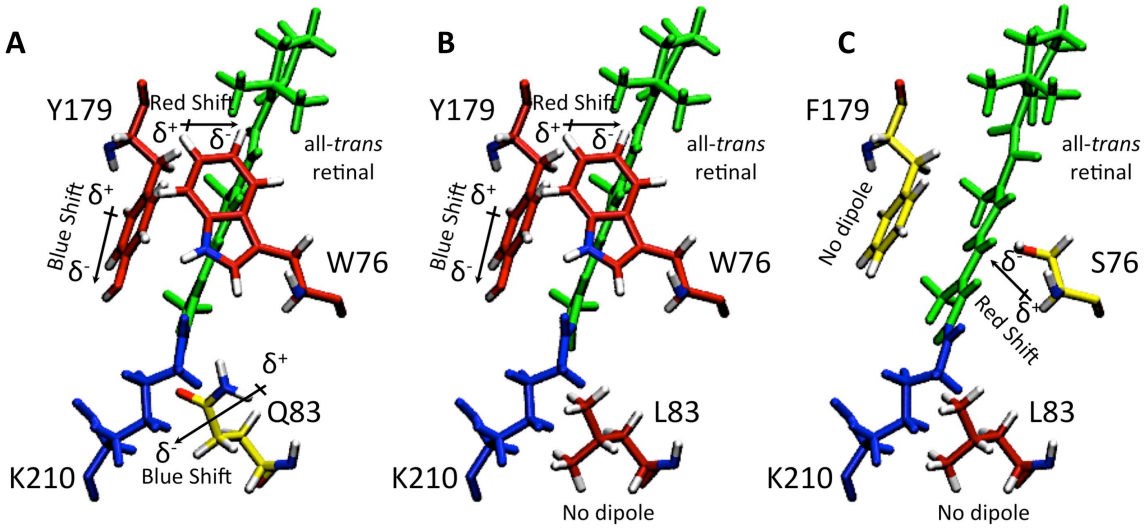

Figure S1. Comparison between ASR_{AT} retinal chromophore and residues 83, 112 and 179 in (A) L83Q mutant, (B) WT model and (C) W76S/Y179F mutant.

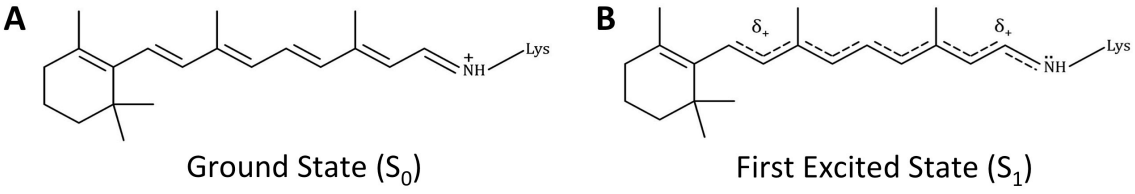

Figure S2. Electronic distribution of (A) ground state (S_0) and (B) first excited state (S_1). In S_0, the protonated Schiff base (PSB) linkage of Lysine and the retinal chromophore is protonated. Photoexcitation in S_1 and the subsequence C=C bond length alternation lead to a partial charge transfer of the positive charge towards the β–ionone ring

These effects are due to the different stabilization of the chromophore ground (S_0) and the first excited states (S_1), which are characterized by different electronic distributions (Figure S2), due to the change in the protein charges and positions induced by the mutation. It is well know that the PSBR's photo-excited state S_1 is characterized by a partial charge transfer (ca. 30%)[20] electronic configuration. On the other hand, S_0 is dominated by a covalent electronic configuration, with the positive charge localized at

the protonated Schiff base. The interactions of both electronic configurations with the mutated PSBR binding cavity explains the observed blue-shifts.

Table S2. CASPT2/CASSCF/6-31G*/AMBER S_1-S_0, S_2-S_0 and S_2-S_1 energy gaps (in kcal/mol) for ASR_{AT} FC structures optimized in the ground state (S_0) (Absorption) and for the minimum (MIN) structures, optimized in the first excited state (S_1) (Emission), when the retinal chromophore is inside the protein (Protein Environment) and in vacuum (Vacuo PSB6), supposing the same conformation as in the protein. This allows separating the dominant electrostatic effect of the mutations from the conformational changes.

Absorption						
	Protein Environment			**Vacuo (PSB6)**		
Sample	**ΔE_{S1-S0} (kcal/mol)**	**ΔE_{S2-S0} (kcal/mol)**	**ΔE_{S2-S1} (kcal/mol)**	**ΔE_{S1-S0} (kcal/mol)**	**ΔE_{S2-S0} (kcal/mol)**	**ΔE_{S2-S1} (kcal/mol)**
WT_{AT}	52.6	67.9	15.3	44.7	56.2	11.5
$L83Q_{AT}$	56.2 (+3.6)	70.2 (+2.3)	14.0 (-1.3)	42.1 (-2.6)	58.1 (+1.9)	16.0 (+4.5)
$W76S/Y179F_{AT}$	58.5 (+5.9)	65.9 (-2.0)	7.4 (-7.9)	46.5 (+1.8)	52.9 (-3.3)	6.5 (-5.0)
Emission						
	Protein Environment			**Vacuo (PSB6)**		
Sample	**ΔE_{S1-S0} (kcal/mol)**	**ΔE_{S2-S0} (kcal/mol)**	**ΔE_{S2-S1} (kcal/mol)**	**ΔE_{S1-S0} (kcal/mol)**	**ΔE_{S2-S0} (kcal/mol)**	**ΔE_{S2-S1} (kcal/mol)**
WT_{AT}	37.7	57.6	19.9	29.3	47.5	18.1
$W76S/Y179F_{AT}$	41.7 (+4.0)	38.4 (-19.0)	-3.3 (-16.6)	34.4 (+5.1)	31.7 (-15.8)	-2.7 (-15.4)

Notice that, as usually found in the literature[21], the chromophores separated from their protein environments present ΔE_{S1-S0} values about 10-20 kcal/mol (ΔE_{S1-S0} Vacuo) lower that the chromophore inside the protein (ΔE_{S1-S0} Protein Environment) (Table S2). Interesting, the mutations on the PSB configuration of L83Q, with respect to the WT, induced a red shift instead of a blue-shift in the ΔE_{S1-S0} value in Vacuo, while ΔE_{S2-S0} value remains blue-shifted in both situations. However, in the case of W76S/Y179F mutant, the effects are the same as in the protein (i.e. blue-shits ΔE_{S1-S0} and ΔE_{S2-S0} values with respect WT). It shows that the change in the chromophore geometry are dominating in the W76S/Y179F mutant and not the environment electrostatics as in the case of L83Q mutant.

2.3. Relaxed Scan

Table S3. Computed ground state (S_0), first excited state (S_1) and second excited state (S_2) energies (a.u.), vertical excitation energies $\Delta E_{S1\text{-}S0}$ and $\Delta E_{S2\text{-}S0}$ (kcal/mol) and maximum absorption and emmision wavelengths (λ^{a}_{max} and λ^{f}_{max}) (nm) for ASR_{AT} WT and its mutants L83Q and W76S/Y179F for S_0 and S_1 mimimum optimized geometries.

Absorption								
Sample	**S_0 Energy**	**S_1 Energy**	**S_2 Energy**	**$\Delta E_{S1\text{-}S0}$ (λ_{max})**	**$\Delta E_{S2\text{-}S0}$ (λ_{max})**	**$fOsc_{S0\text{-}S1}$**	**$fOsc_{S0\text{-}S2}$**	**$fOsc_{S1\text{-}S2}$**
WT_{AT}	-872.008819	-871.925616	-871.900526	52.6 (543)	67.9 (421)	1.14	0.50	0.07
$L83Q_{AT}$	-872.075805	-871.986164	-871.963913	56.2 (508)	70.2 (407)	1.17	0.48	0.06
$W76S/Y179F_{AT}$	-871.964482	-871.871175	-871.859325	58.5 (488)	65.9 (433)	0.99	0.82	0.30
Emission								
Sample	**S_0 Energy**	**S_1 Energy**	**S_2 Energy**	**$\Delta E_{S1\text{-}S0}$ (λ^{f}_{max})**	**$\Delta E_{S2\text{-}S0}$ (λ^{f}_{max})**	**$fOsc_{S0\text{-}S1}$**	**$fOsc_{S0\text{-}S2}$**	**$fOsc_{S1\text{-}S2}$**
WT_{AT}	-872.002426	-871.942391	-871.910630	37.7 (758)	57.6 (496)	1.07	0.52	0.07
$W76S/Y179F_{AT}$	-871.954285	-871.887702	-871.893000	41.7 (685)	38.4 (744)	0.90	0.92	0.42

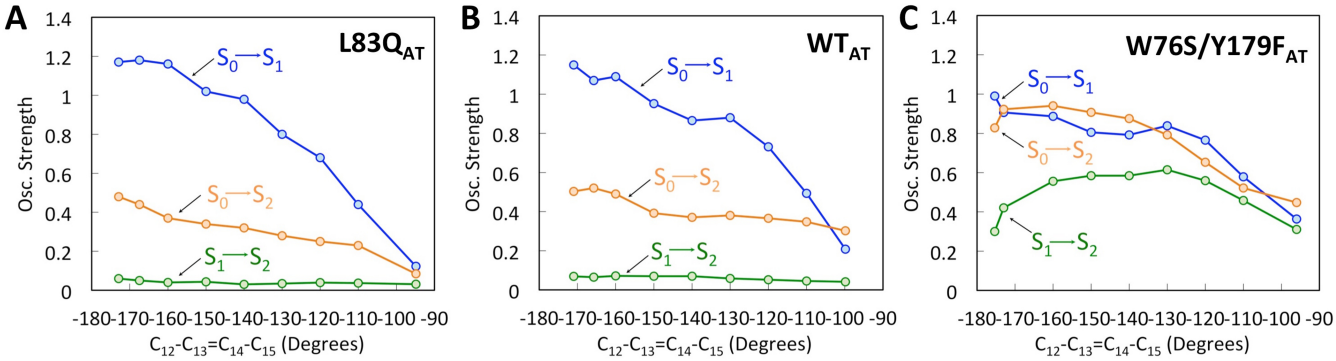

Figure S3. Computed oscillator strengths along the relax scan of ASR_{AT} (A) L83Q mutant (B) wild-type (WT) and, (C) W76S/Y179F double mutant.

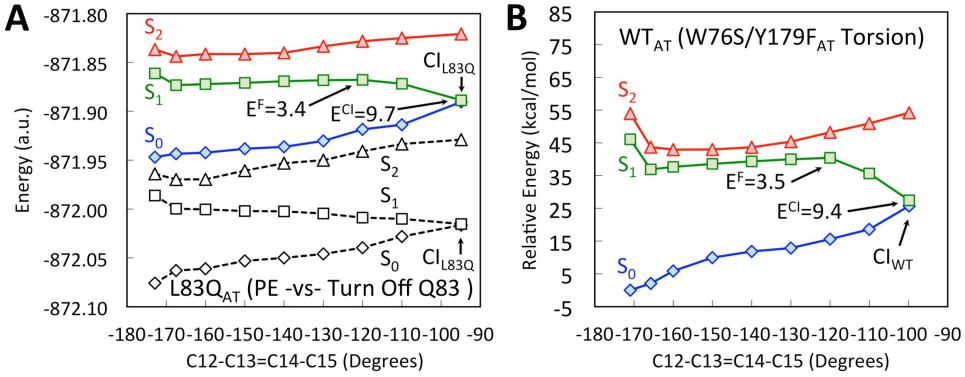

Figure S4. CASPT2//CASSCF(12,12)/AMBER energy profiles along S_1. (A) Protein environment and Vacuo energy profiles comparison of ASR_{AT} L83Q mutant when (absolute energy, a.u.). (B) Vacuo energy profile of ASR_{AT} WT with the torsional angles extracted from the W76S/Y179F mutant. S_0 (red diamonds) and S_2 (blue triangles) profiles along the S_1 (green squares) path are also given. The S_1 is computed in terms of a relaxed scan along C_{12}-C_{13}=C_{14}-C_{15} dihedral angle.

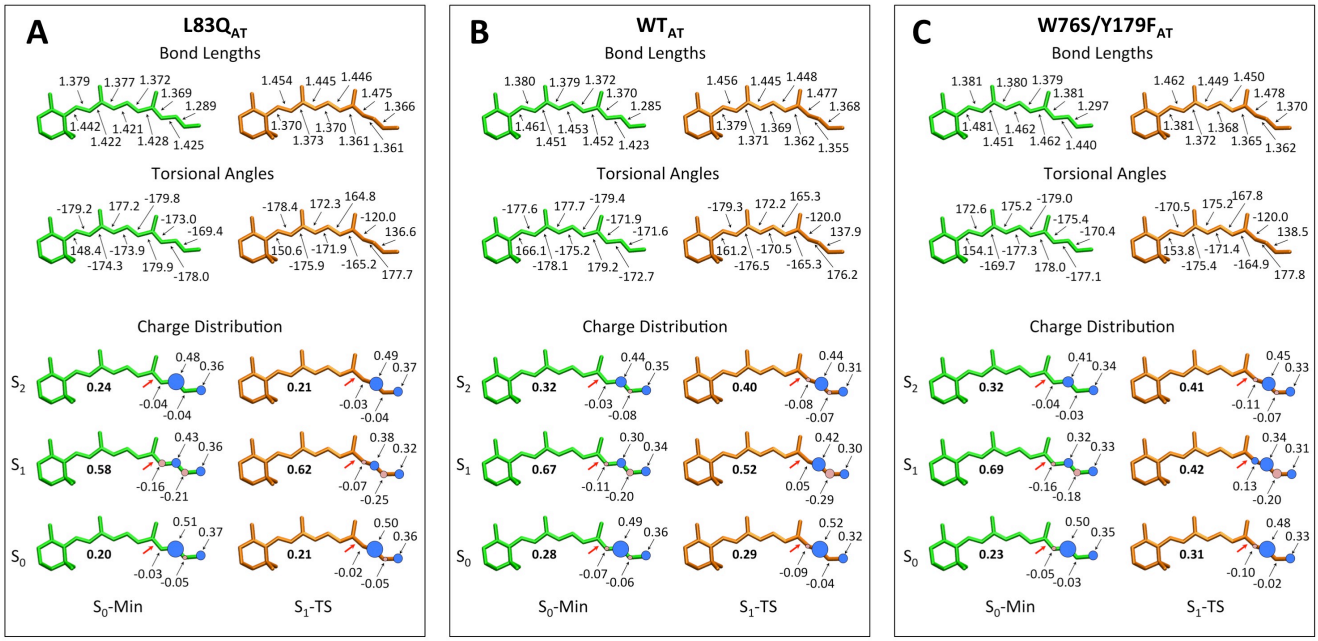

Figure S5. (Top) Franck-Condon (FC) (S_0-Min, green skeleton) and transition state (TS) (S_1-TS, orange skeleton) geometries for ASR_{AT} (A) L83Q mutant, (B) WT model and (C) W76S/Y179F mutant. The relevant bond lengths and backbone dihedral angles are given in Å and degrees, respectively. The geometry denominate as TS geometry of L83Q, is not a saddle point. It was selected at the same point of the relaxed scan correspond with the TS geometries of WT and W76S/Y179F (-120 degrees) to perform a comparison between geometries. (Bottom) Franck-Condon (FC) (S_0-Min, green skeleton) and transition state (TS) (S_1-TS, orange skeleton) charge distribution along ASR_{AT} chromophore backbone for the lowest three electronic states for (A) L83Q mutant, (B) WT model and (C) W76S/Y179F mutant. The charge residing on the β–ionone ring fragment is reported in bold. The red arrow indicates the isomerizing C13=C14 bond.

2.4. Franck-Condon Trajectories

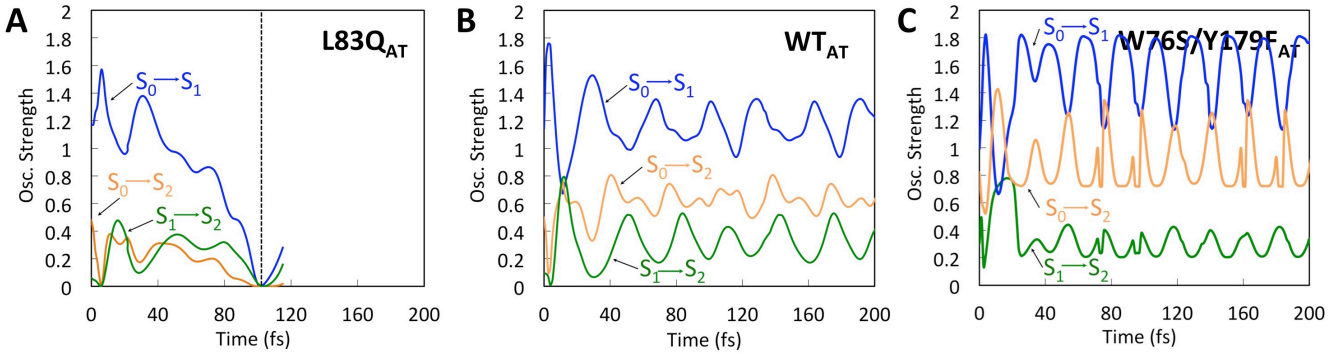

Figure S6 Computed oscillator strengths along the Franck-Condon trajectories of ASR_{AT} (A) L83Q mutant (B) wild-type (WT) and, (C) W76S/Y179F double mutant.

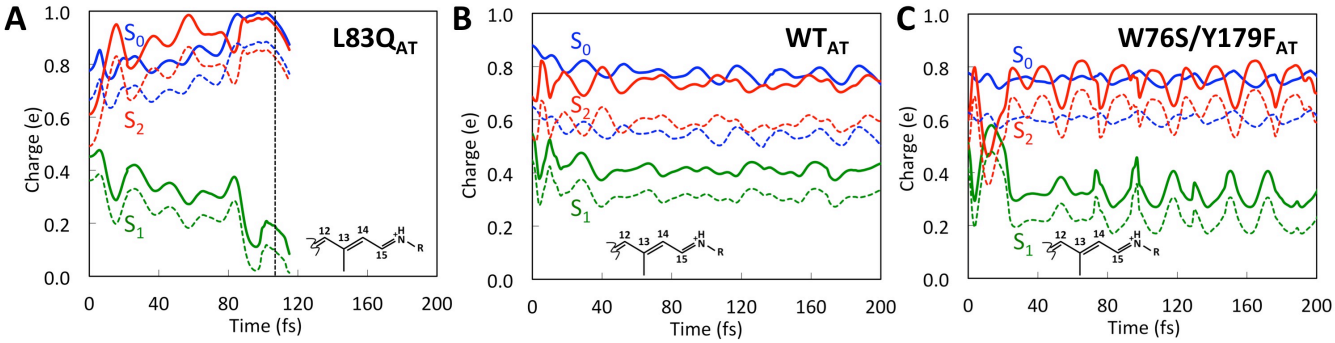

Figure S7. Total positive charge on the displayed moiety (a small charge indicates 1Bu character). Dashed lines represent the charge on the shorter C13(Me)-C14H-C15H-NHR moiety (i.e. relevant to the C13=C14 isomerization).

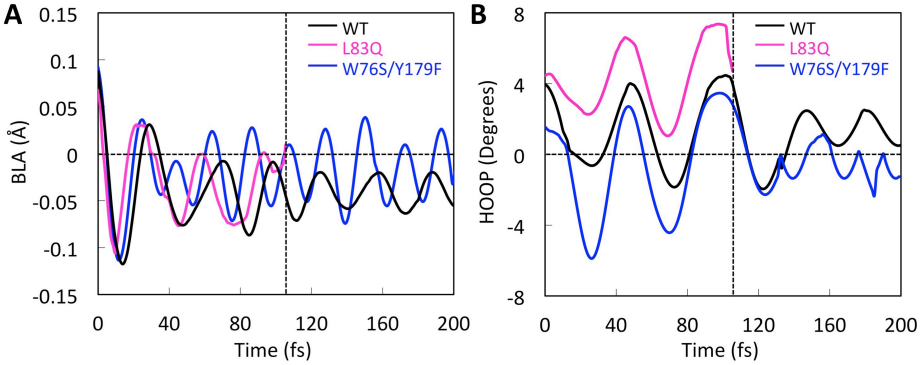

Figure S8. (A) BLA and (B) HOOP evolution along the full conjugated chains for ASR$_{AT}$ WT (black) and its mutants L83Q (pink) and W76S/Y179F (blue) .

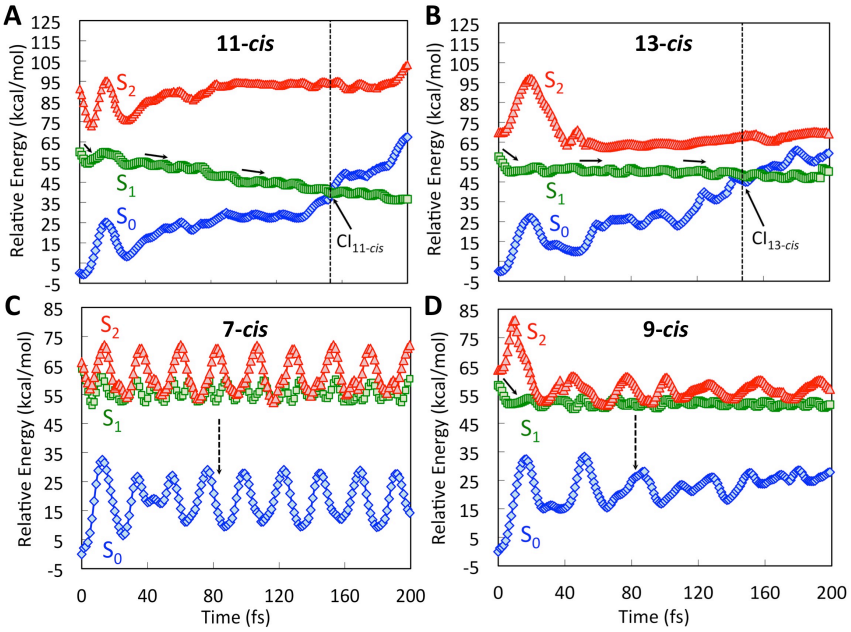

Figure S9. CASPT2 energy profiles of ASR$_{AT}$ W76S/Y179F mutant for the isomers (A) 11-*cis*, (B) 13-*cis*, (C) 7-*cis* and (D) 9-*cis*, along two-root state-averaged CASSCF FC trajectories and corrected at the CASPT2 level. S_0 (red diamonds), S_1 (green squares) and S_2 (blue triangles) CASPT2/CASSCF/AMBER energy profiles along the FC trajectories.

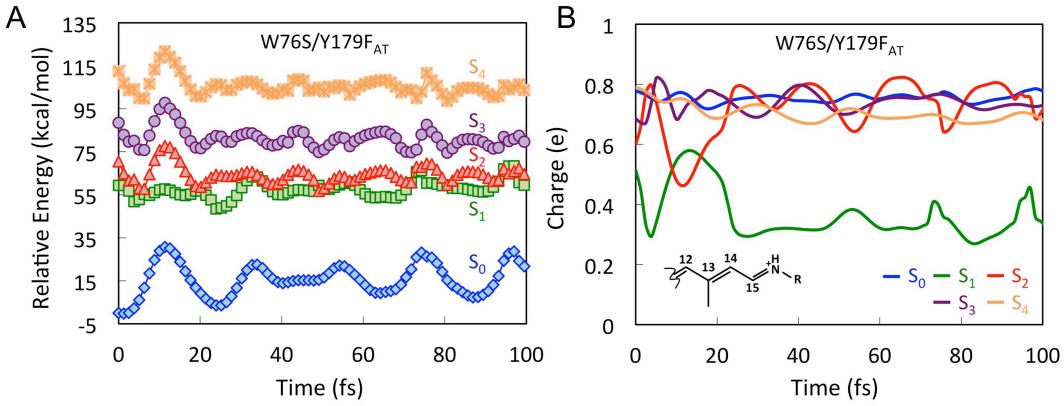

Figure S10. (A) 5-root-state-average CASPT2/CASSCF/6-31G*/Amber Franck-Condon trajectory of ASR_{AT} W76S/Y179F mutant. (B) Evolution of Mulliken charges along the trajectory.

3. Experimental Details

3.1. HPLC Method

An isocratic method was used for the first 10 min of retention time and the eluents ratio was kept 88% Cyclohexane, 12% Ethyl-acetate:Ethanol [100:1], while a linear gradient was applied afterwards reaching a ratio of 75% Cyclohexane, 25% Ethyl-acetate:Ethanol [100:1] by the end of the measurement. The flow rate was kept at 1 mL/min and detection was set at 360nm where AT and 13C retinal oxime derivatives have the same extinction coefficient (ε) value. Determination of each isomers retention time was done by using commercial standards and reference[22]. Scaling of the absorbance of 7-*cis*, 9-*cis*, and 11-*cis* retinal oximes according to their ε was not done since the ε values for 7-*cis* and 9-*cis* were not provided. The -syn and -anti forms of the later were not resolved clearly.

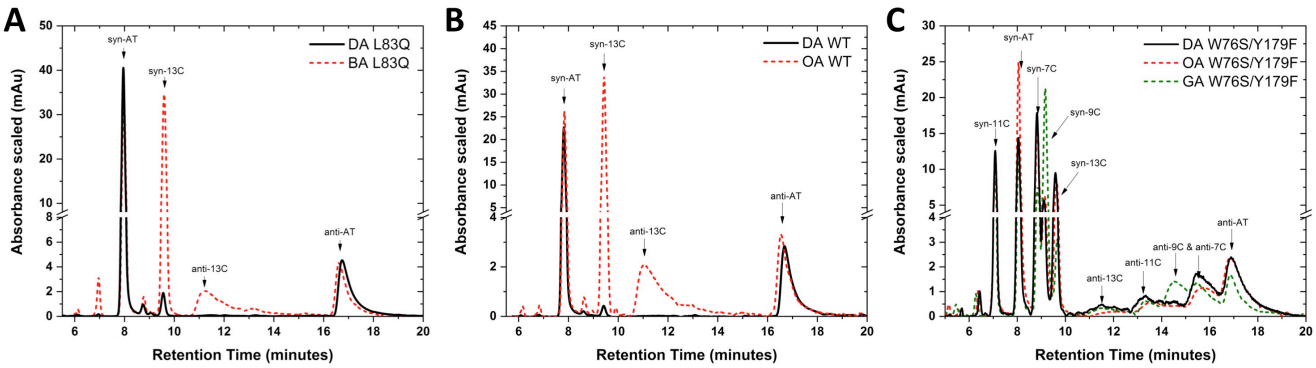

Figure S11. HPLC results for DA and LA states of (A) L83Q, (B) WT and (C) W76S/Y179F samples.

Table S4. Isomeric ratio in each-stationary state.

Sample	all-*trans* (%)	13-*cis* (%)	11-*cis* (%)	9-*cis* and 7-*cis* (%)	Other (%)
DA L83Q	95±1	3±1	-	-	2±1
BA L83Q	44±1	54±1	-	-	2±1
DA WT	97±1	2±1	-	-	1±1
OA WT	40±1	59±1	-	-	1±1
DA W76S/Y179F	30±1	15±1	18±1	36±1	1±1
OA W76S/Y179F	39±1	12±1	16±1	31±1	2±1
GA W76S/Y179F	23±1	8±1	12±1	54±1	3±1

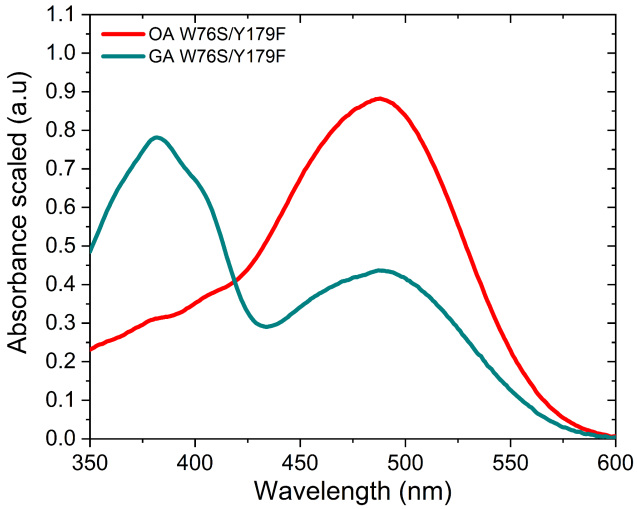

Figure S12. Steady state absorption spectra for OA and GA states of W76S/Y179F mutant.

Figure S12 shows the steady state absorption spectra for the two light adapted states of W76S/Y179F mutant. In the OA state (red solid line) the dominant isomers contribution (Table S4) comes from the AT and 13C isomers (39% + 12%), leading to a main absorption peak with a maximum at 488 nm. On the other hand, the GA state (dark cyan line) is constructed mainly by the pair of 9-*cis* and 7-*cis* isomers (54%). The increment of these isomers percentage in the particular state, is accompanied with the presence of an absorption peak ranging between 350-420 nm (max. at 382 nm). While the peak at 488 nm is still present with almost the half amplitude, attributed already to the all-*trans* and 13-*cis* isomers and by having in mind the 20% reduction of the all-*trans*+13-*cis* percentage, we conclude that the 7-*cis*+9-*cis* isomers absorb at 382 nm. The latter suggests that excitation of the samples with a source above 500 nm will provide information only for the all-*trans* and 13-*cis* isomers.

3.2. Steady State Absorption

The disentanglement of the AT and 13-*cis* isomers absorption spectrum for WT-ASR, was done assuming the linear combination of the two isomers[23] for constructing each state (DA and LA) according to the Equation 1. The absorption spectra shown in Fig. 2A are normalized to the absorbance of the DA state.

$$\begin{bmatrix} AT \\ 13C \end{bmatrix} = R^{-1} \times \begin{bmatrix} A_{DA} \\ A_{LA} \end{bmatrix} \quad with \quad R = \begin{bmatrix} r_{DA}^{AT} & r_{DA}^{13C} \\ r_{LA}^{AT} & r_{LA}^{13C} \end{bmatrix} \qquad \text{Equation 1}$$

3.3. Static Fluorescence. Determination of fluorescence Quantum Yield (Φ)

The static fluorescence spectra were recorded on a home-made fluorescence set-up, optimized for the low emission quantum yield of retinal proteins.

The laser source used was a Ti:Sapphire amplifier (Amplitude) at 5kHz repetition rate, delivering 40 fs pulses centered at 800 nm with 0.6 mJ output energy. The excitation pulse (60 fs centered at 517 nm) was produced by an Optical Parametric Amplifier (TOPAS prime - Light Conversion). 3 nJ of the later were focused on the sample using a plano-convex lens (f = 10 cm). A pair of parabolic mirrors (3-inch diameter) was used for collecting the emitted luminescence and afterwards focusing it in an optical fiber (200 μm core diameter – Avantes) for collection. The optical fiber was coupled to a Princeton Instruments spectrometer "SP-2300i", used for dispersing the luminescence on a Pylon's nitrogen cooled CCD (-120 ºC). During the experiment, to avoid residual parasitic scattered light due to the excitation beam, a long pass filter was used, allowing the fluorescence transmission above 550 nm. Protein samples are circulated in a flow cell. The 5kHz laser rep rate and a sufficiently large volume in the sample reservoir, avoids excitation of late photo-cycle intermediates.

Each emission spectrum shown in Figure 2A, in the main text, is an average out of 150-300 spectra, where the acquisition time for each was set at 0.7 seconds. The spectra plotted are scaled according to the absorbance of each sample in the 0.5 mm flow cell. Emission spectra are not corrected for the spectral sensitivity of the spectrometer and CCD camera.

The Φ of the different samples was calculated according to the Equation 2 using orange-adapted bacteriorhodopsin (OA bR, >95% AT), as a reference. The Φ_{ref} value of light-adapted bacteriorhodopsin (bR) is quoted to be 2.5×10^{-4} in ref. 24, but using this value for calculations of the radiative rates leads to excessively high values in particular for DA L83Q ($k_r > (1ns)^{-1}$). The overestimation of Φ_{bR} in ref. 24 is most probably related to the fact that it is determined under cw illumination of a static, non-circulating purple membrane sample, leading to contributions from spectrally similar photo-cycle intermediates such as N.

$$\Phi = \Phi_{ref} \frac{n^2 I_s (1-10^{-OD_{ref}})}{n_{ref}^2 I_{ref} (1-10^{-OD})} \qquad \text{Equation 2}$$

where:

Φ_{ref} is the quantum yield of reference

n: refractive index of samples buffer solution

n_{ref}: refractive index of reference sample

I_s : fluorescence intensity after integration along all wavelengths of the emission

I_{ref} : fluorescence intensity of reference after integration along all wavelengths of the emission

The OD of the samples in the 0.5 mm path length flow cell was 0.05, 0.09, 0.08, 0.06, 0.03 for DA WT, DA L83Q, DA W76S/Y179F,OA W76S/Y179F and GA W76S/Y179F respectively.

The wavelength range used for integration of the fluorescence intensities is 536-1000 nm for all samples.

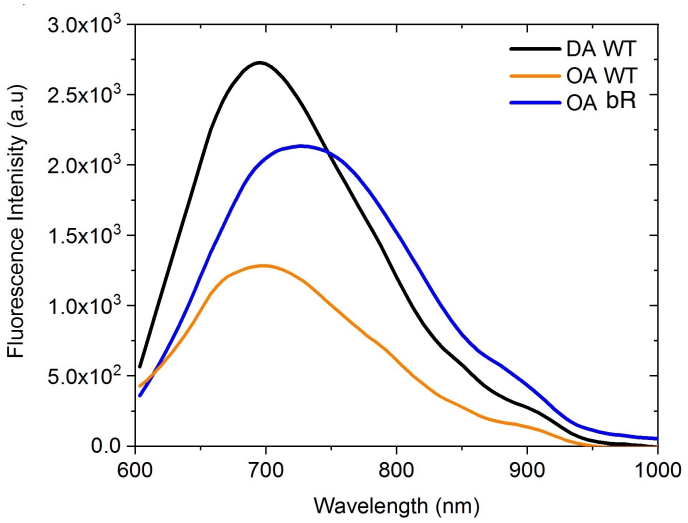

Figure S13. Determination of the quantum yield Φ relative values, using OA bR as reference. Intensities are corrected for the number of absorbed photons, according to eq. 3, but not corrected for the spectral sensitivity of the apparatus.

The measurements relative to OA bR allow as to disregard any complications concerning the sensitivity of the apparatus, as the fluorescence spectrum of the latter is overlapped with those of ASR samples along the whole detection range. Figure S13 shows initial experiments on DA WT and OA WT in respect with OA bR, used for determination of relative values of Φ and for reproducing equivalent experiments on WT ASR (ref. 23). From the integrated spectra we observe a relative increase of DA WT with respect to OA bR by a factor of 1.11.

The radiative rate (k_r), excited state lifetime (ESL) and Φ are related by Equation 3:

$$\Phi = ESL \times kr \qquad \text{Equation 3}$$

An analysis of Φ and ESL for DA WT and OA W76S/Y179F show that they share the same value of k_r. Again, due to the lack of absolute fluorescence quantum yields we do not quote the radiative rates. It is however apparent from the values in table 1, main text, that DA L83Q has a 3-4 times higher radiative rate than DA WT ASR and OA W76S/Y179F. This is in agreement with the predicted larger splitting between S1 and S2 states (Figure 3A), and thus reduced mixing with the lower emissive character of S2.

3.4. Transient Absorption Spectroscopy (TAS)

The experiments were performed using a 0.5 mm flow cell (Starna), while in the case of DA L83Q a 0.2 mm flow cell with ultra-thin windows (Starna) was used instead. The excitation wavelength was set at 515 nm and 525 nm for OA and GA W76S/Y179F respectively, 540 nm for DA L83Q and 565 nm for DA WT ASR. The excitation energy was kept below 60 nJ among all measurements and the pump size was at least a factor of 2 larger than the probe beam. The kinetic traces shown in Figure 2D, in the main text, are from the central wavelength of Stimulated Emission signature (SE) and are normalized to 1 for direct comparison.

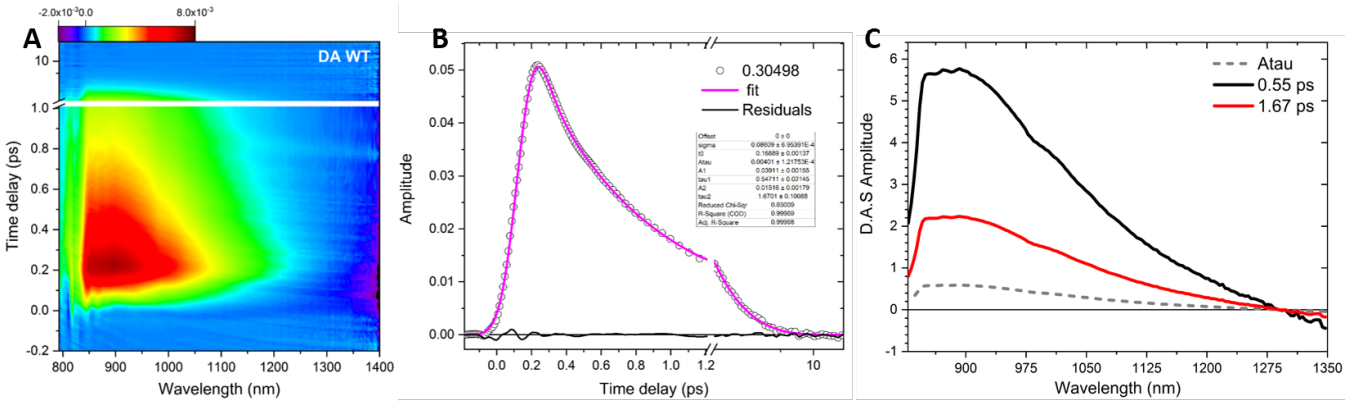

Figure S14. Global fit procedure for the stimulated emission of DA WT ASR (A) Transient Absorption 2D map, (B) Fit of dominant singular transient and (C) Decay Associated Differential Spectra (DADS). The differential absorption is displayed with inverted sign (SE>0), for improved reading.

In Figure S14 the global fit procedure for DA WT ASR is presented. Figure S14A shows the 2D plot of the data recorded in the probing region between 800-1400 nm varying the time delay between pump and probe. In the region between 800-1300 nm the signature of Stimulated Emission (SE) is presented as a positive signal, while a weak Excited State absorption (ESA) is observed in the spectral region above 1300 nm as negative signal. As no dynamic spectral shift is observed, a global fit of all the wavelengths is allowed. The latter means that kinetic traces for different wavelengths should share the same time constants but not necessary the same amplitudes according to Equation 4:

$$\Delta A(\lambda, t) = \sum_{i=1}^{N} A_i(\lambda)\exp(-t/\tau_i) \qquad \text{Equation 4}$$

where "i" correspond to the number of time constants describing the excited population evolution (decay or rise).

To make the fitting procedure even simpler, we apply a mathematical operation called Singular Value Decomposition (SVD). In this way the 2D map can be decomposed to numerous kinetic traces, each associated with a spectrum and a singular value which is the weight contribution to the dataset. For our analysis only 1 singular value is needed to reconstruct our data avoiding noise contributions. The kinetic trace corresponding to that 1 singular value is shown in Figure S14B with the fitting shown with pink solid line and the residuals with black solid line. An ideal fit was obtained using two exponential decay constants and an "Atau" non-resolved amplitude component (within instrument response function). Finally, using the fitting result we can associate the different time constants to a characteristic spectrum resulting in the Decay Associated Differential Spectra (DADS) as shown in Figure S14C. The DADS is basically the sum of the dynamic spectral evolution of the excited species. In the particular case the unchanged shape of the spectra for 0.55 ps and 1.7 ps suggests a bi-phasic decay of population from the S_1 and the weighted average corresponds to an average Excited State Lifetime (ESL) of 0.86 ps.

3.5. λ^{a}_{max} and λ^{f}_{max} Measurements

Table S5. Experimentally determined absorption and emission maxima.

Sample	Observed λ^{a}_{max} (nm)	Observed λ^{f}_{max} (nm)
DA L83Q	517	630
DA W76S/Y179F	498	661
OA W76S/Y179F	488	658
GA W76S/Y179F	488	658

DA WT	549	674

4. Voltage sensitivity

In this section we present a preliminary and approximate study of the sensitivity of the fluorescence signal of the ASR_{AT} mutant W76S/Y179F to a voltage variation across the cell membrane. Such a variation is described in terms of opposite ion concentration changes in the inner and outer surfaces of the protein. More specifically, we take as a reference the QM/MM model used in the main text to represent the relaxed S_1 equilibrium structure of the mutant (this corresponds to the central 0/0 structure in Figure S15) and corresponding to the $MIN_{W76S/Y179F}$ in Figure 3 of the main text. We then construct two additional models with altered charge balances and, therefore, voltage. In the first model the number of ions is altered in such a way that the inner and outer surfaces of the protein feature an additional positive ion (Na^+) and an additional negative ion (Cl^-) respectively (see +1/-1 model in Figure S15). In contrast, in the second model the number of ions is altered in such a way that the inner and outer surfaces of the protein feature one less positive ion (Na^+) and one less negative ion (Cl^-) respectively (see -1/+1 model in Figure S15). Notice that the two additional models are generated by a QM/MM geometry optimization on S_1 starting from the reference structure and after altering the number of ions.

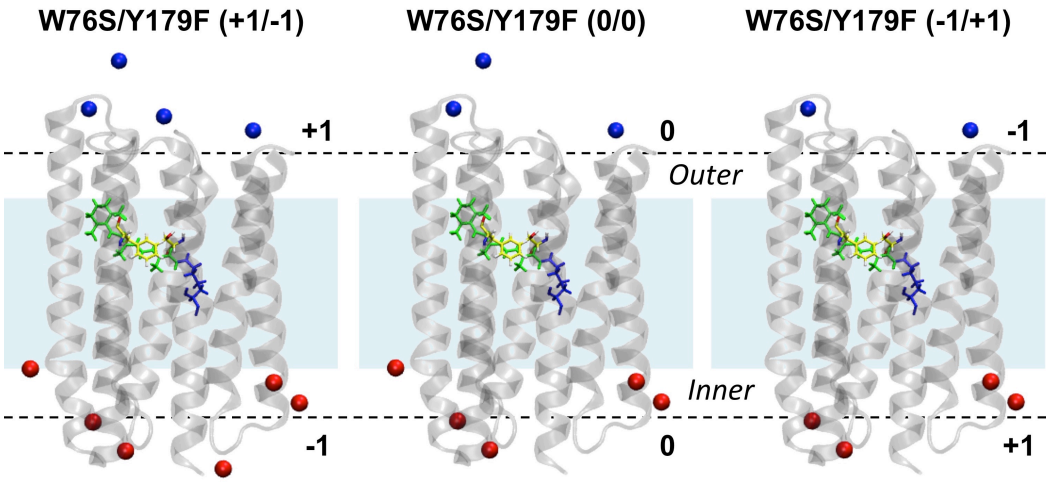

Figure S15. Different external ion numbers in the ASRAT W76S/Y179F mutant. Red and blue spheres correspond with Cl- and Na+, respectively. The central ASR W76S/Y179F model is a standard ARM model generated via S_1 geometry optimization. The two alternative models (+1/-1 and -1/+1) where the inner and outer surface charges have been increased or decreased by one unit (see left and right structures) are generated via S_1 geometry optimization starting from the central structure.

The results of the $\Delta E_{S1\text{-}S0}$ calculations providing the λ^f_{max} values are given in Table S6 for both ASR_{AT} WT and the ASR_{AT} W76S/Y179F mutant.

Table S6. Computed ground state (S_0), first (S_1) and second (S_2) excited state vertical excitation energies (a.u.), $\Delta ES_1\text{-}S_0$ and $\Delta ES_2\text{-}S_0$ (kcal/mol) for ASR_{AT} WT and its W76S/Y179F mutant for S_1 minimum optimized geometries, computed at CASPT2//CASSCF(12,12)/6-31G* level of theory. The corresponding λ^f_{max} is given in nm.

Sample	S_0 Energy	S_1 Energy	S_2 Energy	$\Delta E_{S1\text{-}S0}$ (λ^f_{max})	$\Delta E_{S2\text{-}S0}$ (λ^f_{max})	$f_{Osc\ S1\text{-}S0}$	$f_{Osc\ S2\text{-}S0}$	$f_{Osc\ S2\text{-}S1}$
WT (+1/-1)	-871.937202	-871.876352	-871.843884	38.2 (748)	58.6 (488)	1.10	0.53	0.04
WT (0/0)	-872.002426	-871.942391	-871.910630	37.7 (758)	57.6 (496)	1.07	0.52	0.07

WT (-1/+1)	-871.924232	-871.866635	-871.835635	36.1 (792)	55.6 (514)	1.08	0.49	0.02
W76S/Y179F (+1/-1)	-871.920325	-871.854777	-871.850009	41.1 (696)	44.1 (648)	1.02	0.95	0.53
W76S/Y179F (0/0)	-871.954285	-871.893000	-871.887702	38.4 (744)	41.7 (685)	0.92	0.90	0.42
W76S/Y179F (-1/+1)	-871.903732	-871.844442	-871.840334	37.2 (769)	39.8 (718)	0.93	0.89	0.41

In order to support the general reliability of +1/-1 and -1/+1 models derived via geometry optimization of the 0/0 model, we also perform $\Delta E_{S1\text{-}S0}$ calculations for absorption and, therefore, starting from the 0/0 model optimized on S_0 (corresponds to the model whose λ^{a}_{max} value is closest to the average of the ten geometry optimization repeated by the ARM protocol. See subsection 1.1 above). The results are given on Table S7.

Table S7. Computed ground state (S_0), first (S_1) and second (S_2) excited state vertical excitation energies (a.u.), $\Delta ES_1\text{-}S_0$ and $\Delta ES_2\text{-}S_0$ (kcal/mol) for ASR_{AT} WT and its W76S/Y179F mutant for S_0 optimized geometries, computed at CASPT2//CASSCF(12,12)/6-31G* level of theory. The corresponding λ^{a}_{max} is given in nm.

Sample	**S_0 Energy**	**S_1 Energy**	**S_2 Energy**	**$\Delta E_{S1\text{-}S0}$ (λ^{f}_{max})**	**$\Delta E_{S2\text{-}S0}$ (λ^{f}_{max})**	**$f_{Osc\ S1\text{-}S0}$**	**$f_{Osc\ S2\text{-}S0}$**	**$f_{Osc\ S2\text{-}S1}$**
WT (+1/-1)	-871.984022	-871.896732	-871.873211	54.8 (522)	69.5 (432)	1.20	0.53	0.08
WT (0/0)	-872.008819	-871.925616	-871.900526	52.6 (543)	67.9 (421)	1.14	0.50	0.07
WT (-1/+1)	-871.958912	-871.877832	-871.856672	50.9 (562)	64.2 (445)	1.18	0.54	0.04
W76S/Y179F (+1/-1)	-871.951530	-871.855633	-871.846092	60.2 (475)	66.2 (432)	1.10	0.85	0.32
W76S/Y179F (0/0)	-871.964482	-871.871175	-871.859325	58.5 (488)	65.9 (433)	0.99	0.82	0.30
W76S/Y179F (-1/+1)	-871.945455	-871.854443	-871.849423	57.1 (501)	60.3 (474)	1.03	0.84	0.33

Finally, in Figure S16 we report the results of the voltage sensitivity calculations for both absorption and emission of ASR_{AT} WT and its W76S/Y179F mutant. Notice that in Figure S16 A we compare the absorption values of ASR_{AT} WT computed in this work with those previously reported in ref. 1 where the three QM/MM models 0/0, +1/-1 and -1/+1 QM/MM models correspond to the S_0 optimized structure whose λ^{a}_{max} value is closest to the average of the ten geometry optimization repetitions of the ARM protocol (see subsection 1.1 above). The comparison shows that the more approximate +1/-1 and -1/+1 QM/MM models used in the present work (i.e. obtained via geometry optimization starting from the 0/0 model) produce $\Delta E_{S1\text{-}S0}$ values close to the published one from ref. 1.

It is evident that $\Delta E_{S1\text{-}S0}$ for both absorption and emission (i.e. the computed λ^{a}_{max} and λ^{f}_{max}) are, according to our model, sensitive to the change in voltage and display similar sensitivities (somehow the W76S/Y179F mutant appears to be more sensitive in emission as displayed in Figure S16 B).

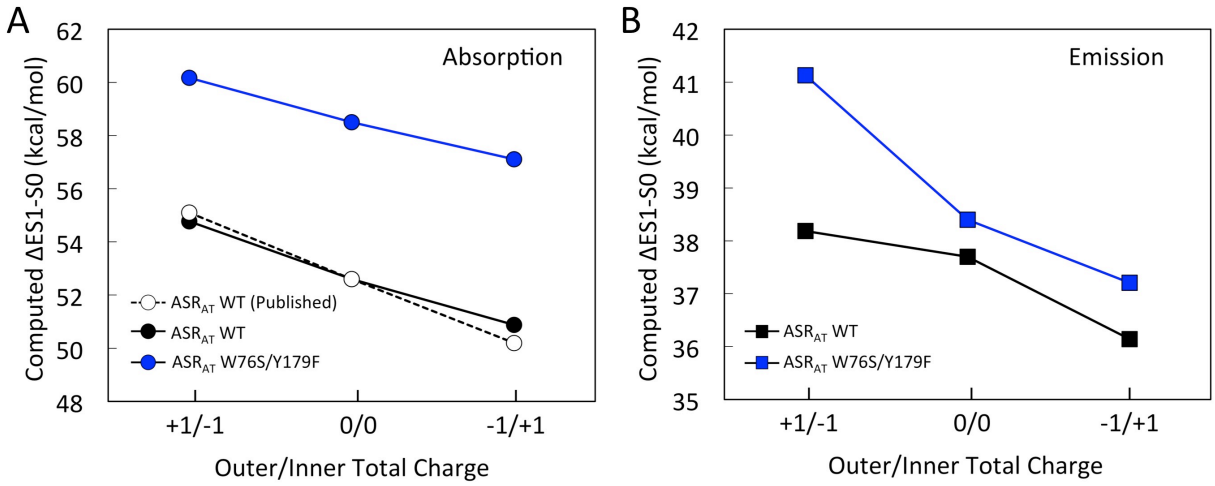

Figure S16. Variations in (A) absorption and (B) emission of ΔES_1-S_0 values as function of excess surface charges of ASR_{AT} WT (black) and W76S/Y179F mutant (blue). In dashed lines are shown the previous published (see ref. 1) absorption ΔES_1-S_0 values of ASR_{AT} WT.

References

1. Melaccio, F., del Carmen Marín, M., Valentini, A., Montisci, F., Rinaldi, S., Cherubini, M., Yang, X., Kato, Y., Stenrup, M., Orozco-Gonzalez, Y., Ferré, N., Luk, H. L., Kandori, H. & Olivucci, M. Toward Automatic Rhodopsin Modeling as a Tool for High-Throughput Computational Photobiology. *J. Chem. Theory Comput.* **12,** 6020–6034 (2016).

2. Altun, A., Yokoyama, S. & Morokuma, K. Spectral Tuning in Visual Pigments: An ONIOM(QM:MM) Study on Bovine Rhodopsin and its Mutants. *J. Phys. Chem. B* **112,** 6814–6827 (2008).

3. Altun, A., Yokoyama, S. & Morokuma, K. Mechanism of Spectral Tuning Going from Retinal in Vacuo to Bovine Rhodopsin and its Mutants: Multireference ab Initio Quantum Mechanics/Molecular Mechanics Studies. *J. Phys. Chem. B* **112,** 16883–16890 (2008).

4. Sekharan, S., Altun, A. & Morokuma, K. Photochemistry of Visual Pigment in a G_q Protein-Coupled Receptor (GPCR)-Insights from Structural and Spectral Tuning Studies on Squid Rhodopsin. *Chem. - A Eur. J.* **16,** 1744–1749 (2010).

5. Sekharan, S., Wei, J. N. & Batista, V. S. The Active Site of Melanopsin: The Biological Clock Photoreceptor. *J. Am. Chem. Soc.* **134,** 19536–19539 (2012).

6. Roos, B. O. *Ab Initio Methods in Quantum Chemistry II. Wiley-VCH* (1987).

7. Andersson, K., Malmqvist, P. A., Roos, B. O., Sadlej, A. J. & Wolinski, K. Second-order perturbation theory with a CASSCF reference function. *J. Phys. Chem.* **94,** 5483–5488 (1990).

8. Andruniów, T., Ferré, N. & Olivucci, M. Structure, initial excited-state relaxation, and energy storage of rhodopsin resolved at the multiconfigurational perturbation theory level. *Proc. Natl. Acad. Sci. U. S. A.* **101,** 17908–13 (2004).

9. Coto, P. B., Strambi, A., Ferré, N. & Olivucci, M. The color of rhodopsins at the ab initio multiconfigurational perturbation theory resolution. *Proc. Natl. Acad. Sci. U. S. A.* **103,** 17154–9

(2006).

10. Coto, P. B., Martí, S., Oliva, M., Olivucci, M., Merchán, M. & Andrés, J. Origin of the Absorption Maxima of the Photoactive Yellow Protein Resolved via Ab Initio Multiconfigurational Methods. *J. Phys. Chem. B* **112,** 7153–7156 (2008).

11. Sinicropi, A., Andruniow, T., Ferré, N., Basosi, R. & Olivucci, M. Properties of the Emitting State of the Green Fluorescent Protein Resolved at the CASPT2//CASSCF/CHARMM Level. *J. Am. Chem. Soc.* **127,** 11534–11535 (2005).

12. Coutinho, K., Georg, H. C., Fonseca, T. L., Ludwig, V. & Canuto, S. An efficient statistically converged average configuration for solvent effects. *Chem. Phys. Lett.* **437,** 148–152 (2007).

13. Pronk, S., Páll, S., Schulz, R., Larsson, P., Bjelkmar, P., Apostolov, R., Schirts, M. R., Smith, J. C., Kasson, P. M., Spoel, D., Hess, B. & Lindahl, E. GROMACS 4.5: a high-throughput and highly parallel open source molecular simulation toolkit. *Bioinformatics* **29,** 845–854 (2013).

14. Aquilante, F., Autschbach, J., Carlson, R. K., Chibotaru, L. F., Delcey, M. G., Vico, L. D., Galván, I. F., Ferré, N., Frutos, L. M., Gagliardi, L., Garavelli, M., Giassani, A., Hoyer, C. E., Manni, G. L., Lischka, H., Ma, D., Malmqvist, P. A., Müller, T., Nenov, A., Olivucci, M., Pedersen, T. B., Peng, D., Plasser, F., Pritchard, B., Reiher, M., Rivalta, I., Schapiro, I., Segarra-Martí, J., Stenrup, M., Truhlar, D. G., Ungur, L., Valentini, A., Vancoillie, S., Veryazov, V., Vysotskiy, V. P., Weingart, P., Zapata, F., & Lindh, R. Molcas 8: New capabilities for multiconfigurational quantum chemical calculations across the periodic table. *J. Comput. Chem.* **37,** 506–541 (2016).

15. Vogeley, L., Sinechchekov, O. A., Trivedi, V. D., Sasaki, J., Spudich, J. L. & Hartmut, L. Anabaena Sensory Rhodopsin: A Photochromic Color Sensor at 2.0 Å. *Science*. **306,** 1390–1393 (2004).

16. Olsson, M. H. M., Søndergaard, C. R., Rostkowski, M. & Jensen, J. H. PROPKA3: Consistent Treatment of Internal and Surface Residues in Empirical pK_a Predictions. *J. Chem. Theory Comput*. **7,** 525–537 (2011).

17. Tian, W., Chen, C., Lei, X., Zhao, J. & Liang, J. CASTp 3.0: computed atlas of surface topography of proteins. *Nucleic Acids Res*. **46,** W363-W367 (2018).

18. Schapiro, I., Ryazantsev, M. N., Frutos, L. M., Ferré, N., Lindh, R. & Olivucci, M. The Ultrafast Photoisomerizations of Rhodopsin and Bathorhodopsin Are Modulated by Bond Length Alternation and HOOP Driven Electronic Effects. *J. Am. Chem. Soc.* **133,** 3354–3364 (2011).

19. Gozem, S., Huntress, M., Schapiro, I., Lindh, R., Granovsky, A. A., Angeli, C. & Olivucci, M. Dynamic Electron Correlation Effects on the Ground State Potential Energy Surface of a Retinal Chromophore Model. *J. Chem. Theory Comput*. **8,** 4069–4080 (2012).

20. Zen, A., Coccia, E., Gozem, S., Olivucci, M. & Guidoni, L. Quantum Monte Carlo Treatment of the Charge Transfer and Diradical Electronic Character in a Retinal Chromophore Minimal Model. *J. Chem. Theory Comput*. **11,** 992–1005 (2015).

21. Andersen, L. H., Nielsen, I. B., Kristensen, M. B., Ghazaly, M. O. A. E., Haccke, S., Nielsen, M. B. & Petersen, M. Å. Absorption of Schiff-Base Retinal Chromophores in Vacuo. *J. Am. Chem. Soc*. **127,** 12347–12350 (2005).

22. Landers, G. M. & Olson, J. A. Rapid, simultaneous determination of isomers of retinal, retinal oxime and retinol by high-performance liquid chromatography. *J. Chromatogr. A* **438,** 383–392 (1988).

23. Cheminal, A., Léonard, J., Kim, S-Y., Jung, K-H., Kandori, H. & Haacke, S. 100 fs photo-isomerization with vibrational coherences but low quantum yield in Anabaena Sensory Rhodopsin. *Phys. Chem. Chem. Phys.* **17,** 25429–25439 (2015).

24. Kouyama, T., Kinosita, K., Ikegami, A., S. Excited-state dynamics of Bacteriorhodopsin. *Biophysical Journal*. **47,** 43–54 (1985).

Part VI

Conclusions - Perspectives

6.1 Conclusions

From our studies on WT-ASR and the mutants, we provided T.A data for DA and LA proteins revealing the spectroscopic signatures in the (330-1400) nm spectral range. The HPLC measurements during the experiments allowed us to have the precise knowledge of the isomeric content in these photostationary states and be able to disentangle AT- and 13C-PSBR dynamics.

From our analysis, the ESL of both isomers was determined for all samples. Initially, we confirmed previous reports on WT ASR with the ESL for AT and 13C isomers being 0.83ps and 0.2ps respectively. In addition, the introduced point mutations at positions 76, 83 and 112 appeared to accelerate the isomerization reaction for AT isomers, accompanied with a blue shift of their absorption maxima. The highest impact was observed for L83Q mutant with a ~2 fold reduction of the ESL (0.48ps). The origin of this difference was assigned to S1/S2 electronic mixing (computational work of M. Del Carmen Marín, Y.Orozco-Gonzalez and M.Olivucci).

On the contrary, 13C-PSBR excited state dynamics in the mutants appeared to decay lower with respect to WT-ASR. Surprisingly, for W76F case we observed an order of magnitude difference (2.1ps), while a less pronounced effect was observed for V112N and L83Q mutants (~2-3 times longer). Having in mind that the ESL values obtained for AT and 13C isomer in WT-ASR differ by a factor of ~4, the latter effect was not so pronounced for the mutants case. The largest effect was observed for W76F, where a ~3 fold longer ESL holds for 13C isomer. Moreover, for V112N and L83Q mutants no striking differences were observed, with the ESL of both isomers varying within ~20%.

In addition to the ESL, we provided information concerning the vibrational activity of low in frequency modes (<400cm^{-1} range). The performed experiments for DA and LA proteins, resulted in four low frequency modes presented for all mutants and WT-ASR ranging between 60cm^{-1} - 400cm^{-1}. The latter results was previously reported in literature for other retinal proteins, attributing these modes to the chromophore's skeletal delocalized torsions.

From our experiments in the UV-Vis spectral range, we were able to record the long differential spectra for DA and LA proteins. Supplementary to the ASR data, we measured BR under identical excitation conditions. The latter allowed us to have a reference which can be used for relative measurements of isomerization quantum yield of both isomers. However, the study on WT-ASR resulted in values different from what was previously reported. From the latter we understood that there are still some small experimental details that I was not able to control resulting in different shape for the long differential spectra. The corresponding data for the mutants were not analyzed as the molar extinction coefficients of GS and K species were not available.

Our work on ASR mutants resulted in the discovery of a W76S/Y179F mutant which shows a ~8 fold increment of fluorescence quantum yield with respect to WT-ASR. The particular mutant has a picosecond lifetime (ESL of 5.7ps) with a fluorescence QY (2.17x10^{-3}) not too far from the improved Arch3 mutants applied in optogenetics. In the submitted manuscript presented in this thesis a comparison with respect to WT-ASR and L83Q mutant is described. The reaction path and trajectory computations show, that the observed change in ESL is due to an opposite change in charge transfer character of the S_1 state of the molecule. Such

changes, that can be described as an increase in unreactive 2Ag diradical character along the L83Q, WT, W76S/Y179F series. The L83Q to WT variation is dominated by an electrostatic effect while the WT to W76S/Y179F variation is controlled by steric effects: a change in the details of the isomerization coordinate.

Concerning our contribution on developing new spectroscopic tools, we were able to upgrade of T.A spectrometer previously used for Vibrational Coherence Spectroscopy (VCS), into a 2DES one operating in the UV-Vis spectral range. The 2DES spectrometer uses a pair of phase-locked sub-10fs pulses in the near UV-blue range 360-430nm and can be used for performing 2DES on (bio)molecular systems that absorb in this spectral range.

In addition a T.A spectrometer performing in the NIR spectral range (800-1400) nm was built, used for the study of ASR samples. The latter setup sensitivity allows measuring signals $<10^{-3}$, with the level of noise down to $\sim 20 \times 10^{-6}$ upon 5s of acquisition time at 910nm.

6.2 Perspectives

The study of ASR samples in the UV-Vis spectral range showed an overlap between the different contributions (ESA/GSB/PA/SE). Upon our attempt to determine the isomerization time by looking at the photoproduct rise, we saw that only one rising component was determined while the SE data support a bi-exponential ES decay. The time constant of this component was close to the values found for the dominant decay component of SE. Nevertheless, the second and lower in amplitude component of SE decay was not detected on the PA dynamics, as it was probably smeared out by the J-species vibrational cooling mechanism (same timescale). A future work would have been to perform pump-dump-probe experiments, which will allow to see if the second component of SE is really contributing to the isomerization reaction, or if it corresponds to a non-reactive pathway.

On the same context of understanding if the second component in SE is contributing to the isomerization reaction we could perform a pump-vis/probe-mid IR experiment. By probing in the range of 1450-1600cm^{-1}, we could get the dynamics of the C=C isomerizing bond (1530 cm^{-1}-1540 cm^{-1}). This will be a direct indication for the isomerization timescale.

Concerning the Q.Y of isomerization, a future work would be the determination of the molar extinction coefficients both for GS and K-species at room temperature. This is a valuable information needed in order to determine the Q.Ys of ASR mutants.

Using sub-60fs pulses we were able to resolve vibrational oscillatory signals on top of the PSBR electronic dynamics. The pulses duration and probe's delay step allowed determination of low frequency modes. In a future experiment we could perform a VCS measurement using the NOPA in broadband operation (sub-10fs pulses) and the fast scanning method (using a piezoelectric stage instead of a motorized delay line). Thus determination of vibrational modes up to 2000cm^{-1} could provide new information for C=C stretch modes, out of plane modes (HOOP) and localized torsion modes (500cm^{-1}-700cm^{-1}).

The S1/S2 electronic mixing proposed by the theoretical study of ASR could be addressed experimental. Particularly, we could perform a pump probe measurement by exciting ASR samples using two-photons of different energy. The latter could be achieved by using a part of the fundamental 800nm pulse and a tunable NIR pulse delivered by a commercial OPA (TOPAS-Light conversion) to excite the sample. Then by delaying our probe we could

monitor the dynamics of S2, which is predicted to be close in energy with respect to S1 in WT-ASR and W76S/Y179F mutant, and splited for L83Q mutant.

Improvements on the experimental setups that could help in the future concern both the 2DES setup and the NIR spectrometer. Starting from the 2DES spectrometer, we could adjust the optical paths in such a way that we could perform 2DES using the NOPA's green pulse, covering the excitation between 475-700nm. Thus the same spectrometer and TWINS device could provide a pair of phase-locked pulses in the (360-430)nm, (475-700)nm and (600-930)nm range.

Supplementary to the previous, the NIR spectrometer could be used for a two-color 2DES experiment. The generation of the near-UV-Blue pulses should place as close as possible to the NIR spectrometer, once a long propagation path for the pulse will be translated in additional dispersion on the pulses.

Finally, the suggested pump-dump-probe experiments on ASR samples could be performed on the same experimental setup as the one used for UV-Vis probing. There we will have to implement a delayed in time NIR pulse centered on SE contribution.

Annexes

A. Anabaena Sensory Rhodopsin

I) High Performance Liquid Chromatography (HPLC) - Calibration

An isocratic method was used for the first 10min of retention time and the eluents ratio was kept 88% Cyclohexane, 12% Ethyl-acetate:Ethanol [100:1], while a linear gradient was applied afterwards reaching a ratio of 75% Cyclohexane, 25% Ethyl-acetate:Ethanol [100:1] by the end of the measurement. The flow rate was kept at 1mL/min and detection was set at 360nm where AT and 13C retinal oxime derivatives have the same ε value. The apparatus was a commercial Dionex UltiMate 3000 System, equipped with a Zorbax SIL 70A 4.6 x 250 mm – 5μm Column.

Determination of each isomers retention time was done by using commercial standards of all-trans & 13-cis retinal from Sigma Aldrich (fig.1) and reference[1,2]. The percentage of purity for all-trans and 13-cis retinals was >98% and >85% respectively. The protocol is described below:

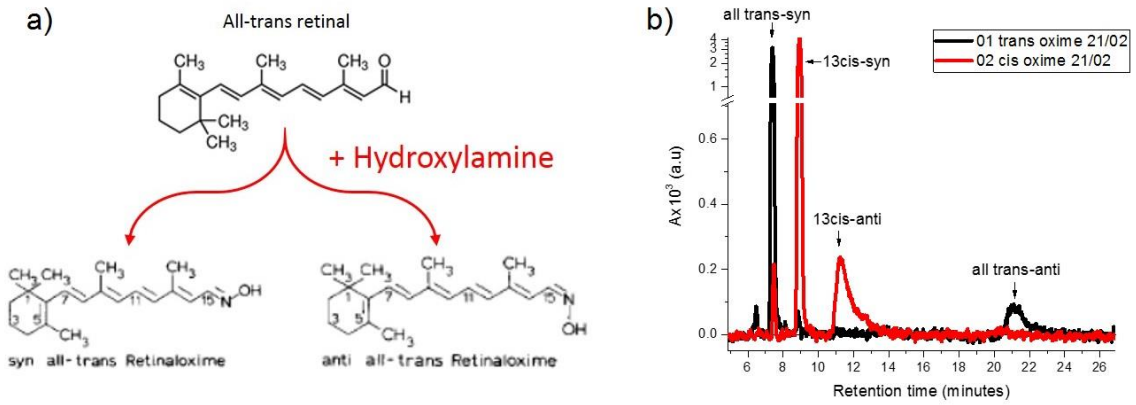

Fig. 1: a) Formation of syn- and anti- retinal-oxime forms after using hydroxylamine solution (for all-trans retinal) b) chromatograph showing the arrival for each oxime derivative (syn- or anti-); black line and red solid lines corresponds to the absorbance of all-trans retinal and 13-cis retinal oxime derivatives respectively

We transformed the two samples (all-trans and 13-cis retinals) to derive the oxime forms by adding hydroxyl amine (50% sample- 50% hydroxylamine). Then we added 600μl of cyclohexane cyclohexane. The latter procedure was followed because we used an apolar solvent in our colon (88% cyclohexane). Dilution in cyclohexane was done to avoid having the sample in a polar environment (methanol).

Fig.1b confirms that each retinal (all-trans or 13-cis) results in a syn- and anti- oxime form which arrives at a specific retention time. The retention time and percentage of each oxime derivative from these measurements are summarized in Table 1. The total percentage of all-trans quantified from our experiment is 96.7% while the one by the provider is >98%. The latter is an indication for the error bar in our measurements (±2%).

The reproducibility of the apparatus was checked by measuring the same sample after 4 days. The deviation on the isomer content was only 0.1% while the retention time within 1%. From our tests the oxime derivatives are stable for at least 4 days and they didn't show any effect between temperatures between 4º and 50º.

Table 1: HPLC results for all-trans and 13-cis oxime derivatives

Retention Time (min)	Form	Percentage of absorbance in %	
		All-trans oxime >98%	13cis oxime>85%
7.2-7.7	All-trans-syn-	**88.4 %**	**3.4 %**
8.7-9.3	13-Cis syn-	**2 %**	**79.8 %**
10.8-12.4	13-Cis anti-		**16.8 %**
20.5-22	All-trans anti-	**8.3 %**	
<7	Unknown	**1.3 %**	
		Total	
		96.7% All-trans	**96.6% 13-cis**

II) Protocol for extraction of retinal oximes from the protein

0-2: under safety light > 670nm, on ice (prevent the isomerization by unintended ways)

(0) Prepare 50 µl of the dark or light-adapted sample(0.5 OD) in 1.5 ml tube
(1) Add 50 µl of the 1M Hydroxyl amine (final concentration 0.50 M), shake for 1 min
(2) Add Methanol 300 µl in order to denature ASR, shake for 1 min

3-6: under safety light > 500 nm, on ice

(3) Add Hexane 600µl, shake for 1 minute
(4) Centrifuge the tube (10,000-15,000 rpm, 60 sec). Collection of the upper layer : hexane including retinal oxime, lower layer : buffer
(5) Take up to 300 µl of the upper layer (hexane layer including retinal oxime), and transfer to another 1.5 ml tube.
(6) Load 300 µl of Hexane layer including retinal oxime to sample loop.
(7) Inject 50 µl

III) Transient Absorption data for DA, OA and 13C-PSBR of WT-ASR

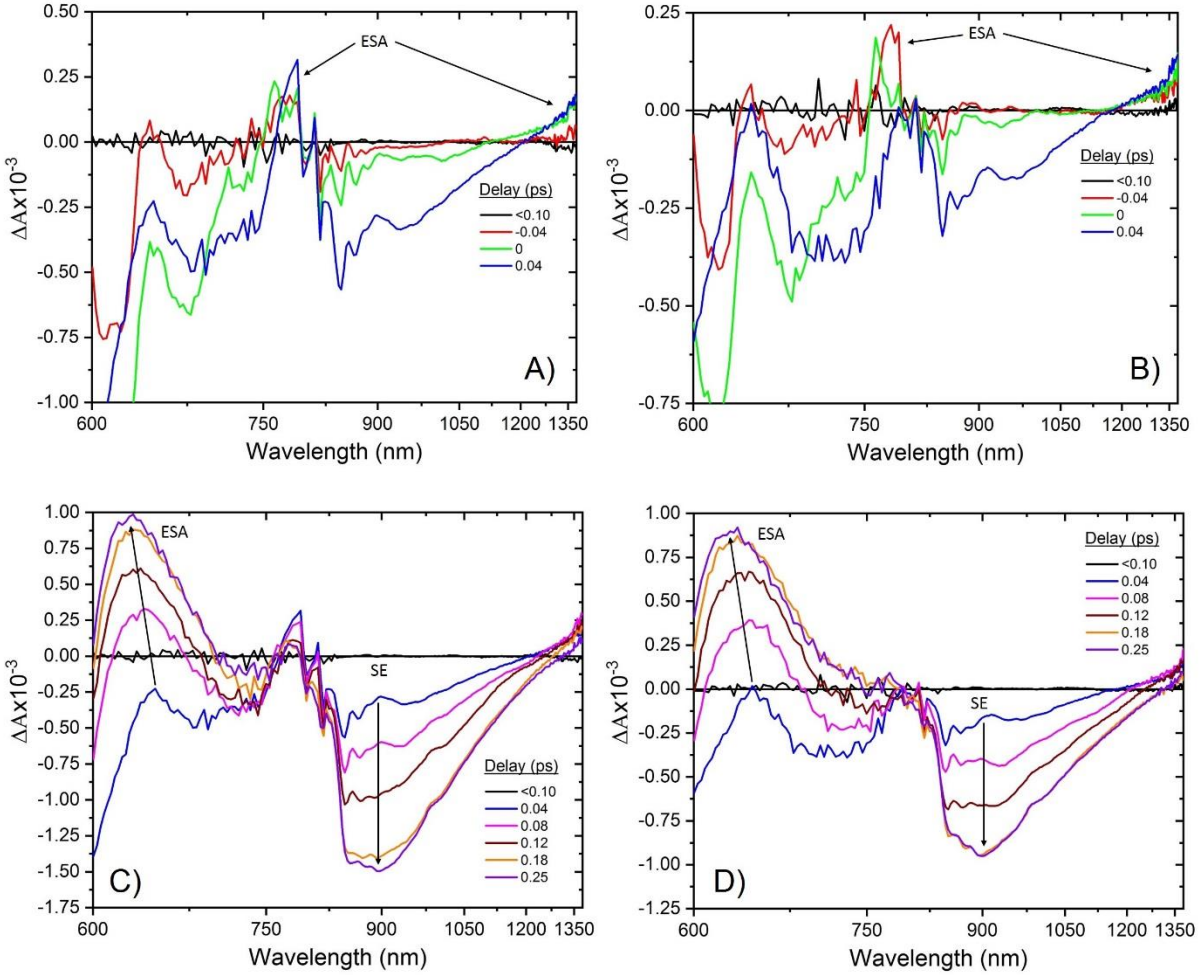

Fig. 2: Spectral evolution of DA (A,C) and OA WT (B,D) ASR for the <250fs pump-probe delays (600-1380nm region). Panels A) and B) show the presence of ESA at 760nm and >1250nm overcoming SE contribution. Panels C) and D) show the blue-shift of ESA 640nm to 620nm and the formation of SE ~900nm.

IV) Determination of ESL by SE Global fit (AT-PSBR)

The global fit in the NIR region can be performed only for the 850nm-1100nm range due to spectral shifts. Sign-inverted and normalized kinetic traces along the whole NIR region are shown in figure 3. Particularly, ESA appears in the <850nm and >1200nm probing regions, and it most probably also contributes to the initial <0.2 ps of the DE rise (see traces at 1198 and 1102 nm). The red and blue dotted curves correspond to dominant ESA contribution while the magenta and black dotted lines to SE contributions displaying a time zero shift with respect to the 850-1100nm SE kinetics (solid lines).

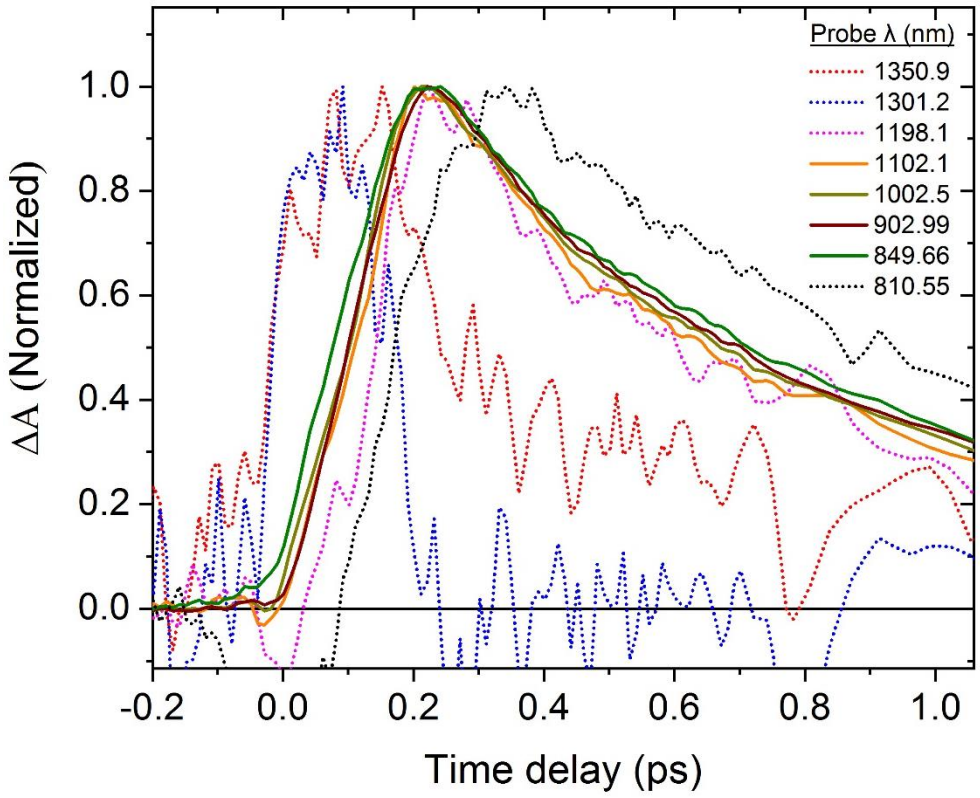

Fig. 3 : Sign-inverted and normalized kinetic traces for AT-PSBR showing the dynamic shift effect for specific probe wavelength; Dotted lines correspond to the ESA (1351nm,1301nm) and SE (1198nm,810nm) kinetic traces which cannot be included in a global fit analysis. Solid lines correspond to SE kinetic traces which have identical dynamics. (- delta A)

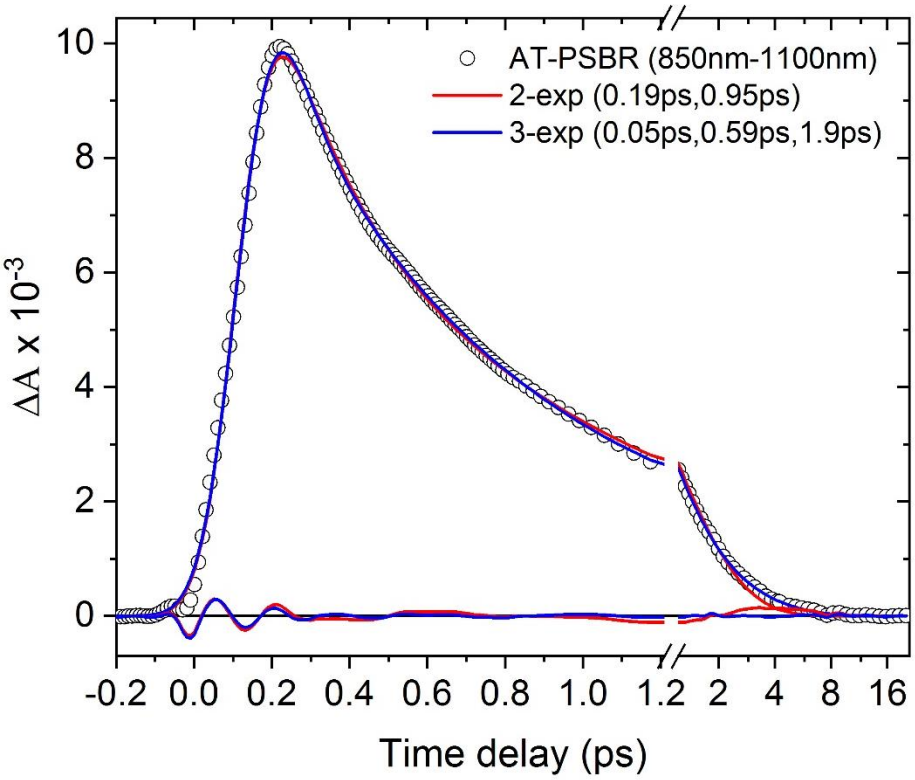

Fig. 4 : Fitting procedure of AT-PSBR (850nm-1100nm);Black circles represent the dominant singular transient from the SVD procedure; Red and Blue solid lines correspond to the 2-exp and 3-exp fits respectively with the time constants mentioned in the legend. Residuals for each fit are shown with the respective colour at the bottom

A two exponential fit (0.19ps and 0.95ps) shown with red solid line fails to capture the ps component of the kinetic trace (see residuals). The use of an additional 50fs constant improves the quality of the fit resulting in the 0.59ps and 1.9ps constants. While our temporal resolution does not allow discrimination of such a short time constant we used an unresolved component mentioned as Atau in the main text. The presence of this 50fs component dominates the sub-200fs range and is most likely not related to a population decay.

V) Isomerization Quantum Yield determination for DA WT

Using the K-GS spectrum from ref.25 and the calculated value $C_0^* = 3\mu M$ for DA WT we retrieve a $\Phi_{AT \rightarrow 13C}$ close to ~0.9 (figure 5). It is clear that both negative and positive features do not match the experimental data and a shift is required though.

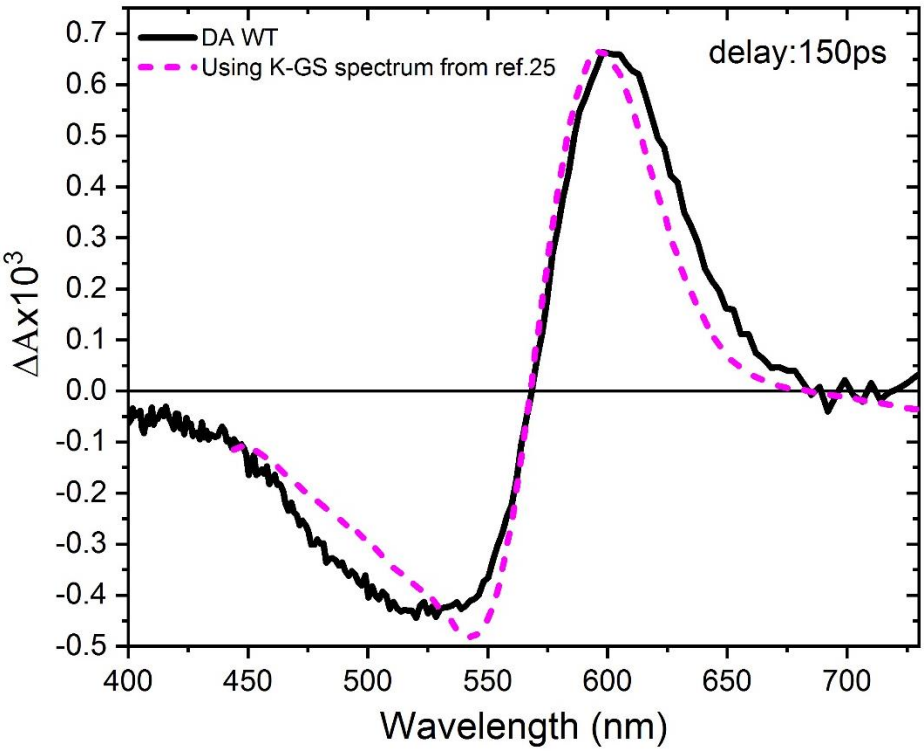

Fig. 5 : Long-time difference spectrum for DA WT-ASR (150ps); Dashed magenta line corresponds to the scaled K-GS spectrum taken from ref.25 with a resulting quantum yield ~0.9.

B. ASR mutants

I) Ground state absorption spectra of AT- and 13C- PSBR

The normalized GS absorption spectra of AT- and 13C-PSBR of WT-ASR, W76F, V112N and L83Q mutants are shown in figure 6. The resulting spectra are according to the isomer composition present in the GS determined by HPLC. In all cases the light adapted state was dominated by the 13C's contribution (exceeded 56%). While for the WT and W76F case we used an orange LED, for the case of V112N and L83Q mutants a blue one was used instead. Particularly, when an orange LED was used for these mutants the percentage of 13C couldn't exceed 46%.

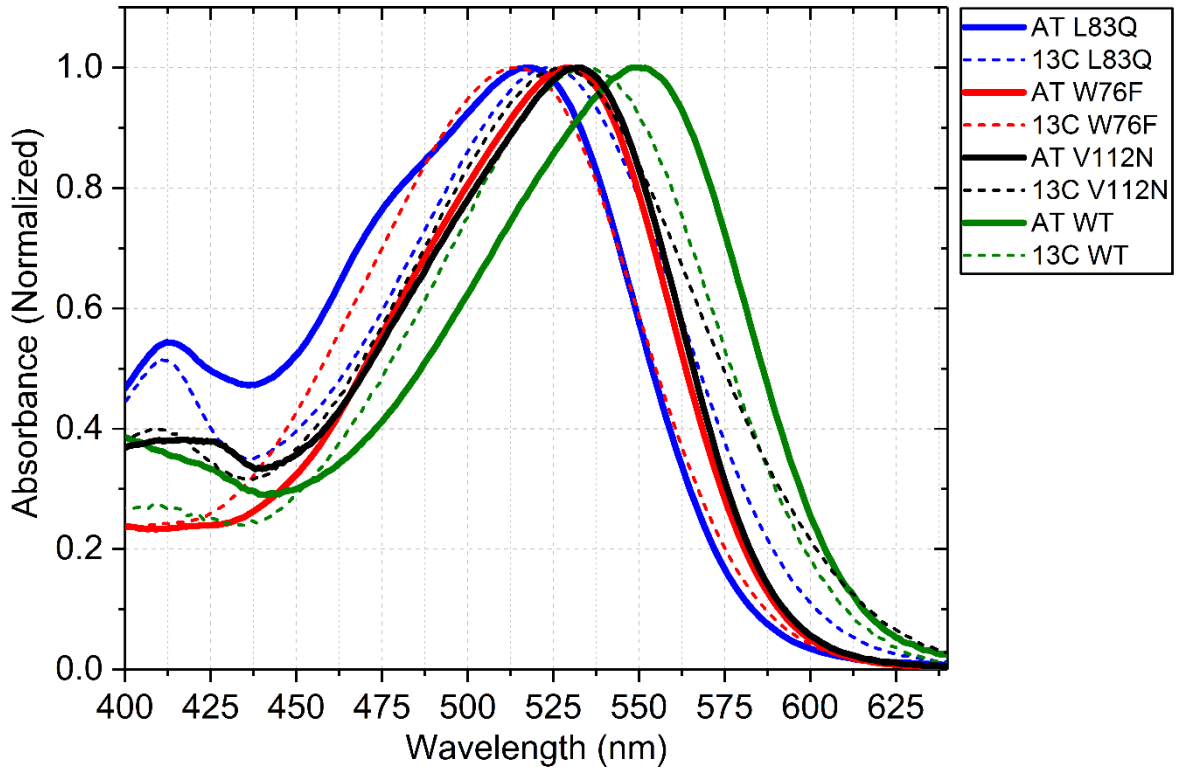

Fig. 6 : Normalized GS absorption spectra of AT-(solid lines) and 13C-PSBR (dashed lines) for WT-ASR W76F, V112N and L83Q mutants.

Figure 7 shows a comparison between the computed and observed $\Delta E_{S0\text{-}S1}$ (Kcal/mol) values from ARM models for WT ASR and the three mutants. While the trend for the absorption maxima is reproduced when comparing the computed values with respect to the experimental ones, a systematic error of overestimating the values is observed as a shift in energy above the perfect correlation line (grey dashed line). Here we notice that the models used are derived upon using the crystallographic structure of WT ASR which was available to date. Thus, models I and II for L83Q mutant previously reported in ref[3] couldn't reproduce the experimental data. An update of the model mentioned with latin number III, reproduces the experimental data and by modifications on the orientation of the Lysine residue at position 210. Further information can be found in ref[4].

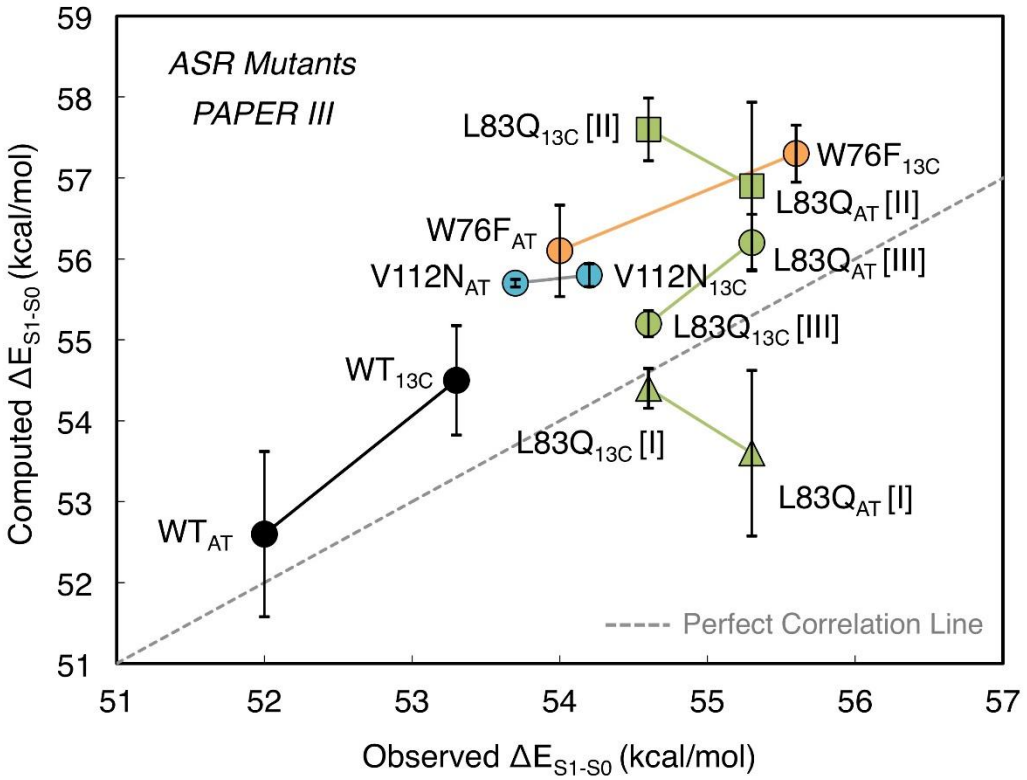

Fig. 7 : Comparison between computed and observed $\Delta E_{S1\text{-}S0}$ (Kcal/mol) values from ARM models of ASR WT (black), V112N (light blue), W76F (orange), L83Q [III] (green) mutants. The error bars of the standart deviation are shown with black; The indices shown in bracket for the case of L83Q [I,II,III] correspond to deferent ARM models where the correct one I and II correspond to a different conformation of the O-H dipole orientation on the Glutamine residue (position 83) reported in ref[3]. The correct model reproducing the experimental data was obtained by modification of the Lys210 residue (more information can be found in ref[4])

II) HPLC measurements on ASR mutants

Figure 8 shows the result from HPLC measurements of DA and LA stats of WT ASR and mutants when the T.A measurements were performed. The isomeric ration between AT and 13C isomer is shown in the legend for each state.

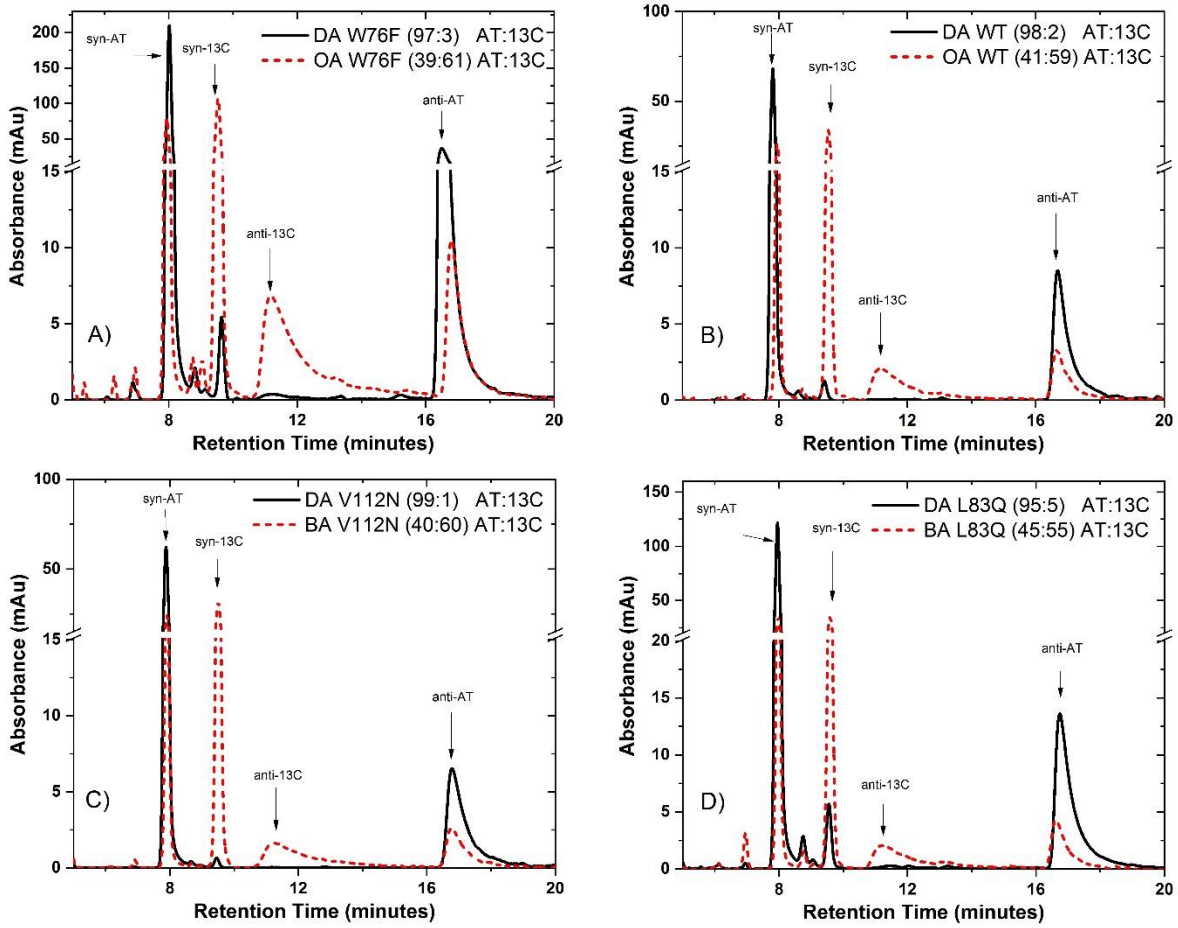

Fig. 8 : HPLC measurements of DA and LA stats of WT ASR and mutants when the T.A measurements were performed. Panel A,B,C,D correspond to W76F, WT, V112N and L83Q samples respectively. The GS isomeric content is shown in the legend of each panel for each photostationary state.

III) Mutations using WT-ASR crystallographic structure

By using PyMol software and the crystallographic structure available for WT-ASR (library:1XIO from RCSB protein bank), we can estimate the distances of the replacing residues with respect to the protonated Schiff base and the β-ionone ring.

Figure 9 shows the mutation at position 83, where Leucine is replaced by Glutamine. Depending on the orientation of O-H dipole the average distance from the PSB is ~5Å. The latter can stabilize S0 resulting in a 33nm blue shift with respect to AT- WT ASR.

Figure 10 shows the corresponding mutation at position 112, where Valine is replaced by Asparagine. In this case the average distance of the residue's polar side chain is ~4Å with respect to the β-ionone ring and ~15Å with respect to the PSB.

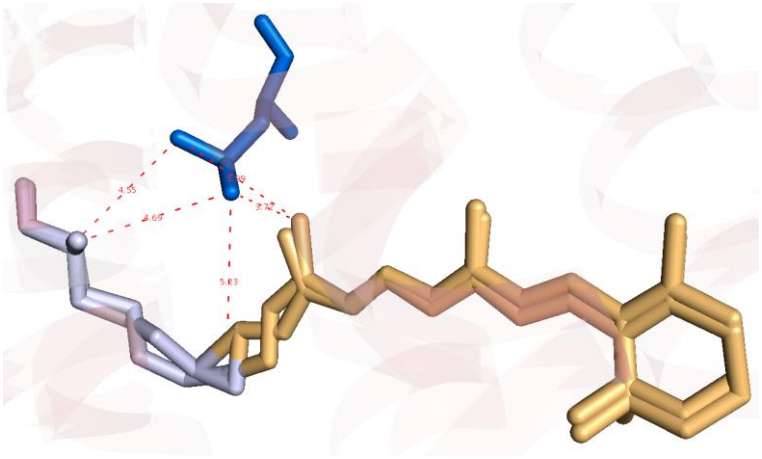

Fig. 9 : Mutation at position 83 where Leucine residue is replaced by Glutamine. The average distance of the polar side chain of Glutamine is ~5Å from the PSB.

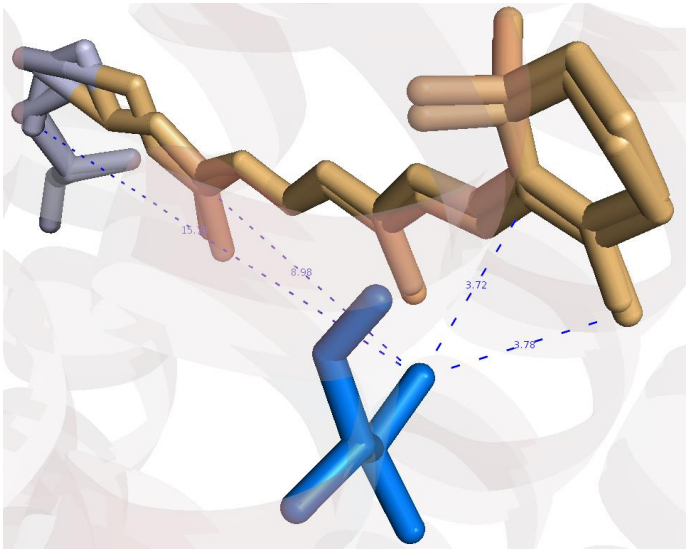

Fig. 10 : Mutation at position 112 where Valine residue is replaced by Asparagine. The average distance of the polar side chain of Asparagine is ~4Å from the β-ionone ring and ~15Å from the PSB.

IV) Fits for AT- and 13C-PSBR for ASR mutants

In the main text we rely on the description of the dynamics for all mutants without showing the fits. This is done in order to have a clear re-presentation of the data. As an example here we show the evaluation of the fitting procedure for W76F mutant kinetics (figure 11). In the two panels of fig.11 the AT- and 13C-PSBR kinetics are shown respectively for different probing wavelength. In the AT-PSBR case the fit yields a bi-exponential fit with 0.5ps and 1.86ps as described in the main text yielding in an average ESL of 0.7±0.05ps. Supplementary, in the case of 13C-PSBR the fit was performed with three exponentials, with 0.18ps, 2.48ps and 19ps time constants. The recorded time delays don't allow us to have an equally good determination of the longer time constant as with the shorter ones, with the errors in ±5ps range. Thus the resulting ESL for 13C isomer is 2.1±0.3ps. The plotted residuals show the quality of the fit.

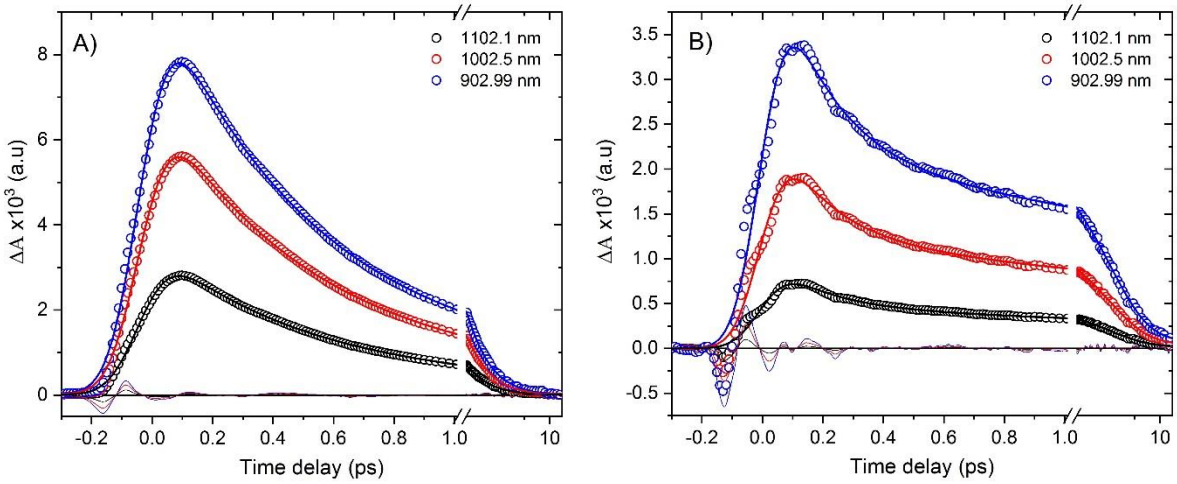

Fig. 11 : Fits of AT (A) & 13C (B) PSBR W76F mutant. The data from different probe wavelength are shown with open circles while the fits with solid lines. The residuals of the fits are shown with thin solid lines.

V) Vibrational coherences in ASR mutants

Figure 12 shows the vibrational modes presented in the PA contribution for DA L83Q mutant. Panels A and B show the resulting FFT spectra for short and longer probe wavelengths with respect to what is described in the main text. Particularly, the modes of 175cm^{-1} and 290cm^{-1} discussed in the main text the vary within ~15cm^{-1} (190cm^{-1} and 300cm^{-1} peaks).

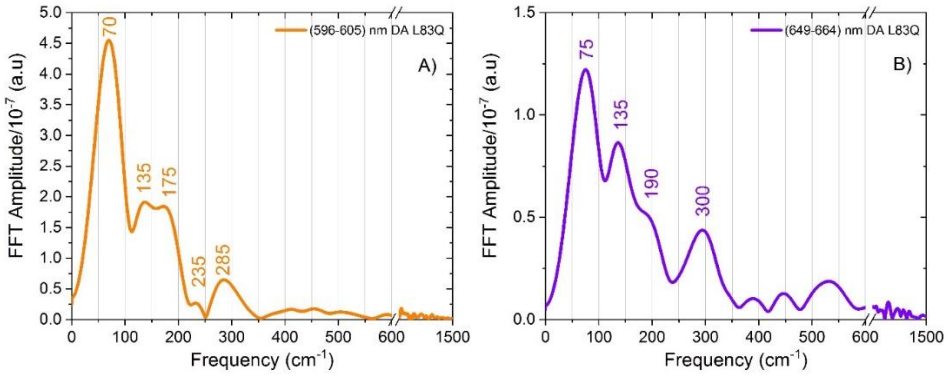

Fig. 12 : FFT-Amplitude of residuals from PA band for DA L83Q mutant.

Figure 13 shows the FFT spectra of ESA and ESA/PA contributions for V112N mutant. The resulting modes are similar to what was obtained for W76F and L83Q.

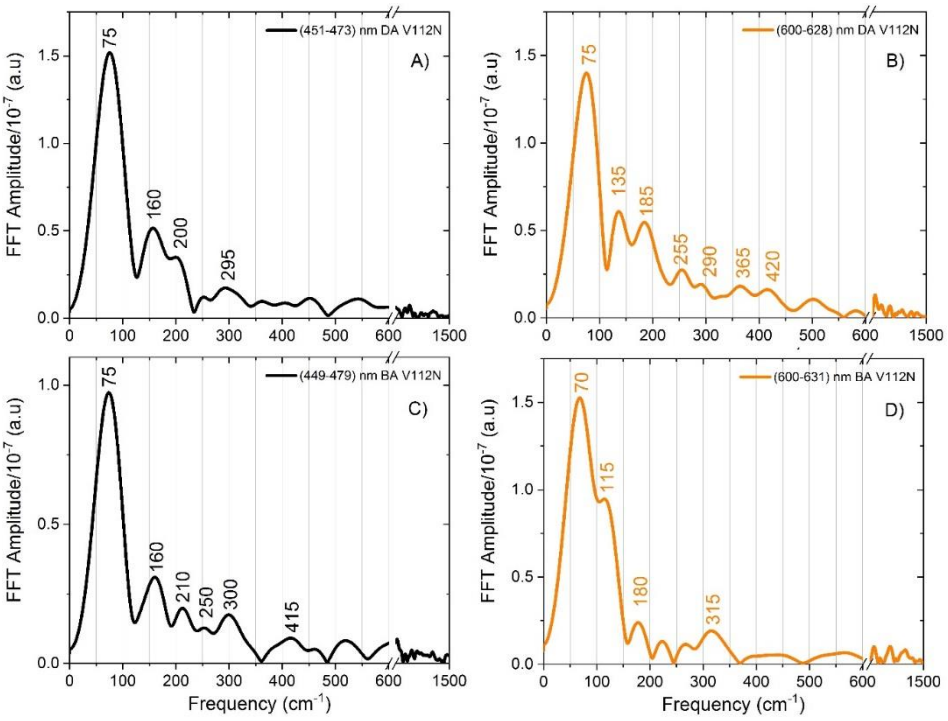

Fig. 13 : FFT-Amplitude of residuals from ESA (449nm-479nm) and PA (600nm-631nm) bands for DA (A,B) and OA (C,D) W76F mutant.

VI) UV-Vis TAS for ASR mutants

Complementary to the results presented in the main text concerning DA W76F and DA L83Q mutants, here we show the TAS data for DA V112N. Figure 14 shows the 2D map with the signatures of ESA, GSB, PA and SE spanning in the (330-830) nm spectral range.

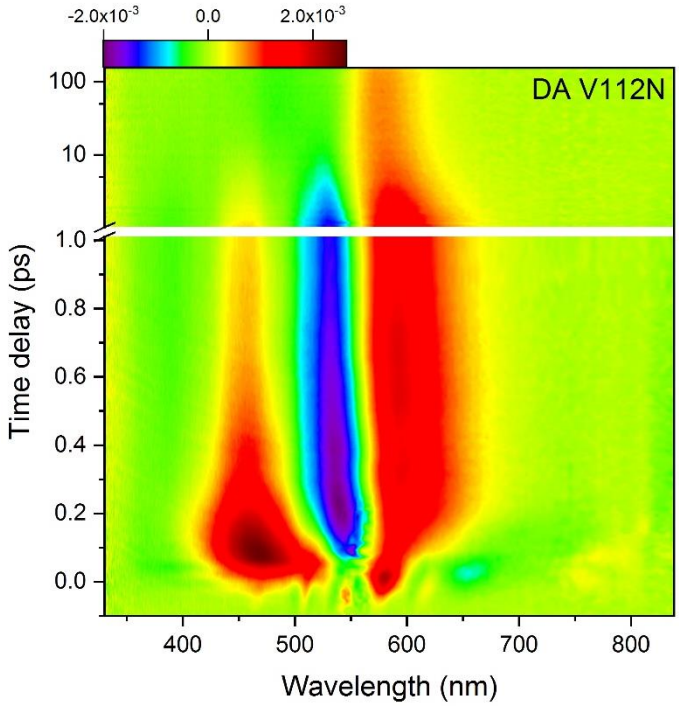

Fig. 14 : Transient absorption maps of DA V112N mutant. The excited state fraction of AT isomer is >97%. The colour bar on top of each map shows the scale for ΔA magnitude.

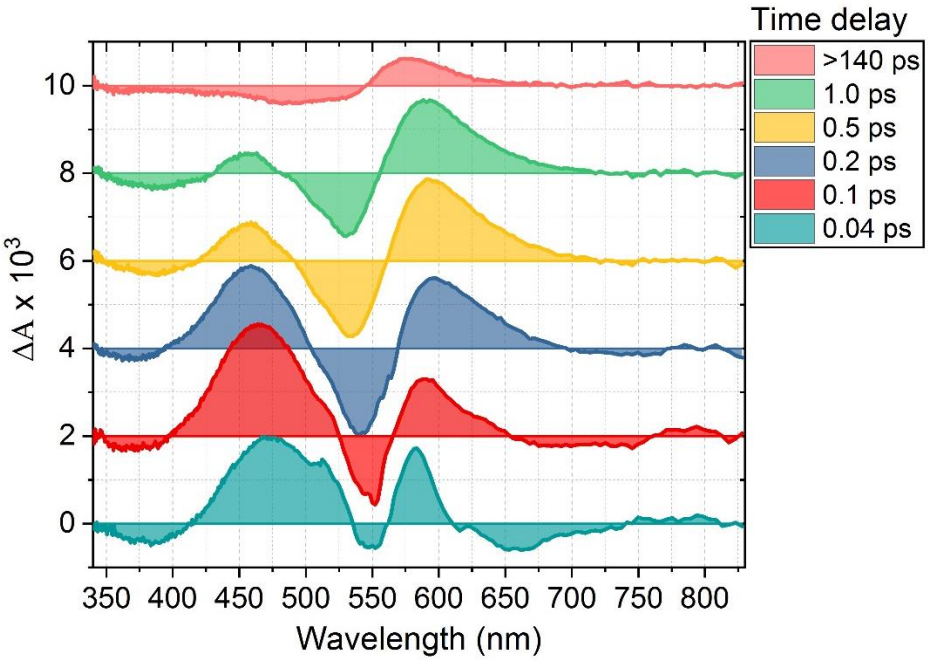

Fig. 15 : Time-resolved TAS spectra for DA V112N mutant for high-lighting delays up to 1ps and a long-time, 140ps, GS-K difference spectrum.

References

(1) Landers, G. M.; Olson, J. A. Rapid, Simultaneous Determination of Isomers of Retinal, Retinal Oxime and Retinol by High-Performance Liquid Chromatography. *J. Chromatogr. A* **1988**, *438*, 383–392. https://doi.org/10.1016/S0021-9673(00)90269-3.

(2) Groenendijk, G. W. T.; de Grip, W. J.; Daemen, F. J. M. Identification and Characterization of Syn- and Anti-Isomers of Retinaloximes. *Anal. Biochem.* **1979**, *99* (2), 304–310. https://doi.org/10.1016/S0003-2697(79)80011-1.

(3) Agathangelou, D.; Orozco-Gonzalez, Y.; del Carmen Marín, M.; Roy, P. P.; Brazard, J.; Kandori, H.; Jung, K.-H.; Léonard, J.; Buckup, T.; Ferré, N.; et al. Effect of Point Mutations on the Ultrafast Photo-Isomerization of Anabaena Sensory Rhodopsin. *Faraday Discuss.* **2018**, *207*, 55–75. https://doi.org/10.1039/C7FD00200A.

(4) Marín-Pérez, M. del C. Benchmarking and Applications of a Computational Photobiology Tool for Design of Novel and Highly Fluorescent Rhodopsin Proteins. Thesis, University of Siena: Italy.

C. Table of Abbreviations

Abbreviations	Description
“o” or “e”	Ordinary or extraordinary axes
13C	13-cis
2DES	Two Dimensional Electronic Spectroscopy
2DSI	Two Dimensional Spectral Shearing Interferometry
ARM	Automatic Rhodopsin Modelling
ASR	Anabaena Sensory Rhodopsin
AT	All trans
B.S	Beam splitter
BA	Blue adapted
BBO	Barium Borate
BLA	Bond length alternation
BR	Bacteriorhodopsin
CaF2	Calcium fluoride
CASSCF	Complete active space self-consistent field
CCD	Charge coupled device
CI	Conical Intersection
D.L	Delay line
D.M	Dichroic Mirror
DA	Dark Adapted
DADS	Decay Associated Differential Spectra
DCM	Dielectric compensating mirrors
E(t)	Electric field
ESA	Excited State Absorption
ESL	Excited State Lifetime
F.L	Fourier Limited
FC	Franck-Condon
FFT	Fast Fourier Transform
FWHM	Full Width at Half Maximum
GA	Green Adapted
GD	Group Delay
GDD	Group Delay Dispersion
GSB	Ground State Bleach
GVD	Group Velocity Dispersion
GVM	Group Velocity Mismatch
HCF	Hollow Core Fiber
HOOP	Hydrogen out of plane
HPLC	High Performance Liquid Chromatography
I.C	Internal Conversion
IRF	Instrument Response Function
IVR	Intramolecular Vibrational Relaxation
LA	Light Adapted
LED	Light Emitting Diode
NIR	Near Infrared
NLC	Non Linear Crystal
NOPA	Non-Collinear Optical Parametric Amplifier

OA	Orange Adapted
OPA	Optical Parametric Amplifier
$P^{(3)}_{NL}$	Third Order Non Linear Polarization
P.M	Parabolic Mirror
PA	Photoproduct Absorption
PES	Potential Energy Surface
PSB	Protonated Schiff Base
PSBR	Protonated Schiff Base of the Retinal
QM/MM	Quantum Mechanics/ Molecular Mechanics
R or NR	Rephasing or Non-Rephasing
Rh	Rhodopsin
Rms	Root mean square
RP	Retinal Protein
S.M	Spherical Mirror
Sa	Sapphire
SE	Stimulated Emission
SFG	Sum Frequency Generation
SHG	Second Harmonic Generation
SPM	Self-Phase Modulation
SRA	Stimulated Raman Amplification
SVD	Singular Value Decomposition
T	Waiting (Population) time
TAS	Transient Absorption Spectroscopy
TPA	Two Photon Absorption
TWINS	Translating Wedge-based Identical Pulses eNconding System
UV	Ultra Violet
VCS	Vibrational Coherence Spectroscopy
Vis	Visible
WLG	White Light Generation
WT	Wild Type
XPM	Cross-Phase Modulation
YAG	Yttrium Aluminium Garnet
ΔA	Differential Absorption
ρ	Density matrix
τ	Coherence time
Φ or QY	Quantum Yield
$\varphi(\omega)$	Spectral phase
Ω	Shear frequency

D. List of publications

1. D. Agathangelou , Y. El Khoury , A. Cheminal , J. Léonard , H. Kandori , K.-H. Jung and S. Haacke, "*Ultrafast Photoisomerization in Anabaena Sensory Rhodopsin: High Speed but Small Quantum Yield",* Ultrafast Phenomena XX , 2016
2. A-I. Skilitsi , D. Agathangelou , A. Klymchenko , Y. Mély , S. Haacke , J. Léonard, "*Ultrafast, Solvation-Controlled Excited-State Intramolecular Proton Transfer in 4'-Methoxy-3-Hydroxyflavone*", Ultrafast Phenomena XX , 2016
3. Y. Orozco-Gonzalez, M. Manathunga, M. Del Carmen Marin, D. Agathangelou, K-H. Jung, F. Melaccio, N. Ferré , S. Haacke, K. Coutinho, S. Canuto, M. Olivucci, "*An Average Solvent Electrostatic Configuration Protocol for QM/MM Free Energy Optimization: Implementation and Application to Rhodopsin Systems", Journal of Chemical Theory and Computation*", 2017,13 (12)
4. M. Gueye, M. Manathunga, D. Agathangelou, Y. Orozco-Gonzalez, M. Paolino, S. Fusi, S. Haacke, M. Olivucci, J. Léonard, *"Engineering the vibrational coherence of vision into a synthetic molecular device"*, Nat. Comm. , 2017 ,9 (1), 313
5. D. Agathangelou , Y. Orozco-Gonzalez, M.del Carmen Marin Perez, P.P. Roy, J. Brazard, H. Kandori, H-H Jung, J. Leonard, T. Buckup, N. Ferre, M. Olivucci and S. Haacke , J. Léonard, "*Effect of point mutations on the ultrafast photo-isomerization of Anabaena Sensory Rhodopsin*", Faraday Discussions, 2018, **207**, 55-75
6. A.I. Skilitsi, D. Agathangelou, I. Shulov, J. Conyard, S. Haacke, Y. Mély, A. S. Klymchenko, J. Léonard, *"Ultrafast photophysics of the environment-sensitive 4'-methoxy-3-hydroxyflavone fluorescent dye"*, PCCP, 2018 , 20 (11)
7. M. del Carmen Marin, D. Agathangelou , Y. Orozco-Gonzalez, A. Valentini, Y. Kato, R. Abe-Yoshizumi, H. Kandori, K-H Jung, S. Haacke, M. Olivucci, "*Fluorescence Enhancement of a Microbial Rhodopsin via Electronic Reprogramming*" J. Am. Chem. Soc., 2019, 141 (1), 262-271